

BULLETIN OF MAGNETIC RESONANCE

*The Quarterly Review Journal of the
International Society of Magnetic Resonance*

VOLUME 18

August 1996

NUMBER 1/2

Proceedings of the International Society of Magnetic Resonance XIIth Meeting Part II



16th - 21st JULY 1995 • SYDNEY • AUSTRALIA

ISMAR 95

... the next 50 years

TWELFTH CONFERENCE OF THE INTERNATIONAL SOCIETY OF MAGNETIC RESONANCE

BULLETIN OF MAGNETIC RESONANCE

*The Quarterly Review Journal of the
International Society of Magnetic Resonance*

Editor:

DAVID G. GORENSTEIN

*Sealy Center for Structural Biology
The University of Texas Medical Branch
Galveston, Texas 77555-1157 U.S.A.
Phone: 409-747-6800
Fax: 409-747-6850
INTERNET: david@nmr.utmb.edu*

Editorial Board:

E.R. ANDREW
*University of Florida
Gainesville, Florida, U.S.A.*

LAWRENCE BERLINER
*Ohio State University
Columbus, Ohio, U.S.A.*

ROBERT BLINC
*University of Ljubljana
Ljubljana, Slovenia*

H. CHIHARA
*Osaka University
Toyonaka, Japan*

GARETH R. EATON
*University of Denver
Denver, Colorado, U.S.A.*

DANIEL FIAT
*University of Illinois at Chicago
Chicago, Illinois, U.S.A.*

SHIZUO FUJIWARA
*University of Tokyo
Bunkyo-Ku, Tokyo, Japan*

DAVID GRANT
*University of Utah
Salt Lake City, Utah, U.S.A.*

ALEXANDER PINES
*University of California
Berkeley, California, U.S.A.*

M. MIK PINTAR
*University of Waterloo
Waterloo, Ontario, Canada*

CHARLES P. POOLE, JR.
*University of South Carolina
Columbia, South Carolina, U.S.A.*

BRIAN SYKES
*University of Alberta
Edmonton, Alberta, Canada*

The *Bulletin of Magnetic Resonance* is a quarterly review journal by the International Society of Magnetic Resonance. Reviews cover all parts of the broad field of magnetic resonance, viz., the theory and practice of nuclear magnetic resonance, electron paramagnetic resonance, and nuclear quadrupole resonance spectroscopy including applications in physics, chemistry, biology, and medicine. The *BULLETIN* also acts as a house journal for the International Society of Magnetic Resonance.

CODEN: BUMRDT

ISSN: 0163-559X

Bulletin of Magnetic Resonance, The Quarterly Journal of International Society of Magnetic Resonance. 1996 copyright by the International Society of Magnetic Resonance. Rates: Libraries and non-ISMAR members \$90.00, members of ISMAR, \$30.00. All subscriptions are for a volume year. All rights reserved. No part of this journal may be reproduced in any form for any purpose or by any means, abstracted, or entered into any data base, electronic or otherwise, without specific permission in writing from the publisher.

Council of the International Society of Magnetic Resonance

President: A. PINES, U.S.A.

Vice-President: M. GOLDMAN, France

Founding Chairman: D. FIAT, U.S.A.

Secretary-General: P. SERVOZ-GAVIN, France

Treasurer: R.R. VOLD, U.S.A.

Past President: R. FREEMAN, England

J. ANGLISTER <i>Israel</i>	E.D. BECKER <i>U.S.A.</i>	M.R. BENDALL <i>Australia</i>
G. BODENHAUSEN <i>Switzerland</i>	P.T. CALLAGHAN <i>New Zealand</i>	S. CLOUGH <i>England</i>
R. DESLAURIERS <i>Canada</i>	S. FORSEN <i>Sweden</i>	C. FYFE <i>Canada</i>
E.L. HAHN <i>U.S.A.</i>	R.K. HARRIS <i>England</i>	M.J.R. HOCH <i>S. Africa</i>
H-J. JAKOBSEN <i>Denmark</i>	R. KAPTEIN <i>The Netherlands</i>	D. KELLY <i>Australia</i>
C.L. KHETRAPAL <i>India</i>	B. MARAVIGLIA <i>Italy</i>	M. MEHRING <i>Germany</i>
H.C. PANEPUCCI <i>Brazil</i>	V. PETROSIAN <i>C.I.S.</i>	M.M. PINTAR <i>Canada</i>
M. PUNKKINEN <i>Finland</i>	J. REISSE <i>Belgium</i>	G.C.K. ROBERTS <i>England</i>
V. SKLENAR <i>Czechoslovakia</i>	C.P. SLICHTER <i>U.S.A.</i>	P. SOHAR <i>Hungary</i>
H.W. SPIESS <i>Germany</i>	H. STERK <i>Austria</i>	T. TERAOKA <i>Japan</i>
J.S. WAUGH <i>U.S.A.</i>	A.B. WIECKOWSKI <i>Poland</i>	X-W. WU <i>China</i>
K. WÜTHRICH <i>Switzerland</i>	C.S. YANNONI <i>U.S.A.</i>	

The aims of the International Society of Magnetic Resonance are to advance and diffuse knowledge of magnetic resonance and its applications in physics, chemistry, biology, and medicine, and to encourage and develop international contacts between scientists.

The Society sponsors international meetings and schools in magnetic resonance and its applications and publishes the quarterly review journal. The *Bulletin of Magnetic Resonance*, the house journal of ISMAR.

The annual fee for ISMAR membership is \$25 plus \$30 for a member subscription to the *Bulletin of Magnetic Resonance*.

Send subscription to: International Society of Magnetic Resonance
Professor Regitze R. Vold, Treasurer
Department of Chemistry & Biochemistry
University of California, San Diego
9500 Gilman Drive
La Jolla, CA 92093-0359
(619) 534-0200; FAX (619) 534-6174
e-mail: rrvold@ucsd.edu

ORGANIZING COMMITTEE
for
ISMAR 95

L.D. FIELD, CHAIRMAN

Department of Organic Chemistry
University of Sydney
Sydney, NSW 2006
Australia

M. BATLEY

School of Chemistry
Macquarie University
North Ryde, NSW 2109
Australia

W.A. BUBB

Department of Biochemistry
University of Sydney
Sydney, NSW 2006
Australia

E.J. DELIKATNY

Department of Cancer Medicine D06
University of Sydney
Sydney, NSW 2006
Australia

G.L. MENDZ

School of Biochemistry
& Molecular Genetics
UNSW
Sydney, NSW 2052
Australia

B.A. MESSERIE

Department of Organic Chemistry
University of Sydney
Sydney, NSW 2006
Australia

J.M. POPE

School of Physics
Queensland University of Technology
GPO Box 2434
Brisbane, QLD 4001
Australia

F. SEPAROVIC

Division of Food Science & Technology
CSIRO
PO Box 52
North Ryde, NSW 2113
Australia

G. TOWN

Department of Electrical
Engineering (J03)
University of Sydney
Sydney, NSW 2006
Australia

CO-EDITORS OF THE PROCEEDINGS

D.G. GORENSTEIN

Department of HBC&G
Sealy Center for Structural Biology
University of Texas Medical Branch
Galveston, TX 77555-1157

L.D. FIELD

Department of Organic Chemistry
University of Sydney
Sydney, NSW 2006
Australia

ACKNOWLEDGMENTS

On behalf of everyone attending the Conference, the Organizing Committee thanks all those who have provided us with financial or material support. We are extremely grateful to the following organizations for their generous assistance.

US Department of Energy/Lawrence Berkeley Laboratory
Bruker Australia Pty. Ltd.
Siemens, Medical Applications Pty. Ltd.
Varian Australia Pty. Ltd.
Society of Magnetic Resonance
Australian Tourist Commission
General Electric Medical Systems
NMR Magnex Scientific Inc.
Australian Institute of Physics
Australian Society for Biochemistry and Molecular Biology
Royal Australian Chemical Institute (Polymer Division)
NSW Travel Centre
Air New Zealand
Adrich Chemical Co.
National Australian Bank

Proceedings of the XIIth Meeting of the
International Society of Magnetic Resonance

Part II

July 16 - 21, 1995

Sydney, Australia

Contents

Precise and Accurate Determination of Isotope Ratios by Nuclear Magnetic Resonance Spectroscopy , G.J.Martin, M.L. Martin & Y.L. Martin.....	9
FT Pulsed ESR/ESTN (Electron Spin Transient Nutation) Spectroscopy Applied to High-Spin Systems; Direct Evidence of the First High-Spin Polymer as Models for Organic Ferro- and Superpara-Magnets , T. Takui, K. Sato, D. Shiomi, K. Itoh, T. Kaneko, E. Tsuchida & H. Nishide.....	21
Strategies for CW and Pulsed EPR in Materials Science , J.R. Pilbrow	30
Functional Magnetic Resonance Imaging of the Human Brain , K.R. Thulborn, J. Gillen, B. McCurtain, C. Betancourt & J.A. Sweeney	37
Dependence on Electronic Structure of the Site of Proton Transfer from Alkane Radical Cations to Alkane Molecules: ESR Evidence in Irradiated CCl₃F/Alkane and Pentane-d₁₂/ Alkane Systems , D. Steinlet & J. Ceulemans	43
Rotating Magnetic Gradient Fields for Imaging Couette Flow of Simple and Complex Fluids , J.A. Hopkins, R.E. Santini & J.B. Grutzner	48
<i>In Vivo</i> ESR Observation of Nitrosobenzene-based Bioradicals in Living Animals: Free Radical Scavenging Activities of Natural Carotenoids , H. Fujii, H. Nishino, J. Koscielniak & L.J. Berliner.....	55
The Active Site Structure of Bovine Meizothrombin(desF1) as Probed by ESR Spin Labels , P.D. Boxrud & L.J. Berliner	60
NMR Studies on Antarctic Sea Ice , P. Callaghan & C. Eccles	62
Application of Radiation Damping Line Shape Theory to Interpreting the Harmonic Peaks in Two Dimensional Spectra of Liquid Water , X-A. Mao & J-X. Guo	65
Determination of the Three-Dimensional Solution Structure of the Oxidised Form of Mesophilic Thioredoxin from <i>Escherichia coli</i> and Modeling by Homology of the Thermophilic Thioredoxin from <i>Bacillus Acidocaldarius</i> , G. Nicastro, C. de Chiara, L. Franzoni, M. Tato, F. Nozza, E. Carrara & C. Nicolini.....	71
750 MHz NMR Studies of Chemically Modified DNA Structure/Dynamics: Sequence Context Effects and Protein Recognition. , M.A. Kennedy, K. McAteer, J.M. Lingbeck, B.D. Thrall, D.L. Springer, M.G. Kubinec & P.D. Ellis	77
Structural Studies of O-Vanillin Derivatives and Their Metal Complexes by One and Two Dimensional NMR , G.A. Naganagowda, S. Raghothama, B.V. Agarwala, C.L. Khetrpal	81
Solid State NMR Characterization of Highly Conductive Lithium-Based Ceramics , K.M. Nairn, M. Forsyth, M. Greville, T.J. Bastow, M.E. Smith & D.R. Mac Farlane.....	85

NMR Investigation of a New Semisynthetic Bioactive Compound , C. Rossi, A. Donati, D. Renzoni, C. Bonechi & N. Marchettini.....	87
A Comparison by NMR of a C-MYC Binding DNA Oligomer and its Non-Binding Methylated Analogue , W. Bicknell, K.J. Cross & K.J. Embrey.....	91
Temperature Dependence of ^7Li Linewidth in Poly(propylene oxide) Complexed with LiClO_4 and LiBF_4 Under Different Decoupling Conditions , T.J. Bonagamba, N.C. Mello, L.H. Mattoso, H. Panepucci & J.P. Donoso.....	92
^7Li NMR Investigation of the Poly (ethylene glycol-400) Disterate-LiClO_4 Complex , T.J. Bonagamba, M.V. Giotto, H. Panepucci, A.L. de Oliveira & C.L. Sangioge.....	94
Elimination of Longitudinal and Transverse Multiple Quantum Artifacts in 2D COSY NMR Spectra , G.J. Bowden, T.H. Heseltine, G.E. Ball & M.J. Prandolini.....	96
Application of Adaptive Simulated Annealing to Optimization of Transverse Gradient Coils with Concentric Return Paths , M.L. Buszko, M.F. Kempka, E. Szczesniak, D.C. Wang & E.R. Andrew.....	98
NMR and the Information Superhighway: What is on the Net? , M.L. Buszko.....	100
Mechanochemical Reduction of Haematite - The Effect of NaCl Electrolyte , S.J. Campbell, W.A. Kaczmarek, E. Wu & G-M. Wang.....	101
Powder ESR Spectra of Specific Alkyl Radicals: Selective ESR Observation of Specific Alkyl Radicals in γ-Irradiated cis-Decalin-d_{18}/Chloroalkane and Bromoalkane Systems at Cryogenic Temperatures , D. Stienlet & J. Ceulemans.....	104
Alkane Aggregation and Proton Transfer from Alkane Radical Cations to Alkane Molecules in γ-Irradiated CCl_3F/Alkane Systems at Cryogenic Temperatures: a Summary of ESR Evidence , G. Luyckx & J. Ceulemans.....	107
<i>In Vivo</i> Non-Invasive Determination of Abnormal Water Diffusion of EAE in the Rat by Diffusion-Weighted NMR Imaging , M.R. Verhoye, E.J. s-Gravenmade, E.R. Raman, J. Van Reempts, R. Dommissie & A. Van der Linden.....	110
<i>In Vivo</i> and Non Invasive Measurement of Temperature Stress Induced Changes in the Energy Metabolism of the Common Carp, by ^{31}P-NMRS , R. Borger, J. Van Audekerke, R. Blust, R. Dommissie & A. Van der Linden.....	112
Parahydrogen: The Means to See the Unseen. NMR Studies of Metal Complexes with Parahydrogen , S.B. Duckett, G.K. Barlow, M.G. Partridge, R.J. Mawby & B.A. Messerle.....	114
Magic-Angle-Spinning Two-Dimensional NMR for the Study of Conformation of Leucine Enkephalin Oriented in Lyotropic Liquid Crystal , A. Kimura, N. Kuni, T. Jikihara & H. Fugiwara.....	117
Tertiary Structure Determination of a Potent C5a Semi-synthetic Antagonist in Solution by Nuclear Magnetic Resonance Spectroscopy , X. Zhang, W. Boyar, M. Toth, N. Galakatos & N.C. Gonnella.....	119
Proton Magnetic Resonance Study of High Resolution Solution Structure of Hordothionin-α , K-H. Han, K-H. Park, H-J. Yoo, H. Cha, S.W. Suh, F. Thomas, T-S. Moon & S-M. Kim.....	123

- Nuclear Magnetic Resonance Solution Structure of Calciseptine, a Small Protein with Ca²⁺ Channel Blocking Activity from Black Mamba (*Dendroaspis polylepis polylepis*),** H. Haruyama, T. Takayama & H. Hanzawa 125
- Are NMR Chemical Shift Calculations of Small Molecules Inexpensive? You Get What You Pay For!,** J.F. Hinton, K.Wolinski, P. Kozlowski & P. Pulay 127
- A Method for Removing Geminal Proton Resonances from Oligonucleotide Spectra: 1D and 2D Applications,** H.A. Berthon & M.A. Keniry 129
- ¹H, ¹³C, ¹⁵N, and ³¹P NMR Methods for Studying Metabolites in an N₂-Fixing Root Nodule Symbiosis, *Alnus incana* x *Frankia*,** P. Lundberg, P-O. Lundquist & K. Huss-Danell 131
- In vivo NMR monitoring of the Metabolism of [1-¹³C] Glucose in the Sophorose Lipid Producing Yeast *Candida (Torulopsis) apicola*,** R. Meusinger, R.K. Hommel and U. Himmelreich 133
- Phosphoryl Group - Metal Ion Interactions Probed by ¹⁷O NMR Spectroscopy,** M.P. Belciug, A.M. Modro, T.A. Modro & P.L. Wessels 135
- Comparison of Counterion Effects in Ionomer Membranes Using ¹⁴N NMR Spectroscopy,** M. Rankothge, J. Hook & G. Moran 137
- NMR as a Tool for Understanding Fundamental Dynamic Properties of Solid Polymer Electrolytes.,** S.Ng, M.E. Smith, M. Garcia, D. MacFarlane & M. Forsyth 139
- EPR Investigation of Unstable Intermediates in Photoinduced Reactions at CdS Semiconductor Particles Dispersed on CdO ,** Y. Nakaoka & Y. Nosaka 141
- Carbon-Proton Coupling Constants in Aromatic and in Alicyclic Compounds,** B. Podanyi & M. Morvai 143
- ¹³C Relaxation in Natural Diamond,** E.C. Reynhardt & C.J. Terblanche 145
- NMR Solves Drug Problems with Speed,** M.J. McTigue, R.T.C. Brownlee, J.R. Pearson, S.J. Pratt, J.E. Rowe, M. Sadek & E.M. Sear 147
- INEPT NMR of Paramagnetic Compounds.,** M. Sadek, R.T.C. Brownlee, S.D.B. Scrofani & A.G. Wedd 149
- The Voids Analysis of the Refractories Using NMR Micro-imaging Method,** K. Saito, M. Shinohara, H. Tsuno & K. Hasegawa 151
- Oxygen Permselective Hollow Fiber Membrane of Fluoren-based Polyimides (studies on structural analysis and its mechanisms),** K. Saito, M. Hatakeyama, M. Shinohara & K. Fujishiro 153
- FT Pulsed EPR of Exchange-coupled Spin Systems in Transition Metal Clusters and Low-dimensional Magnets,** D. Shiomi, K. Sato, T. Takui & K. Itoh 155
- NMR Studies of the Active Site of the HIV-1 Protease by Site-Specific Labeling,** R. Smith, I.M. Brereton, R.Y. Chai & S.B.H. Kent 157
- Towards TOCSY-free ROESY,** T. Kanthimathi & S. Subramanian 159
- Structural Elucidation of Calmodulin Fragments Using NMR and CD Studies,** L. Gomathi, T. Fairwell, G.A. Krishna, J.A. Ferretti & S. Subramanian 161

Pattern Recognition of Specific Dipolar Networks , C. Seetharaman, S. Subramanian	163
An Ft-Pulsed ESR/ESTN (Electron Spin Transient Nutation) Study of Hyperbranched (π)-Aryl Based Stable High-Spins as Models for Organic Superpara- and Ferro-Magnets T. Takui, K. Sato, D. Shiomi, K. Itoh, J. Veciana, C. Rovira	165
Ferric Iron Porphyrin as Studied by Single-Crystal CW and FT Pulsed ESR/ESTN (Electron Spin Transient Nutation) Spectroscopy , A.S. Ichimura, K. Sato, D. Shiomi, T. Takui, K. Itoh, W.C. Lin, D.H. Dolphin, C.A. McDowell	167
An FT Pulsed ESR/Electron Spin Transient Nutation Study of the Quartet State of Cr(III) in MgO Powder: Detection of its Apparently Vanishing ZFS , K. Sato, D. Shiomi, T. Takui & K. Itoh.....	169
A Powder-Pattern ESR Study of the Quartet States of the Precursors of a Square-Pyramidal Nitridochromium(V) Complex, Cr(III)(bpb)Cl(H₂O) and Cr(III)(bpb)(N₃)₂: Analysis by the Use of Exact Analytical Expressions , K. Sato, D. Shiomi, T. Takui, K. Itoh, T. Shimozono, H. Yoshida, K. Tajima & N. Azuma	171
Exact Analytical Solutions of Eigenfields and Eigenenergies for High Spins ($S \leq 4$) , K. Sato, T. Takui & K. Itoh.....	173
¹³C NMR of Triglycerides , M-R. Van Calsteren, C. Barr, P. Angers & J. Arul	175
Aqueous Silica Sols: A Study of the Spin-lattice Relaxation Time T₁ by the Field-Cycling NMR Technique , J. Van Craen, P. Roose, Y. De Smet & H. Eisendrath.....	178
Solution Structure of a Biologically-active Cyclic LDV Peptide Containing a β-turn Mimetic , J.H. Viles, J. Uppenbrink, C.M. Moody, M. Sims, P.M. Doyle, J. Harris, P.J. Sadler & J.M. Thornton	180
¹H and ¹¹³Cd NMR Studies of Metal Binding to Isolated Albumin and Albumin in Blood Plasma , J.H. Viles, A. Tucker, S.U. Patel & P.J. Sadler.....	182
Demonstration of Tissue Cation Compartmentation Using ¹¹³Cs NMR , R.M. Wellard, B.P. Shehen, D.J. Craik & W.R. Adam.....	184
A ²⁷Al NMR Study of Aluminium: Humic Substances Interactions , J. Hook, L. Xiaoqiao & R.F. Howe.....	186
Calendar of Forthcoming Conferences	188
Instructions for Authors	189

Precise and Accurate Determination of Isotope Ratios by Nuclear Magnetic Resonance Spectroscopy

Gérard J. Martin, Maryvonne L. Martin
NMR Laboratory, University of Nantes - CNRS
2 rue de la Houssinière
44072 Nantes cedex 03 (France)

Yves-Loïc Martin
Analytical Chemistry Laboratory, INA-PG
16 rue Claude Bernard
75231 Paris cedex 05 (France)
Present address : EUROFIN S.A, Site de la Géraudière, CP 4001
44073 Nantes cedex 03 (France)

Abstract

Stable isotopes at the natural abundance are very powerful tools for tracing the origin of products and the nature of manufacturing processes. A chemical species is a complex mixture of isotopomers containing one (or more) heavy isotopes (^2H , ^{13}C , ...). These isotopomers have specific genealogies related to the various transformations undergone by their precursors. NMR spectroscopy is the only analytical technique which is able to determine site-specific isotope ratios without prior transformation of the sample. The overall performance of high resolution ^2H -NMR in determining (D/H) ratios is discussed in terms of acquisition and handling of the FID with a view to minimising random and systematic errors. The signal-to-noise ratio and therefore the number of spectra replications have a critical influence on precision. Systematic deviations, which deteriorate the reproducibility, are greatly reduced by using a dedicated curve fitting procedure. Data treatment is illustrated in the case of origin assessment and analysis of mixtures. The investigation of Site-specific Natural Isotope Fractionation by NMR (SNIF-NMR), initially devoted to hydrogen, can be extended to other quadrupolar isotopes (^{17}O)

and to important dipolar nuclei (^{13}C , ^{15}N) and some trends are presented.

SITE-SPECIFIC ISOTOPE RATIOS

When a plant absorbs water from different sources, CO_2 from the atmosphere, and nitrogen and nutrients from the soil, in order to photosynthesize glucose which is subsequently transformed into various metabolites, a great number of enzymic transformations take place and induce specific isotopic fractionation of H, C, N and O. As a result, the different natural products (cellulose, carbohydrates, proteins, lipids or smaller metabolites) which may be recovered from the plant, exhibit characteristic isotope contents⁽¹⁻³⁾. These isotopic fingerprints depend not only on the cumulated kinetic (KIE) and thermodynamic (TIE) isotope effects which govern the successive transformation steps but also on the isotopic contents of the starting raw materials used by the plant⁽⁴⁾.

If local variations induced by the proximity of large urban conglomerates or fossil fuel power stations are ignored, the isotopic content of atmospheric CO_2 is nearly constant all over the world. Expressed on the δ -scale⁽⁵⁻⁸⁾

$$\delta (\text{‰}) = \frac{(\text{H/L})_i - (\text{H/L})_{\text{ref}}}{(\text{H/L})_{\text{ref}}} 1000 \quad [1]$$

(where H and L denote the heavy and the light isotopes respectively), the carbon isotopic parameter of CO₂ is $\delta^{13}\text{C} \simeq 8 \text{ ‰}$ with respect to the reference PDB^(9,10). Some regional and seasonal isotopic variations⁽¹¹⁾ are exhibited by

oxygen which is characterized by a value $\delta^{18}\text{O} \simeq 40 \text{ ‰}$ with respect to the reference V. SMOW (table 1).

	² H (ppm)	¹³ C (%)	¹⁵ N (%)	¹⁸ O (%)
R	155.76	1.12372	0.36765	0.20052
A	155.74	1.11123	0.3663	0.20012
Ref.	V. SMOW	PDB	air	V. SMOW
Product	H ₂ O	CaCO ₃	N ₂	H ₂ O

Table 1 : Isotopic values of the international standards used to refer the isotopic ratios of light elements^(5-8,10,27). The isotopic ratio, R, is defined as the ratio of the numbers of heavy and light isotopes and the isotopic abundance, A, is the ratio heavy/(light + heavy). V.SMOW denotes Standard Mean Ocean Water managed in Vienna by IAEA, and PDB refers to Pee Dee Belemnite (South Carolina).

For water on the other hand, each region of the world is characterised by a typical isotopic ratio which can be directly related to the climatic conditions of the location considered⁽¹²⁾

$$\delta^{18}\text{O}(\text{‰}) = -11.8 + 0.42(\pm 0.03)T - 0.008(\pm 0.005)P \quad [2]$$

$$\text{and } \delta^2\text{H}(\text{‰}) = -85.8 + 3.4T - 0.065 P \quad [3]$$

where T and P are respectively the monthly averages for temperature (°C) and precipitation (mm). Equation [3] has been computed by taking into account the Craig relationship^(12,13) between $\delta^2\text{H}$ and $\delta^{18}\text{O}$ of meteoric water.

The site-specific isotope ratio, R_i, of a given molecular site, i⁽¹⁴⁾, can be calculated from :

$$R_i = \frac{P_{ws} M_{ws} M_A t_{ws} I_{iA}}{P_{iA} m_A M_{ws} t_A I_{ws}} R_{ws} \quad [4]$$

where m, P, M, t and I denote respectively the mass of product, A, or of working standard, WS, in the NMR cell, the site population, the molecular weight, the purity of the product and the ²H, ¹³C, ¹⁵N ... NMR signal intensity⁽¹⁵⁾. The isotope ratio of the working reference, R_{ws}, must be carefully calibrated against the relevant international standard.

Alternatively, if the product A must be recovered intact or if signals of the working

reference interfere with those of the product, R_i may be obtained from the molar fraction, f_i, of isotopomer i without adding any isotopic reference in the NMR tube :

$$R_i = \left(\frac{f_i}{F_i} \right) \bar{R}_A \quad [5]$$

where F_i is the statistical molar fraction of isotopomer i

$$F_i = P_i / \sum_{i=1}^n P_i \quad [6]$$

The actual molar fraction, f_i, can be directly obtained from the signal intensities measured in the ²H-NMR spectrum

$$f_i = I_i / \sum_{i=1}^n I_i \quad [7]$$

In this strategy, the overall isotope ratio of product A,

$$\bar{R}_A = \sum_{i=1}^n F_i R_i \quad [8]$$

must be measured independently by isotope ratio mass spectrometry⁽¹⁶⁾

ACCURACY OF THE DETERMINATION OF ISOTOPE RATIOS

The advantages and disadvantages of HR deuterium NMR are well known. Having a spin quantum number $I=1$, ^2H exhibits a quadrupolar relaxation mechanism. However the signals remain relatively narrow in the liquid state (0.2 to 10 Hz) and the quenching of the dipolar mechanism has the advantage of eliminating nuclear Overhauser effects. Since sensitivity is not really a problem for most studies of foods and beverages, the most striking disadvantage is probably the small chemical shift discriminating potential of ^2H , even at very high fields. In practice, a dedicated instrument is required to obtain precise and accurate quantitative values. Since a given spectrum is usually replicated several times in order to reduce the contribution of random errors, a specific locking device (^{19}F) and an automatic sample changer are included on the spectrometer. Compared to deuterium, dipolar nuclei such as ^{13}C or ^{15}N present small but significant intensity instabilities under ^1H decoupling conditions. Precise but sometimes inaccurate isotope ratios are obtained and tricky and cumbersome experimental acquisition protocols must be followed to avoid systematic errors. Random errors are directly proportional to the reciprocal of the signal-to-noise ratio. In order to minimize possible bias, it is recommended that n replicate experiments are run and that spectra with intensity values outside a given confidence region are detected and generally eliminated. In theory, the signal intensity corresponding to a series of $NS \times n$ acquisitions (NS being the number of scans) is equivalent to that of a single spectrum having the same number of scans. However, from statistical considerations, the strategy of spectra replications is preferable. According to the ISO definition, the standard deviation of repeatability, S_r , is the square root of the mean of the intensity variance of p series of n replications of a spectrum carried out in a given laboratory during a short period of time

$$S_r = \sqrt{\frac{1}{p} \sum_{j=1}^p S_j^2} \quad \text{with}$$

$$S_j^2 = \sum_{i=1}^n \frac{(I_{ji} - \bar{I}_j)^2}{n-1} \quad [9]$$

Using appropriate tests for variance homogeneity, such as the Cochran test⁽¹⁷⁾, it is permissible to eliminate one outlying spectrum among a series of 8 to 10. The remaining variance may be significantly decreased, whereas the mean intensity only changes slightly.

When an analytical technique is to be used for legal purposes or for quality control in industry, its *reproducibility* is the critical criterion. The standard deviation of reproducibility, S_R , is the square root of the sum of the *repeatability*, S_r^2 , and *inter-laboratory* variances, S_L^2 . In NMR spectroscopy, S_L^2 is mainly conditioned by systematic variations arising from different FID handling skills (base line and phases corrections, curve fitting procedures ...) in the different laboratories. The second most notable source of systematic deviations is related to sample treatment. The various steps of sample preparation (extraction, purification, derivatization ...) may be the source of kinetic or thermodynamic isotope effects which will induce isotopic fractionation to a greater or lesser extent. These effects, which must be eliminated or corrected for, will not be considered here since they are not directly relevant to NMR spectroscopy.

During the first inter-laboratory study on the determination of site-specific isotope ratios, organised in 1989 on behalf of the Community "Bureau of References" of the E. U., three sealed NMR tubes containing ethanol samples from different origins were distributed to fifteen laboratories. Each participant was asked to run 8 or 10 spectra of the three samples, to store the FID's on a magnetic support, and to process the FID following either his own or a defined experimental protocol. In addition, all the stored FID's were processed independently by one operator, following the recommended protocol. The repeatability variance for individual processing was nearly twice that obtained for homogeneous treatment by a single operator.

In our experience, when a suitable protocol of good analytical practices is installed in a laboratory and scrupulously followed by the operator, the precision and accuracy of quantitative NMR spectroscopy may be of the order of 0.1%. As far as hydrogen isotope ratios are concerned, this performance compares very favourably with that of Mass Spectrometry (Table 2).

Isotope Ratio	Substrate Studied	Analytical Technique	Product Concerned	Repeatability S_r (‰)	Reproducibility S_R (‰)	Normalization Institute (a)
(D/H)	Water	MS	Juices	1.3	2.7	ECN 1994
	Ethanol	NMR	Wines	1.2	1.8	JRC-EU 1994
	Sugars	NMR	Juices	1.2	1.8	ECN-AOAC 1995
$(^{13}\text{C}/^{12}\text{C})$ (b)	Ethanol	MS	Wines	0.2	0.25	ECN-OIV 1996
	Sugars	MS	Juices	0.1	0.25	ECN 1993
	Pulps	MS	Juices	0.2	0.4	ECN 1996
$(^{18}\text{O}/^{16}\text{O})$	Water	MS	Juices	0.1	0.15	ECN 1994
	Water	MS	Wines	0.09	0.19	OIV 1995

Table 2 : Comparison of the repeatability, S_r , and reproducibility, S_R , performances of NMR and Mass Spectrometry in the determination of natural abundance isotope ratios^(28,29). The various substrates have been extracted from fruit juices or wines. The values of S_r and S_R are expressed in ‰ units on the δ -scale (eq. 1).

a) ECN : European Committee of Normalization, OIV : Office International de la Vigne et du Vin, AOAC : Ass. Official Analytical Chemists, JRC-EU : Joint Research Center-European Union

b) No official normalization operation has yet been conducted for $(^{13}\text{C}/^{12}\text{C})$ by NMR spectroscopy. Different inter-laboratory studies indicate that S_r is on the order of 1‰ but S_R is much larger and depends critically on the equipment available.

PROCESSING OF NMR SPECTRA FOR QUANTITATIVE DETERMINATIONS

Processing of frequency domain spectra is usually the source of operator dependent errors originating from the phasing and fitting operations⁽¹⁸⁻²⁰⁾. Moreover, manually processing large numbers of repetitive spectra is a time-consuming and tedious task. It is therefore desirable to dispose of a fully automatic quantitative treatment grounded on a rigorous theoretical analysis of the NMR signal. In the absence of truncation of the free induction decay, for reasonable values of the signal to noise ratio (>20), and in the hypothesis of Gaussian noise, complex least squares was theoretically proved to ensure optimum precision compared to all other exact and differentiable algorithms⁽²¹⁾. The linear prediction method⁽²²⁾ is shown to be equivalent to the complex least squares approach but data treatment in the frequency domain offers the advantageous possibility of estimating the quality of the curve-fitting separately for every resonance⁽²¹⁾. A dedicated software, Interliss⁽²³⁾, which works on a Pentium-based PC may also be implemented in the spectrometer computer. It involves a rigorous management of all the

experimental parameters : frequencies, damping factors, intensities, phases, acquisition delay (which is described by intensity and phase parameters). This approach avoids both semi-empirical corrections of the base line, such as polynomial approximations, and modifications of the convergence due to phase adjustments performed on the whole spectrum. The treatment of 16K data points requires about 15s and the programme is very efficient for quantifying spectra with less than 20 signals in the absence of strong overlapping (frequency separation preferably higher than two half-height line widths). It has been shown that data manipulations such as exponential multiplication or zero filling do not improve the precision of the quantitative determinations. In practice the precision is therefore mainly conditioned by the signal to noise ratio. The residuals between the experimental spectrum and the simulated lorentzian spectrum estimate the magnitude of instrumental imperfections due to bad shimming, heterogeneity of the radio frequency field, temperature instabilities... Typical residuals recorded for the same product but with two different spectrometers are illustrated in Figure 1.

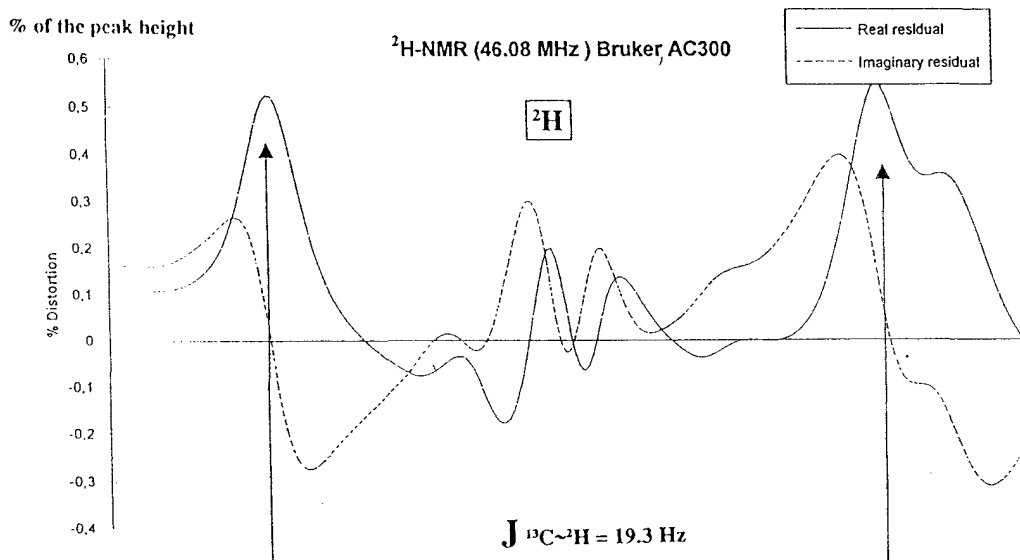
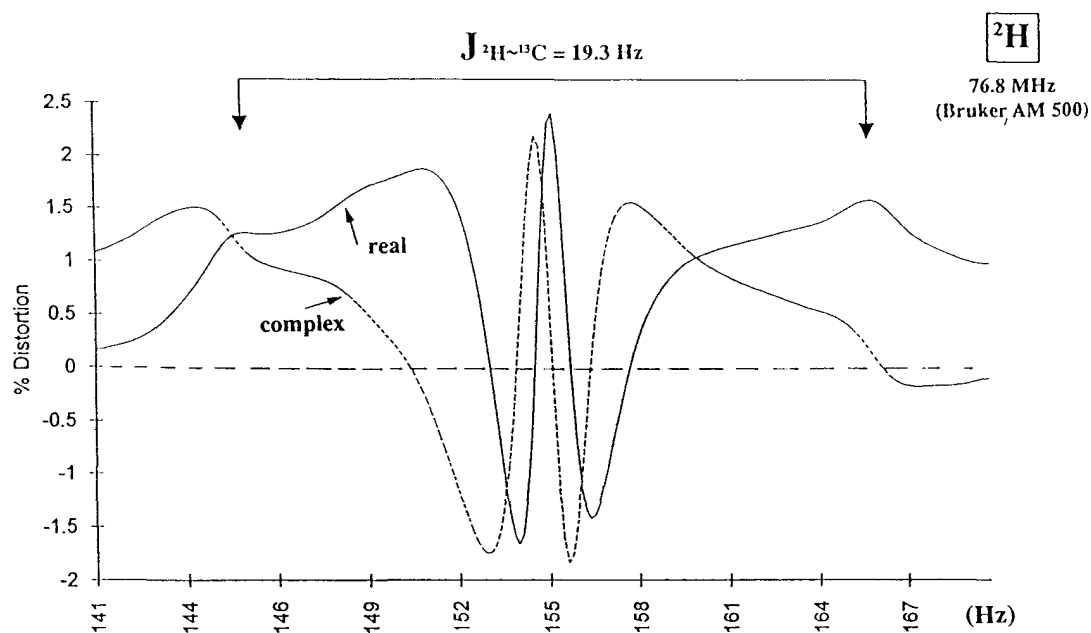


Figure 1 : Estimation of the quality of a complex least squares treatment of NMR spectra⁽²¹⁾. The curve-fitting⁽²³⁾ has been performed on the frequency domain ^2H -NMR spectrum of a mixture of ethanol and tetramethylurea. The residuals between the experimental and theoretical spectra have been represented in the frequency range corresponding to the resonance of the methyl signal of tetramethyl urea. The results of several series of experiments performed at different times could be summed up thanks to the possibility of correcting for chemical shift differences in the frequency domain. The amplitude of the residual is significantly higher with the 76.8 MHz spectrometer than with the 46.1 MHz

equipment which benefited in particular from a more efficient shimming procedure. The pair of satellite signals associated with the isotomers containing both a ^2H and ^{13}C nucleus at natural abundance are clearly detected at 46 MHz.

The residual is larger with the higher field spectrometer. This behaviour is probably due to the greater difficulty to shim very finely the 11.4 T machine with a 10mm OD tube. Operating in the frequency domain offers the possibility of correcting for frequency shifts

between different sets of spectra of the same sample acquired at different periods. Numerous residuals can therefore be coadded in order to detect coherent components normally lost in the Gaussian noise. The extraction of satellite ^2H lines due to isotopomers bi-labelled by ^{13}C and ^2H at the natural abundance level (fig. 1) illustrates the quality of the curve-fitting procedure and the high performance which can be reached in terms of sensitivity. Even in a

situation of one percent dynamic range, species present at a level of $1.5 \cdot 10^{-6}$ are observed via the ^2H nucleus which has an intrinsic sensitivity of about one per cent with respect to ^1H . A sensitivity deficiency of $1.5 \cdot 10^{-8}$ with respect to proton has therefore been overcome. Figure 2 illustrates the performances of the quantitative analysis in the treatment of the six lines spectrum of frambinone.

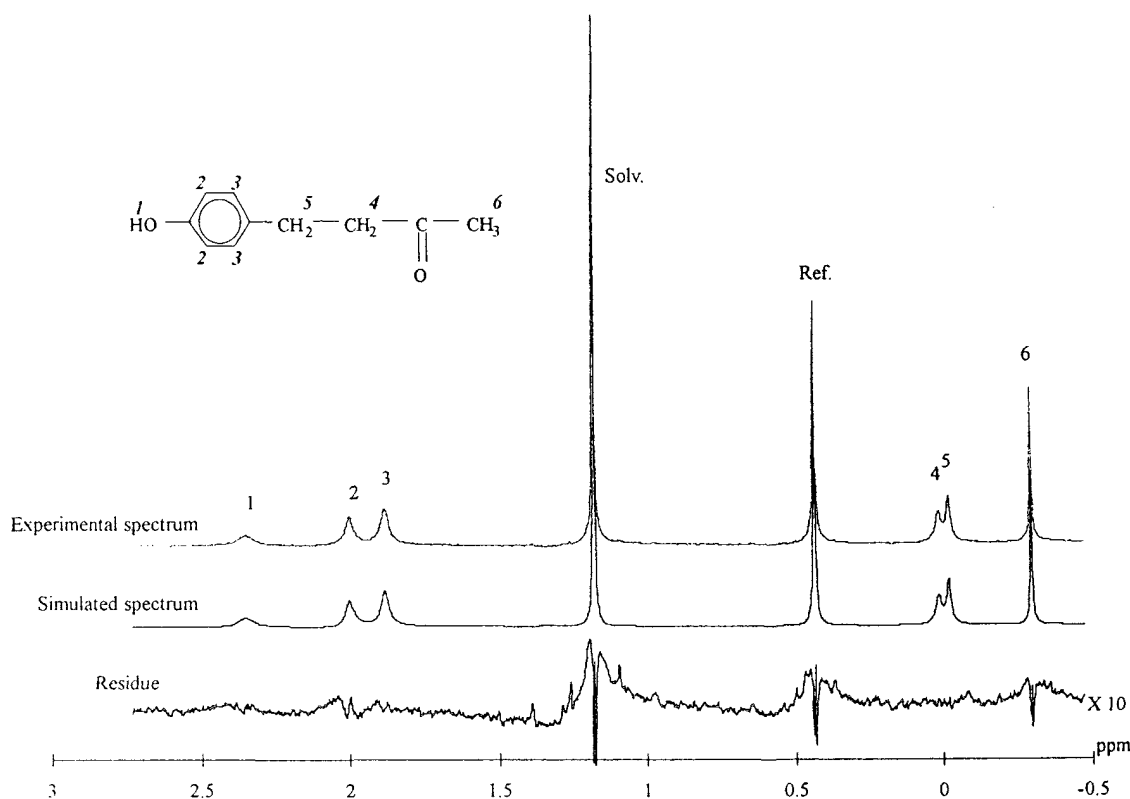


Figure 2 : Comparison of the experimental and theoretical ^2H -NMR spectra of frambinone. The theoretical spectrum has been simulated from the results of a fully automatic complex least squares analysis ("Interliss" software⁽²³⁾) which integrates the whole set of spectral parameters : frequencies, intensities, phases. The experimental spectrum has been obtained at 76.8 MHz with an AMX Bruker spectrometer equipped with the SNIF-NMR concept system. The residual, C, is represented on an expanded intensity scale. The solvent is CH_2Cl_2 and the isotopic reference is tetramethylurea.

COMPARISON WITH ISOTOPE RATIO DETERMINATIONS BY MASS SPECTROMETRY

Isotope ratio mass spectrometry (IRMS) has the reputation of being a sensitive and

precise method of isotope ratio determination. However in order to measure the $^{13}\text{C}/^{12}\text{C}$ or $^2\text{H}/^1\text{H}$ ratios it is necessary to burn the product first to produce CO_2 and H_2O which is subsequently reduced to H_2 . Consequently the IRMS method provides isotopic values which are averaged over the different molecular positions. In principle the overall isotope ratio is also accessible by NMR provided that a reference substance, the isotopic ratio of which is accurately known, has been added to the sample. The isotope ratios computed from equation 4 can then be used to estimate the mean isotope content of the molecule, \overline{R}_A , by means of equation 8. A statistical evaluation of

SNIF-NMR and IRMS data obtained on three molecular species, ethanol, anethol and vanillin, extracted from different kinds of natural

products or obtained by chemical synthesis, is given in table 3.

Product		MS		NMR	
		$(\overline{D/H})_{tot}$	n	$(\overline{D/H})_{tot}$	n
ETHANOL	Sugar beet	113.7	5	113.9	72
	Vine	123.2	16	121.8	385
	Sugar cane	124.4	8	122.2	76
	Synthesis	135.2	4	134.7	4
ANETHOL	Star anise	142.1	17	143.2	10
	Fennel	143.2	11	142.7	11
	Synthesis	150.1	15	150.4	4
VANILLIN	V. Planifolia	143.2	18	143.7	30
	Lignin	126.8	12	127.1	14
	Guaiacol	163.4	8	162.5	8

Table 3 : Comparison of overall hydrogen isotope ratios, obtained by the SNIF-NMR and IRMS methods, on different molecular species from different origins. The average values, $(\overline{D/H})_{tot}$, are expressed in ppm. n is the number of experiments.

The agreement between the results of the two techniques is satisfactory. In the case of hydrogen isotope ratios the repeatability is comparable but a better reproducibility can often be achieved with the NMR method. In contrast, NMR can scarcely compete with IRMS for the determination of overall carbon isotope ratios. In spite of its better sensitivity compared to deuterium, ^{13}C -NMR has the disadvantage of high and varied relaxation times. Taking into account the limited range of the natural ^{13}C contents, very high performances in proton decoupling and in the suppression of discriminating nuclear Overhauser effects must be ensured. Moreover, due to the large range of ^{13}C chemical shifts, several internal isotopic references may be required in order to quantify an entire set of ^{13}C isotopomeric species. In practice, the comparison of a given isotopomer between two different samples may be more

precise than that of different isotopomers within the same sample⁽²⁴⁾

APPLICATIONS TO THE ISOTOPIC CHARACTERIZATION OF PRODUCTS

The potential and limits of SNIF-NMR can be illustrated by several examples. We shall consider firstly the case of molecules for which the signals pertaining to the different isotopomers are clearly differentiated and do not overlap significantly. The simplest case is obviously that of ethanol and, since the ISMAR conference was held in Sydney, we shall select the example of Australian wines. About fifty wines from New-South Wales, Victoria, South and West Australia were investigated, along with some authentic wines from New-Zealand. The deuterium and ^{13}C isotope ratios of these wines are given in Table 4.

	(D/H) _I (ppm)	(D/H) _{II} (ppm)	(¹³ C/ ¹² C) (‰)
New South Wales	105.4	134.0	-25.2
South Australia	104.6	133.4	-26.1
Victoria	104.7	133.5	-25.6
West Australia	103.2	132.9	-26.2
New Zealand	102.6	130.1	-27.4

Table 4 : Hydrogen and carbon isotope ratios typical of South-Pacific wines. The (D/H)_I values have been determined by SNIF-NMR. (D/H)_I and (D/H)_{II} refer respectively to the methyl and methylene sites of ethanol extracted from the wine. The differences in the carbon isotopomeric contents are too small to be determined by ¹³C-NMR with a sufficient accuracy. Only average (¹³C/¹²C) ratios obtained by IRMS are therefore available.

It should be noted that a difference of 1ppm between the hydrogen isotope ratios of two wine ethanols corresponds nearly to a 1% difference in the ²H signal intensities. The

confidence regions for the existence domains of wines from the five geographical areas considered are represented in figure 3.

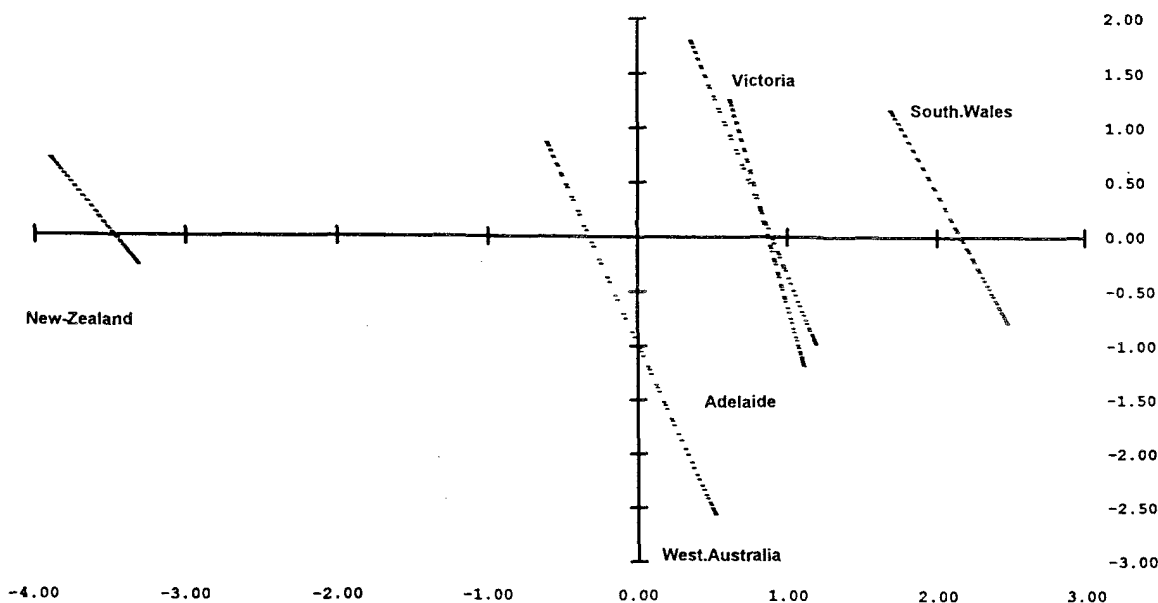


Figure 3 : Representation of the confidence regions (at a 95% level) of Australian and New-Zealand wines defined in terms of five geographical areas of production. The isotopic parameters used in the discriminant analysis are the hydrogen isotope ratios of the methyl and methylene sites of ethanol obtained by NMR and the overall ¹³C content measured by Isotope Ratio Mass Spectrometry.

The New-Zealand, New South-Wales and West Australia regions are easily differentiated but the

Victoria and Adelaide regions are hardly distinguished.

Since isotope ratios are additive parameters, a mixture M of samples of a given chemical species but from different origins can be analysed in terms of composition. From a general point of view the observed isotope ratios, R(M), are weighted averages over the isotope ratios of the individual components, i

$$R(M) = \frac{\sum_i^n f_i p_i R_i}{\sum_i^n f_i p_i} \quad [10]$$

where f_i and p_i are respectively the molar fraction and the site population of isotopomer i in the mixture M . Since a number of natural factors, such as micro-climates, may exert an influence on the fractionation effects some dispersion of the isotopic values occurs for a given region. The individual parameters R_i are therefore defined as means over several samples collected in the considered region and variances V_i are attached to the retained R_i values.

In practice different kinds of problems can be solved by isotopic analysis. For instance the question may be: "does this wine belongs to one of the three reference groups: New-Zealand, West Australia or New South Wales?"; or "has beet sugar been added to the must before fermentation and to what extent?" or "is this wine a mixture of two samples from different regions and in what proportions?".

Thus an unknown sample X will be assigned an origin j if the Mahalanobis distance d_{Xj}^2 is the minimum among the distances to all possible origins. The Mahalanobis distance is defined as

$$d_{Xj}^2 = (\mathbf{X} - \mu_j)^T [V_j]^{-1} (\mathbf{X} - \mu_j) \quad [11]$$

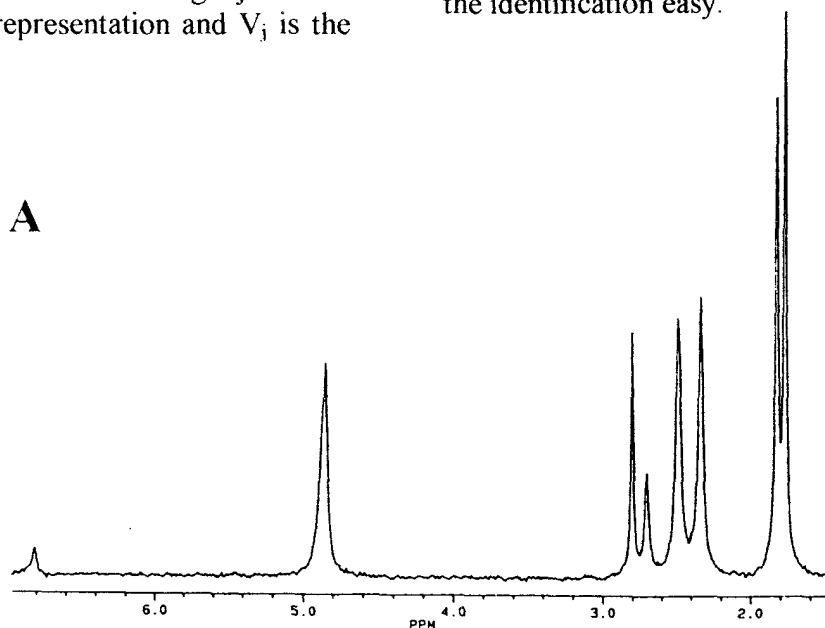
where \mathbf{X} and μ_j are the vectors of the isotope ratios of the unknown and of the origin j in the n dimension space of representation and V_j is the

(n,n) variance-covariance matrix of the isotope ratios of j . A confidence interval $(1-\alpha)$ may be associated to d_{Xj}^2 by the χ^2 statistics:

$$d_{Xj}^2 \leq \chi^2(n, (1-\alpha)) \quad [12]$$

More generally the reliability of compositional analyses grounded on equation [10] depends obviously on the magnitude of the isotopic discrimination between the individual components.

Another field of basic and industrial interest is the study of isotope fractionation in aromas, and especially in terpenes which are frequently the main constituents of flavours and fragrances⁽¹⁵⁾. Substituting or mixing synthetic analogues to the natural products extracted from plants is tempting since the former are significantly less expensive than the second. An interesting example is that of carvone the two enantiomers of which have different flavours, one being typical of spearmint and the other of caraway. The 4*R*(*l*)-enantiomer of carvone can be synthesised by chemical reactions from *d*-limonene, which is a cheap raw material, but this hemi-synthetic product has no natural status. The 76.8MHz deuterium spectra of carvone samples from different sources are represented in figure 4. Most isotopomers are clearly differentiated and notable differences in the ²H contents are observed. In the two natural products, the ethylenic sites are considerably depleted with respect to the methyl sites. The strong enrichment in the ethylenic isotopomers observed in the hemi-synthetic carvone makes the identification easy.



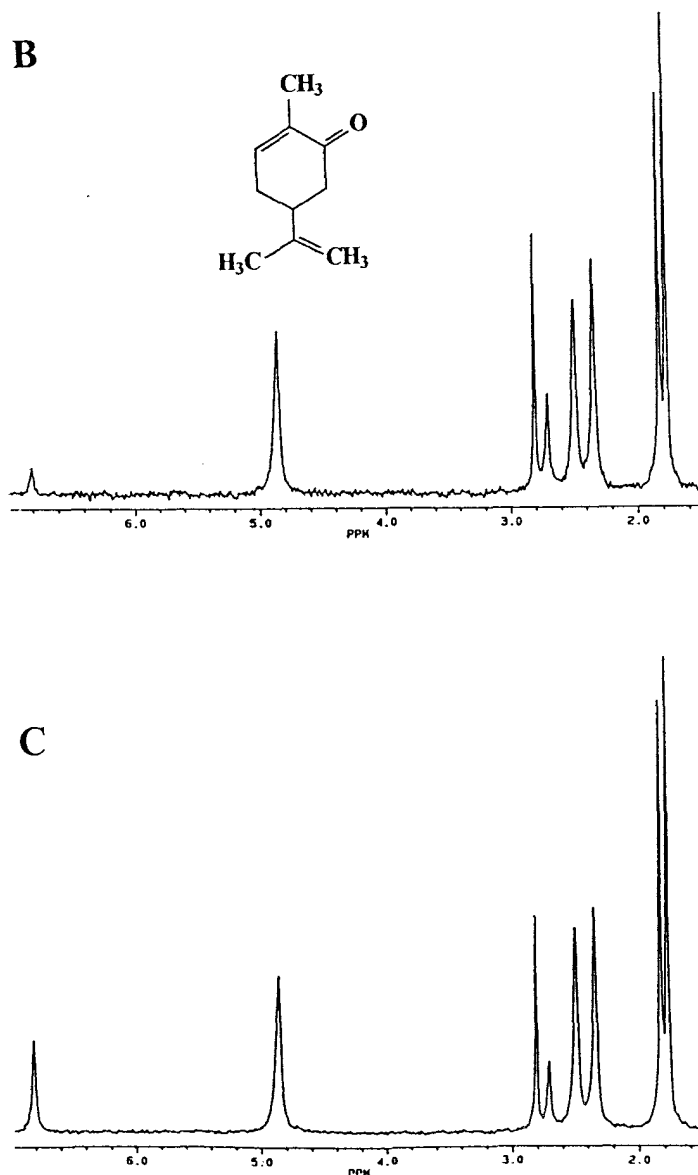


Figure 4 : Deuterium distribution in carvone samples from different origins. The ^2H -NMR spectra have been obtained at 76.8 MHz. Sample A is (+) carvone extracted from *carvi*, sample B is (-) carvone from *mentha* and sample C is (-) carvone obtained by hemi-synthesis from limonene.

In addition, since the isotopic fingerprints of synthetic or natural products are the results of kinetic and thermodynamic isotope effects occurring in the course of the reaction pathways, analysis of the natural isotope distribution is a source of mechanistic information⁽²⁵⁾.

The accuracy of the hydrogen isotope ratios determination is strongly dependent on the

isotopomeric resolution in the ^2H -NMR spectrum. This resolution is itself conditioned by the chemical shift discrimination, the magnitude of the relaxation times, and the number of isotopomeric positions in the product or in the mixture. Thus carbohydrates, which are interesting key compounds for investigating photosynthetic behaviour, are not convenient isotopic probes. The case of lipids also requires specific analytical procedures since most observed signals (fig. 5) are the sum of isotopomers of different fatty acids⁽²⁶⁾.

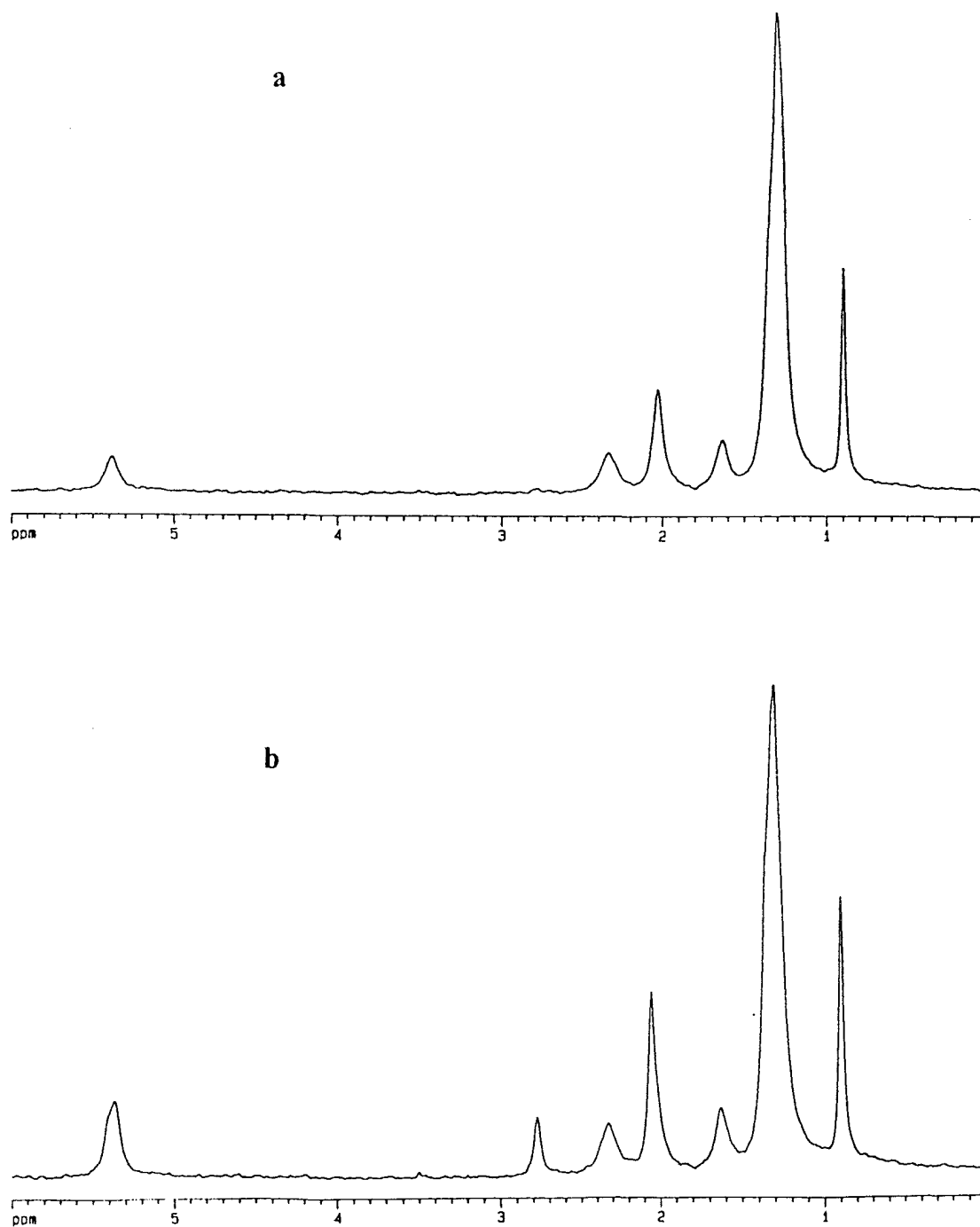


Figure 5 : Quantitative analysis of mixtures. The $^1\text{H-NMR}$ spectra of mixtures of fatty acids can be analysed in terms of clusters of overlapping signals which must be previously identified⁽²⁶⁾. Seven clusters are considered in the 61.4 MHz spectra of two different mixtures corresponding to natural olive (a) and sunflower (b) oil. These samples contain different amounts of stearic, palmitic, oleic and linoleic acids. In spite of the complexity of the spectra the quantitative treatment often provides efficient authentication criteria.

Acknowledgements : We are grateful to all our co-workers involved in the SNIF project and in particular to M. M. Trierweiler and Mrs F. Mabon (University of Nantes) and to Dr. G. Remaud (Eurofins) who cooperate to the improvement of the NMR experiments.

References

- (1) M.H. O'Leary, *Phytochemistry* 20, 553, 1981
- (2) W.W. Cleland, *CRC Critical Rev. Biochem.* 13, 385, 1982
- (3) B.N. Smith, H. Ziegler, *Bot. Acta* 103, 335, 1990
- (4) M.L. Martin, G.J. Martin, *NMR Basic Principles and Progress* 23, 1, 1990
- (5) H. Craig, *Geochim. Cosmochim. Acta* 12, 133, 1957
- (6) G. Junk, H.J. Svec, *Geochim. Cosmochim. Acta* 14, 234, 1958
- (7) R. Hagemann, G. Nief, E. Roth, *Tellus* 22, 712, 1970
- (8) P. Baertschi, *Earth Planet Sci. Lett.* 31, 341, 1976
- (9) C.D. Keeling, W.G. Mook, P.P. Tans, *Nature* 277, 121, 1979
- (10) P. De Bievre, P.D.P. Taylor, *Intern. J. Mass Spectrom. Ion Proc.* 123, 149, 1993
- (11) R.J. Francey, P.P. Tans, *Nature* 327, 495, 1987
- (12) Y. Yurtsever, J.R. Gat, *IAEA Technical Reports* 210, 103, 1981
- (13) H. Craig, *Science* 133, 1702, 1961
- (14) G.J. Martin, M.L. Martin, *Tetrahedron Letters* 22, 3525, 1981
- (15) G.J. Martin, M.L. Martin, B.L. Zhang, *Plant Cell Environm.* 15, 1037, 1992
- (16) J. Santrock, S.A. Studley, J.M. Hayes, *Anal. Chem.* 57, 1444, 1985
- (17) E.S. Pearson, H.O. Hartley, Test for heterogeneity of variance. *Biometrika Tables for Statisticians, 3^d Ed. Cambridge University Press* Vol. 1, Ch. 16, 1976
- (18) J.C. Lindon, A.G. Ferridge, *Progress in NMR Spectroscopy* 14, 27, 1980
- (19) R.E. Hoffman, G.C. Levy, *Progress in NMR Spectroscopy* 23, 211, 1991
- (20) A.D. Bain, L. Lao, *Isotopes in the Physical and Biomedical Science* 2, 411, 1991
- (21) Y.L. Martin, *J. Magn. Res.* A111, 1, 1994
- (22) R. de Beer, D. van Ormondt, *NMR Basic Principles and Progress* 26, 201, 1992
- (23) Interliss™ Eurofins S.A. Nantes
- (24) V. Caer, M. Trierweiler, G.J. Martin, M.L. Martin, *Anal. Chem.* 63, 2306, 1991
- (25) B.L. Zhang, Yunianta, M.L. Martin, *J. Biol. Chem.* 270, 16023, 1995
- (26) B. Quemerais, F. Mabon, N. Naulet, G.J. Martin, *Plant Cell Environm.* 18, 989, 1995
- (27) W.G. Mook, J. Jongsma, *Tellus* 39B, 96, 1987
- (28) J. Koziat, A. Rossmann, G.J. Martin, P.R. Ashurst, *Anal. Chim. Acta* 271, 31, 1993
- (29) J. Koziat, A. Rossmann, G.J. Martin, P. Johnson, *Anal. Chim. Acta* 302, 29, 1995

FT Pulsed ESR/ESTN(Electron Spin Transient Nutation) Spectroscopy Applied to High-Spin Systems; Direct Evidence of the First High-Spin Polymer as Models for Organic Ferro- and Superpara-Magnets

Takeji Takui,¹ Kazunobu Sato,¹ Daisuke Shiomi,² Koichi Itoh,²
Takashi Kaneko,³ Eishun Tsuchida,³ and Hiroyuki Nishide³
The Department of Chemistry¹ and Department of Material Science,² Faculty of science,
Osaka City University, Sumiyoshi-ku, Osaka 558, Japan and
the Department of Applied Chemistry,³ Faculty of Science and Engineering,
Waseda University, Shinjuku-ku, Tokyo 169, Japan

1. Introduction

Last decade has found ever increasing interest in organic molecular based magnetism (abbreviated to organic magnetism)[1,2] from both the pure and applied sciences[3a-c]. The conceptual proposals of organic magnetism were made at early times[1,2]. A rapid development of this research field is partly due to the rich variety of novel physical phenomena and properties which synthetic organomagnetic materials are expected to exhibit both macro- and mesoscopically and partly due to their underlying potential applications as future technology in materials scienc[4,5].

During last decade, spin manipulation chemistry developed to bring diverse topics in chemistry, physics, and related interdisciplinary areas[3-5]. Among those, organic neutral high-spin polymers of elaborate molecular designs based on the through-bond approach and molecular high-spin clusters have recently emerged in addition to charged high-spin frustrated systems in which charge fluctuation (delocalisation) and spin polarisation coexist[6]. They have been designed to be through-bond models for high-Tc organic magnets.

With the increasing molecular spin quantum number S and molecular weight of the polymers or clusters, however, conventional cw ESR spectroscopy manifests its inherent disadvantages in resolving and discriminating high spins from $S=1/2$, and in determining the S 's for the complex mixture of various spin assemblages. In order to overcome this methodological difficulty we have introduced ESTN (Electron Spin Transient Nutation) spectroscopy based on pulsed FT-spectroscopic methods and applied for the first time to non-oriented high-spin systems. In ESR spectroscopy, pulsed FT-spectroscopic techniques continue to emerge because of their advantages intrinsic to FT spectroscopy in many experimental aspects. Particularly, two-dimensional representation is capable of disclosing new aspects of coherence and micro-/meso-scopic details of spin systems.

The main purposes of the present work have been methodology-oriented and twofold. The first is to apply ESTN spectroscopy to inorganic high-spin systems in non-oriented powder states in order to demonstrate that ESTN spectroscopy is capable of elaborating useful information on electronic and environmental structures of transition metal high-spin centres, which conventional cw ESR cannot afford. From a methodological point of view, we have developed ESTN spectroscopy in experimental and theoretical aspects, emphasising the intrinsic advantages of time-domain spec-

troscopy. In addition, features of ESTN phenomena in multiple quantum transitions have been disclosed in this work. The second is to apply ESTN spectroscopy to an organic magnetic polymer as one of the most complex spin systems in amorphous solids, where robust intermolecular exchange interaction takes place. For this purpose, we have adopted a quasi one-dimensional magnetic polymer **A** as models for high-Tc organic ferro- and superpara-magnets[26], identifying that **A** consists of high-spin ensembles. This gives the direct microscopic evidence of the first neutral high-spin polymer that chemistry has ever had. The results illustrate that ESTN spectroscopy possesses the inherent potentiality to resolve and identify molecular spin multiplicities of complex spin assemblages in amorphous materials.

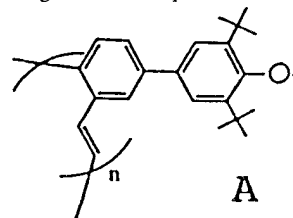


Figure 1. Quasi 1D magnetic polymer as models for quasi 1D organic ferrromagnets. The π -conjugated electron network is governed by topologically controlled spin polarisation (through-bond approach).

2. Fundamental Bases for Electron Spin Transient Nutation (ESTN) Spectroscopy

Pulse Fourier transform NMR spectroscopy has made traditional cw NMR obsolete during the past two decades, leading to a continuing and unprecedented expansion of NMR applications. Recently in ESR spectroscopy, pulsed FT-spectroscopic techniques continue to emerge [7-13] because of the advantages intrinsic to FT spectroscopy in many experimental aspects, emphasising the capability of measuring transient properties of electron-nuclear spin systems, the adaptability to other pulsed spectroscopic techniques, and the inherent advantages of coherence-transfer based 2D time-domain spectroscopy.

The methodology of quantum spin transient nutation to measure the spin Hamiltonian in terms of the rotating frame has been developed in NMR/NQR spectroscopy [14-20] and appeared in ESR spectroscopy at early times [21-23]. It was not until recently that nutation methods were introduced as pulsed ESR spectroscopic techniques [24,25]. Isoya *et al.* have determined the effective spin quantum number S for the nickel impurity in synthetic diamond to be $S=3/2$ with non-vanishing fine-structure constants due

to a distortion of the impurity site from tetrahedral symmetry [24]. Astashkin and Schweiger have demonstrated that an electron spin transient nutation method facilitates the identification of complex single-crystal ESR spectra from transition metal ions by exploiting the nutation frequency dependence of the allowed and forbidden transitions [25].

We describe the electron spin transient nutation of single quantum transitions first in terms of a classical vectorial picture for the motion of the spin magnetisation and next in terms of a quantum mechanical approach. This is for the convenience of the readers who might not be familiar with nutation phenomena in magnetic resonance. Next we describe the features of the transient nutation appearing in multiple quantum transitions. These features have been disclosed in the present work.

2.1. NUTATION SPECTRUM OF SINGLE QUANTUM TRANSITIONS

Electron spin transient nutation spectroscopy is based on electron spin resonance to measure the spin Hamiltonian in terms of the rotating frame [24-26]. The electron spin magnetisation \mathbf{M}_0 in the presence of a static magnetic field \mathbf{B}_0 precesses at the corresponding nutation angle ϕ from the initial direction around the effective field $\mathbf{B}_{\text{eff}} = \mathbf{B}_0 + \mathbf{B}_1$ by applying the microwave field (\mathbf{B}_1) pulse with the width t_1 . Then the magnetisation \mathbf{M}_0 in thermal equilibrium undergoes free induction decay (FID) when the excitation pulse is turned off. The nutation is described in terms of the above classical vectorial picture for the motion of the magnetisation as follows. The magnetisation components M_x and M_y in the frame xyz rotating with a frequency ω are given as

$$M_x = M_0 \sin \phi / (1+x^2)^{1/2} \quad (1)$$

$$M_y = M_0 [2x / (1+x^2)] \sin^2 \{\phi/2\} \quad (2)$$

$$M_m = M_0 \{1 / (1+x^2)\} \{ \sin^2 \phi + x^2 (1 - \cos \phi)^2 / (1+x^2) \}^{1/2} \\ = (M_x^2 + M_y^2)^{1/2} \quad (3)$$

where M_m is the projection of \mathbf{M} in the rotating xy plane and $M_0 = |\mathbf{M}_0| = |\mathbf{M}|$. $B_e = [(B_0 - \omega/\gamma)^2 + B_1^2]^{1/2}$, $\tan \theta = B_1 / (B_0 - \omega/\gamma)$, and x is an offset parameter given as $x = (B_0 - \omega/\gamma) / B_1$ with $\tan \theta = 1/x$, $\sin \theta = (1+x^2)^{-1/2}$, and $B_e = B_1 (1+x^2)^{1/2}$. ϕ is defined as a nutation angle of \mathbf{M}_0 around \mathbf{B}_e in time t and ϕ_0 is defined as the rotation angle of \mathbf{M}_0 in the same duration time t around \mathbf{B}_1 , thus $\phi = \gamma B_e t$, $\phi_0 = \gamma B_1 t$, and $\phi = \phi_0 (1+x^2)^{1/2}$ holds. The phase angle Ω of M_m from the x axis in the xy plane is defined as $\Omega = \tan^{-1}(M_y/M_x)$ and the tipping angle α of \mathbf{M} with respect to the z axis after the microwave pulse excitation is defined as $\sin \alpha = M_m / M_0 = \{ \{ \sin^2 \phi + x^2 (1 - \cos \phi)^2 / (1+x^2) \} / (1+x^2) \}^{1/2}$.

The quantum mechanical description of an ensemble of spin systems in pulse experiments frequently invokes the equation of motion of the density matrix $|\rho(t)\rangle$ (a ket in Liouville space) governed by the Liouville-von Neuman

equation. The effect of a coherent microwave field \mathbf{B}_1 perpendicular to the magnetic field \mathbf{B}_0 beginning at $t=0$ is given as

$$H_1 = -\omega_1 S_y (e^{i\omega t} + e^{-i\omega t}) \quad (4)$$

with $\omega_1 = -\gamma B_1$. The equation of motion for $|\rho(t)\rangle$ is governed by

$$d|\rho(t)\rangle/dt = -i(H_0 + H_1(t))|\rho(t)\rangle, \quad (5)$$

where only the electron Zeeman term is considered, thus $H_0 = -\omega_0 S_z$ and $\omega_0 = B_0/\gamma$. Transforming into the rotating frame with the frequency ω of the microwave field around the z -direction // \mathbf{B}_0 gives

$$d|\rho_R(t)\rangle/dt = -iH_R(t)|\rho_R(t)\rangle \quad (6)$$

where $H_R(t)$ and $|\rho_R(t)\rangle$ stand for the Hamiltonian and the density matrix defined in the rotating frame, respectively, as

$$|\rho_R(t)\rangle = e^{-i\omega t S_z} |\rho(t)\rangle \quad (7)$$

and

$$H_R(t) = -[\Delta\omega S_z + H_{1,R}(t)] \quad (8)$$

with

$$H_{1,R}(t) = e^{-i\omega t S_z} H_1(t) e^{i\omega t S_z} \quad (9)$$

and the resonance offset frequency $\Delta\omega$ is defined as $\Delta\omega = -(\omega - \omega_0)$. Equation (9) is rewritten as

$$H_{1,R}(t) = -\omega_1 S_y (1 + \cos 2\omega t) - \omega S_x \sin 2\omega t. \quad (10)$$

The secular term $-\omega_1 S_y$ causes a rotation around the y axis with the frequency ω_1 . The non-secular (time dependent) term arising from the counter-rotating part of the microwave field does not contribute to the rotation in the first order and contributes only in the higher order. The non-secular contribution called the Bloch-Siegert shift can be neglected in the first order. Thus, the rotating-frame Hamiltonian is given as

$$H_R(t) = -(\Delta\omega S_z + \omega_1 S_y). \quad (11)$$

Assuming the initial density matrix $|\rho(0)\rangle = |S_z\rangle$, the solution for Equation (6) in the rotating frame is given as

$$|\rho_R(t)\rangle = e^{it(\Delta\omega S_z + \omega_1 S_y)} |\rho(0)\rangle \\ = e^{i\theta S_x} e^{it\omega_e S_z} e^{-i\theta S_x} |S_z\rangle, \quad (12)$$

where

$$\omega_e^2 = \Delta\omega^2 + \omega_1^2 \quad (13)$$

and

$$\tan \theta = \omega_1 / \Delta\omega. \quad (14)$$

From Equation (12) we obtain

$$|\rho_R(t)\rangle = -\sin\theta\sin\omega_e t |S_x\rangle + \sin\theta\cos\theta(1-\cos\omega_e t) |S_y\rangle + (\cos^2\theta + \sin^2\theta\cos\omega_e t) |S_z\rangle. \quad (15)$$

Equation (15) is equivalent to Equations (1)-(3) obtained from the classical vectorial description. In the case of on-resonance, i.e. $\Delta\omega = -(\omega - \omega_0) = 0$,

$$|\rho_R(t)\rangle = e^{it\omega_1 S_y} |S_z\rangle = \cos\omega_1 t |S_z\rangle - \sin\omega_1 t |S_x\rangle. \quad (16)$$

Particularly, applying B_1 for a period corresponding to a $\pi/2$ -pulse transfers the initial magnetisation $|\rho(0)\rangle = |S_z\rangle$ into the magnetisation along the x axis, i.e. $|\rho(\pi/2\omega_1)\rangle = |S_x\rangle$.

For the high-spin state with the spin quantum number S , the fine-structure term $H_D = S \cdot D \cdot S$ features in the total spin Hamiltonian, where

$$H_D = \omega_D(S_z^2 - S^2/3) + \omega_E(S_x^2 - S_y^2) \quad (17)$$

in the principal-axis system of the fine-structure tensor D . For vanishing H_D or $H_D \ll H_1$ the ensemble of high spins nutates at the frequency of $\omega_1 = -\gamma B_1$ under the on-resonance condition, where ω_1 is independent of S . For non-vanishing H_D , the nutation is modified due to the presence of H_D in the rotating frame and is not described by a single frequency. In the extreme limit of $H_D \gg H_1$, however, the nutation frequency ω_n is simply expressed as

$$\omega_n = \omega_1 [S(S+1) - M_S M_S']^{1/2}, \quad (18)$$

where M_S and M_S' denote the electron spin sublevels involved in the ESR allowed transition [24,25]: The rotating-frame matrix element corresponding to the transition is given in first order as

$$\langle S, M_S | H_{1,R} | S, M_S' \rangle = -\omega_1 [(S+M_S)(S-M_S')]^{1/2}, \quad (19)$$

where $M_S' = M_S - 1$ for the allowed ESR transitions. Thus, for $H_D \gg H_1$, the nutation spectrum depends on S and M_S [38,39]. For integral spins, $S=1,2,3,4,\dots$, $\omega_n = \omega_1 [S(S+1)]^{1/2}$ for the $|S, M_S=1\rangle \leftrightarrow |S, M_S'=0\rangle$ or $|S, M_S=0\rangle \leftrightarrow |S, M_S'=-1\rangle$ transition. Therefore, even if the ESR transitions involving the $|S, M_S=0\rangle$ level overlap due to the small ω_D values, the spin quantum number S can be discriminated in the nutation spectrum. Practically, the offset frequency effect on the nutation must be carefully considered in some cases in order to carry out magnetic-field swept nutation spectroscopy. For half-integral spins, $S=3/2, 5/2, \dots$, the fine-structure term $\omega_D(2M_S-1)$ in first order is vanishing for the $|S, M_S=1/2\rangle \leftrightarrow |S, M_S'=-1/2\rangle$ transition, and higher-order corrections due to the fine-structure term contribute only as off-axis extra lines in the powder-pattern fine-structure spectrum if ω_D is large [27]. The corresponding nutation frequency ω_n is given as $\omega_n =$

$\omega_1(S+1/2)$. Thus, the nutation spectrum is distinguishable from both $S=1/2$ and other S 's even if the fine-structure splitting does not feature in the cw ESR spectrum because of line-broadening, large ω_D values and so on. For intermediate cases, i.e. $H_D \sim H_1$, the nutation spectrum appears more or less complicated, but the spectrum can be interpretable using the rotating-frame total spin

TABLE I. On-resonance nutation Frequencies for various cases

	$\omega_n, \omega_n^{dq}, \omega_n^{tq}$
$H_D = 0$	$\omega_n = \omega_1$
$H_D \ll H_1$	$\omega_n \sim \omega_1$
$H_D \sim H_1$	not single ω_n
$H_D \gg H_1$	$\omega_n = \omega_1 [S(S+1) - M_S M_S']^{1/2}$ with $M_S' = M_S - 1$
	$\omega_n = \omega_1(S+1/2)$ for the $M_S=1/2 \leftrightarrow M_S'=-1/2$ transition ($S = 3/2, 5/2, 7/2, \dots$).
	$\omega_n = \omega_1 [S(S+1)]$ for the $M_S=0 \leftrightarrow M_S'=-1$ or $M_S=1 \leftrightarrow M_S'=0$ transition ($S = 1, 2, 3, \dots$).
	$\omega_n^{dq} = \omega_1(\omega_1/\omega_D)$ for $S = 1$
	$\omega_n^{dq} = \omega_1(7\omega_1/4\omega_D)$ for $S = 3/2$
	$\omega_n^{tq} = \omega_1(3\omega_1/8\omega_D)^2$ for $S = 3/2$

ω_n^{dq} and ω_n^{tq} denote the nutation frequency for double and triple quantum transitions ($S \geq 1$), respectively.

Hamiltonian [32,33]. In addition, multiple quantum transitions can be observable in the nutation spectrum even in the extreme limit of $H_D \gg H_1$. The nutation frequency arising from the multiple quantum transition is considerably reduced due to the scaling effect of the effective field which spin ensembles experience in the rotating frame, as described below. In Table I are summarized nutation frequencies ω_n on resonance for various cases of S and H_D at experimentally typical discretions.

2.2. NUTATION SPECTRUM OF MULTIPLE QUANTUM TRANSITIONS

The three-sublevel system is a well-established model to discuss double quantum transitions and coherence effects in spectroscopy [28]. The three-level model also has been applied to other multi-level systems, simplifying actual systems to give reasonable theoretical interpretations to a variety of transient phenomena [29-31]. Nevertheless, the nutation of multiple quantum transitions has not been fully expounded in ESR spectroscopy.

Following Vega-Pines-Wokaun-Ernst approach of the fictitious spin 1/2 operator in terms of the Zeeman basis [32,33], we treat the $S=1$ spin Hamiltonian in the rotating frame to obtain a physical picture of transient nutation phenomena for double quantum transitions. The spin Hamiltonian for an $S=1$ system is

$$H_0 = -\omega_0 S_z + \omega_D \{S_z^2 - S(S+1)/3\} + \omega_E (S_x^2 - S_y^2). \quad (20)$$

For simplicity, we will neglect the third term hereafter. The single quantum ESR transitions appear at $\omega_0 = \omega_D$ and the double quantum transition appears at ω_D . Introducing fictitious spin 1/2 operators in terms of the Zeeman basis, the total spin operators in Equation (20) are expressed as

$$\left. \begin{aligned} S_k &= \sqrt{2} (S_k^{1-2} + S_k^{2-3}) & (k=x,y) \\ S_z &= 2(S_z^{1-2} + S_z^{2-3}) = 2S_z^{1-3}, & \end{aligned} \right\} \quad (21)$$

where S_1^{1-2} and S_1^{2-3} ($1=x,y,z$) are single quantum operators, and S_1^{1-3} ($1=x,y,z$) is a double quantum operator. Other bilinear combinations of total spin operators appearing in Equation (20) can be generally expressed by linear combinations of fictitious spin 1/2 operators. Thus, the spin Hamiltonian of Equation (20) can be rewritten in terms of the fictitious spin 1/2 operator as

$$H_0 = -2\omega_0 S_z^{1-3} + (2\omega_D/3)(S_z^{1-2} - S_z^{2-3}) \quad (22)$$

and similarly, the secular part of the microwave field Hamiltonian is given as

$$H_1 = -\omega_1 S_k = -\sqrt{2}\omega_1 (S_k^{1-2} + S_k^{2-3}), \quad (k=x,y) \quad (23)$$

Thus, the total spin Hamiltonian H_R in the rotating frame is written in terms of the fictitious spin 1/2 operator as

$$H_R = -2(\omega_0 - \omega) S_z^{1-3} + (2\omega_D/3)(S_z^{1-2} - S_z^{2-3}) - \sqrt{2}\omega_1 (S_k^{1-2} + S_k^{2-3}). \quad (24)$$

Now, for simplicity we first treat the single quantum transition and next the double quantum transition for an $S=1$ system with the offset frequency effect taken into account. The two single quantum transitions appear at $\omega = \omega_1 = \omega_D$. First, let us consider the 2-3 transition. Defining $\Delta\omega = \omega_0 + \omega_D - \omega$ with $\Delta\omega \ll \omega_D$ makes us rewrite Equation (22) as

$$H_{0,R} = -\Delta\omega S_z^{2-3} + (4\omega_D/3 - \Delta\omega)(S_z^{1-2} + S_z^{1-3}), \quad (25)$$

where the triangular relation for the z-component of the fictitious spin 1/2 operator $S_z^{1-2} + S_z^{2-3} + S_z^{1-3} = 0$ and the similar relation under cyclic permutation with respect to 1, 2 and 3, and $S_z^{3-1} = S_z^{1-3}$ are used. The eigenvalues E_0^R ($i=1,2,3$) in the rotating frame are given as

$$\left. \begin{aligned} E_0^R &= 4\omega_D/3 - \Delta\omega \\ E_0^R &= -2\omega_D/3 \\ E_0^R &= -2\omega_D/3 + \Delta\omega. \end{aligned} \right\} \quad (26)$$

In the extreme limit of $H_D \gg H_1$, i.e. $\omega_D \gg \omega_1$, the term

$\sqrt{2}\omega_1 S_k^{1-2}$ in Equation (24) can be neglected since it couples 1 and 2 levels separated by $2\omega_D$. Thus, the total spin Hamiltonian in the rotating frame H_R is truncated to

$$H_R = H_R^{2-3} + H_R^{1-2,1-3}, \quad (27)$$

where

$$H_R^{2-3} = -\Delta\omega S_z^{2-3} - \sqrt{2}\omega_1 S_k^{2-3}, \quad (28)$$

$$H_R^{1-2,1-3} = (4\omega_D/3 - \Delta\omega)(S_z^{1-2} + S_z^{1-3}), \quad (29)$$

and $[H_R^{2-3}, H_R^{1-2,1-3}] = 0$. Here, we arrive at a physical picture for the 2-3 transition, which is described by H_R^{2-3} . The $S=1$ spin (spin magnetisation) nutates around an effective field with a frequency $\omega_e = (\Delta\omega^2 + 2\omega_1^2)^{1/2}$ which is tilted by an angle of $\theta = \tan^{-1}(\sqrt{2}\omega_1/\Delta\omega)$ with respect to the z-axis. If microwave excitation is carried out on-resonance for the 2-3 transition, i.e. $\Delta\omega = 0$, the spin precesses at the nutation frequency $\omega_n = \omega_e = \sqrt{2}\omega_1$, as given in the preceding section: $\omega_n = [S(S+1)]^{1/2}\omega_1$ ($S=1$). The on-resonance nutation is given as

$$\begin{aligned} & \exp(i\sqrt{2}\omega_1 t S_y^{2-3}) S_z^{2-3} \exp(-i\sqrt{2}\omega_1 t S_y^{2-3}) \\ &= S_z^{2-3} \cos(\sqrt{2}\omega_1 t) - S_x^{2-3} \sin(\sqrt{2}\omega_1 t), \end{aligned} \quad (30)$$

where $\rho^{2-3}(0) = S_z^{2-3}$ is assumed. Corresponding arguments in terms of the density matrix hold.

Now we treat the nutation of the 1-3 double quantum transition appearing at ω_0 for the $S=1$ system. Again we define $\Delta\omega = -(\omega - \omega_0)$ with $\Delta\omega \ll \omega_D$. The rotating-frame total spin Hamiltonian is given as

$$H_R = -2\Delta\omega S_z^{1-3} + (2\omega_D/3)(S_z^{1-2} - S_z^{2-3}) - \sqrt{2}\omega_1 (S_k^{1-2} + S_k^{2-3}). \quad (31)$$

H_R can be rewritten by unitary transformations as

$$\begin{aligned} H_R^U &= -2\Delta\omega \cos(\theta/2) S_z^{1-3} + (1/2)(\omega_e - \omega_D) S_k^{1-3} \\ &+ [2\omega_D/3 + (1/2)(\omega_e - \omega_D)] (S_z^{1-2} - S_z^{2-3}) \\ &- \sqrt{2}\Delta\omega \sin(\theta/2) (S_k^{1-2} - S_k^{2-3}) \end{aligned} \quad (32)$$

with $\sin\theta = 2\omega_1/\omega_e$, $\cos\theta = \omega_D/\omega_e$, and $\omega_e = \{\omega_D^2 + 4\omega_1^2\}^{1/2}$. In the extreme limit of $H_D \gg H_1$, i.e., $\omega_D \gg \omega_1$, we obtain

$$H_R^U = H_R^{U,1-3} + H_R^{U,1-2,2-3}, \quad (33)$$

where

$$H_R^{U,1-3} = -2\Delta\omega S_z^{1-3} + (\omega_1^2/\omega_D) S_k^{1-3} \quad (34)$$

and

$$H_R^{U,1-2,2-3} = [2\omega_D/3 + (\omega_1^2/\omega_D)] (S_z^{1-2} - S_z^{2-3}), \quad (35)$$

noting $[H_R^{U,1-3}, H_R^{U,1-2,2-3}] = 0$. Any action on the 1-3 double quantum transition is described by $H_R^{U,1-3}$. The

$S=1$ spin system nutates around an effective field with $\omega_e = [4\Delta\omega^2 + (\omega_1^2/\omega_D)^2]^{1/2}$ and a tilting angle $\theta = \tan^{-1}[-\omega_1^2/(2\omega_D\Delta\omega)]$. If microwave excitation is carried out on-resonance for the 1-3 transition, the nutation frequency is given as $\omega_n = \omega_e = \omega_1(\omega_1/\omega_D)$, showing that $\omega_n \rightarrow 0$ is obtained due to the scaling factor $\omega_1/\omega_D \ll 1$.

Corresponding treatment can be applied to an $S=3/2$ system for the two double quantum transitions appearing at $\omega_0 = \omega_D$ and corresponding nutation frequency ω_n undergoes a scaled field $\omega_1(7\omega_1/4\omega_D) = \omega_n[32b,34]$, giving $\omega_D \ll \omega_1$ in the extreme limit of $H_1 \ll H_D$, i.e. $\omega_1 \ll \omega_D$. For a triple quantum transition appearing at ω_0 for the $S=3/2$ system, the corresponding nutation is induced by an effective field $B_e = -\gamma\omega_e$, i.e., $\omega_n = \omega_e = \omega_1(3\omega_1^2/8\omega_D^2)[34]$, showing that the scaling factor for the nutation frequency is $3\omega_1^2/8\omega_D^2$.

The above arguments predict that if nutation components near zero frequency are discriminated due to multiple quantum transitions and the frequency shifts as a function of the microwave amplitude are measured, the fine-structure constant ω_D can be evaluated from the nutation experiment under the assumption of $H_D \gg H_1$. The nutation spectrum of multiple quantum transitions can be a measure for small ω_D values which are undetectable by conventional cw ESR spectroscopy [35]. Since the multiple quantum nutation is intrinsic to multi-level systems ($S \geq 1$), it can be used for discriminating high spins from $S=1/2$. The Vega-Pines-Wokaun-Ernst approach can be extended to transient nutation phenomena of arbitrary spins and more general cases, and useful experimental aspects can be predicted [35].

3. Experimental Method

The nutation experiment can be made by either observing the FID or electron spin(or rotary) echo(ESE) signal $s(t_1, t_2)$ as time-domain spectroscopy (time axis t_2) by incrementing the time interval t_1 of microwave pulse excitation parametrically. The two time variables t_1 and t_2 are independent. $s(t_1, t_2)$ measured as a function of t_1 and t_2 is converted into a 1D or 2D frequency domain spectrum, i.e. $S(f_1, t_2)$ (or $S(t_1, f_2)$) or $S(f_1, f_2)$ by Fourier transformation. Our nutation experiment was carried out by the FID-detected method. The ESE-detected method applied to high-spin systems which undergo inhomogeneous line-broadening will be published elsewhere [44]. The timing diagram for our nutation experiment is schematically shown in Figure 2 [12]. A current Bruker, Inc. ESP300E/380 2D FT ESR spectrometer equipped with a dielectric cavity of tunable $Q_u = 100 \sim 5000$ was used for our nutation experiment [36] and cryogenic temperature was controlled with an Oxford helium gas-flow variable-temperature system. The microwave pulse was amplified by a 1kW pulsed travelling wave tube (TWT) amplifier. Electron spin transient nutation experiments are sensitive to a B_1 homogeneity and the B_1 gradient effect must be taken into account in the experimental interpretation [26], but the gradient effect across the sample was not considered in our interpretation since only a small

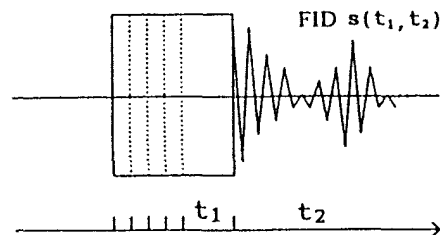


Figure 2. Schematic timing diagram for the FID-detected transient nutation experiment. The FID signal $s(t_1, t_2)$ is measured as a function of the time width t_1 of the microwave pulse and is converted into a frequency-domain spectrum $S(f_1, t_2)$ (or $S(t_1, f_2)$) or $S(f_1, f_2)$ by a 1D or 2D Fourier transformation, respectively.

portion inside the cavity was filled with our samples. The molecular structure of a quasi 1D organic magnetic polymer A employed in our nutation experiment is depicted in Figure 1. The polymer as models for quasi 1D organic ferromagnets was elaborately designed [26] based on through-bond approach to high Tc organic ferromagnets [1]. The sample preparation of the polymer has been published elsewhere [26]. The Mn^{2+} - and Cr^{3+} -doped MgO powder samples were prepared by the usual methods.

4. Results and Discussion

4.1. INORGANIC HIGH-SPIN SYSTEMS: Mn^{2+} - AND Cr^{3+} -DOPED MgO POWDER

Figures 3 and 4 show a cw ESR spectrum and a typical nutation spectrum of the $^{55}Mn^{2+}(S=5/2, I=5/2)$ -doped MgO powder observed at ambient temperature, respectively. The cw spectrum is comprised of the six hyperfine allowed ($\Delta M_I = 0$) transitions belonging to the $|S, M_S = 1/2\rangle \leftrightarrow |S, M_S' = -1/2\rangle$ fine-structure transition. All the six lines gave the same nutation frequency $\omega_n = 12.24$ MHz at the microwave amplitude of 20db (the corresponding absolute microwave power at the sample site has not been known yet), showing that the six lines are attributable to the ESR transition involving the same electron spin sublevels and the same ΔM_I selection rule. The observed frequency ω_n agreed with three times of $\omega_1 = \omega_n(S=1/2)$ observed for a reference standard (a single crystal of DPPH), demonstrating that the particular relationship $\omega_n = (S+1/2)\omega_1$ in the extreme limit of $H_D \gg H_1$ holds, i.e. $\omega_n = 3\omega_1$ as expected for $S=5/2$. Thus, the six hyperfine lines are identified to arise from the $|S=5/2, M_S = 1/2\rangle \leftrightarrow |S=5/2, M_S' = -1/2\rangle$ transition. Since the hyperfine splitting ($A = 0.008111 \text{ cm}^{-1}$) is much greater than the fine structure splitting ($a' = 0.001901 \text{ cm}^{-1}$), the angular anomaly due to the higher-order contribution of the fine-structure term does not show up for the $|S, M_S = 1/2\rangle \leftrightarrow |S, M_S' = -1/2\rangle$ transition, this particular $|\Delta M_S| = 1$ transition is apparently intensified even in the powder-pattern fine-structure spectrum of the ground state ($^6S_{5/2}$) of $^{55}Mn^{2+}$ in MgO, where the parameters A and a' refer to the isotropic hyperfine coupling constant and the additional higher-order fine-structure constant defined as

$$H_c = (a'/120) \{ 35S_z^4 - 30S(S+1)S_z^2 + 25S_z^2 - 6S(S+1) + 3S^2(S+1)^2 \} + (a'/48)(S_+^4 + S_-^4) \quad (36)$$

with $a' = \beta_c/6$ and β_c refers to the octahedral constant. For $S=5/2$, Equation (36) reduces to

$$H_c = (a'/384)(112S_Z^4 - 760S_Z^2 + 567) + (a'/48)(S_+^4 + S_-^4), \quad (37)$$

which is comprised of the octahedral crystal-field operators connecting spin sublevels with M_S values differing by ± 4 [37,38].

Cr^{3+} and its complexes among the $3d^3$ ions have been extensively studied. Figure 5 shows a typical ESR spectrum of Cr^{3+} in octahedral symmetry in MgO powder and the signal from the reference standard of DPPH. It has been well-documented that the Cr^{3+} spectrum is isotropic with $g=1.9796$ and the vanishing fine-structure term at ambient temperature and the central line arises from $^{50,52,54}\text{Cr}^{3+}$ ($I=0$) and the hyperfine quartet satellite lines are due to $^{53}\text{Cr}^{3+}$ ($I=3/2$, natural abundance; 9.54%) with $A=0.00163 \text{ cm}^{-1}$ [39]. Figures 6(a)-(d) show nutation spectra obtained from the central line of Cr^{3+} in MgO powder at ambient temperature at various microwave amplitude levels. In Figure 6(d) two nutation frequencies are seen near 15 (ω_1) and 30 MHz ($2\omega_1$). The nutation frequency component at ω_1 (15 MHz at 10db) coincided with $\omega_n(S=1/2)=\omega_n$ of the reference standard in the whole range of the microwave excitation power level. With diminishing microwave amplitude, the $2\omega_1$ peak approached the ω_1 peak, as seen from Figure 10(d) to 10(a), and coincided with the ω_1 peak at weak levels of the microwave amplitude. The nutation spectra shown in Figure 6(d)-(b) can be classified in the intermediate regime $H_D \sim H_1$, since the $2\omega_1$ frequency corresponds to $\omega_n(S=3/2) = (3/2+1/2)\omega_1$ in the extreme limit of $H_D \gg H_1$, identifying the nutation frequency $\omega_n(S)=2\omega_1$ to arise from the $|S, M_S=1/2\rangle \leftrightarrow |S, M_S'=-1/2\rangle$ ESR transition ($S=3/2$). As described in the preceding theoretical treatment, the vanishing H_D won't produce any single-quantum nutation frequency different from ω_1 . Thus, the present nutation experiment shows that Cr^{3+} in MgO is located in lower symmetric environments than octahedral symmetry. Conventional cw ESR spectroscopy has never detected such symmetry reduction due to a distortion taking place at the impurity lattice site in MgO. Isoya *et al.* are the first who have found such a subtle distortion responsible for non-vanishing fine-structure terms with the help of the electron spin transient nutation technique [24].

It is interesting to note a behavior of the nutation frequency near $\omega_n \sim 0$ in Figure 6. Microwave amplitude dependence of the nutation frequency, i.e., an appreciable higher-frequency shift and enhanced intensity near $\omega_n \sim 0$ with increasing the amplitude, suggests the occurrence of double quantum transitions for the high-spin system with a small ω_D value in the extreme limit of $H_D \gg H_1$. According to the theoretical prediction described in the second section, the two double quantum transitions occur for an $S=3/2$ system with the microwave field B_1 , i.e., ω_1 ($B_1 =$

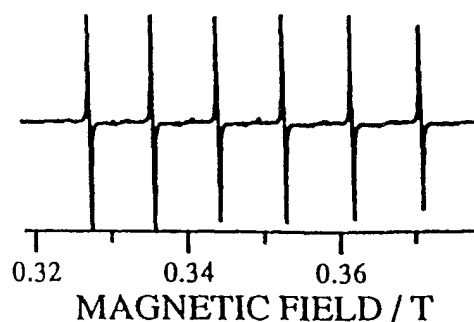


Figure 3. Cw ESR spectrum of $\text{Mn}^{2+}(S=5/2, l=5/2)$ -doped MgO powder observed at ambient temperature. The six absorption lines arise from the hyperfine allowed transitions ($\Delta M_l=0$) belonging to the $|S, M_S=1/2\rangle$ --- $|S, M_S'=-1/2\rangle$.

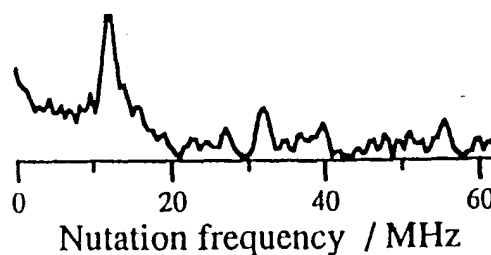


Figure 4. Nutation spectrum of $^{55}\text{Mn}^{2+}(S=5/2, l=5/2)$ -doped MgO powder observed at ambient temperature. The hyperfine transition at 0.3357T was monitored for the measurement of the transient nutation (microwave amplitude: 20db). The absolute power level of microwave was not calibrated.

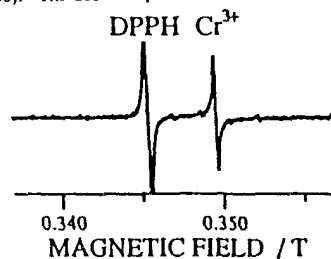


Figure 5. Cw ESR spectrum of $\text{Cr}^{3+}(S=3/2)$ -doped MgO powder observed at ambient temperature. The signal appearing on the lower field side arises from a DPPH single crystal as the reference standard.

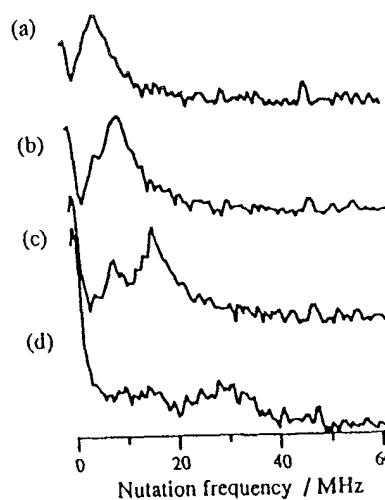


Figure 6. Nutation spectra of $\text{Cr}^{3+}(S=3/2)$ -doped MgO powder observed at ambient temperature. The nutation was measured on the central line of $^{50,52,54}\text{Cr}^{3+}$: (a) - (d) show the dependence of the nutation on microwave excitation amplitude: (a) 25db (b) 20db (c) 15db (d) 10db. The power levels are given only for relative comparison, but they were linear.

$-\gamma\omega_1$) scaled by $7\omega_1/4\omega_D$, showing that the nutation arising from the double quantum transition appears near $\omega_n \sim 0$ in the extreme limit of $H_1 \ll H_D$ and that ω_n departs from nearby zero frequency with increasing microwave amplitude, i.e. ω_1 . Thus, the theoretical prediction can qualitatively interpret the observed behavior of the nutation spectrum of the nearby zero frequency. Also, the possible occurrence of the contribution from a triple quantum transition appearing at the central ESR line ω_0 can not be excluded. For the triple quantum transition of $S=3/2$ systems the scaling factor is $3\omega_1^2/8\omega_D^2$, as given in Table 1 and the triple quantum nutation appears at $\omega_n \sim 0$ in the extreme limit of $H_1 \ll H_D$.

4.2. A QUASI 1D ORGANIC HIGH-SPIN POLYMER A

Figure 7 shows a cw ESR spectrum of the solid-state polymer A observed at 6.7K. The ESR line shape was Lorentzian, indicating the exchange-narrowing taking place in the system. Figures 8(a) and (b) show the microwave amplitude dependence of the on-resonance nutation spectra of the polymer A where the FID signal $s(t_1, t_2)$ was measured at 6.7K. Figure 9 shows a 2D representation of the 1D Fourier-transformed FID signal $s(t_1, t_2)$ as a function of the time-domain nutation defined by the time-axis t_1 segmentation, noting that the FID signal $s(t_1, t_2)$ was Fourier-transformed only along the time-axis t_2 into the frequency-domain power spectra. The FID signal $s(t_1, t_2)$ was obtained at good signal-to-noise ratios by incrementing the interval t_1 , as seen in Figure 9.

In Figure 8 many nutation-frequency components depending on the microwave amplitude are seen. They were reproducible and were not distinguishable at elevated temperatures. In the extreme limit of $H_D \gg H_1$ the lowest distinguishable nutation peak $\omega_n(S_i)$ besides the strong one near zero frequency corresponds to an effective spin quantum number $S_i > 2$, which was evaluated by comparison with the nutation frequency $\omega_n(S=1/2)$ of the reference standard (a single crystal of DPPH): $\omega_n(S_i) > 2\omega_n(S=1/2)$. Table 2 shows the peak assignments to effective molecular spin quantum numbers assuming that $M_S=0 \leftrightarrow M_S'=1$ transitions are dominant in the nutation spectra. The nutation experiment on the polymer A clearly identified the polymer A in the solid state to be a mixture of high-spin assemblages with various spin quantum numbers S_i 's some of which exceed two. This finding unequivocally supports the experimental result from the magnetisation curve fitting for the same polymer: the Brillouin function fitting gave an effective $S=2$ [26]. The magnetisation curve fitting is insensitive to an ensemble of various spin quantum numbers S 's. This fitting procedure is problematic and impractical with the increasing number of S 's expected for extended spin structures of magnetic polymers or spin clusters. The present nutation experiment demonstrates that electron spin transient nutation techniques are more suitable for the spectroscopic discrimination of S 's for high-spin assemblages, noticing that one of the drawbacks of the nutation

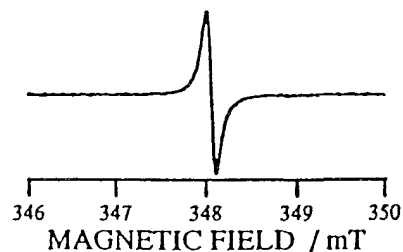


Figure 7. Cw ESR spectrum of a quasi 1D organic high-spin polymer A in the solid state observed at 6.7K.

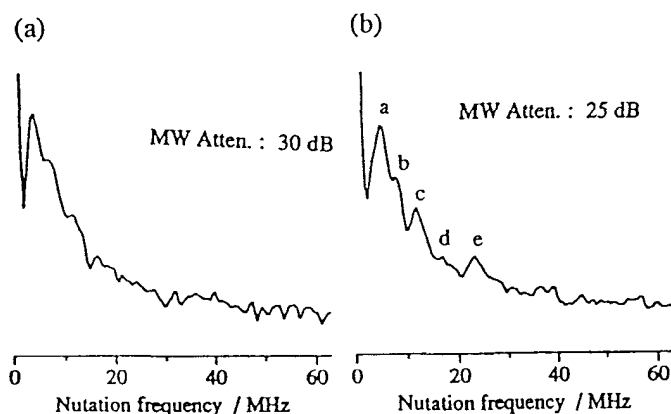


Figure 8. Nutation spectra of a solid-state polymer A observed at 6.7K. The microwave amplitude dependence of the on-resonance nutation is shown: (a) 30db (b) 25db: The corresponding absolute microwave power was not calibrated.

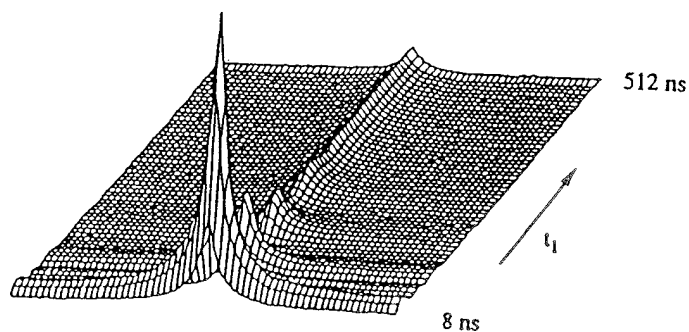


Figure 9. 2D representation of the 1D Fourier-transformed FID signal $s(t_1, t_2)$ of a solid-state polymer A as a function of the time-domain nutation defined by the time axis t_1 . The FID signal $s(t_1, t_2)$ was Fourier transformed only along the time-axis t_2 into the frequency-domain power spectra.

TABLE 2. The nutation peak assignments to effective spin quantum numbers appearing in the nutation spectra observed from the quasi-1D polymer A at 6.7 K.

	ω_n	ω_n/ω_1	S	$[S(S+1)]^{1/2}$
a	4.84 ($= \omega_1$)	1	1/2	
b	7.88	1.63	1	$[1(1+1)]^{1/2} = 1.41$
c	11.47	2.37	2	$[2(2+1)]^{1/2} = 2.45$
d	16.73	3.45	3	$[3(3+1)]^{1/2} = 3.46$
e	22.95	4.74	4	$[4(4+1)]^{1/2} = 4.47$

method is time resolution. For further systematic identification of S's and quantitative determination of their concentration, the sample preparation and nutation experiments of high-spin oligomers **A** with $S=1$ or $3/2$ are under way.

The effective spin multiplicities of molecular high-spin components in the solid-state polymer **A** can be hampered by both inter- and intra-molecular antiferromagnetic couplings and the structural disconnection or termination of the topologically controlled π spin network. The present spectroscopic evidence of the occurrence of molecular high-spin components, however, illustrates that the molecular design controlling the topological spin polarisation is workable for constructing π -conjugated organic super high-spin/super paramagnetic polymers.

5. Prospects of ESTN Spectroscopy

It is, indeed, apparent that X-band ESTN spectroscopy is subject to a technical limitation to time resolution which is interrelated to the detection sensitivity, whether the detection scheme is FID- or ESE-based, but this drawback can be overcome by introducing easy-to access high frequency/high field FT-pulsed electron magnetic resonance spectroscopy such as W-band (~95GHz) ESTN spectroscopy. High frequency/high field FT-pulsed techniques meet much prospect of zero deadtime spectroscopy with enormously enhanced sensitivity.

In view of the time resolution, ESTN spectroscopy can be applied for studying spin assemblages in semimacro-/meso- scales and low dimension in which there are prospects of slowing-down (long time tailing of spin relaxation) of exchange rates among spins. Also, ESTN spectroscopy can see much prospect of characterising semi-classical "giant" or "soft" spin systems appearing in reduced-dimensional magnetic materials to study residual or genuine quantum effects in terms of coherency-transferred 2D spectroscopy. In this context, superparamagnets or super high-spin polymers can be a good prospect for semimacroscopic quantum effects from prototypical examples of soft-spin systems [41,42,44]. Among various topics ESTN spectroscopy applied to spin systems of non-vanishing orbital angular momenta is of fundamental importance in understanding electron magnetic resonance phenomena [40-43].

6. Conclusions

The FID-detected electron spin transient nutation spectroscopy applied for the first time to non-oriented samples was described, exemplifying MgO powder samples doped with $Mn^{2+}(S=5/2)$ and $Cr^{3+}(S=3/2)$ in their high-spin ground state, to demonstrate the advantages inherent in the nutation spectroscopy. The nutation experiment in the extreme limit of $H_D \gg H_1$ (weak microwave excitation limit) can identify the ESR transition. A non-vanishing H_D (the ZFS in order of $1 \times 10^{-4}T$) due to a slight departure from octahedral symmetry was detected at ambient temperature for Cr^{3+} in MgO powder. This finding contrasts with the well-documented fact that the electronic ground state of

Cr^{3+} in MgO is characteristic of the vanishing fine-structure term in the spin Hamiltonian. The nutation spectrum appearing at $\omega_n \sim 0$ indicates the possible occurrence of multiple quantum transitions for an $S=3/2$ system. A particular spectroscopic feature associated with the double or triple quantum transition was qualitatively interpretable by the theoretical consideration in the extreme limit of $H_D \gg H_1$.

The nutation method was for the first time applied to a quasi 1D high-spin organic polymer as one of the most complex amorphous spin assemblages, identifying that the polymer with an exchange-narrowed ESR lineshape is comprised of high-spin assemblages with effective molecular spin quantum numbers S's greater than two.

It can be concluded that electron spin transient nutation spectroscopy is a simple and useful method for the identification of spin quantum numbers and ESR transitions even for the cases of only apparently vanishing fine-structure splittings and the method is applicable to spin systems with residual fine-structure terms in the spin Hamiltonian.

Fundamental theoretical bases for single-quantum electron spin transient nutation were described, particularly for $S=1$ and $3/2$, in the extreme limit of $H_D \gg H_1$, emphasising a viewpoint of nutation spectroscopy. Also, theoretical aspects of multiple-quantum transition ESTN spectroscopy were described.

Finally, the prospects of ESTN spectroscopy were briefly discussed in some aspects, emphasising both the potential applicability to supramolecular functionality magnetic model systems and the usefulness in studying semimacro-/microscopic quantum nature of spins and interacting-spin assemblages in terms of coherency-transferred dynamics and time-domain spectroscopy.

Acknowledgements

This work has been supported by a Grand-in-Aid for Scientific Research on Priority Area "Molecular Magnetism" (Area No.228/04242 103, 04242 104 and 04242 105) from the Ministry of Education, Culture and Science, Japan and also by the Ministry of International Trade and Industries (NEDO Project). One of the authors (T.T.) is grateful to Professor A. Schweiger (E.T.H., Zürich) and Professor J. Isoya (Univ. of Library and Information Science, Tsukuba) for their stimulating suggestions.

References

- (a) S. Morimoto, F. Tanaka, K. Itoh, and N. Mataga, *Preprints of Symposium on Molecular Structure, Chem. Soc. Japan*, 67(1968).
 (b) N. Mataga, *Theor. Chim. Acta.* **10**, 372(1968).
 (c) K. Itoh, *Bussei*, **12**, 635(1971).
 (d) K. Itoh, *Pure Appl. Chem.*, **50**, 1251(1978).
 (e) A. A. Ovchinnikov, *Theor. Chim. Acta.*, **47**, 297(1978).
 (f) T. Takui, *Dr. Thesis* (Osaka University, 1973).
- (a) H. M. McConnell, *J. Chem. Phys.*, **39**, 1910(1963).
 (b) H. M. McConnell, *Proc. R. A. Welch Found. Chem. Res.*, **11**, 144(1967).
- For a recent overview, see the following references.
 (a) J. S. Miller and D. A. Dougherty (eds.), *Mol. Cryst. Liq. Cryst.*, **176**, 1-562(1989).
 (b) L. Y. Chang, P. M. Chaikin, and D. O. Cowan (eds.),

- Advanced Organic Solid State Materials* (Am. Mat. Res. Soc., 1990)p.1-92.
- (c) D. Gatteschi, O. Kahn, J. S. Miller, and F. Palacio (eds.), *Molecular Magnetic Materials* (Kluwer Academic Publishers, 1990).
- (d) H. Iwamura and J. S. Miller (eds.), *Mol. Cryst. Liq. Cryst.*, **232/233**, 1-724(1993).
- (e) J. S. Miller and A. J. Epstein (eds.), *Mol. Cryst. Liq. Cryst.*, in press (1995).
- (f) J. S. Miller, A. J. Epstein, and W. M. Reiff, *Chem. Rev.*, **88**, 201(1988) and references therein.
- (g) J. S. Miller, A. J. Epstein, and W. M. Reiff, *Acc. Chem. Res.*, **22**, 114(1988) and references therein.
- (h) T. Takui, *Organic Magnetic Materials in Electronic Optical Organic Functionality Materials*, A. Taniguchi et al.(eds.)(Asakura Publishers, Tokyo, 1995).
- (i) K. Itoh(ed.), *Molecular Magnetism -- New Magnetic Materials and Magnetic Field Control in Chemical Reactions* (Gakkai Shuppan Centre, 1995).
- 4.(a) T. Takui and K. Itoh, *Polyfile*, **27**, 49 (1990).
 (b) T. Takui and K. Itoh, *J. Mat. Sci. Japan*, **28**, 315 (1991).
 (c) T. Takui, *Polyfile*, **29**, 48 (1992).
 (d) T. Takui, *Chemistry*, **47**, 167 (1992).
- 5.(a) J. S. Miller and A. J. Epstein, *Chemtech.*, **21**, 168(1991).
 (b) C. P. Landee, D. Melville, and J. S. Miller, in *Molecular Magnetic Materials*, D. Gatteschi, O. Kahn, J. S. Miller, and F. Palacio, (eds.) (Kluwer Academic Publishers, 1991).
6. T. Nakamura et al., to be published.
7. T. Ichikawa, *Bunseki*, No.12, 890(1982).
8. J. Isoya, *Bunseki*, No.4, 229(1988).
9. A. Schweiger, *Angew. Chem. Int. Ed. Engl.*, **30**, 265(1991).
10. C. P. Keijzers, E. J. Reijerse, and J. Schmidt (eds.), *Pulsed EPR: A New Field of Applications* (North Holland, Amsterdam /Oxford/New York/Tokyo, 1989).
11. A. J. Hoff (ed.), *Advanced EPR, Applications in Biology and Biochemistry* (Elsevier, Amsterdam/ Oxford/ New York/Tokyo, 1989).
12. L. Kevan and M. K. Bowman (eds), *Modern Pulsed and Continuous-wave Electron Spin Resonance* (John Wiley and Sons, New York/Chichester/Brisbane/Toronto/ Singapore, 1990).
13. S. A. Dikanov and Y. D. Tsvetkov, *Electron Spin Echo Envelope Modulation (ESEEM) Spectroscopy* (CRC Press, Boca Raton/Ann Arbor/London/Tokyo, 1992)
- 14.(a)H. C. Torrey, *Phys. Rev.*, **76**, 1059(1949). (b)E. L. Hahn, unpublished(1949).
15. I. Solomon, *Phys. Rev. Lett.*, **2**, 301(1959).
16. C. S. Yannoni and R. D. Kendrick, *J. Chem. Phys.*, **74**, 747(1981).
- 17.(a) A. Samoson and E. Lippmaa, *Chem. Phys. Lett.*, **100**, 205(1983).
 (b) A. Samoson and E. Lippmaa, *Phys. Rev. B***28**, 6567(1983).
18. F. M. M. Geruts, A. P. M. Kenthens, and W. S. Veeman, *Chem. Phys. Lett.*, **120**, 206 (1985).
19. A. P. M. Kenthens, J. J. M. Lemmens, F. M. M. Geruts, and W. S. Veeman, *J. Magn. Reson.*, **71**, 62(1987).
- 20.(a) R. Janssen, G. A. H. Tjink, and W. S. Veeman, *J. Chem. Phys.*, **88**, 518(1988).
 (b) R. Janssen and W.S. Veeman, *J. Chem. Soc. Faraday Trans.*, **84**, 374(1988).
21. S. S. Kim and S. I. Weissman, *Rev. Chem. Intermed.*, **3**, 107(1980).
22. R. Furrer, F. Fujara, C. Lange, D. Stehlik, H. M. Vieth, and W. Vollman, *Chem. Phys. Lett.*, **75**, 332(1980).
23. D. Stehlik, C. H. Bock, and M. C. Thurnauer, *Advanced EPR*, ed. A. J. Hoff (Elsevier, Amsterdam/Oxford/New York/Tokyo, 1989), p.371.
24. J. Isoya, H. Kanda, J. R. Norris, J. Tang, and M. K. Bowman, *Phys. Rev.*, **B41**, 3905(1990).
25. A. V. Astaskin and A. Schweiger, *Chem. Phys. Lett.*, **174**, 595(1990).
26. H. Nishide, T. Kaneko, T. Nii, K. Katoh, E. Tsuchida, and K. Yamaguchi, *J. Am. Chem. Soc.*, **117**, 548(1994).
27. Y. Teki, T. Takui, and K. Itoh, *J. Chem. Phys.*, **88**, 6134(1988).
28. R. G. Brewer and E. L. Hahn, *Phys. Rev.*, **All**, 1641(1975).
29. N. M. T. Loy, *Phys. Rev. Lett.*, **36**, 5624(1977).
30. H. Hatanaka, T. Terao, and T. Hashi, *J. Phys. Soc. Japan*, **39**, 835(1975).
31. H. Hatanaka and T. Hashi, *J. Phys. Soc. Japan*, **39**, 1139(1975).
- 32.(a) S. Vega and A. Pines, *J. Chem. Phys.*, **66**, 5624(1977).
 (b) S. Vega, *J. Chem. Phys.*, **68**, 5518(1978).
33. A. Wokaun and R. R. Ernst, *J. Chem. Phys.*, **67**, 1752(1977).
34. S. Vega and Y. Naor, *J. Chem. Phys.*, **75**, 75(1981).
35. K. Sato, D. Shiomi, T. Takui, and K. Itoh, to be published.
- 36.(a) K. Holczer, D. Schmalbein, and P. Barker, *Bruker Rep.*, **7**, 4(1988).
 (b) H. Barth, P. Höfer, and K. Holczer, *Bruker Rep.*, **2**, 28(1988).
37. G. R. Hertel and H. M. Clark, *J. Phys. Chem.*, **65**, 1930(1961).
38. M. T. Hutchings, *Solid State Phys.*, **16**, 227(1964).
39. W. Low and E. L. Offenbacher, *Solid State Physics*, ed F. Seitz and D. Turnbull (Academic Press, New York 1965) vol. 17, p. 135.
40. A. S. Ichimura, K. Sato, D. Shiomi, T. Takui, K. Itoh, W. C. Lin, D. H. Dolphin, and C. A. McDowell, to be published.
41. K. Sato, D. Shiomi, T. Takui, and K. Itoh, to be published.
42. T. Takui et al., to be published.
43. T. Takui and K. Itoh, unpublished.
44. K. Sato, D. Shiomi, T. Takui, K. Itoh, C. Rovira, and J. Veciana, to be published.

Strategies for CW and Pulsed EPR in Materials Science¹

John R Pilbrow

*Department of Physics
Monash University
Clayton Victoria,
Australia, 3168*

I. Introduction

Electron Paramagnetic Resonance (EPR), often called Electron Spin Resonance (ESR), as normally practiced for the past 50 years is a spectroscopic technique that is based on sweeping the magnetic field while keeping the microwave frequency fixed.

This fact alone raises some fundamental issues regarding the nature of the spectroscopy under field sweep conditions, matters that have been addressed previously by the author (1-3). This paper will focus on four main themes:- the information content of field swept CW EPR, computer simulations and lineshape modelling, pulsed EPR methods and opportunities for CW and pulsed EPR in materials science. The last point is not new for in the more than 50 years since the discovery of EPR in Kazan, Russia, by Zavoisky in 1944, materials science applications have always been evident.

CW-EPR Spectra are readily interpreted in terms of spin Hamiltonian parameters appropriate to the assumed point symmetry of the paramagnetic centres. In the past, data analysis often depended on perturbation theory solutions because they did not require large computational capacity, but that has now changed so that numerical diagonalisation of the Hamiltonian can increasingly be carried out on PC's. Coupled with this is the need for more adequate computer simulations that provide for physically appropriate lineshapes and which allow for modelling of disorder, even in crystals.

Pulsed EPR has become rather more accessible these days through the advent of the commercial Bruker ESP380E series of FT/CW spectrometers. Whilst a suite of options is readily available, for transition metal ions, as the FID cannot normally be observed, the results of interest are

based on electron spin echoes, especially, electron spin echo envelope modulation (ESEEM). The earliest ESEEM was based on two-pulse and three-pulse sequences (4,5), the latter permitting both 1D and 2D experiments. The four-pulse HYSCORE method (6) was introduced to improve the quality of 2D correlations compared with 2D three-pulse experiments, the 5 pulse method of Gemperle et al. (7) improved the modulation depth and the six pulse sequence experiments developed in our laboratory (8-11) have overcome some of the shortcomings of HYSCORE and provided additional options for spectral resolution and correlation. Echo-detected EPR is also being actively pursued in our laboratory (12).

In reporting spin Hamiltonian parameters the impression can sometimes be conveyed that the mean values of the parameters are equivalent to the spectrum. This is not strictly correct and information regarding sources of linewidths, for example, often gives more than a hint of local disorder. It is a contention of this author that disorder is present in probably every example investigated by EPR. A good case in an otherwise 'clean' spectrum concerns the old result for ²³¹Pa doped Cs₂ZrCl₆ measured at 9.168 GHz (13). Here the mean g- and A- values show the centre to be accurately isotropic with $I = 3/2$. Unequal spacing of the four hyperfine lines at X-band is consistent with the spin Hamiltonian parameters originally reported and the four lines have exactly the same integrated intensities. The unequal peak heights reported but not explained in the original paper arise from the field or frequency dependent g-A correlation effects now well-known in CW-EPR (14, 1-3). Therefore it is concluded that there is local disorder even in such a case.

It is also important to recall that the intrinsic sensitivity of magnetic dipole transitions is many orders of magnitude below that for electric dipole transitions. This intrinsic low sensitivity has the potential to make EPR, at

¹ Based upon an Invited Lecture given to the Conference of the International Society for Magnetic Resonance (ISMAR-95) Sydney, Australia 16-20 July 1995.

least, a very unattractive spectroscopic technique in practice. However, the use of resonant sample cavities, loop-gap resonators and other structures with combinations of quality factor and filling factor to enhance the detected signal, makes EPR a feasible technique for a wide variety of problems, sometimes the only way to address certain kinds of questions. We need reminding, of course, that the use of EPR probe in materials science will depend on relatively low concentrations of the paramagnetic centres. In many cases these will be added impurities and their effect on other properties of the materials should always be tested. In ideal cases the probes would be an intrinsic component of the system.

II. Fundamentals of EPR

Most detection methods in EPR record a signal a function of magnetic field which is proportional to the absorption χ'' and to achieve this the microwave bridge needs to be set up carefully. Further, CW-EPR are almost always obtained using field modulation where one normally detects the first harmonic after phase sensitive detection. It is usually stated that the first derivative of absorption was observed. This is only approximately correct as the spectra almost always contains information due to higher harmonics. The higher harmonics can be removed by means of the technique of pseudomodulation (15).

It has been known for many years (1) that the detected signal is really a function $S(B, \nu)$ of two variables, field (B) and frequency (ν). An immediate consequence is that the integrated intensities in field and frequency domains are not equivalent, nor do they have the same units (1)! The integrated field swept lineshape is, however, a characteristic of the spectrum.

On the experimental side, since the range of resonant sample structures from cavities, with non-uniform B_1 fields, to loop-gap resonators and dielectric resonators, with very uniform B_1 fields, emphasis should shift from power levels to magnitudes and distributions in B_1 .

Care should always be exercised in the setting up of the microwave bridge and in seeking to use the minimum modulation settings consistent with a usable signal. In this way one can be sure of what is being measured (see reference 3, chapter 4).

There are a number of levels at which EPR may be understood. Since the energy levels are typically 0.3 cm^{-1} apart under usual X-band conditions, there is competition between the transitions induced by the microwave field and relaxation processes. These can best be understood using quantum mechanics but the modified classical equations of motion or Bloch Equations, modified by addition of relaxation terms, provides a useful phenomenological level

of understanding that is useful for CW-EPR but particularly for understanding pulsed EPR when $S = 1/2$.

The immediate consequence of field sweeping is that in order to obtain quantitative simulations with the minimum number of parameters, the detected signal is properly described in such a way that both field sweep and frequency sweep are readily accounted for using a single master equation. This matter has been explained at length elsewhere (1-3). The simplest way to understand the connection between field and frequency sweep is to realise that if one observes say the peak of a line and that were all one knew about the spectrum, and all other information were blocked out, then one would not know whether the field or the frequency was being swept. The relation (see e.g. reference 2, Eqn. 3)

$$S(B, \nu) = C\nu\eta Q_o |V_{ij}|^2 f(\nu - \nu_o[B], \sigma_\nu) \quad (1)$$

was used successfully to explain many of the puzzles surrounding field swept EPR particularly of highly anisotropic systems and to account for asymmetric looping transitions for $S = 3/2$ due to 'non-crossing' levels. An extended version of Eq. 1 can be written down for $S > 1/2$ (16). In the analysis of Zhong and Pilbrow (16), distinction is made between the *resonance condition* and the *resonance centre* and this enables one to relate the original quantum statistical derivation of Slichter (17) to the lineshape function and also to correct an error in the expression due to Coffman (18) where the distinction was blurred.

A. Spin Hamiltonian, Crystal and Ligand Field Theories

Quantitation of spectral data, whether from CW-EPR or from pulsed EPR and ENDOR, is achieved through Spin Hamiltonian parametrisation. The Spin Hamiltonian is well-established and is simply noted here. It is the first of four important equations in EPR, the others being expressions that indicate the temperature dependence of spin-lattice relaxation, the equation that describes the detected signal, and expressions that describe the linewidth.

The Spin Hamiltonian is a device for parametrising the lowest set of energy levels and in most models, finding the connection between the parameters and the energy splittings of the total system. is non-trivial and is compounded by the presence of electron spin that is only indirectly connected to the cartesian coordinates of the paramagnetic centre via spin-orbit coupling. The connection between the Spin Hamiltonian and the 'real

world' occupied by the transition metal ion or free radical in its own local environment, is found in one or more of the crystal or ligand field theories which provide a parametrised description of the modification of free ion energy levels caused by the local environment viz. surrounding ligand atoms. These vary from the Angular Overlap Model (AOM), LCAO-MO and, ideally, *ab initio* calculations which are ligand field models. With regard to Crystal field theories, one has the old point-charge model and the Superposition Model (SPM). AOM and SPM are related and both prescribe local parameters for each near neighbour atom and are in a very real sense an advance on what Gerloch (19) has described as 'global' models such as the traditional crystal field models or LCAO-MO theory.

In EPR practice, it is usually assumed that \mathbf{g} and \mathbf{A} are tensors. Abragam and Bleaney (20) showed that, in general, these should be regarded as 'tensors' but this author refers to them as interaction matrices. It is the 'squares' of \mathbf{g} and \mathbf{A} that are tensors in the strict physical sense. In fact the clue was always present through the characteristic g^2 and g^2A^2 formula. The symmetry or otherwise of \mathbf{g} and \mathbf{A} has no measurable consequence.

Low symmetry sites have non-coincident principal directions for the various interactions and there are many examples going back to the 1950's (21). For example, for monoclinic symmetry (C_2 , C_{2h} and C_s) there is only one symmetry determined principal direction. In the case of C_s it is the normal to the reflection plane. For copper with selenium coordination, the large selenium spin orbit constant complicates any simple intuition one would otherwise have had (22). For most cases it appears that the \mathbf{g} axes are rotated in characteristic ways relating to the orientation of the out-of-plane orbitals whereas \mathbf{A} axes lie close to principal ground state lobes or between them (see reference 3, chapter 3).

There is another twist to this story. Belford and the author (23) showed that for monoclinic symmetry the motionally averaged hyperfine coupling depends on the trace of \mathbf{A} in any representation and is not, for low symmetries, the mean of the three principal hyperfine constants! This result is also presumed to hold for triclinic symmetry (C_1 and C_i).

B. Bloch Equations and the Rotating Frame

The Bloch equations in the rotating frame and slow passage solutions to them have been widely exploited over the past nearly 50 years for $S = 1/2$ (or $I = 1/2$) systems. Whilst the general ideas are found to have utility when $S > 1/2$, the situation resulting from state mixing requires that

simple pictures so valuable for $S = 1/2$ is less obvious and so this approach must be used with caution (24).

C. Implications for Computer Simulations (1-3, 25)

Use of Eqn. 1 leads to a choice of a minimum theoretical parameter set and does not require unwarranted guessing of the correct field-swept lineshape function, which can easily be asymmetric, as would be required in the conventional approaches to CW-EPR spectroscopy. Other consequences of the use of Eqn. 1 are that linewidth anisotropy becomes less of a mystery since much of the anisotropy seen in highly anisotropic $S = 1/2$ systems is no more than a consequence of scaling imposed by sweeping the field. Asymmetric lineshapes, seen whenever there is a distribution of g -factors, arises quite naturally within the theory. Finally, correlated, frequency dependent linewidth behaviour has been built into the application of Eqn. 1 in a consistent way. Both the latter and a detailed explanation for strain broadening in proteins shows that the orientational behaviour of the linewidths depends on the *fourth order in the direction cosines* (26). Anisotropy in transition matrix elements has long been allowed for in simulations, particularly powder simulations (see e.g. reference 3, chapter 5).

III. Pulsed EPR

For transition metal ion EPR, pulse experiments are in almost all cases based on the spin echo and not on the FID simply because of the finite dead-time of the instrument, usually about 72 nsec for the Bruker ESP380E. We consider briefly the electron spin echo, echo-detected EPR, the various ESEEM options and now, particularly, with regard to materials science applications, 2D forms of ESEEM, spin-locked ESEEM, and finally, the six-pulse experiments discovered and developed in our laboratory. ESEEM is a major technique for the determination of distances from the paramagnetic centre to particularly distant nuclei, supplementing information from ENDOR.

A. 2 and 3 pulse ESEEM

These were studied in depth by Mims and associates over more than 20 years and the theory is due to Mims (4, 5). In 2 pulse ESEEM the interval between the two pulses is stepped sequentially by a small sampling interval. What is

observed is that the profile of the echo response is modulated in a characteristic fashion which upon Fourier transforming yields sum and difference frequencies of the nuclear frequencies associated with the combined effect of hyperfine structure and the nuclear Zeeman effect. There are two options with three-pulse ESEEM. One can step either the time τ between the first two pulses or the time T between second and third pulses. In either case a modulation occurs and it is a function of the separate nuclear frequencies and the two times. For 1D ESEEM, one keeps either τ or T fixed and steps the other and the frequencies obtained after Fourier Transforming are just the ENDOR frequencies though it is typically the case that the strong ESEEM frequencies are weak ENDOR frequencies and *vice versa*. To achieve a 2D outcome, both times are stepped sequentially and one looks for correlations between transitions which arise from a single centre.

B. Improvement to Correlation and to Modulation Depth

There is a limitation to three-pulse 2D ESEEM since the first interval is limited by T_M and the second interval by T_1 so the two dimensions are not symmetrical. To overcome this deficiency, Hofer et al. (1986) developed the 4 pulse HYSORE method by inserting a π pulse between second and third pulses of the three-pulse sequence, thus dividing T into two intervals and then stepping both intervals. In this way the 2D frequencies are symmetrical unlike the 2D three-pulse ESEEM experiment and are limited only by the spin-lattice relaxation time, T_1 . Thus it becomes more feasible to examine correlations. In order to improve the modulation depth, Schweiger's group (7) have introduced a 5 pulse sequence.

C. Six-pulse options

During 1994, a member of my research group, Mr Ruitian Song, worked out that the six-pulse sequence $(\pi/2)_x - (\pi)_x - (\pi/2)_y - (\pi)_x - (\pi/2)_y - (\pi/2)_x$ not only retains the gain in modulation of the five pulse method, but succeeds in putting more of the intensity into the off-diagonal peaks than in a comparable HYSORE experiment (8).

Developments from the original six-pulse observation involve 1D strategies that also lead to correlation information and improved spectral resolution and precision. One of the techniques involves line shifting rather than line narrowing (9-11). We are engaged in in-depth applications of these methods to problems in

materials science since the methods do not appear to be limited to any particular kind of paramagnetic centre.

D. Spin Locking and Hyperfine Decoupling

In another development, Dr Y C Zhong found that spin locking (27) also worked for EPR (28) and that a 2D form of it is also achievable (30). This is called SLESEEM. In a response to the first paper, Jeschke and Schweiger (29) repeated the observation and argued that there is also some hyperfine decoupling occurring as well.

E. Echo-Detected EPR

Part of our interest is in modulation free forms of spectroscopy and to that end we have investigated echo-detected EPR due to alanine, as an example of a free radical system of some practical importance as a radiation dosimeter. The procedure was to record the whole of the echo profile and then to take the Fourier Transform (FT) at each magnetic field. The true echo-detected response is then simply the slice through the maximum of the FT and this agrees exactly with the field dependent profile based on integration of the whole echo (12). Owners of Bruker ESP380E spectrometers can do these experiments using the software package either on the spectrometer or using WINEPR software. It is not necessary to have a hardware integrator. It is our view that echo-detected EPR based simply on peak amplitudes of the echoes is, in fact, not very useful. Further investigations of echo-detected EPR have been made for Cr^{3+} in ruby single crystals which show e.g. for non-crossing levels, the energy spacing between the levels may be obtained directly from the FT of the echoes and that there are significant anisotropies seen for some transitions. In one case the echo intensity falls to almost zero within 0.5° of a turning direction. This latter study involved consideration of nutation frequencies for $S > 1/2$, effects due to finite bandwidth and incorrect turn angles, simply because the presence of significant state mixing means that the very useful intuition obtained from the usual rotating frame considerations for $S = 1/2$ require modification. Evidence has been found for very anisotropic relaxation times. The presence of the aluminium nuclei in the lattice cause modification of the phase memory time. By adjusting one of the times in the pulse sequence so that one nuclear modulation is suppressed, one can use this to separate different lines in the spectrum. So a modulation of the echo-detected EPR can occur (24).

IV. Materials Science

There is enormous scope for applications of both CW and pulsed EPR methods in materials science as well as in Chemistry and Biology. There is now an impressive suite of possible experiments most of which have been referred to already. The measurable parameters or potential importance include the following:-

- Mean Spin Hamiltonian parameters
- CW lineshape information (gleaned from simulations)
- T_1 - temperature dependence, anisotropy, particle size, molecular size
- Weak couplings from ESEEM and ENDOR - distance information
- Phase transitions and relation to other data
- Effect of stoichiometry or lack of it
- Disorder (gleaned from distributions of measured parameters)

A. Range of Materials

In one of the earliest books on EPR, published by Ingram as long ago as 1955, there is a very interesting table with reference to applications of EPR to materials science (31). It is remarkable how current much of that remains today!

EPR investigations in materials science will inevitably focus on insulating materials though there is a place for semiconductors. Classes of materials should include crystals and disordered materials such as ceramics and glasses. The following list has been compiled by the author from a typical conference proceedings (32) though something comparable could just as easily have been obtained from any issue of Physical Review B or Journal of Physics (Condensed Matter Physics) and many others. It would appear that the motivation for much of the work reported here is towards new high technology devices and solid state properties.

- Tunable solid state lasers
- Conductive oxides
- Solid State Electrolytes
- Fluoride glasses (optical waveguides)
- Ceramics
- Photo-refractive and non-linear materials
- Catalysts
- Radiation dosimeters
- Non-stoichiometric compounds
- High T_c superconductors

B. Disorder

As already indicated in the Introduction, disorder, in a variety of ways, is found in all materials. We may list obvious kinds of disorder as follows:-

In crystals

- Effect of impurity ions and loss of strict translational symmetry
- Twinning
- Crystal mosaic effects (33)
- Dislocations
- Random Strains, electric fields, efg's
- Non-stoichiometry
- Plastic deformation
- Radiation induced defects, vacancies etc.

In Systems with partial order (see reference 3, chapter 5)

- Pillared clays
- Probes in oriented liquid crystals

In disordered structures

- Glasses - random networks, short-range order (34)
- Ceramics

In Low Dimensional Systems

- Layer structures
- Films

Orientalional Disorder

- randomly oriented molecules in powders and frozen solutions

On a small-scale

- Surface vs volume effects in 'nano-particles'
- phonon processes versus localised modes in small molecules and 'nano-particles'

C. Modelling Disorder in EPR of Solids

In the first instance this is usually tackled through making assumptions regarding distributions of Spin Hamiltonian parameters and incorporating the model into a computer simulation program. Whilst such models are strictly phenomenological, they work in the sense that acceptable EPR spectral profiles are often obtainable. But they lack connection to real source of the disorder. Realistic models of disorder were developed in the 1960's for lineshapes due to radiation defects in crystals (34) leading to the following model lineshapes in different circumstances (Table 1).

Table 1. Inhomogeneously Broadened Lineshapes (35)

<p><u>Random Strains & Random Electric Fields</u> <i>Lorentzian lineshape</i></p> $f(\nu) = f_m \Gamma^2 / [\Gamma^2 + (\nu - \nu)^2]$
<p><u>Random Electric Fields</u> <i>Holtzmark function</i></p> $f(\nu) = f_m \exp[-(\ln 2)\{(\nu - \nu) / \Gamma\}^{3/2}]$
<p><u>Dislocation Strains</u> <i>Stoneham</i></p> $f(\nu) = f_m \exp[-(\ln 2)\{(\nu - \nu) / \Gamma\}^2] \times \{1 - C \ln (\nu - \nu) / \Gamma \}$
<p><u>Unresolved Hyperfine Splittings</u> <i>Gaussian</i></p> $f(\nu) = f_m \exp[-(\ln 2)\{(\nu - \nu) / \Gamma\}^2]$

D. Glasses

Glasses pose a more difficult problem in that there is only short range order and site-to-site variations leading to random bond angles and bond lengths (34). Even here models are often limited to postulating distributions of spin Hamiltonian parameters.

There is a new aspect to properties of glasses due to Orbach and his colleagues and collaborators (36-8). Recent theoretical work on spin-lattice relaxation and thermal conductivity of glasses has indicated characteristic length scales of about 2 nm for silicate glasses (hard glasses) and about 5 nm for phosphate glasses (soft glasses) (39). More recent correspondence has indicated factors that affect spin-lattice relaxation and the switching off of phonon processes and importance of local vibrational phenomena. Specific temperature dependences of the spin-lattice relaxation rate have been calculated and they await a

more systematic experimental verification. Conversely, we might ask "What are the properties of particles whose dimensions are comparable to the length scales referred to above and what interesting properties might such particles have?"

E. Current activities

To indicate the range of our commitment to materials science, the following is a list of projects involved in our laboratory at Monash University:-

- CW and Pulsed EPR (free radical systems, metal complexes and crystals)
 - Further work on six-pulse sequence
 - 2D correlation strategies
- Transition metal ions in:
 - crystals
 - natural and synthetic gemstones (distinction between natural and synthetic stones)
 - Ti^{3+} , V^{4+} in recrystallised emeralds with narrow EPR lines
 - oxide catalysts
 - aluminosilicates (Al ESEEM, $I = 5/2$)
 - Origin of color centres in Argyle Diamonds
 - Jahn Teller Effect
 - relaxation theory and experiment on disordered systems
 - Ce doped fluoride glass
 - chemical complexes and metal proteins
- Alanine dosimetry
- Computer simulation

V. Conclusion

With regard to CW-EPR in materials science, it is clear that there will be an on-going need for improved, high quality simulations. To that end, there will be increasing pressure to obtain spectra at more than one microwave frequency in some cases from about 1 GHz to around 100 GHz. An important goal will be to exploit the many pulsed EPR options as tools in the characterisation of new and technologically important materials. here is a future for EPR in materials science and it is predicted that a higher level of modelling will be found to make this a reality.

Acknowledgments

Contributions from many members of the of the Monash EPR group are acknowledged: Drs Don Hutton, Yong Zhong, Philip Tregenna-Piggott and George Lazarev; PhD students: Chris Noble and Ruitian Song.; Sabbatical visitors: Prof David Shaltiel (Hebrew University of Jerusalem) and Dr Y.Y. Lim (University of Malaya). Professor R L Orbach, Chancellor of the University of California, Riverside, is thanked for the provision of published and unpublished material relating to magnetic relaxation in glasses. Support from the Australian Research Council and Monash University is gratefully acknowledged.

References

- J.R. Pilbrow, *J. Magn. Reson.* **58**, 186 (1984).
- J.R. Pilbrow, *Bull. Mag. Res.* **10**, 32 (1987)
- J.R. Pilbrow, *Transition Ion Electron Paramagnetic Resonance*, Oxford Univ. Press, London/New York (1990).
- W.B. Mims, *Phys. Rev. B* **5**, 2409 (1972).
- W.B. Mims, *Phys. Rev. B* **6**, 3543 (1972).
- P. Höfer, A. Grupp, H. Nebenfür and M. Mehring, *Chem. Phys. Lett.* **132**, 279 (1986)
- C. Gemperle, A. Schweiger and R.R. Ernst, *Chem. Phys. Lett.* **178**, 565 (1991).
- R. Song, Y.C. Zhong, C.J. Noble, J.R. Pilbrow and D.R. Hutton, *Chem. Phys. Lett.* **237**, 86 (1995).
- R. Song, Y.C. Zhong, C.J. Noble, J.R. Pilbrow and D.R. Hutton, *Chem Phys Lett* **243**, 324-9. (1995).
- R. Song, Y.C. Zhong, C.J. Noble, J.R. Pilbrow and D.R. Hutton, *Chem Phys Lett* (1995). (In press)
- R. Song, Y.C. Zhong, C.J. Noble, J.R. Pilbrow and D.R. Hutton *J. Magn. Res A* (1995). (In press)
- C.J. Noble, Y.C. Zhong, J.R. Pilbrow and D.R. Hutton, *J. Magn. Res. A* **105**, 323-5 (1993).
- J.D. Axe, H.J. Stapleto and C.D. Jeffries *Phys. Rev.* **121**, 1630, 1960)
- J. R. Pilbrow, *Applied Mag. Res.* **6**, 161 (1994).
- J.S. Hyde, M. Pasnekiewicz-Gierula, A. Jesmanowicz and W.E. Antholine *Applied Mag Res* **1**, 483 (1990)
- Y.C. Zhong and J.R. Pilbrow, *J. Magn. Res.* **93**, 447-57. (1991).
- C.P. Slichter, *Principles of Magnetic Resonance*, Harper and Row, New York (1963).
- R.E. Coffman, *J. Phys. Chem.* **79**, 1129 (1975).
- M. Gerloch, *Magnetism and Ligand Field Analysis*. Cambridge University Press (1983).
- Abragam, A. and Bleaney, B., *Electron Paramagnetic Resonance of Transition Ions*. Clarendon Press, Oxford (1970).
- J.R. Pilbrow and M.R. Lowrey, *Rep. Prog. Phys.* **43**, 433 (1980).
- C.P. Keijzers, G.F.M. Paulussen and E. de Boer, *Molec. Phys.* **29**, 973 (1975).
- R.L. Belford and J.R. Pilbrow, *J. Magn. Res.* **11**, 381(1973).
- C.J. Noble, Private Communication (1995).
- A.R. Bizzarri and S. Cannistraro, *Molec. Phys.* **85**, 913 (1995).
- W.R. Hagen, D.O. Hearshen, R.H. Sands and W.R. J. *Magn. Res.* **61**, 220 (1985); W.R. Hagen, D.O. Hearshen, L.J. Harding and W.R. Dunham, *J. Magn. Res.* **61**, 233 (1985).
- S.R. Hartmann and E.L. Hahn, *Phys. Rev.* **128**, 2042 (1962).
- Y.C. Zhong and J.R. Pilbrow, *Chem. Phys. Lett.* **222**, 592-6 (1994).
- G. Jesckhe and A. Schweiger, *Chem. Phys. Lett.* **231**, 574 (1994).
- Y.C. Zhong and J.R. Pilbrow, *J Magn Res A* **110**, 245-7 (1994)..
- D.J.E. Ingram, *Spectroscopy at Radio and Microwave Frequencies*, Butterworth Scientific Publications, London (1955).
- O. Kannert and J.-M. Spaeth, *Defects in Insulating Materials*, World Scientific, Singapore, Vols 1, 2 (1993).
- D. Shaltiel and W. Low, *Phys. Rev.* **124**, 1062 (1961).
- J. Kliava, *phys. stat. sol. (b)* **134**, 411 (1986).
- A.M. Stoneham, *Rev. Mod. Phys.* **41**, 82 (1969).
- R. Orbach, *Hyperfine Interactions* **49**, 325 (1989)
- R. Orbach *Transport and vibrational lifetimes in amorphous structures* Proceedings of 4th International Conference on Phonon Physics and 8th International Conference on Phonon Scattering in Condensed Matter Physics, July 24-28 Hokkaido University, Sapporo, Japan (in press)
- R. Orbach, S. Alexander and O. Entin-Wohlman *Magnetic Relaxation in Random Structures* (Unpublished lecture notes, 1989).
- R. Orbach, Quoted in Lecture at Symposium in honour of the 80th Birthday of Professor B. Bleaney, St. John's College, Oxford, June 29th 1995.

Functional Magnetic Resonance Imaging of the Human Brain

Keith R. Thulborn, Joseph Gillen, Benjamin McCurtain*,
Carlos Betancourt, John A. Sweeney*

Magnetic Resonance Research Center
Departments of Radiology and Psychiatry*
University of Pittsburgh Medical Center
Pittsburgh, PA 15213
USA

Contents

I.	Introduction	1
II.	Instrumentation	1
III.	Experimental Results	4
IV.	Conclusions	6
V.	Acknowledgments	6
VI.	References	6

I. Introduction

Since the first demonstration of the localization of human brain function in response to photic stimulation (1), many reports of the application of functional magnetic resonance imaging (fMRI) to the mapping of sensory, motor and cognitive functions have appeared in the literature. These results have been based largely on the small increases in MR signal intensity (1-5%) arising from changes in the concentration of paramagnetic deoxyhemoglobin in blood in the microvasculature and has been termed blood oxygenation level dependent (BOLD) contrast (2). The decrease in the deoxygenation of blood that occurs when blood flow increases in response to increased neuronal activity (3) changes the tissue bulk magnetic susceptibility, thereby changing transverse relaxation conditions. Using the paired subtraction technique, images of the brain obtained under conditions of rest and task performance can be compared statistically to map the regions of the brain involved in the performance of the task. Although the effect is small, instrumentation has been designed to exploit this effect as a powerful probe of brain function for research and clinical purposes. The requirements and constraints for the instrumentation for fMRI are described and the performance of fMRI at 1.5 and 3.0 Tesla is illustrated by reference to human studies of a motor task.

II. Instrumentation

The spatial and temporal resolution of the MR image must be matched to the target size of the functional structures of the brain. The compromise between spatial and temporal resolution ultimately is limited by the available signal-to-noise ratio (SNR). As SNR increases with the magnetic field strength, higher field strength offers a better match of both spatial and temporal resolution to the brain anatomy and function. Although a small number of 4 Tesla research systems have been in use for a number of years, the applications have been limited. Routine human studies, especially when patients are involved, are constrained usually to less than 60 minutes for full subject cooperation. This time constraint requires very efficient subject handling, localization and data acquisition. Additionally, radiofrequency (RF) coil technology of the type used at clinical field strengths must be modified at very high fields for the large FOV required for humans. The introduction of the 3.0 Tesla whole body system by General Electric Medical Systems based on modifications to the clinical 1.5 Tesla Signa scanner provides an excellent compromise between clinical efficiency and the SNR advantage at twice the field strength. The system has all the conventional imaging, angiographic and spectroscopic functionality as well as ultra-fast echo-planar capabilities (Advanced NMR Systems, Inc.) of the 1.5 Tesla clinical system. The decade of experience with the clinical system ensures a robust high field system for which service and quality assurance are

available.

The realization of the full SNR advantage of high field required optimization of the field homogeneity. Such homogeneity was achieved by combined adjustment of the superconducting shims and passive shimming. In particular, this adjustment required fine adjustment of the current supplied to the superconducting coils. Using a spherical phantom, a final linewidth of about 5Hz over a 22 cm diameter spherical volume was achieved on the 3.0 Tesla magnet (Magnex Scientific, Inc.). This compared favorably with a value of 2Hz over 22 cm diameter spherical volume for the 1.5 Tesla magnet installed in the same manner. Through the use of closely-coupled passive shielding, this magnet provides the same clear bore access (55 cm) as the standard clinical scanner while maintaining a similar fringe field footprint of the 1.5 Tesla magnet. This allows the

magnet to be sited within the hospital without excessive space or shielding requirements of 4.0 Tesla systems.

So as not to waste the gain in signal with field strength, the background noise of the receiver must be minimized. This was achieved by rigorous adherence to 100dB isolation at all operating frequencies and was achieved with a continuously soldered solid copper room and appropriate filtering of all wiring and electrical power entering the scan room. For long term performance, the door is sealed with a continuous, pneumatically-inflated RF seal, rather than the more common pressure contact system used clinically. As fMRI requires transmission of various stimuli and responses into and out of the room, respectively, a multi-channel, fiber-optic transmission system avoids the introduction of unwanted stray noise. Such a system is described in Figure 1.

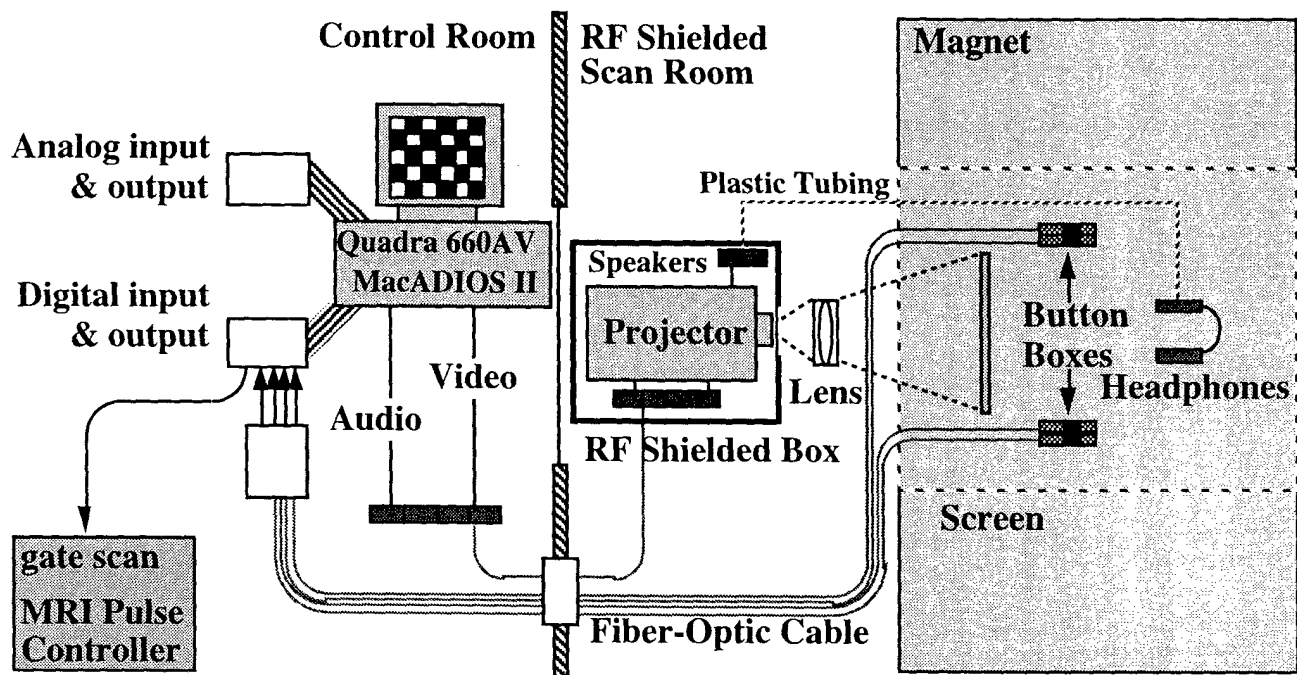


Figure 1. Schematic diagram of the fMRI control system in which a Macintosh 660AV computer containing a Mac ADIOS II board provides the master clock to time audiovisual stimuli from the Macintosh, the trigger for image acquisition for the fMRI scanner and physiological records of cardiac pulsations via pulse oximeter and respiration via a thoracic tension transducer. The transmission of audiovisual stimuli into the scan room is via a fiber-optic system that carries the video signals for three colors and sound to the high-resolution, color, single LCD projector contained within a RF sealed box. High fidelity visual stimuli are projected through a lens to a rear projection screen located within the bore of the magnet for viewing by a supine subject via an angled flat mirror. Audio stimuli are transmitted to the subject via pneumatic tubes and ear muffs. Image acquisition can be gated to the stimulus while responses are recorded by up to four finger switches.

Because fMRI is a paired subtraction technique in which images are acquired at different times and compared for small differences in signal intensity, instrument stability must ensure that instrumental fluctuations in signal intensity are smaller than the size of the signal change to be detected (1-5%). Signal stability of better than 1%

over 30 minutes is achieved routinely on a water phantom for both the 1.5 and 3.0 Tesla systems, as shown in Figure 2. Care must be taken to control instrument room temperature, without temperature gradients and to operate with all rack covers in place to ensure adequate air circulation.

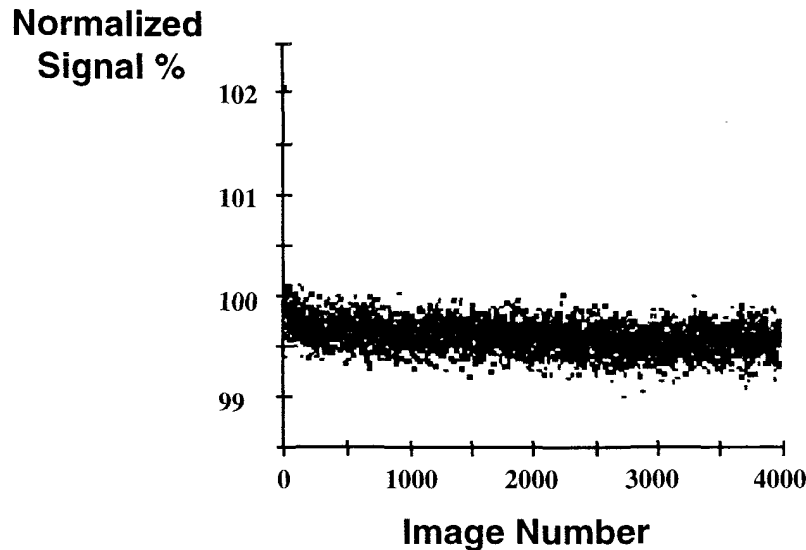


Figure 2. Normalized SNR for echo-planar images (single shot, spin echo, TE = 50ms, 128 x 64, 5mm slice thickness, TR = 5s) for a doped water phantom measured over 30 minutes.

Cerebral function occurs in the cortical gray and deep gray matter of the brain while the communication of neuronal processing between different gray matter regions is via the white matter. The spatial dimensions to be contended with are the thickness of the gray matter, which is about 6 mm thick in a young adult, and the volumes of the nuclei which are often less than 6 mm in diameter. This small target size is coupled to a highly convoluted cortical surface in which neuronal pathways are widely distributed. Such anatomy imposes requirements for spatial resolution to be better than this target size over a large field of view (FOV). As cerebral processing is rapid, fast data acquisition is desirable. Because BOLD contrast relies on a vascular response that may take as long as 5 to 10s to reach a maximum, very fast imaging such as echo-planar imaging (EPI) allows the kinetics of the vascular response to be examined and signal averaging to improve SNR. Importantly for fMRI of widely distributed neural pathways, multiple slices can be obtained rapidly to meet the requirement of a large FOV in three spatial dimensions while providing

acceptable voxel size of 3 x 3 mm in-plane and 3 to 5 mm through-plane resolution, as shown in Figure 3. The echo-planar systems used in both the 1.5 and 3.0 Tesla systems are the three axis, resonant gradient technology of Advanced NMR Systems, Inc. This technology was adapted to allow the continuous acquisition of 0.5GB data with links to a high performance multi CPU computer (Silicon Graphics Computer Systems) via a high performance local area network (CDDI-LAN) for high speed, off-line processing.

Having optimal SNR by maximizing the signal through field strength and magnet homogeneity and minimal noise through judicious RF isolation, and having achieved the instrument stability adequate for the paired subtraction technique on a platform that allows efficient human subject studies, at least three other areas must be examined. These are subject preparation, paradigm presentation in the scanner and the statistical processing of the data.

As fMRI requires that the subject participate in a task during scanning, subject preparation is important to remove the effects of

the novel environment on task performance. Anxiety, confinement and acoustical stimuli from the scanning protocol are extraneous background noise to brain function and can perturb performance. This complication can be minimized through the use of a simulator that replicates the scanner environment. The simulator was constructed from the fiberglass patient tube used in manufacturing the actual whole body gradient set, thereby reproducing the spatial dimensions of the scanner. Acoustic effects are simulated with a tape recording of the particular protocol to be used. The emphasis is on the scan setup sounds as these tend to change in level and frequency most quickly and can be disturbing, particularly to pediatric subjects. Anxiety is monitored by a simple anxiety scale and physiological parameters of heart rate and blood pressure. With a relaxed approach away from the scanner in which time constraints are removed, previously anxious subjects are able to adapt to the simulator in less than 30 minutes and enter the scanner without anxiety. The simulator is also equipped for paradigm presentation and can be used to obtain behavioral data on training effects if this is appropriate to the investigation.

The method of presentation of the paradigm task to the subject must minimize degradation of the SNR of the imaging as described above, be simple to use for the operator and be flexible for paradigm redesign. The system described in Figure 1 uses a custom-designed software package in the Macintosh environment that achieves versatility and flexibility.

Processing of the information requires a statistical analysis of the difference in signal intensity between images acquired during the rest and active states. As many fMRI paradigms cycle between rest and active states several times, reproducibility of response can be built into the analysis by requiring signal changes to follow the cycles of the paradigm. Modeling the response to the mechanisms producing the effect will be a powerful approach to improving our understanding of how to develop appropriate statistical methods. However such methods are still investigational and a conservative approach is to use a two tailed t-test on a voxel by voxel basis to examine signal differences that are reproducible over multiple repeats of the paradigm. This provides some consideration of the variability of the signal in each condition of rest and activity. Other approaches are numerous and include regression and Fourier analyses.

III. Experimental Results

To demonstrate the performance of the entire fMRI instrumentation, a simple motor paradigm of bilateral finger coordination was used. During the active condition, the thumbs are apposed, in order and sequence, to the second, third, fourth and fifth fingers, continuously for 30 seconds. The rest condition has no finger movement. Such a task is expected to show activation in at least the motor cortex and somatosensory cortex. The results are shown in Figure 3. The volume of activation at 3.0 Tesla is greater than that at 1.5 Tesla indicating that the higher field strength offers greater sensitivity to such functional changes.

Such motor tasks of primary cortical functions can be extended to more complicated cognitive paradigms such as involving eye movement control during visuo-spatial processing. The control pathway of visually-guided saccadic eye movement (VGS) can be demonstrated by comparing images obtained for eye fixation on a central unmoving target with images in which saccadic eye movements are made to a randomly changing target along a horizontal line. Activation regions in the frontal eye fields (FEF), supplementary area (SMA), parietal lobes (PL) and visual cortex (V) are readily demonstrated. A memory component can be added to this paradigm to give a memory-guided saccade task (MGS). The subject remains centrally fixated when a peripheral target appears briefly on the screen. The subject remembers the location until the central fixation point is removed at some variable but controlled delay time. Then the subject looks to the remembered location. Statistical comparison of the differences between images obtained during the rest condition (fixation) and the images acquired during the active condition (MGS) is shown in Figure 4. In addition to the regions of activation shown for VGS, the dorsolateral prefrontal cortex (DLPFC) is demonstrated indicating its role in working visuo-spatial memory.

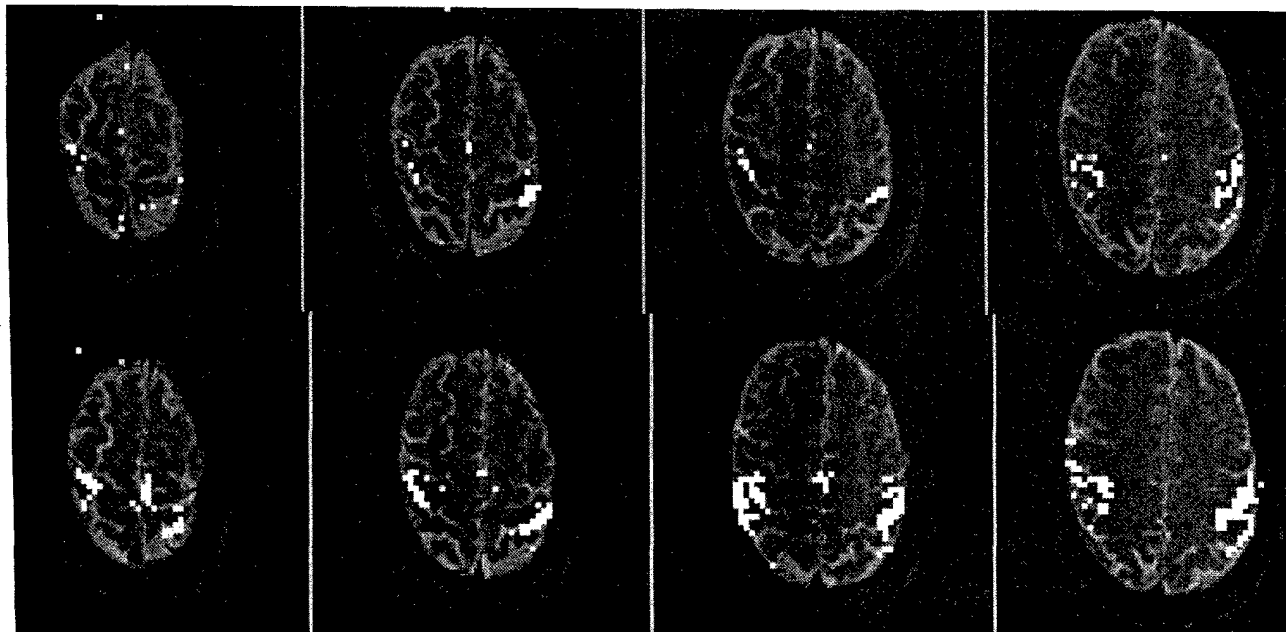


Figure 3. Regions of cerebral activation (color) during finger tapping paradigm obtained using high temporal resolution echo-planar images (1 image every 1.5 s at a spatial resolution of 3 x 3 x 5 mm) superimposed over axial high resolution echo-planar images (1.5 x 1.5 x 3 mm). Activation used a two-tailed t-test with a threshold t-statistic of 5 for 1.5 Tesla (top), and 3.0 Tesla (bottom), respectively. The higher SNR and sensitivity to magnetic susceptibility effects at 3.0 Tesla are demonstrated at the same statistical threshold by larger volumes of activation in the motor, somatosensory and supplementary motor areas. Increased spatial resolution of the motor and somatosensory regions of activation is also evident.

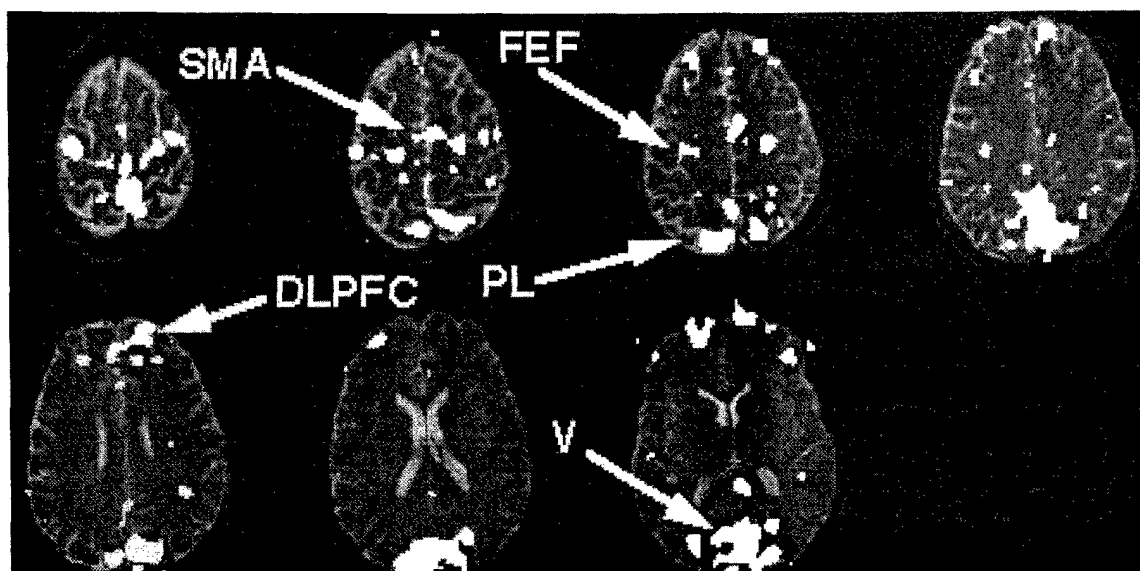


Figure 4. Activation map for memory-guided saccades at 3.0T. The functional map is derived from the t-test comparison of multi-slice, gradient-echo, echo-planar images (TR = 1.5s, TE = 30ms, acquisition matrix = 128 x 64) in a 6 cycle paradigm of fixation (30s) and memory-guided saccades (30s). The activation is displayed over high resolution multi-slice, spin-echo, echo-planar images (TR = 6s, TE = 100ms, acquisition matrix = 256 x 128)

IV. Conclusions

Functional MRI can be performed routinely for clinical and research studies when care is taken to prepare the subjects for the tasks, instrumentation setup is designed to maximize SNR and the neuropsychological paradigm is controlled in a manner that allows the entire imaging acquisition, stimulus presentation and behavioral responses to be coordinated. The system described above can be operated by a trained MR technologist. The availability of a 3.0 Tesla scanner based on a clinical platform provides a clear SNR advantage over 1.5 Tesla without the complexity of a research system. Through the use of echo-planar imaging and high performance computing, neuronal pathways involved in primary cortical and higher cognitive functions can be mapped rapidly and reliably in individual subjects.

V. Acknowledgments

We gratefully acknowledge support from General Electric Medical Systems, USA, Advanced NMR Systems, Inc. and General Electric Medical Systems, Australia.

VI. References

- 1 K. Kwong, J. Belliveau, D. Chesler, I. Goldberg, R. Weisskoff, B. Poncelet, D. Kennedy, B. Hoppel, M. Cohen, R. Turner, H. Cheng, T. Brady, B. Rosen. Dynamic magnetic resonance imaging of human brain activity during primary sensory stimulation. *Proc.Natl. Acad.Sci. (U. S. A.)* **89** (12), 5675-5679 (1992).
- 2 S. Ogawa, T. Lee, A. Nayak, P. Glynn. Oxygenation-sensitive contrast in magnetic resonance image of rodent brain at high magnetic fields. *Magn .Reson .Med.* **14**, 68-78 (1990).
- 3 C. Roy, C. Sherrington. On the regulation of the blood-supply of the brain. *J. Physiol. (London)* **11**, 85-108 (1890).

Dependence on Electronic Structure of the Site of Proton Transfer from Alkane Radical Cations to Alkane Molecules: ESR Evidence in Irradiated CCl_3F /Alkane and Pentane- d_{12} /Alkane Systems

Dominique Stienlet and Jan Ceulemans

Department of Chemistry, K.U.Leuven
Celestijnenlaan 200-F, B-3001 Leuven, Belgium

I. Introduction

ESR experiments and INDO calculations consistently reveal that in alkane radical cations the unpaired-electron and positive-hole density in carbon-hydrogen bonds is restricted to only a few sites and to very specific C-H bonds indeed (1). In *n*-alkane radical cations in the extended conformation, the unpaired electron is delocalized over the carbon-carbon σ -bonds as well as the two chain-end carbon-hydrogen bonds that are in the plane of the C-C skeleton. In various other conformations of *n*-alkane radical cations obtained by 120° rotation around specific C-C bonds, the unpaired-electron and positive-hole density in carbon-hydrogen bonds is again restricted to those C-H bonds that are in the plane of the planar C-C skeleton. In view of this, it is intuitively expected that proton donation (at least to neutral alkane molecules) takes place from such planar C-H bonds, because of the weakening of these bonds and the presence of positive-charge (hole) density on the respective hydrogen atoms. A number of experiments have been carried out on irradiated CCl_3F /alkane and pentane- d_{12} /alkane systems, which clearly demonstrate this dependence on electronic structure of the site of proton donation (2-4).

II. Evidence in Irradiated CCl_3F /Heptane

The ESR spectrum obtained after irradiation of heptane at 1.75 mol % in CCl_3F is shown in Figure 1. The spectrum mainly consists of a (distorted) triplet due to heptane radical cations in the extended all-*trans* conformation. In this conformation, there is extensive hyperfine interaction only with the two *chain-end* C-H bonds that are in the plane of the C-C skeleton, resulting in a triplet spectrum with relative intensities 1 : 2 : 1. In addition to the triplet, a small ESR absorption is observed on each side of the triplet spectrum. The spectral spacing of this absorption corresponds with that of the outermost lines in the spectrum of irradiated *cis*-decalin- d_{18} /1-chloroheptane shown in Figure 2. Enlargement by increasing both the detector signal gain and the number of repetitive scans reveals that the (first-derivative) absorption consists of a double-humped curve in this spectral region and that no other absorptions are present in the more lateral region of the spectrum (*i.e.*, spectral position of the outermost band in the powder spectrum of secondary heptyl radicals). On the basis of this, the lateral absorption in irradiated

CCl_3F /heptane can be attributed *exclusively* to 1-heptyl radicals at this concentration. ESR spectra obtained after irradiation of heptane at various higher concentrations in CCl_3F are shown in Figure 3. Both the absolute and relative signal intensities (relative to that of the triplet spectrum) of the lateral absorption increase with increasing concentration of heptane. The lateral absorption also gradually changes in appearance; the double-humped structure becomes less prominent and an additional band appears in the more lateral region of the spectrum. As a result, the lateral ESR absorption at the higher concentrations corresponds more closely to that of powder spectra of secondary heptyl radicals, as obtained by irradiation of *cis*-decalin- $d_{18}/2-$, 3- and 4-bromoheptane systems.

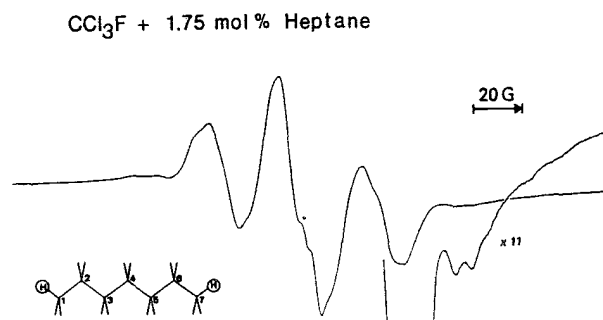
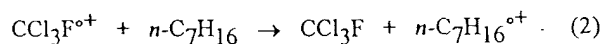
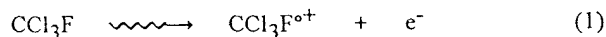


Figure 1: First-derivative ESR spectrum obtained after irradiation of trichlorofluoromethane containing 1.75 mol % heptane; (● indicates a background signal). The inset shows $n\text{-C}_7\text{H}_{16}$ in its extended all-*trans* conformation.

The mode of formation of the trapped paramagnetic species in irradiated CCl_3F /heptane can be briefly outlined as follows. Heptane radical cations are formed as a result of positive-hole transfer from radiation-produced matrix cations to solute heptane molecules.



With increasing heptane concentration, heptane molecules increasingly form small aggregates to which positive-hole transfer still takes place efficiently. As a result, proton transfer occurs from heptane radical cations to heptane molecules resulting in the formation of heptyl radicals and

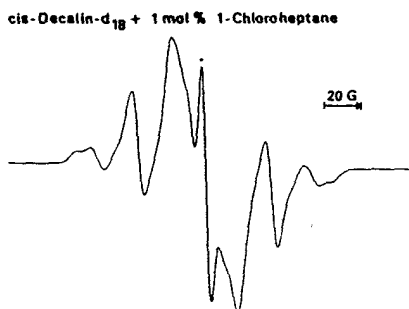


Figure 2: First-derivative ESR spectrum obtained after irradiation of *cis*-decalin- d_{18} containing 1 mol % 1-chloroheptane; (● indicates a background signal).

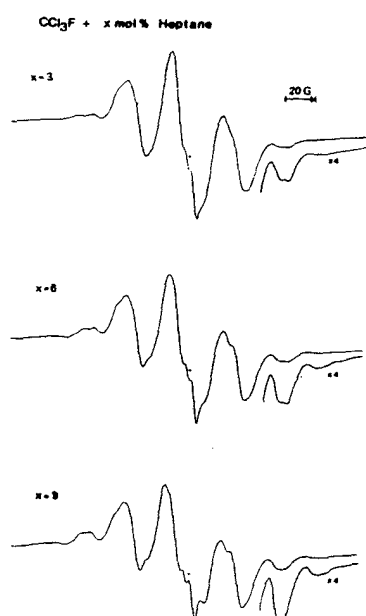
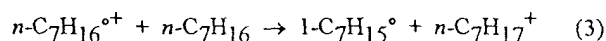


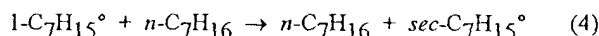
Figure 3: First-derivative ESR spectra obtained after irradiation of heptane at 3, 6, and 9 mol % in trichlorofluoromethane; (● indicates a background signal).

protonated heptanes (heptane carbonium ions), the latter being diamagnetic.



Alternative mechanisms can be ruled out as a major source for heptyl radical formation on different grounds (5). The attribution to proton transfer from heptane radical cations to heptane molecules rather than to hydrogen abstraction by these cations can be made on the basis of the observed selectivity in *chain-end* heptyl radical formation at low heptane concentration, which is incompatible with an hydrogen-abstraction mechanism. The formation of secondary heptyl radicals at higher heptane concentration must be attributed to increases in the size of the heptane aggregates, resulting in the transformation of primary into

secondary radicals by intermolecular radical site transfer.



The experimental results at low heptane concentration (≤ 1.75 mol %) provide clear evidence that the proton transfer from heptane radical cations to heptane molecules results in the selective formation of 1-heptyl radicals in CCl_3F matrices at 77 K. Under these conditions, heptane radical cations are in the extended all-*trans* conformation, as evidenced by their ESR spectrum. In this conformation, the unpaired electron is delocalized over the carbon-carbon σ -bonds as well as the two in-plane *chain-end* carbon-hydrogen bonds. The experimental results thus clearly indicate that the nature of the heptyl radicals formed by proton transfer from heptane radical cations to heptane molecules is related to the structure of the semi-occupied molecular orbital in this cation. The high unpaired-electron density in the in-plane chain-end carbon-hydrogen bonds leads indeed to proton transfer from those sites, giving rise to the selective formation of chain-end heptyl radicals.

III. Evidence in Irradiated CCl_3F /Octane

The ESR spectrum obtained after irradiation of 0.5 mol % octane in CCl_3F is shown in Figure 4. The spectrum contains a very prominent absorption due to octane radical cations, which extends over *ca.* 140 G. Since this absorption extends over a considerably larger spectral region than the triplet absorption of extended octane radical cations, which is observed in *e.g.* 1,1,1- and 1,1,2-trichlorotrifluoroethane (5,6), it must be attributed to a different conformer. On the basis of ESR simulations and INDO calculations an assignment has been made to a *gauche* conformer, obtained by one 120° rotation around $\text{C}_2\text{-C}_3$ in the extended conformer (6,7). In this *gauche-at-C}_2* conformer, there is large unpaired-electron density in the in-plane carbon chain and in the in-plane carbon-hydrogen bonds at C_2 and C_8 , with the unpaired-electron density at C_2 being considerably larger than at C_8 (see Figure 4). This *gauche* conformer therefore possesses two non-equivalent protons which may give extensive hyperfine coupling, resulting in a four-line spectrum with equal intensities. The central region of the spectrum is very weak as a result of mutual cancellation of the different (first-derivative) ESR lines and is largely obscured by matrix absorption (*i.e.* absorption of the irradiated matrix) and by spurious lines from irradiated Suprasil. Indications are that there is some contribution in the central part from the extended conformer of octane radical cations; it has been estimated that *ca.* 20 % of octane cations in CCl_3F are in this conformation (7).

ESR spectra obtained after irradiation of octane at higher concentrations in CCl_3F indicate the presence of an additional ESR absorption, which extends over a larger spectral region. The central part of the absorption due to

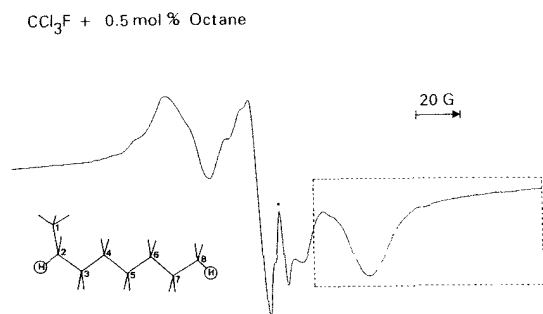


Figure 4: First-derivative ESR spectrum obtained after irradiation of trichlorofluoromethane containing 0.5 mol % octane; (• indicates a background signal). The dashed line indicates the spectral region in which changes in the spectrum as a result of changes in the octane concentration are most easily detected. The inset shows $n\text{-C}_8\text{H}_{18}$ in its gauche-at- C_2 conformation.

octane radical cations is badly distorted by matrix absorption and spurious lines; the left lateral part is also distorted, although to a much lesser extent. The right lateral part, on the other hand, is not distorted to any appreciable extent and changes in the spectrum as a result of changes in the octane concentration are therefore most easily detected in this spectral region. The right lateral part of the ESR spectrum obtained after irradiation of octane at a number of different concentrations in CCl_3F is displayed in Figure 5, clearly showing the presence of an additional ESR absorption. Two main features, designated A and B, are clearly discernible in this absorption. The inner feature (A) appears to contain a 'double-humped' curve, typical of 1-alkyl radicals (8), although this structure is not clearly discernible at all concentrations and may be nearly absent at high concentration. The outer feature (B), on the other hand, is a broad unresolved band, which is situated in a spectral region where 1-alkyl radicals show no ESR absorption. From these observations, it may be concluded that both primary and secondary octyl radicals are present in irradiated $\text{CCl}_3\text{F}/\text{octane}$ and, most importantly, that secondary octyl radicals are present from the very first appearance of octyl radicals with increasing octane concentration in this system.

The mode of formation of octane radical cations and octyl radicals in irradiated $\text{CCl}_3\text{F}/\text{octane}$ is undoubtedly identical to that of the corresponding paramagnetic species in irradiated $\text{CCl}_3\text{F}/\text{heptane}$. The observation that secondary octyl radicals are present in irradiated $\text{CCl}_3\text{F}/\text{octane}$ from the very first appearance of octyl radicals with increasing octane concentration contrasts strongly with that of irradiated $\text{CCl}_3\text{F}/\text{heptane}$, in which at low concentration (≤ 1.75 mol %) only primary heptyl radicals are observed. The difference must be attributed to differences in conformation and ensuing differences in electronic structure of heptane and octane radical cations in CCl_3F matrices at 77 K. Heptane radical cations are fully in

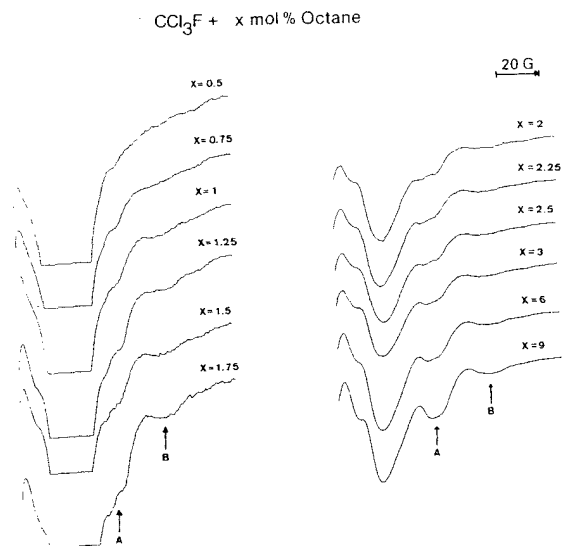


Figure 5: Right lateral part of the first-derivative ESR spectrum obtained after irradiation of octane at various concentrations in trichlorofluoromethane. The symbols A and B point to important spectral features. Spectra at low concentration were enlarged by an increase in both the detector signal gain and the number of repetitive scans.

the extended conformation in CCl_3F whereas octane radical cations are largely in a gauche-at- C_2 conformation in this matrix, with large unpaired-electron density in the in-plane carbon chain and in-plane carbon-hydrogen bonds at C_2 and C_8 , the unpaired-electron density at C_2 considerably exceeding that at C_8 . This electronic structure correlates with the nature of the octyl radicals formed by proton transfer to octane molecules, secondary octyl radicals being quite prominent (relative to chain-end octyl radicals) even at low octane concentration. Chain-end octyl radicals are also present in irradiated $\text{CCl}_3\text{F}/\text{octane}$ systems, as is evidenced by the 'double-humped' structure in the observed ESR spectra (feature A in spectra shown in Figure 5). Their formation can be explained by proton transfer from the chain-end positions in the extended conformer, which is present to some extent (*ca.* 20 %), and by proton transfer from the C_8 position in the gauche conformer.

IV. Evidence in Irradiated Pentane- d_{12} /Octane

The ESR spectrum obtained after irradiation of neat deuterated pentane, to which CO_2 was added as electron acceptor, is shown in Figure 6. The ESR absorption only extends over a relatively narrow spectral region and no distinct ESR features appear to be present in the more lateral region of the spectrum. The absorption can be attributed to deuterated pentyl radicals; trapped CO_2^{\ominus} anions appear to be absent in the system.

The ESR spectrum obtained after irradiation of deuterated pentane, containing 0.5 mol % protiated octane

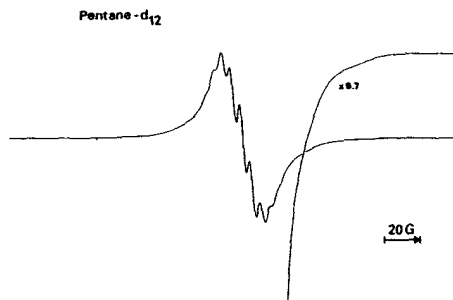


Figure 6: First-derivative ESR spectrum obtained after irradiation of neat deuterated pentane, to which CO_2 was added as electron acceptor.

as well as CO_2 , is shown in Figure 7. This spectrum contains a number of additional absorptions. First, a very intense and relatively sharp ESR absorption is clearly discernible near the center of the spectrum; obviously, this absorption is asymmetric with a pseudodoublet structure at the high-field side of the spectrum. Second, additional ESR absorptions are observed in the more lateral region of the spectrum. Spectral enlargement reveals that these consist of a 'double-humped' curve as well as a relatively sharp and more intense hyperfine component, which is only partially resolved from the much stronger central absorption. The additional lateral absorptions do not correspond with the ESR absorption of irradiated neat octane reported earlier (9), either in appearance or in spectral spacing. In Figure 8, a comparison is made between the enlarged ESR spectrum of the irradiated pentane- d_{12} /octane/ CO_2 system and the spectrum obtained by irradiation of 1-bromooctane in *cis*-decalin- d_{18} . From this, it is evident that the lateral ESR features in these spectra correspond quite closely, both in appearance and in spectral spacing.

The additional absorptions in the ESR spectrum obtained after irradiation of deuterated pentane, containing 0.5 mol % protiated octane as well as CO_2 , can be attributed to two different paramagnetic species. (i) The intense narrow and asymmetric central absorption can be attributed to $\text{CO}_2^{\circ-}$ anions, formed by electron attachment to CO_2 . There is no splitting due to hyperfine interaction in this anion, but the (first-derivative) ESR absorption is asymmetric as a result of g -factor anisotropy (10). Interestingly, this absorption is not present in irradiated neat pentane- d_{12} (with added CO_2), indicating that CO_2 is not included in neat pentane crystals. (ii) The additional ESR absorptions in the more lateral region of the spectrum correspond quite closely, both in appearance and in spectral spacing, with the lateral absorption of irradiated *cis*-decalin- d_{18} /1-bromooctane systems and can therefore be attributed with certainty to 1-octyl radicals. Powder ESR spectra of secondary octyl radicals, obtained by irradiation of the appropriate bromooctanes in *cis*-decalin- d_{18} , have a quite different appearance and extend over a considerably wider

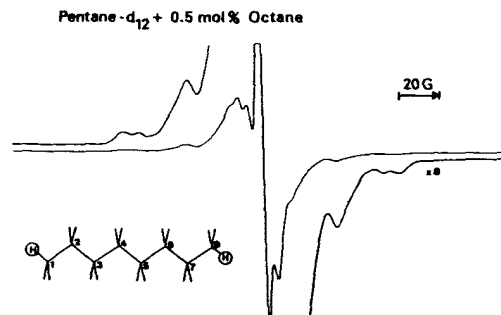


Figure 7: First-derivative ESR spectrum obtained after irradiation of 0.5 mol % octane in deuterated pentane, containing CO_2 as electron acceptor. The inset shows $n\text{-C}_8\text{H}_{18}$ in its extended all-*trans* conformation.

spectral region than the ESR absorption of irradiated pentane- d_{12} /octane/ CO_2 . The latter spectrum clearly shows no indication of the presence of secondary octyl radicals, which should easily be detectable if present in the system.

The selective formation of chain-end octyl radicals by irradiation of deuterated pentane, containing 0.5 mol % protiated octane as well as CO_2 , can be attributed to proton transfer to pentane- d_{12} molecules from octane radical cations, which are formed by hole transfer from matrix cations and are trapped in the solid matrix. Alternative mechanisms such as selective hydrogen-atom abstraction from octane molecules by deuterium atoms and unimolecular decomposition of excited octane radical cations can be ruled out on various grounds (4). The selec-

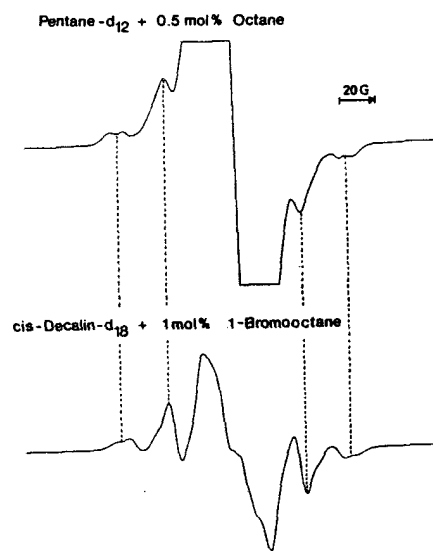
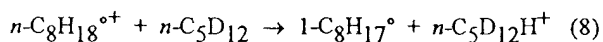
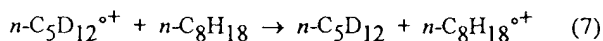
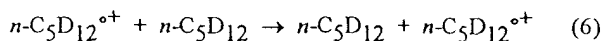
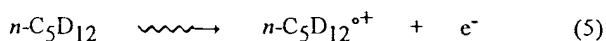


Figure 8: Comparison of the enlarged ESR spectrum obtained after irradiation of 0.5 mol % octane in deuterated pentane, containing CO_2 as electron acceptor, with the spectrum obtained after irradiation of 1 mol % 1-bromooctane in *cis*-decalin- d_{18} .

tive formation of 1-octyl radicals can therefore be attributed to the following sequence of reactions:



The ESR spectrum of octane radical cations in pentane, obtained by difference spectroscopy after illumination of irradiated pentane containing 3 % octane, indicates that such cations are in the extended all-*trans* conformation (11). In this conformation, the unpaired electron is delocalized over the carbon-carbon σ -bonds as well as the two chain-end carbon-hydrogen bonds that are in the plane of the C-C skeleton. The ESR results presented in this paper clearly show that, in accordance with the electronic structure, proton transfer to pentane molecules takes place selectively from chain-end sites, since 1-octyl radicals are formed selectively in the irradiated pentane-*d*₁₂/octane/CO₂ system. The results thus further support the view that the radical site in alkyl radicals formed by proton transfer from alkane radical cations to alkane molecules is related very strictly to the structure of the semi-occupied molecular orbital of the parent cation.

V. Conclusion

The results presented indicate that the nature of alkyl radicals formed by proton transfer from alkane radical cations to alkane molecules is indeed related very strictly to the structure of the semi-occupied molecular orbital of the parent cation. In CCl₃F, heptane radical cations are fully in the extended all-*trans* conformation, with high unpaired-electron density in the carbon-carbon σ bonds as well as the two in-plane *chain-end* carbon-hydrogen bonds and proton transfer to heptane molecules results in the exclusive formation of 1-heptyl radicals. Octane radical cations in *n*-C₅D₁₂/*n*-C₈H₁₈ crystals also are in the extended conformation as indicated by independent ESR results and proton transfer to pentane-*d*₁₂ molecules again results in the quite selective formation of chain-end (primary) octyl radicals. In contrast, in CCl₃F octane radical cations are in a *gauche-at-C*₂ conformation obtained by one 120° rotation around C₂-C₃ in the extended conformer, with large unpaired-electron density in the in-plane carbon chain and in-plane carbon-hydrogen bonds, one at a chain-end and one at a penultimate position. In this system, the ESR results show that secondary octyl radicals are present from the very first appearance of alkyl radicals with increasing octane concentration and thus that the proton transfer to octane molecules also takes place from a secondary position. All

the results indicate that a high unpaired-electron density in a particular carbon-hydrogen bond indeed leads to selective proton transfer from that site, giving rise to a particular alkyl radical, and that there is a strict dependence on electronic structure of the site of proton transfer from alkane radical cations to alkane molecules.

VI. Acknowledgment

The authors thank the National Fund for Scientific Research (N.F.W.O.) of Belgium for financial support.

VII. References

- ¹See for instance: K. Toriyama, K. Nunome and M. Iwasaki, *J. Phys. Chem.* **85**, 2149 (1981); M. Iwasaki, K. Toriyama and K. Nunome, *J. Am. Chem. Soc.* **103**, 3591 (1981); M. Lindgren, A. Lund and G. Dolivo, *Chem. Phys.* **99**, 103 (1985); G. Dolivo and A. Lund, *J. Phys. Chem.* **89**, 3977 (1985); K. Toriyama, K. Nunome and M. Iwasaki, *J. Phys. Chem.* **90**, 6836 (1986).
- ²D. Stienlet and J. Ceulemans, *J. Phys. Chem.* **96**, 8751 (1992).
- ³D. Stienlet and J. Ceulemans, *J. Chem. Soc., Perkin Trans.* **2** 1449 (1992).
- ⁴D. Stienlet and J. Ceulemans, *J. Phys. Chem.* **97**, 8595 (1993).
- ⁵G. Luyckx and J. Ceulemans, *J. Chem. Soc., Chem. Commun.* 988 (1991); G. Luyckx and J. Ceulemans, *J. Chem. Soc., Faraday Trans.* **87**, 3499 (1991).
- ⁶K. Toriyama, K. Nunome and M. Iwasaki, *J. Chem. Phys.* **77**, 5891 (1982).
- ⁷G. Dolivo and A. Lund, *Z. Naturforsch.* **40A**, 52 (1985).
- ⁸E. L. Cochran, F. J. Adrian and V. A. Bowers, *J. Chem. Phys.* **34**, 1161 (1961).
- ⁹K. Toriyama, M. Iwasaki and M. Fukaya, *J. Chem. Soc., Chem. Commun.* 1293 (1982).
- ¹⁰D. W. Ovenall and D. H. Whiffen, *Proc. Chem. Soc.* 420 (1960); D. W. Ovenall and D. H. Whiffen, *Mol. Phys.* **4**, 135 (1961); J. A. Brivati, N. Keen, M. C. R. Symons and P. A. Trevalian, *Proc. Chem. Soc.* 66 (1961); J. E. Bennett, B. Mile and A. Thomas, *Trans. Faraday Soc.* **61**, 2357 (1965); J. H. Lunsford and J. P. Jayne, *J. Phys. Chem.* **69**, 2182 (1965).
- ¹¹T. Ichikawa, M. Shiotani, N. Ohta and S. Katsumata, *J. Phys. Chem.* **93**, 3826 (1989).

Rotating Magnetic Gradient Fields for Imaging Couette

Flow of Simple and Complex Fluids

Jeffrey A. Hopkins, Robert E. Santini, John B. Grutzner*

*Department of Chemistry, Purdue University
West Lafayette, IN 47907-1393*

Contents

- I. Introduction
- II. Z-Storage Pulses with Rotating Magnetic Fields
- III. Radiation Damping
- IV. Couette-Flow Images
- V. Conclusions
- VI. Acknowledgments
- VII. References

I. Introduction

Over the past few years we have been developing methods for obtaining spatially localized spectra of molecules in sheared flow (1). In this note we combine the z-storage pulse technology (2,3) with our rotating magnetic field method to obtain a velocity profile for a non-Newtonian micellar fluid (4,5) under Couette shear flow conditions. The velocity profile reveals that Couette flow for this micellar fluid is complex and 3-dimensional. A simple procedure for overcoming radiation damping effects (6,7) is introduced when calibrating pulse widths in samples containing strong solvent signals.

II. Z-Storage Pulses with Rotating Magnetic Gradient Fields

We have shown that a stroboscopic spin-echo pulse sequence synchronized with a rotating magnetic gradient field (RMF) can be used to obtain spectra of selected fluid layers in a fluid undergoing shearing Couette flow (1). The selectivity was achieved by matching the rotation frequency of the spatially defined magnetic field, RMF, to the rotation frequency of the fluid layer in the shear velocity profile - the synchronized layer. Only layers with rotational periods shorter than T_1 could be

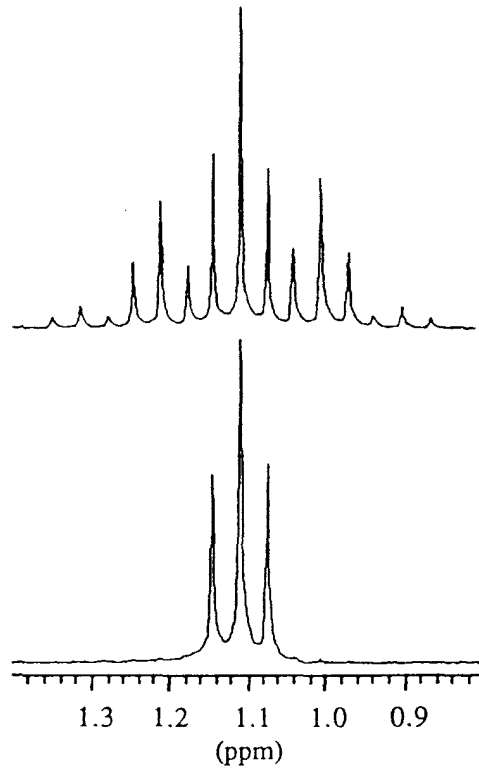


Figure 3. Ethanol triplet with RF damping (bottom) and with a magnetic gradient field used to eliminate RF damping (top).

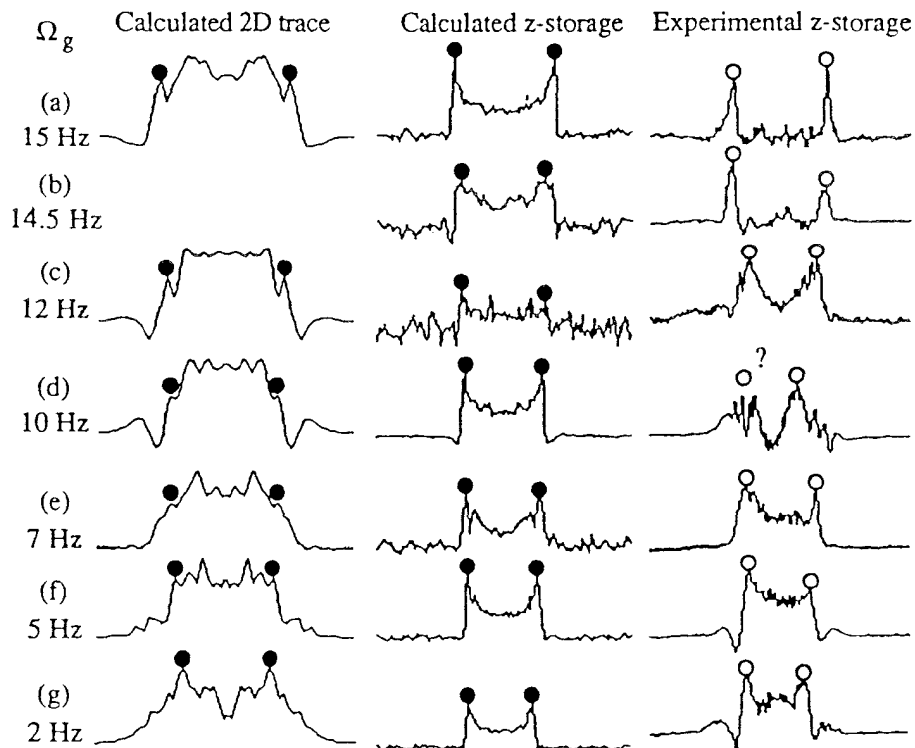


Figure 4. Traces taken from calculated two dimensional spin echo spectra are compared with calculated and experimental results of the z-storage pulse sequence. The two dimensional results were calculated with an outer cylinder rotation rate of 20 Hz. The z-storage results were obtained for a sample with an outer cylinder rotating at 15 Hz. The RMF strength was 1.05 mT/m.

sampled with sufficient signal/noise. This limitation can be removed by using the z-storage pulse strategy of Gibbs and Johnson (2). Furthermore, the isolation of the synchronized layer was limited by harmonics - i.e. fluid layers with rotational periods which were integral fractions of the selected rotation time. These "harmonic layers" can also be discriminated against with the z-pulse sequence by varying the τ time before the 90-x pulse (Figure 1). All layers, with the exception of the synchronized layer, will be modulated as a function of τ and so may be removed with an appropriate filter.

The z-storage pulse sequence (Figure 1b) weights the spectrum by the amount of magnetization that has been refocused. The RMF ensures that magnetization from the synchronous fluid layer refocuses regardless of the echo pulse delay time. The amount of refocusing from asynchronous layers depends on the rotation frequency difference, Ω_{\perp} . The refocused portion of the magnetization - actually any magnetization lying along the axis onto which it was initially excited - is stored along the z axis. The RMF does not alter the stored component, but relaxation processes may. Therefore, the storage delay Δ is kept short with a homospoil (z axis) pulse inserted to dephase all magnetization left in the transverse plane. The stored magnetization is then returned to the transverse axis with a second excitation pulse. The process may be repeated to increase selectivity.

Figure 2 shows the influence of the z-storage pulse sequence when applied to an annular sample undergoing solid body rotation in a synchronized RMF. The signal begins to disappear rapidly after one-quarter of a rotation (12.50 ms), but reappears after three-quarters of a rotation. This practical problem results from eccentricities and static

inhomogeneities in the 0.95 mT/m RMF.

III. Radiation Damping

In order to optimize the z-storage pulse sequence on these high dielectric solutions it was necessary to accurately set the π and $\pi/2$ pulse times. Since we are dealing with solvent signals and high levels of magnetization, radiation damping (6) severely limits the standard null method for determination of the π pulse length (7). The presence of radiation damping under standard operating conditions was confirmed with the Freeman/Frenkiel test (8) using ethanol - Figure 3. The peak height ratio of the center line to the outer pair of lines of the triplet was measured to be 1.7 following a $2 \mu\text{s}$, nominally 9° , pulse. Gradient fields provide a simple solution. A gradient field was applied across the sample with the x shim. The ethanol signals were now split into a spinning side band pattern and radiation damping was essentially eliminated. The peak-height ratio of the inner to outer lines of the triplet was now 1.95 ± 0.05 and was independent of the spinning side band order at which the measurement was made. The determination of the optimum π pulse time was now possible in this modified main magnetic field. The simple procedure of offsetting a shim control permits the π pulse time to be calibrated. This is recommended for samples which generate strong solvent signals.

IV. Couette Flow Images

The velocity selected images for a simple fluid in Couette shear flow are shown in Figure 4. The experimental procedures and RMF equipment are described in detail in Reference 1. Laminar Couette flow was

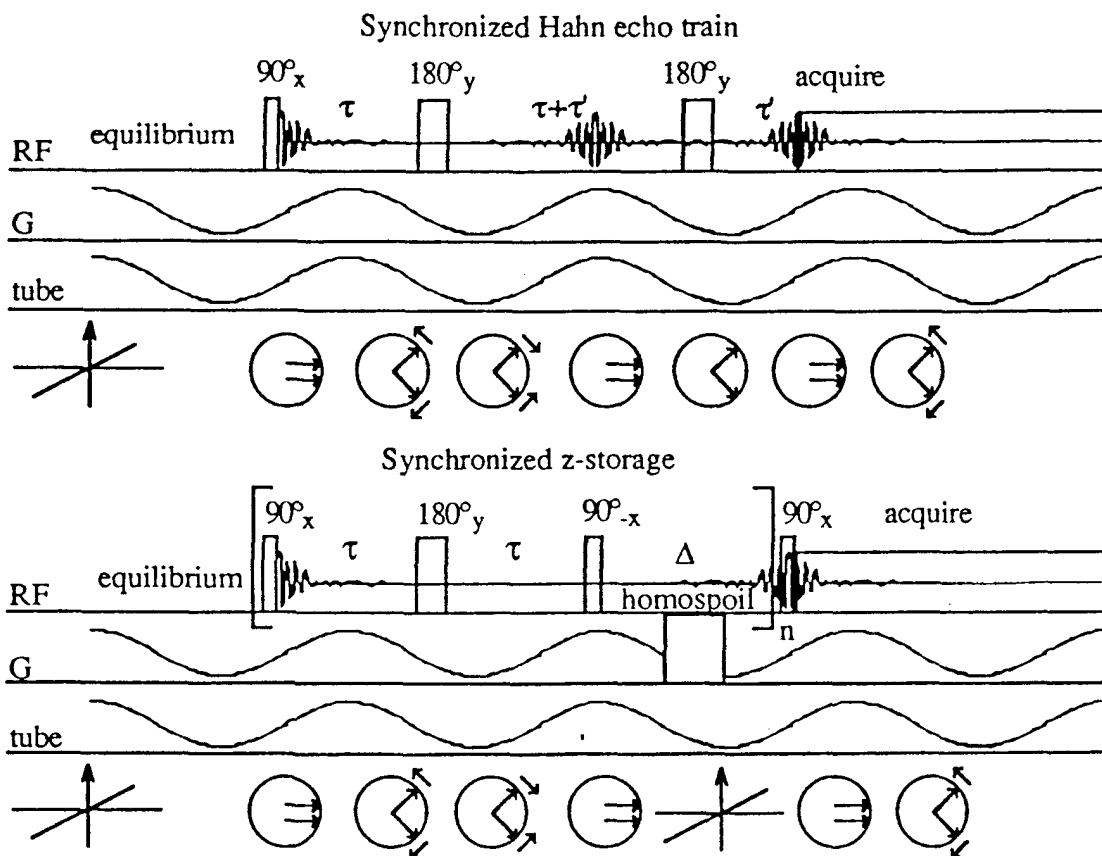


Figure 1. (top) Multiple spin echo pulse sequence, rotating RMF and synchronous rotating sample showing τ independent formation of spin echo. (bottom) Z-storage pulse sequence, rotating RMF and synchronously rotating sample showing storage and recall of spin echo intensity.

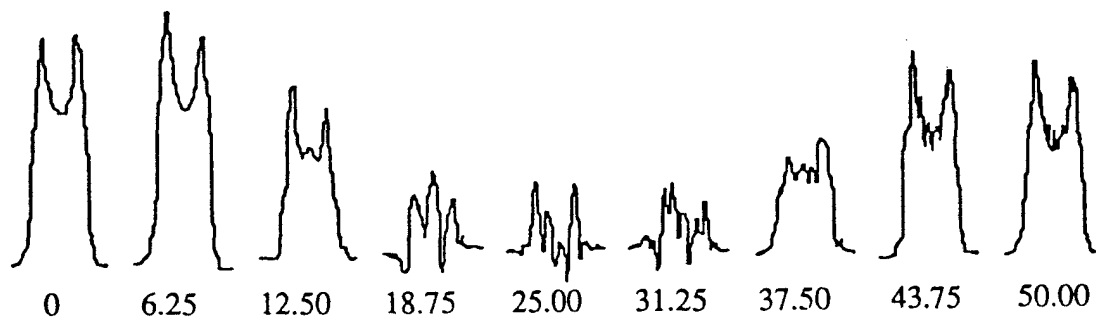


Figure 2. Z-storage pulse sequence applied to solid body rotation of an annular sample spinning at 20 Hz with a synchronous RMF of 1.05 mT/m. The indicated times are spin echo pulse delays (ms) ranging up to one full rotation.

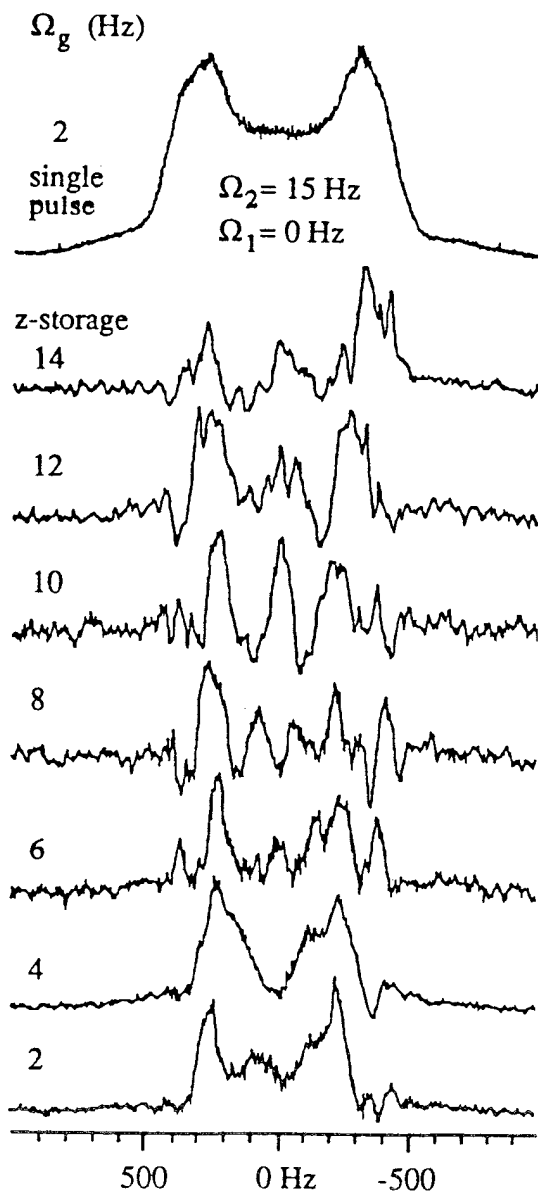


Figure 5. Results for the z-storage pulse sequence applied to a solution of 25 mM cetyl-trimethyl-ammonium bromide and sodium salicylate with the outer cylinder rotated at 15 Hz. The top spectrum was acquired with a single excitation pulse and an RMF of 1.80 mT/m rotating at 2 Hz. The z-storage results were acquired with $\tau=10$ ms, $\Delta=8$ ms, and $n=2$.

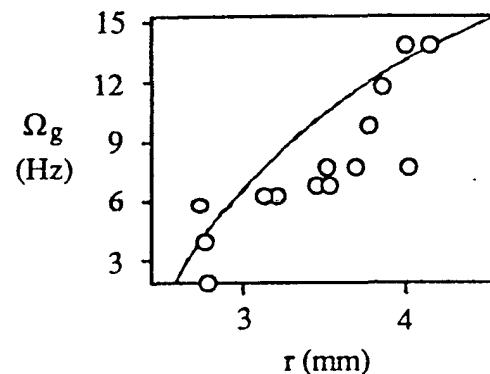


Figure 6. Radial dependence of Couette flow rotational frequency for the 25 mM cetyl-trimethyl-ammonium bromide-sodium salicylate solution. The data points (plotted x as a function of y) were taken from Figure 5 and similar spectra. The solid line is the calculated Couette flow rotational frequency profile, $\Omega(r)$.

established in an annular sample of 85% phosphoric acid with an outer cylinder rotating at 15 Hz against a stationary inner cylinder. Velocity selection was accomplished with the z-storage pulse sequence of Figure 1b with $n = 4$. The experimental spectra clearly show the improved layer selectivity obtained with the z-storage sequence as anticipated from comparison with the calculated spectra. The radial velocity map calculated from the observed peak maxima matched the theoretical Couette velocity flow field within experimental error and with higher accuracy than we obtained previously (1).

The Couette flow experiment was repeated at 15 Hz with the micellar fluid mixture of 25 mM sodium salicylate and 25 mM cetyl-trimethyl-ammonium bromide. The proton images of the HOD resonance were observed - Figure 5. At long τ values, which ideally would select the slow moving layer close to the inner cylinder, the image of the micellar fluid resembled the *complete* static image. At short τ values, corresponding to outer layer selection, the images varied, apparently randomly, with time. The images show in Figure 5 are broadly representative of the observed patterns. Clearly the micellar fluid is not undergoing laminar azimuthal flow. The axial water diffusion coefficient was estimated by the Stejskal and Tanner method and found to be an order of magnitude larger than in the static tubes. This confirmed that the fluid flow had 3 dimensional components. The present RMF procedure may only be applied reliably when 2 dimensional laminar flow fields are present.

An approximate radial velocity map was derived from the spacing of the peak maxima from Figure 5. The central region of the velocity map has a large uncertainty.

The map is inconsistent with the smooth monotonic velocity decrease predicted for a power law fluid undergoing Couette flow (9). Power law flow behavior for a complex fluid in pipe flow has been imaged by Callaghan (10).

V. Conclusions

The z-storage pulse technique synchronized with a rotating magnetic gradient field has generated an accurate radial velocity map for a simple fluid in laminar Couette shear flow. The z-storage pulse technique gives higher discrimination against asynchronous layers, can be used for fluids with short T_2 values, and is simpler to analyze than our previous 2D method (1). When the technique was applied to a micellar fluid, 3-dimensional motion was detected which was too complex for the 2-dimensional analysis introduced here. Full 3D imaging will be required for its characterization.

VI. Acknowledgments

The expert assistance of D. V. Carlson, P. J. Pellechia and W. Vaughn is gratefully acknowledged. J. Hopkins is Department of Education National Needs Fellow. Travel support from Purdue University made this presentation possible.

VII. References

- ¹J.A. Hopkins, R.E. Santini, and J.B. Grutzner, *J. Magn. Reson. A* 117, 0000 (1995) and references therein.
- ²S.J. Gibbs and C.S. Johnson, *J. Magn. Reson.* 93, 395 - 402 (1991).

³K.F. Morris, C.S. Johnson, Jr., and T.C. Wong, *J. Phys. Chem.* **98**, 603-608 (1994).

⁴H. Hoffman, *Adv. Mats.* **6**, 116-129 (1994).

⁵T. Shikata, H. Hirata, and T. Kotaka, *Langmuir* **5**, 398-405 (1989) and references therein.

⁶N. Bloembergen and R.V. Pound, *Phys. Rev.* **95**, 8-12 (1954).

⁷A. Szöke and S. Meiboom, *Phys. Rev.* **113**, 585-586 (1959).

⁸R. Freeman, "A Handbook of Nuclear Magnetic Resonance", Longman, 1987, p. 177-179.

⁹R. Darby, *Viscoelastic Fluids: An Introduction to Their Properties and Behavior*; 1 ed.; Marcel Dekker, Inc.: New York, 1976; Vol. 9, pp 638.

¹⁰C.J. Rofe, R.K. Lambert, and P.T. Callaghan, *Rheology* **38**, 875-887 (1994).

In Vivo ESR Observation of Nitrosobenzene-based Bioradicals in Living Animals: Free Radical Scavenging Activities of Natural Carotenoids

Hirotsada Fujii

The Tokyo Metropolitan Institute of Medical Science
18-22, Honkomagome 3-chome, Bunkyo-ku, Tokyo 113

Hoyoku Nishino

Cancer Prevention Division, National Cancer Center Research Institute
Tsukiji, Chuo-ku, Tokyo 104

Janusz Koscielniak and Lawrence J. Berliner

Department of Chemistry, The Ohio State University
120 West 18th Avenue, Columbus, Ohio 43210-1173, USA

1 Introduction

Nitroso compounds are among the most potent chemical carcinogens and are widely distributed in the environment. Furthermore, the related higher and lower oxidation states, e.g., nitrobenzene, phenylhydroxylamine, and aniline, are all interconvertible to nitrosobenzene by hepatic and other metabolic pathways in vivo [1]. These compounds are also recognized as potentially reactive metabolites of a variety of toxicologically interesting compounds which became carcinogenic or mutagenic, after covalently binding to proteins and DNA.

Very recently, by using L-band ESR(EPR) spectroscopy with a loop-gap resonator we demonstrated the first in vivo detection of a "bioradical", generated from the metabolism of nitrosobenzene (NB) in live mice [2]. A broad three-line ESR spectrum was detected in the stomach and buttocks region of a live mouse after intraperitoneal (i.p.) or intramuscular (i.m.) injection of nitrosobenzene. The signal intensity reached a maximum at 20 to 30 min and remained constant well beyond twelve hours. When muscle tissue was excised within 5 min after injection of nitrosobenzene, a similar three-

line spectrum was also detected at X-band, which was preceded by the rapid growth and subsequent decay of a spectrum *identical* to that of the phenylhydronitroxide radical. A model system containing nitrosobenzene and polyunsaturated fatty acids yielded an identical three-line spectrum which was characterized as the radical adduct of nitrosobenzene across double bonds in polyunsaturated lipid molecules. These results suggest that one of the first possible targets of nitroso compounds in vivo may be regions of polyunsaturated lipid clusters in fat tissue or membranes.

We previously reported that various carotenoids (other than β -carotene) such as fuxoxanthin also has anti-tumor activity [3]. Although the precise mechanism of action of these carotenoids has not been fully elucidated yet, it should be pointed out that free radical scavenging activity may play an important role here [4]. From our success in detecting bioradicals in vivo, generated from one of the most potent carcinogens, i.e., nitrosobenzene, we looked at this compound as a good model system for evaluating free radical scavenging activities of several interesting naturally abundant carotenoids as well as other possible antioxidants, curcumin

and riboflavin tetrabutryate. We discuss below the possibility of these compounds as cancer-preventing drugs.

2 In-vivo Bioradicals from Nitrosobenzene

A 50 mM nitrosobenzene suspension (0.1mL) in either DMPC liposomes or in ethanol was injected i.p. as a 0.2 mmol/Kg dose to 25 g balb/c male mice. The anaesthetized mouse was monitored in a modified loop-gap resonator on a homemade L-band ESR spectrometer described previously [5].

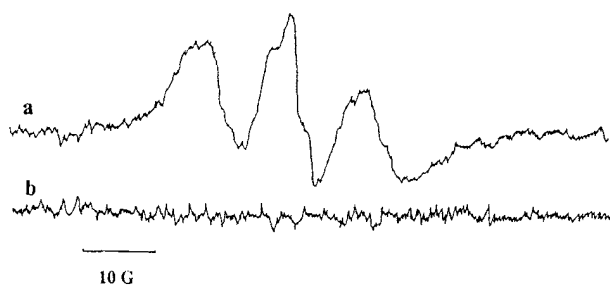
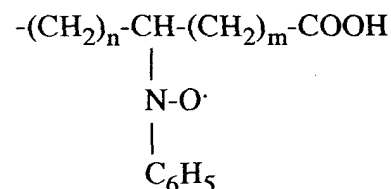


Figure 1. L-Band ESR spectra of an anesthetized (25g) mouse at room temperature. (a) 20 min after an i.p. injection of 0.1ml of 50mM NOB (in a liposome suspension); (b) same as (a), except without nitrosobenzene. Spectrometer conditions were: frequency, 1.128GHz; microwave power, 10mW; modulation, 1.9G; applied magnetic field, 390G; sweep width, 100G; sweep rate, 25G/min; time constant, 1.0. From [2] with permission.

Figure 1a depicts the 1.13 GHz ESR spectrum from the stomach region of a mouse resulting from the administration of nitrosobenzene. The ESR signal started to appear about 20 min after injection and remained stable at a significantly high intensity for more than twelve hours as mentioned earlier [2]. This broad three-line ESR spectrum ($a_N = 11.6 \pm 0.5$ G) was reproduced at X-band in excised muscle tissue doped with nitrosobenzene.

The ESR spectrum of the in-vivo bioradical shown in Figure 1 was identified using a model

system of nitrosobenzene and oleic acid or linolenic acid. The interaction of C-nitroso aromatic compounds with olefins or unsaturated lipids yield N-arylhydroxylamine-lipid adducts via a pseudo Diels-Alder addition which are oxidized by oxygen or another C-nitroso moiety to the nitroxide radical [6]. These nitroxide adducts yield ESR spectra similar to that shown in Figure 1a. The proposed structure of the nitroxide radical adduct observed in both the in-vivo and model lipid systems is depicted below:



This nitroxide radical adduct may be capable of hydrogen abstraction from another unsaturated fatty acid, leading to regeneration of the hydroxylamine adduct and a carbon-centered radical (which itself may be susceptible to oxidation). The nitroxide radical shown above and/or its hydroxylamine may be capable of reducing Fe^{3+} to Fe^{2+} , yielding species critical to the initiation of lipid peroxidation.

3 Free Radical Scavenging Activity of Natural Compounds

We have been studying the relationship between anti-tumor activity and free radical scavenging ability of some natural compounds in order to elucidate the contribution of carcinogen induced free radicals in cancer [3]. Several methods for evaluating free radical scavenging activity have already been reported including systems involving oxyradicals such as superoxide or hydroxyl. However, as reported previously oxyradicals were not found in the nitrosobenzene system in-vivo [2,7]. While these radicals may have been generated transiently, their extremely short lifetimes dictate that they were readily converted to less toxic substances such as H_2O_2 . On the other hand, we have found that nitrosobenzene fatty acid radical adducts are physiologically

long-lived and may be able to abstract hydrogens from fatty acids in-vivo. Therefore, we employed this system to evaluate the free radical scavenging activity of riboflavin tetrabutryate (C-1), fucoxanthin (C-2), and curcumin (C-3) which are promising candidates as cancer preventing agents. We employed two different systems as free radical sources. The first is a free radical generating system of nitrosobenzene and a polyunsaturated fatty acid, linolenic acid. In the second system, stable free radicals, such as 1,1-diphenyl-2-picrylhydrazyl (DPPH), were used.

Radical Adduct of Nitrosobenzene and Linolenic Acid (NB-L•)

Method I (slow generation): 40 mM linolenic acid was reacted with 3.3 mM nitrosobenzene in DMSO. In order to evaluate the free radical scavenging activities of the compounds noted above with each compound dissolved in DMSO to a final concentration of 3 mM, was added at zero time. Figure 2 shows the buildup of ESR signal intensity of a control NB-L• reaction containing only DMSO. Each test compound reaction was measured after 180 min. and the results plotted in Figure 3 relative to the control. The data show that all three compounds have similar significant free radical scavenging activity as measured by the ability to suppress NB-L• accumulation.

Method II (rapid generation): 3 mM nitrosobenzene was reacted with 555 mM linolenic acid in DMSO. Figure 4 shows ESR intensities of NB-L• against time. Note the initial rapid buildup (45 min) followed by a somewhat slower signal decay in the control without added compound. We suggest that this represents the rapid conversion of NB to NB-L• followed by a reaction involving perhaps radical dismutation or hydrogen abstraction from another unsaturated lipid center. In parallel experiments at 45 min the compounds C-1, C-2, or C-3 were added to the mixture. ESR signal intensities were measured at 45 min and 12 hrs later as shown in Figure 5.

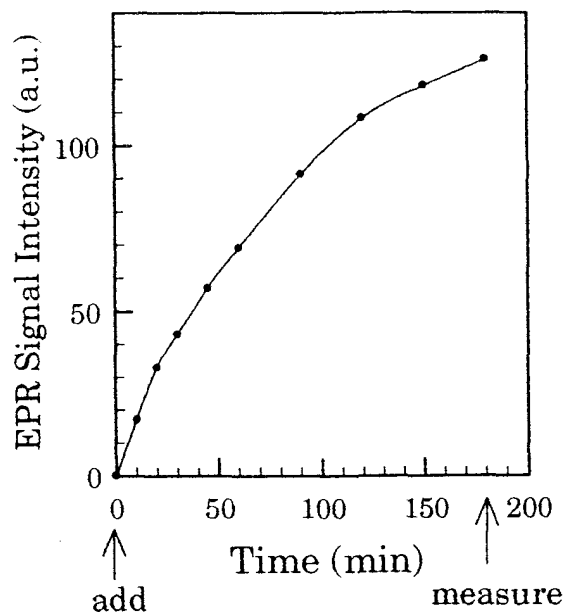


Figure 2. Slow generation (Method I): buildup of X-band ESR signal intensity of NB-L• radical vs time.

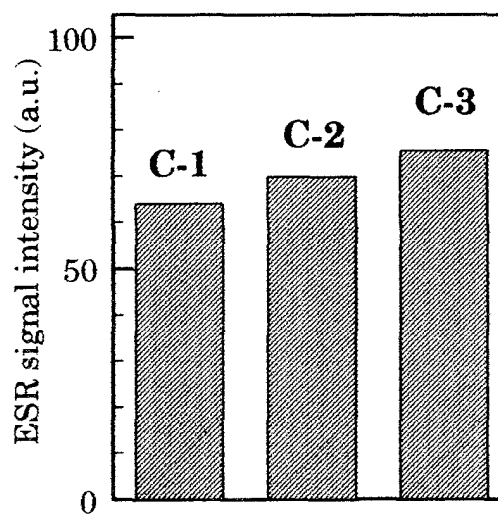


Figure 3. Relative ESR signal intensities of NB-L• in the presence of riboflavin tetrabutryate (C-1), fucoxanthin (C-2), and curcumin (C-3). Each compound (3 mM) was dissolved in a mixture of 3.3 mM NB and 40 mM linolenic acid in DMSO. In the control no test compound was added to the DMSO mixture. The data are expressed as percent of control at 180 min.

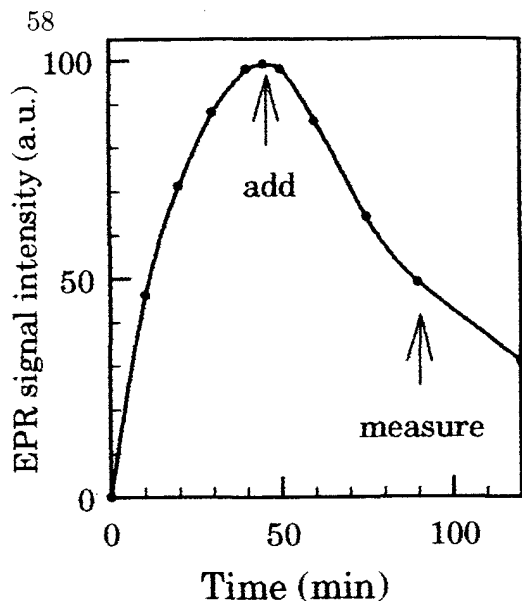


Figure 4 Rapid generation (Method II): buildup and decay of the X-band ESR signal intensity of NB-L• radical vs time.

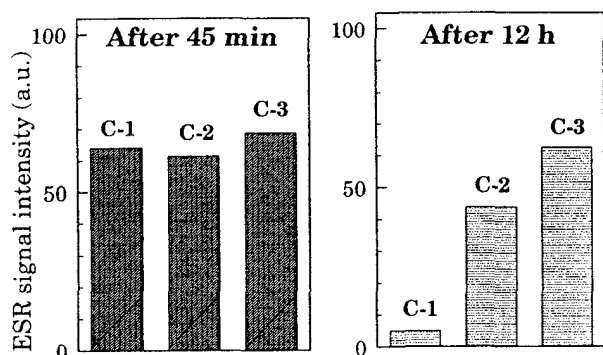


Figure 5 Relative ESR signal intensities of NB-L• in the presence of riboflavin tetrabutyrate (C-1), fucoxanthin (C-2), and curucumin (C-3). Each compound (3 mM) was added after 45min to a mixture of 3.0 mM NB and 555 mM linolenic acid in DMSO. The data are expressed as percent of control at 45 min and 12 hrs after addition of each compound as noted in Figure 4.

Figure 5 shows that riboflavin tetrabutyrate (C-1) and fucoxanthin (C-2) have significant free radical scavenging activity for NB-L•, especially riboflavin tetrabutyrate which had substantial antioxidant activity against NB-L•.

Stable Free Radicals (DPPH)

We also tested very stable radicals, such as DPPH, as the free radical source. After incubating 0.5 mM DPPH with 3 mM of each test compound in DMSO, the ESR signal intensity was measured with time. Figure 6 summarizes the signal intensity data for each compound at 1 hr after mixing. Again here, riboflavin tetrabutyrate (C-1) and fucoxanthin (C-2) showed significant free radical scavenging activities for DPPH.

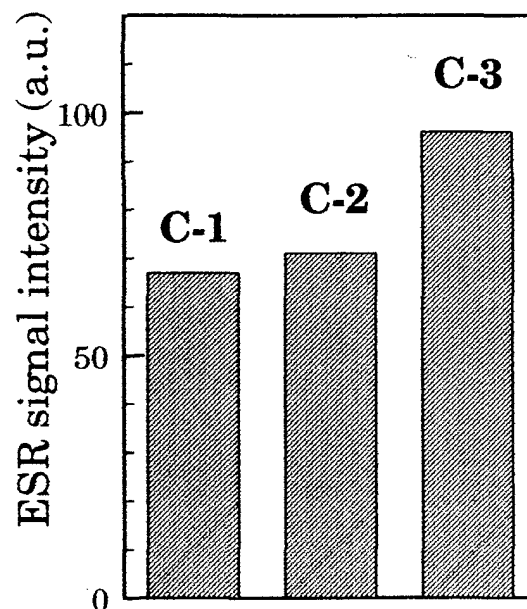


Figure 6 Relative ESR signal intensities of DPPH in the presence of riboflavin tetrabutyrate (C-1), fucoxanthin (C-2), and curucumin (C-3) at 1 hour. Each compound (3 mM) was added to 0.5 mM DPPH dissolved in DMSO. The data are expressed as percent of a control.

From the combined data shown above, it is clear that both riboflavin tetrabutyrate, fucoxanthin and curucumin can scavenge NB-L• and DPPH free radicals. Riboflavin tetrabutyrate has the strongest activity among these compounds.

4 Free Radical Scavenging Activity Means Cancer Preventing?

Previously we have shown the anti-tumor activity of fucoxanthin, a natural carotenoid isolated from edible seaweed [3]. Recently, we found that fucoxanthin not only has the ability to inhibit tumor-promoter induced Epstein-Barr virus activation, but also suppresses the promoting effects of 12-O-tetradecanoylphorbol-13-acetate on skin tumor formation in mice initiated with 7, 12-dimethylbenzene[*a*]anthracene [8]. Curcumin has also been demonstrated to have anti-tumor promoting activity in vivo [9]. From the results in Figures 3, 5, and 6 above, it is also clear that fucoxanthin and curcumin have significant free radical scavenging activity. Furthermore, riboflavin tetrabutryate had even higher activity and hence this compound seems to be a good candidate for an anti-carcinogenic drug. Obviously, further biological studies with riboflavin tetrabutryate must be done to confirm this suggestion.

Acknowledgements

This work was supported in part by a grant from the U.S.P.H.S. and also from the Ministry of Health and Welfare, and the Ministry of Education, Science and Culture, Japan.

REFERENCES

- ¹Maples, R., Eyer, P., and Mason, R. P. (1990) *Mol. Pharmacol.* 37: 311-318.
- ²Fujii, H., Zhao, B., Koscielniak, J. and Berliner, L. J. (1994) *Magn. Reson. Med.* 31:77-80.
- ³Okuzumi, J., Nishino, H., Murakoshi, M., Iwashima, A., Tanaka, Y., Yamane, T., Fujita, Y., and Takahashi, T. (1990) *Cancer Lett.* 55:75-81.
- ⁴Peto, R., Doll, R., Buckley, J.D., and Sporn, M.B. (1981) *Nature* 290:201-208.
- ⁵Koscielniak, J. and Berliner, L.J. (1994) *Rev. Sci. Inst.* 65:2227-2230.

⁶Sullivan, A. B. (1966) *J. Org. Chem.* 31:2811-2817.

⁷Fujii, H., Koscielniak, J., Kakinuma, K., and Berliner, L.J. (1994) *Free Rad. Res. Commun.* 21:235-243.

⁸Satomi, Y., Tokuda, H., Fujii, H., Shimidzu, N., Tanaka, Y., and Nishino, H. (1995) *Cancer Lett.*, submitted.

⁹Nishino, H., Tanaka, Y., Konoshima, T., Takayasu, J., Satomi, Y., Nishino, A., and Iwashima, A. (1992) *Oncol. (Life Sci. Adv.)* 11:65-69.

The Active Site Structure of Bovine Meizothrombin(desF1) as Probed by ESR Spin Labels

Paul D. Boxrud and Lawrence J. Berliner

Department of Chemistry, The Ohio State University
120 West 18th Avenue, Columbus, Ohio 43210-1173, USA

1 Introduction

Thrombin is a serine protease which is the central enzyme in blood coagulation whose major function is to convert soluble fibrinogen into an insoluble fibrin clot. Thrombin circulates as the inactive precursor prothrombin. Upon vascular injury, prothrombin is cleaved by the prothrombinase complex (factor Xa, factor Va, and phospholipids) and proceeds through several active intermediates, before ultimately resulting in α -thrombin. Two of these species, meizothrombin (mzIIa) and meizothrombin(desF₁) (mzIIa-F₁) possess most other functions of α -thrombin, except significant clotting activity. Both of these enzymes retain amidolytic activity of small substrates. The above characteristics suggest an anticoagulant role for mzIIa and mzIIa-F₁, but their exact function (if any) remains a mystery.

The active site of α -thrombin and other serine proteases has been previously investigated by the use of a series of spin labels developed by Berliner and Wong for the study of chymotrypsin [1] (see figure 1). ESR studies using these labels characterized the α -thrombin active site region through the discovery of the apolar binding site [2] and active site differences between several proteolytic forms of thrombin [3]. In this work, these labels were employed to examine the active site region of mzIIa-F₁ and probe for differences between thrombin and mzIIa-F₁ active sites and explain the differences in the macromolecular specificities of the two enzymes.

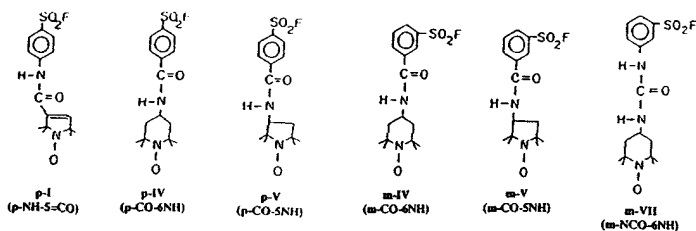


Figure 1. The sulfonyl fluoride spin labels used in this study.

2 Materials and Methods

Enzymes. Bovine α -thrombin was obtained in lyophilized form from Armour Pharmaceuticals, Bradley, IL. Bovine mzIIa-F₁ was prepared from bovine prothrombin as described previously [4]. Bovine prothrombin was purified according to Mann [5] from citrated bovine plasma, a generous gift of Dr. Dan Walz, Wayne State University, Detroit, MI.

Methods. Spin labeling of α -thrombin and mzIIa-F₁ was accomplished as described previously [4]. ESR spectra were measured with a Varian E-12 ESR spectrometer at 25°C. Measurements of the hyperfine extrema, $2T_1$, were taken from "high gain" spectra, which were typically recorded at 2-fold higher modulation amplitude and 4- to 10-fold higher receiver gain. The measurement is designated by arrows in figure 2.

3 Experimental results

The labeling mzIIa-F₁ and α -thrombin with these sulfonyl fluoride spin labels results in moderately immobilized X-band ESR spectra. The resulting $2T_1$'s from spectra of α -thrombin and mzIIa-F₁ labeled with p-I, p-IV, p-V, m-IV, m-V, or m-VII are presented in Table I.

Label	α -thrombin	mzIIa-F ₁	α -thrombin in sucrose
m-IV	45.7 G	46.9 G	48.8 G
m-V	61.5	62.3	61.4
m-VII	54.1	50.1	55.0
p-I	50.0	52.5	52.0
p-IV	57.3	49.0	57.4
p-V	51.9	62.1	53.2

Table I. Comparison of $2T_1$ values (± 0.5 G) obtained for each spin labeled α -thrombin and mzIIa-F₁ used in this study.

Column 3 of this table contains values obtained under isokyndric conditions: that is α -thrombin viscosity adjusted such that its tumbling rate is equal to that of $mzIIa-F_1$. This requires two assumptions: that the proteins are roughly identical in shape and no microviscosity effects of the sucrose are present. Thus, the results showed that there is a clear difference in the region of the active site probed by the *para* labels, but no significant difference in the environment experienced by the *meta* labels. The exception is **m-VII**, which has been previously found to behave as a *para* label in bovine α -thrombin [7].

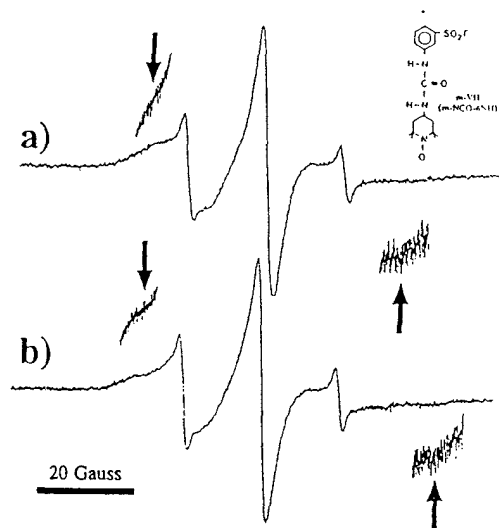


Figure 2. The X-band ESR spectrum of **m-VII** labeled $mzIIa-F_1$ (25 μ M) in 50 mM Tris, 0.75 M NaCl, pH 6.5, 25 $^{\circ}$ C in the a) absence and b) 20 mM indole. Spectrometer conditions: frequency, 9.15 GHz; field, 3280 G; sweep width, 100 G, modulation, 1.0 G; scan time, 30 min; time constant 1.0 s.

Figure 2 depicts an X-band ESR spectrum of **m-VII** labeled $mzIIa-F_1$ in the presence and absence of 20 mM indole. A dramatic shift in $2T_{||}$ was observed for $mzIIa-F_1$ (≈ 11 G) while **m-VII** thrombin exhibited a much smaller shift (≈ 3 G). Similar shifts were observed other labeled α -thrombin and $mzIIa-F_1$ species; however, **m-VII**, **p-I**, and **p-V** for α -thrombin were very sensitive to indole, with only **m-VII** and **p-I** were with $mzIIa-F_1$. Thus, $mzIIa-F_1$ binds indole, which induces different structural changes upon binding vs. α -thrombin. This difference is evident in our kinetic studies of indole on α -thrombin and $mzIIa-F_1$ esterase activity where $mzIIa-F_1$ did not show the dramatic activation as found with α -thrombin [4]. On the other hand, both species gave similar ESR results for

benzamidine binding i.e., a further immobilization of *meta* labels and no effect on *para* labels. The dissociation constant for benzamidine with both **m-IV**- $mzIIa-F_1$ and α -thrombin was 1.0 ± 0.1 mM [4], similar to that of α -thrombin [8].

4 Conclusions

This work has demonstrated that α -thrombin and $mzIIa-F_1$ differ in conformation in the active site region. The mobilities of the **p-IV** and **p-V** labels, which were previously shown to probe an apolar binding site near the active site of α -thrombin [2], were the most sensitive to differences between thrombin and $mzIIa-F_1$. Thus, it is this apolar site in $mzIIa-F_1$ which differs most in structure or conformation from that of thrombin. It was further shown that $mzIIa-F_1$ does not experience indole-induced activation of esterase activity, while $mzIIa-F_1$ retains its indole binding ability. Therefore, it seems that this apolar site is present, but not fully developed in $mzIIa-F_1$.

An apolar binding domain of α -thrombin has been shown crystallographically to be important in the binding of fibrinogen and is necessary for clotting activity. This is one of the two important regions of interaction between fibrinogen and α -thrombin, the other being exosite I on the other side of the active site. Since this site has been demonstrated to be fully functional in $mzIIa-F_1$, it is reasonable to speculate that the differences in the apolar binding region are at least partially responsible for the decreased clotting activity of $mzIIa-F_1$.

5 Acknowledgements

This work was supported in part by grants from the USPHS as well as the U.S. Department of Education through a GANN fellowship.

6 References

- ¹Berliner, L.J. and Wong, S.S. (1974) *J. Biol. Chem.*, 249:1668-1677.
- ²Berliner, L.J. and Shen, Y.Y.L. (1977) *Biochem.*, 16:4622-4626.
- ³Berliner, L.J., Bauer, R.S., Chang, T.-L., Fenton, J.W. II, and Shen, Y.Y.L. (1981) *Biochem.*, 20:1831-1837.
- ⁴Boxrud, P.D. and Berliner, L.J. (1996) *J. Prot. Chem.*, in press.
- ⁵Mann, K.G. (1976) *Meth. Enzymol.*, 45, 123-156.
- ⁶Musci, G., Berliner, L.J., and Esmon, C.T. (1988) *Biochem.*, 27, 769-773.
- ⁷Nienaber, V.L. and Berliner, L.J. (1991) *Throm. Haemost.* 65, 40-45.
- ⁸Sturzebecher, J., Walsmann, P., Voigt, B., and Wagner, G. (1984) *Thromb. Res.* 36:457-465.

NMR Studies on Antarctic Sea Ice

Paul Callaghan and Craig Eccles

*Department of Physics, Massey University
Palmerston North, New Zealand*

INTRODUCTION

With a seasonal variation in surface area of almost 20 million square km and an albedo of 95% the sea ice surrounding the Antarctic continent has a significant impact on global climate. Consisting of frozen sea water, the ice is formed gradually over a period of several months during the Antarctic winter. Far from being a homogenous material, sea ice has a complex structure. As the sea water freezes, concentrated salt water accumulates in small cavities called "brine pockets". Generally less than 0.5 mm in diameter they can extend for many mm vertically. During the winter, gravity causes much of the entrapped brine to move down through the ice resulting in a non-uniform salinity profile.

The presence of the brine pockets gives the sea ice unusual mechanical properties. An understanding of these properties and their implications for annual sea ice formation and break up can be gained by macroscopic stress measurements¹, or by inference from microscopic analysis of sea ice morphology. Until now, microscopic studies have been practically non-existent, apart from some laboratory studies on home-grown sea ice². However given the unusual conditions of Antarctic sea ice formation, such as variable temperature gradients, long growth periods and wave action, an on-site analysis would seem to be preferable.

NMR AS A PROBE OF SEA ICE

NMR provides a non-invasive technique for studying sea ice morphology using imaging or bulk measurement techniques. Not surprisingly, previous work has been done with high field instruments³ (fig 1), however the possibility of taking such a facility to the Antarctic is remote. Given the low level of electromagnetic interference in Antarctica, NMR studies which use the Earth's magnetic field would seem to provide an attractive alternative. Although an imaging system based on the Earth's field has been demonstrated⁴ the resolution is too coarse to allow detailed studies of the microscopic sea ice structure. The alternative is to use NMR to provide bulk measurements of liquid water content and relaxation times. More ambitious experiments using pulsed-gradient

spin-echo NMR can be used to obtain information on restricted self diffusion⁵, from which average brine pocket dimensions can be inferred.

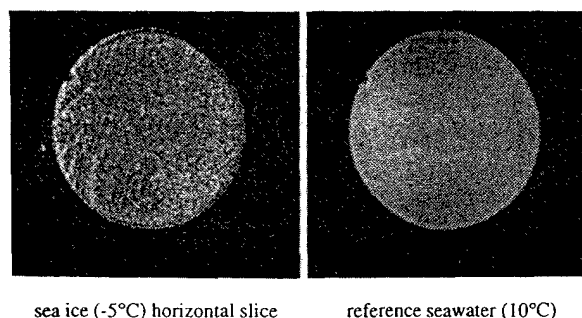


Fig 1. 300MHz proton NMR image of a cross section through some home-grown sea ice. A sea water image is provided for comparison.

NMR IN ANTARCTICA

In the spring of 1994 we spent several days on the sea ice, 25 km from Scott Base, in Antarctica's McMurdo Sound. An Earth's field NMR apparatus, based on a 3rd year student laboratory experiment at Massey University, was assembled in a polar tent and measurements were made on ice cores extracted from the sea ice.

The ice core samples, 120 mm long and 75 mm in diameter, were cut from 2 m long cores, the thickness of the sea ice in this area. Each sample was placed inside the NMR probe which was housed in a snow cave to reduce the effects of generator and computer interference. The probe consisted of a large solenoidal polarizing coil, capable of producing a field of approximately 0.03 Tesla, an excitation coil and 2 receiver coils (fig. 2). The polarizing coil was isolated from the sample by a glass dewer so as to minimise heating effects.

Note that unlike a conventional NMR system the uniformity of the polarizing field is not especially critical since the FID is acquired in the Earth's field, which in isolated areas such as this, is uniform to better than 1 part in 10⁶. This and the fact that we were working at

such low frequencies made for a compact and relatively inexpensive spectrometer.

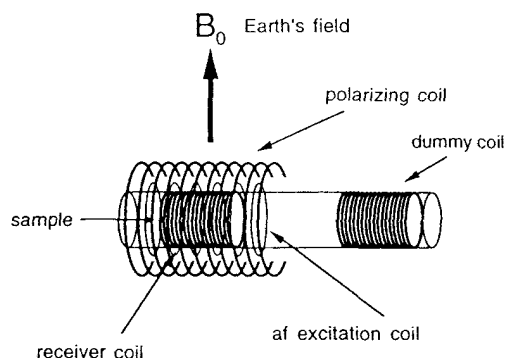


Fig 2. The orientation of the various coils in the NMR probe head with respect to the Earth's magnetic field.

Free induction decays were acquired as indicated in figure 3. The polarizing coil was energised for approximately 5 seconds to produce a bulk magnetization in the sample. The polarizing current pulse was then switched off, but sufficiently slowly so that the magnetization had time to redirect itself along the Earth's magnetic field - almost vertical and of strength $65 \mu\text{T}$ in this location. A 2 ms, 90° pulse at the Larmor frequency of 2.76 kHz, was then applied to the sample via the excitation coil so as to tip the magnetization back into the horizontal plane where it could be subsequently detected as an induced emf in one of the receiver coils. T_2 relaxation data was obtained using a standard spin-echo pulse sequence.

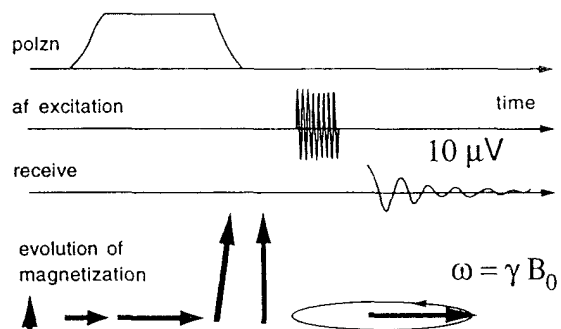


Fig 3. The pulse sequence used to observe a free induction decay in the Earth's magnetic field.

EQUIPMENT

All the necessary switching pulses, including the audio-frequency pulse applied to the excitation coil, were generated by a Tecmag-Aries system⁶ and Macintosh IICI computer. The induced signal ($\sim 10 \mu\text{V}$) was amplified by

a home built, low-noise, differential amplifier and bandpass filter. External, common-mode interference was minimised through the use of a second receiver coil. The resultant signal was digitized and accumulated by the Tecmag system in the usual way (see below).

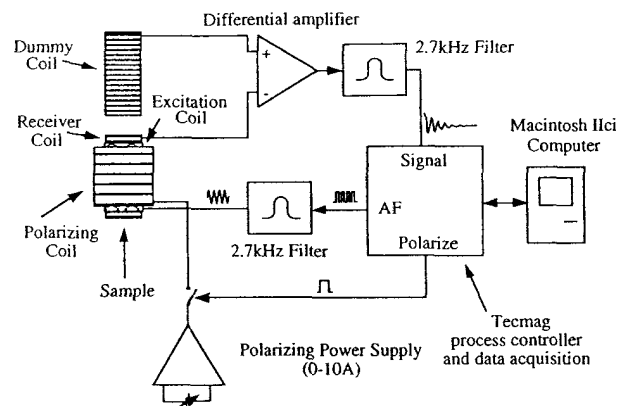


Fig 4. A block diagram of the Earth's field NMR apparatus.

RESULTS

An example of the quality of the NMR data which can be obtained with this equipment can be seen in figure 5 which shows free induction decays from a 500ml water sample and a typical ice core.

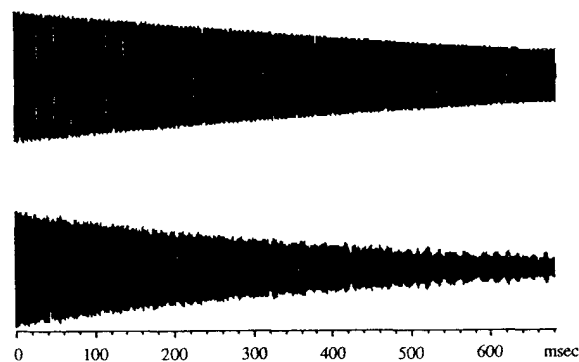


Fig 5. Example free induction decays for water (top trace, 4 accumulations), and sea ice (bottom trace, 64 accumulations, water fraction $\sim 6\%$).

T_2 experiments were performed on 8 sea ice samples taken at depths ranging from 60 to 1810 mm (just above sea level). For each sample a new core was extracted to minimise temperature changes. Even so, a temperature change of $1-2^\circ \text{C}$ was typical during each 20 minute experiment. A reference measurement using (warm) water was made before each T_2 experiment to check on the stability of the apparatus and to provide a reference signal from which the water content in each sample could be determined (fig 6).

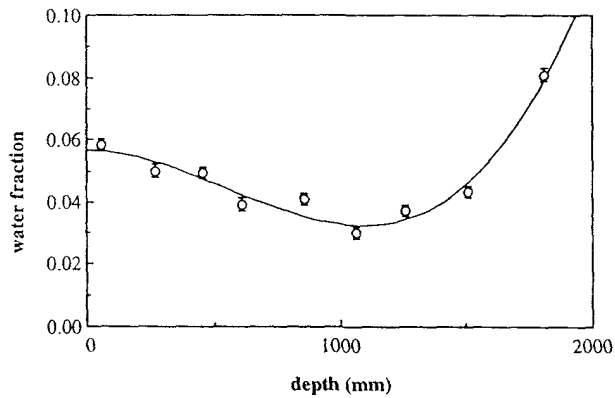


Fig 6. Water fraction in sea ice as a function of depth (the curve is simply a best fit polynomial).

Water fraction data was found to be in qualitative agreement with salinity which had been determined from conductivity measurements made on each sample (fig 7).

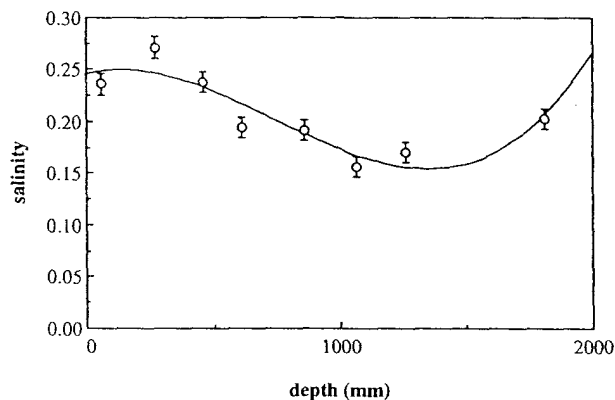


Fig 7. Sea ice salinity as a function of depth (the curve is simply a best fit polynomial).

As expected, the temperature was observed to increase with depth, reflecting the temperature gradient between the air (-10°C to -15°C) and the sea water (-1.7°C).

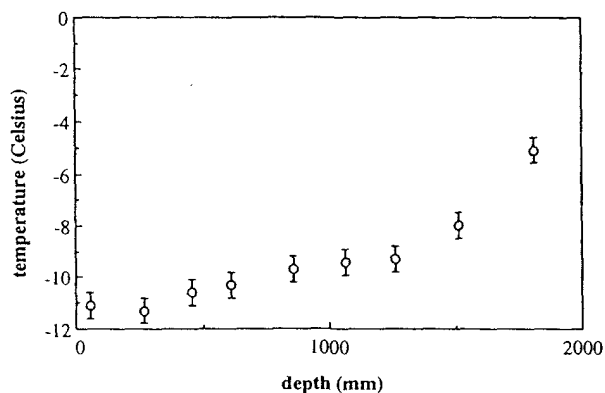


Fig 8. Sea ice temperature as a function of depth

The transverse relaxation time, T_2 , will clearly depend on a number of factors, including brine content, temperature

and pore size. One might expect T_2 to increase with depth since temperature does as well, however a downward trend is observed (fig 9). This could be due to chemical exchange at the solid-liquid interface in the brine-pockets. This would explain the observed trend since the exchange rate will increase with temperature.

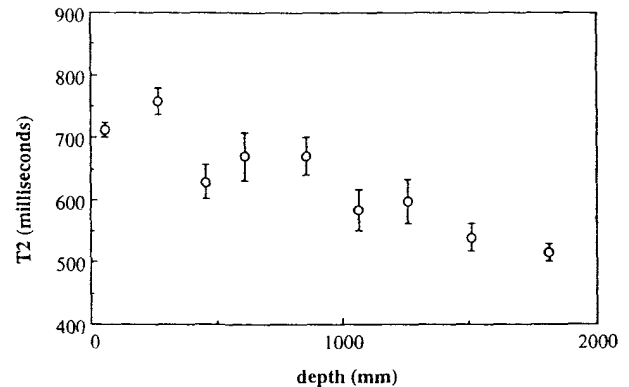


Fig 9. Transverse relaxation in sea ice as a function of depth.

FUTURE EXPERIMENTS

In October 1995 we will return to the Antarctic with improved equipment. In addition to repeating the aforementioned experiments we plan to make restricted diffusion measurements to determine the dimensions of the brine pockets at various depths. With this additional data we hope to be able to provide some insight into the observed macroscopic properties of sea ice.

REFERENCES

1. T. G. Haskell and W. H. Robinson, *Cold Regions Science and Technology*, **23**, p99 (1994).
2. P. Langhorn, *Cold Regions Science and Technology*, **12**, p197 (1986).
3. C. Richardson and E. Keller, *Journal of Glaciology*, **6**, p89 (1966).
4. G. Planinsic, J Stepisnik and M. Kos, *JMR Series A*, **110**, p170 (1994).
5. "Principles of NMR microscopy", P. T. Callaghan, Clarendon Press, Oxford (1991).
6. Tecmag inc., 6006 Bellaire Blvd, Houston, TX 77081 USA.

Application of Radiation Damping Line Shape Theory to Interpreting the Harmonic Peaks in Two Dimensional Spectra of Liquid Water

Xi-An Mao, and Jian-Xin Guo

*Laboratory of Magnetic Resonance and Atomic Molecular Physics, Wuhan Institute of Physics,
The Chinese Academy of Sciences, P.O.Box 71010, Wuhan 430071, China*

1. Introduction

In recent years, radiation damping[1-3] has attracted much attention[4-13] in NMR community due to its unusual effects in experiments. For example, a single π pulse induces an echo-like FID [2,9,13]; with a $\pi/2$ pulse the peak height is much lower than the strongest[9,10]; also in two-dimensional (2D) correlation (COSY) experiments, a radiation-damped sample invariably produces harmonic peaks in the indirectly detected F_1 dimension[4-6,13]. A theory based on the demagnetization field has been proposed by Warren et al.[13-15], trying to give an explanation to these harmonic peaks as well as to the intermolecular cross peaks (the so-called CRAZED signals) observed by asymmetric gradient pulses. In Warren's theory, the harmonic peaks are regarded as intermolecular multiple quantum signals, as they can be selectively observed one by one by asymmetric gradient echo.

However, it is reasonable that the harmonic peaks in 2D NMR spectra on liquid water and the CRAZED signals[13-15] for samples containing isolated molecules are due to different mechanisms. In this paper, we interpret the single-frequency-spaced harmonic peaks in COSY spectrum and the half-frequency-spaced ones in SECSY spectrum of liquid water using the radiation damping line shape theory[16]. Nearly exact simulations of the experimental spectra has been achieved without involving multiple quantum coherences.

2. Experimental

The sample used was 80% H_2O with 20% D_2O as the lock substance. Two dimensional

proton NMR experiments were conducted on a Bruker ARX-500 spectrometer with a 5 mm inverse probe and a 10 mm normal broad band probe tuned at 500.13 MHz using the standard J-resolved and COSY pulse sequences. The transmitter offset was located at 162 Hz up (for SECSY) or down (for COSY) field from the resonance of water for both dimensions. In 2D data acquisition 512 points were used and the number of t_1 -increments was changed. Data matrix for Fourier transformation was 512×512 with zero filling in the t_1 domain only. Detailed description of the experiments will be supplemented in the figure notes.

3. SECSY Spectrum

SECSY (or J-resolved) pulse sequence $\pi/2-t_1/2-\pi-t_1/2-t_2$ is among the simplest 2D experiments with only two pulses. The π pulse in the middle of t_1 focuses the chemical shift effect in the F_1 dimension. If the sample is free of radiation damping, for the isolated spin system like the protons in water, only a single signal should appear on the 2D map at $\omega_1=0$, irrespective of the transmitter offset. However, for 80% H_2O , the radiation damping time T_{rd} is as short as 13 milliseconds, far shorter than the relaxation times ($T_1=T_2=2.3$ s, $T_2^*=0.2$ s). This is a typical radiation-damped sample. The SECSY spectrum (Fig.1) shows a number of resonances in the indirectly detected dimension F_1 , separated by a frequency of $\Delta\omega/2$, where $\Delta\omega$ is the chemical shift offset. This feature is quite different from 2D COSY spectrum, where the harmonic peaks are separated by $\Delta\omega$. It is not possible to interpret the observed multiple frequencies by the intermolecular multiple quantum theory[13-15], since half-integer quantum could not be described in that theory.

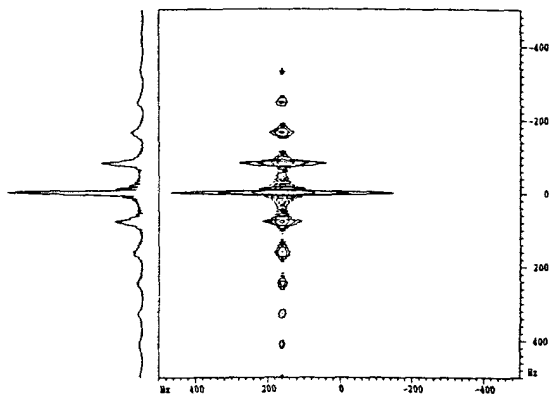


Fig.1 SECSY spectrum on 80% H₂O. Data matrix for acquiring FID was 512×256. The spectral width was 1000 Hz in both dimensions, so that the maximum t_1 was 256 ms (the t_1 increment was 1 ms). The transmitter offset with respect to the water signal was $\Delta\omega=162$ Hz. As a result, the harmonic peaks in the indirectly detected dimension F_1 are separated by 81 Hz. Shown as the projection is the F_1 -slice with $\omega_2=\Delta\omega$

A normal radiation damping analysis cannot predict the harmonic peaks, either. The evolution of the radiation-damped magnetization under the spin-echo pulse sequence can be explicitly analyzed. The first $(\pi/2)_x$ pulse flips the magnetization into the y direction. During the first half of the evolution period, the magnetization precesses and decays as usual, but it returns to the equilibrium state not under the influence of relaxation, but following the radiation damping pathway[17]. In this case, the radiation damping effects become the dominant mechanism for the recovery of the magnetization. At the end of the first $t_1/2$ the magnetization points in a direction characterized by a pair of angles θ_1 and ϕ_1 . The angle θ_1 must be smaller than $\pi/2$ and is described by[3]

$$\tan(\theta_1/2) = \tan(\theta_0/2) \exp(-t_1/2T_{rd}) = \exp(-t_1/2T_{rd}) \quad (1)$$

where the initial angle θ_0 is $\pi/2$ and $\tan(\theta_0/2) = 1$. The angle ϕ_1 is caused by the chemical shift precession and is apparently expressed by $\phi_1 = \Delta\omega t_1/2$ in the rotating frame. When $t_1/2$ is not much longer than T_{rd} , the subsequent π_x pulse turns the magnetization to another direction denoted by θ_2 and ϕ_2 , symmetric with respect to the x -axis, i.e.,

$$\theta_2 = \pi - \theta_1 = \pi - 2 \tan^{-1}[\exp(-t_1/2T_{rd})] \quad (2)$$

$$\phi_2 = \pi - \Delta\omega t_1/2. \quad (3)$$

At the end of the second $t_1/2$, the angle between the magnetization and the B_0 field becomes θ_3 that is found to be $\pi/2$, since

$$\tan(\theta_3/2) = \tan(\theta_2/2) \exp(-t_1/2T_{rd}) \quad (4)$$

and the phase ϕ_3 related to the chemical-shift precession is found to be π since

$$\phi_3 = \Delta\omega t_1/2 + \phi_2. \quad (5)$$

In this case, an echo forms with the magnetization lying in the $-y$ axis, and radiation damping seems not affect the initial value of the 2D FID at all. It appears that the harmonic peaks in F_1 dimension are not due to radiation damping.

However, in recording the spectrum in Fig.1, the maximum of $t_1/2$ was as long as 128

ms, much longer than T_{rd} . For many t_1 -increment with big t_1 values, before the π pulse the magnetization has recovered nearly completely to z direction already, owing to the fast drive of the radiation damping field. Thus

$\theta_2 = \pi$, if inversion is exact. It is well known that the radiation-damped FID is described by a hyperbolic secant function[1,13,16]. Theoretically, with an exact inversion the "echo" will not form until time is infinitely long. However, as has been analyzed in a recent paper[17] dealing with the spin-spin relaxation time measurements, in real situations the "echo" can be observed within tens of milliseconds, i.e., the "echo" does not form at the end of the second $t_1/2$, but at a certain time in advance. This is partly due to the inhomogeneity of the rf field that results in an inaccurate inversion, partly due to the quasi-stable inverted state whose life time could not be long and is sensitive to small vibration outside the spin system. As in experiments these two effects cannot be isolated, it is reasonable to describe both of them by an error in the π pulse, i.e., θ_2 is not equal to π any more, but should be smaller or greater than π . In this case, at the beginning of t_2 the magnetization is not perpendicular to z direction, and the initial value of FID (or the amplitude of FID) is modulated by radiation damping during t_1 (or more accurately speaking, during the second $t_1/2$). The radiation damping

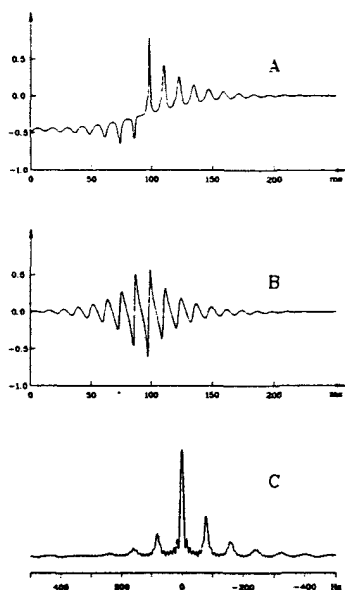


Fig.2 Simulation of the F_1 -slice with $\omega_2 = \Delta\omega$ in Fig.1. (A) and (B) are respectively the real and imaginary part of the signal $s(t_1, \omega_2 = \Delta\omega)$ [see Eq.(7)], while (C) is the final spectrum of $s(\omega_1, \omega_2 = \Delta\omega)$.

effects are thus not refocused by the spin-echo pulse sequence. What we have detected after the second $t_1/2$ is the truncated echo-like NMR maser[2] signal. Therefore, just before the detection, the angle θ_3 should be smaller than $\pi/2$, and becomes t_1 -dependent. Due to the same reason, the chemical shift offset will be effective during t_1 when t_1 is long, and cannot be refocused by the spin-echo sequence.

The analysis above offers us a qualitative picture for the radiation damping effects in a SECSY experiment. Quantitatively, according to the radiation-damped line shape theory[16], the time domain signal in the experiment is described by

$$s(t_1, t_2) = M_0 \sec h\{t_2 / T_{rd} - \ln[\tan(\theta_3 / 2)]\} \times \exp[i(\Delta\omega t_2 + \phi_3)], \quad (6)$$

provided that at the beginning of the detection the direction of the magnetization is characterized by a pair of angles (θ_3, ϕ_3) which are functions of t_1 . Fourier transformation of Eq.(6) with respect to t_2 gives an expression complicated by the superposition of a series of Lorentzian line shapes[16]. Since we are only interested in the F_1 slice at $\omega_2 = \Delta\omega$ where the harmonic peaks appear, we need not discuss

the whole 2D spectrum. For this single slice, the expression is quite simple

$$S(t_1, \omega_2 = \Delta\omega) = M_0 T_{rd} \theta_3 \exp(i\phi_3). \quad (7)$$

It should be pointed out that at this time θ_3 and ϕ_3 are not respectively equal to $\pi/2$ and π any more, although Eqs.(4) and (5) are still valid. In order to derive θ_3 and ϕ_3 , we replace π by $\pi - \delta$ for the second pulse in the spin-echo sequence, where δ is a very small quantity, in order mainly to account for the radiation damping effects in the real system. The deviation in π affects not only θ_2 but also ϕ_2 . As a result, θ_2 and ϕ_2 are determined by Eqs.(8) and (9), respectively

$$\cos \theta_2 = -\cos \theta_1 \cos \delta - \cos(\Delta\omega t_1 / 2) \sin \theta_1 \sin \delta \quad (8)$$

$$\sin \phi_2 = \sin(\Delta\omega t_1 / 2) \sin \theta_1 / \sin \theta_2. \quad (9)$$

With θ_1 , θ_2 and θ_3 expressed in Eqs.(2), (8) and (4), respectively, $S(t_1, \omega_2 = \Delta\omega)$ becomes a complicated function of t_1 and $\Delta\omega$, and the Fourier transformation with respect to t_1 can hardly be done analytically. However, with the help of a computer, we obtained the calculated spectrum depicted in Fig.2. In simulation we set $\delta = 2^\circ$, about 1% as much as π . It can be seen that only 1% inaccuracy for the π pulse produces the half-frequency-spaced harmonic peaks in SECSY spectrum. A negative value for δ yields the same result. However, when π is used for calculation, no harmonic peaks can be simulated. On the other hand, if $\Delta\omega = 0$, from Eqs.(8) and (9) we see that $\phi_3 = 0$, $\phi_2 = \pi - \delta - \theta_1$. In this case, Eq.(7) is no longer a function of $\Delta\omega$ and the harmonic peaks are not expected to appear in the F_1 dimension.

It should be emphasized that when we used $\pi - \delta$ instead of π for calculation, we did not only mean the inaccuracy of the π pulse, which may happen frequently in experiments; more importantly we mean that the real damped spin system cannot stay at the inverted state for long. Since the fast recovery of the damped, inverted system is much like the situation due to the inaccuracy in π pulse, and since no other way

for quantitatively estimating the time the NMR maser takes, we therefore introduced the small deviation quantity δ .

The simulation shown in Fig.2 explains well that the harmonic peaks in the indirectly detected dimension of SECSY spectrum of liquid water are due to the fact that the damped magnetization forms an echo with a time shorter than what is expected by the mathematical expression, particularly when t_1 is much longer than T_{rd} . This implies that if the maximum of t_1 is not much longer than the damping time, harmonic peaks will disappear. Experiments confirm the implication. In Fig.3 we show four projections of four SECSY spectra with different experimental numbers: (A)64, (B)128, (C)256, (D) 512. The dwell time in the t_1 dimension or the t_1 increment was fixed at 400 micro seconds. For (A) and (B), the maximum of $t_1/2$ was not long enough and the harmonic peaks did not appear. When $t_1^{max}/2$ became long in experiment (C), harmonic peaks began to appear. Finally when $t_1^{max}/2$ in experiment (D) was as long as $8T_{rd}$ (still shorter than that for recording the spectrum in Fig.1), harmonic peaks were strong.

We have seen that many factors affect the formation of the harmonic peaks: the frequency offset, the experimental number or the maximum value of t_1 , the error in π pulse and the life time of the inverted state. An interesting question would be that if the system is free from radiation damping, can the harmonic peaks be expected? This case can be analyzed. In the absence of radiation damping, the partially Fourier transformed 2D signal $S(t_1, \omega_2 = \Delta\omega)$ is generally expressed by:

$$S(t_1, \omega_2 = \Delta\omega) = M_0 T_2 \sin \theta_3 \exp(i\phi_3). \quad (10)$$

Since θ_1 keeps $\pi/2$ unchanged, when there is a small error of δ in the π pulse, θ_2 will be equal to $\pi/2 + \delta$, and so will be θ_3 (here the relaxation effects are neglected for simplicity). These angles are no longer t_1 -dependent. After the π pulse, the phase angle ϕ_2 is determined by

$$\tan \phi_2 = \tan(\Delta\omega t_1 / 2) \cos \delta. \quad (11)$$

The angle ϕ_3 should be $\phi_3 = \phi_2 - \Delta\omega t_1 / 2$. As a result, the small δ makes only a negligible

contribution to the signal intensity of the final spectrum[18]. Thus, it can be concluded that the harmonic peaks in 2D SECSY spectrum are caused by radiation damping.

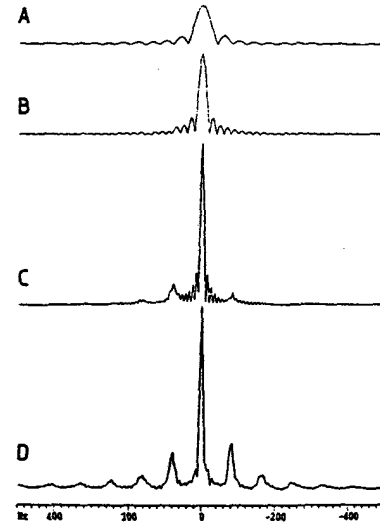


Fig.3 Projections of four SECSY spectra of water with different t_1 -increments: (A)64, (B)128, (C)256 and (D)512. The spectral width was 2500 Hz and 512 points were used for acquiring FID. Thus the increment of t_1 was 400 us. For experiment (A), the maximum of $t_1/2$ was 12.8 ms, just as long as the radiation damping time (13ms). The harmonic peaks did not appear. For (B), $t_1^{max}/2$ was also too short to allow the appearance of the harmonic peaks. For (C), $t_1^{max}/2 = 4T_{rd}$, still not long enough and the harmonic peaks are weak. However, when $t_1^{max}/2 = 102ms = 8T_{rd}$ in experiment (D), strong harmonic peaks spaced by 81 Hz are seen.

4. COSY Spectra

The harmonic peaks in COSY spectrum are different from those in SECSY. Shown in Fig.4 are the COSY spectra. When the harmonic peaks in (A) (with one scan) are spaced by a single frequency, those in (B) and (C) (with four scans by phase cycling) are spaced by four frequencies.

These harmonic peaks can also be interpreted by radiation damping theory. The analysis is easier than for SECSY and is rather straightforward. Suppose we have an operator I_z at equilibrium. After the first $(\pi/2)_x$ pulse, we have I_y . During the evolution period t_1 , both chemical shift and radiation damping should be considered:

$$I_y \rightarrow I_x \sin(\Delta\omega t_1) \sin \theta_1 +$$

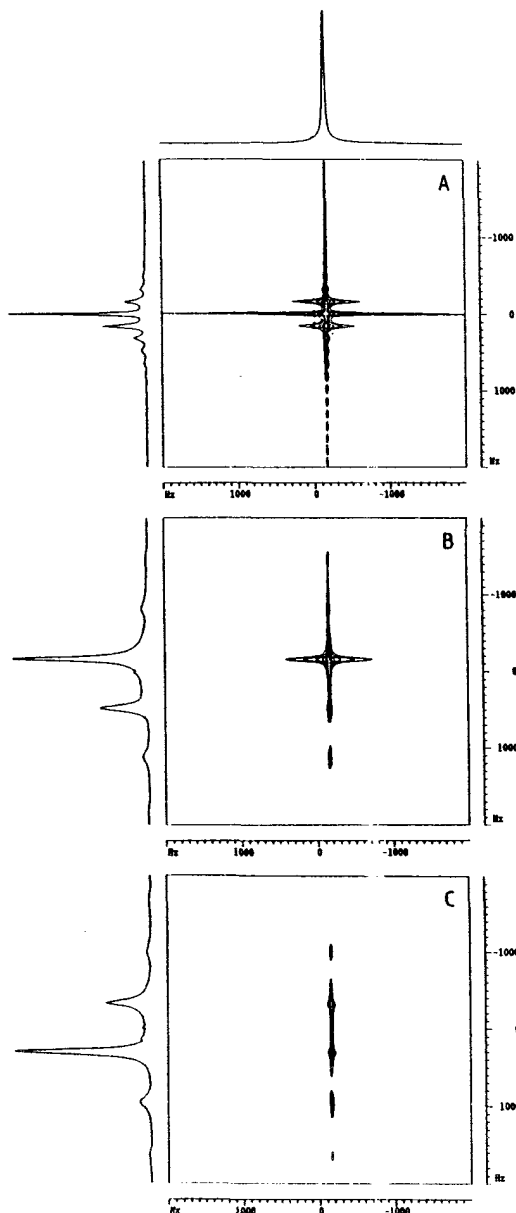


Fig.4 COSY spectra of water: (A) one-scan, (B) four-scan with phase cycle of x, y, -x, -y for the second pulse and x, -x, x, -x for acquisition; (C) The same as for (B) but with x, -y, -x, y for acquisition.

$$+I_y \cos(\Delta\omega t_1) \sin\theta_1 + I_z \cos\theta_1 \quad (12)$$

where θ_1 is determined by Eq.(1). Since no relaxation is considered, the magnetization keeps coherent all the time. Its direction is characterized by θ_1 and $\phi_1 = \Delta\omega t_1$. The second $(\pi/2)_x$ pulse changes the direction, resulting in

$$I_y \rightarrow \rightarrow$$

$$I_x \sin(\Delta\omega t_1) \sin\theta_1 - I_z \cos(\Delta\omega t_1) \sin\theta_1 + I_y \cos\theta_1 \\ = I_x \sin\phi_2 \sin\theta_2 + I_y \cos\phi_2 \sin\theta_2 + I_z \cos\theta_2 \quad (13)$$

Now the direction of the magnetization is (θ_2, ϕ_2) , which are determined by Eq.(13) rather than by Eqs.(8) and (9). Both angles are functions of t_1 . The signal detected is

$$s(t_1, t_2) = M_0 \operatorname{sech}\{t_2 / T_{rd} - \ln[\operatorname{tg}(\theta_2 / 2)]\} \times \\ \times \exp[i(\Delta\omega t_2 + \phi_2)] \quad (14)$$

with the I_y component as the real part and I_x as the imaginary part. Eq.(14) is in fact identical with Eq.(6) in appearance. Fourier transformation of Eq.(14) with respect to t_1 can give an analytical expression of $S(t_1, \omega_2)$. However, as has been done to the SECSY spectra, we need not discuss the whole COSY spectrum. The slice at $\omega_2 = \Delta\omega$ will give the useful information. Setting $\omega_2 = \Delta\omega$, we have

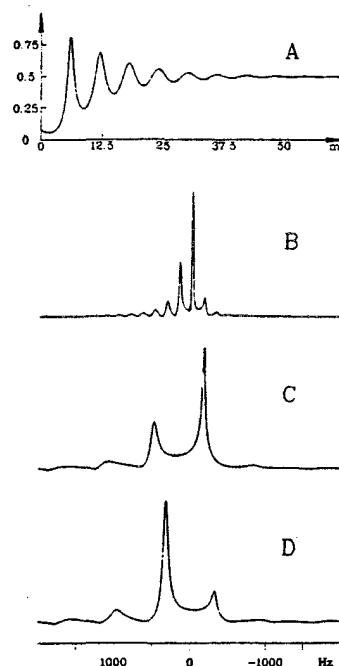


Fig.5 Simulated COSY spectra. (A) is the t_2 -Fourier transformed signal [Eq.(15)]. (B-D) are the simulations of Fig.4(A-C).

$$S(t_1, \omega_2 = \Delta\omega) = M_0 T_{rd} \theta_2 \cos \phi_2 \quad (15)$$

Which is nothing else than Eq.(7). Explicitly, we write out θ_2 and ϕ_2 in Eqs.(16) and (17), respectively, based on Eq.(13)

$$\theta_2 = \cos^{-1}[\cos(\Delta\omega t_1) \operatorname{sech}(-t / T_{rd})], \quad (16)$$

$$\phi_2 = \operatorname{tg}^{-1}[-\sin(\Delta\omega t_1) \exp(-t / T_{rd})]. \quad (17)$$

Inserting Eqs.(16) and (17) into (15), we have a complicated, t_2 -Fourier-transformed signal $S(t_1, \omega_2 = \Delta\omega)$. With the help of a computer, we can view the signal as depicted in Fig.5A. It looks like a FID, but it obviously contains multiple frequencies. Fourier transformation of Eq. (15) with respect to t_1 gives the spectrum of Fig.5B, which simulates the F_1 projection of Fig.4A nearly exactly, particularly the intensities. Taking into account the phase cycling in experiments, we have obtained the calculated spectra as shown in Fig.5C and D. They are in extremely good agreement with the experimental results of Fig.4B and C.

5. Summary

In this paper, we have discussed the harmonic peaks in two dimensional SECSY and COSY spectra by radiation damping line shape theory. It is the radiation damping effects that make the detected 2D FID modulated. The expressions (6) and (14) are most important in analysis, which do not differ from the one-dimensional radiation-damped line shape[16] where the initial angles of the magnetization play a vital role. In the theory of the communication system engineering[19], signal expressed by (6) or (14) is a wave modulated simultaneously in amplitude and angle by both radiation damping and chemical shift offset. The modulation is responsible for the multiple frequencies with the unusual intensities in the indirectly detected dimension. The harmonic peaks have nothing to do with the multiple quantum coherences.

6. Acknowledgment

This work has been supported by the National Natural Science Foundation of China.

One of the authors X. -A. M. gratefully acknowledges the support of K. C. Wong Education Foundation, Hong Kong, for reporting this paper in 12th ISMAR Conference in Sydney, Australia, 1995.

References

- [1] N. Bloembergen and R.V. Pound, *Phys. Rev.* 95 (1954) 8-12.
- [2] A. Szeoke and S. Meiboom, *Phys. Rev.* 113 (1959) 585-596.
- [3] A. Abragam, *The Principles of Nuclear Magnetism*, (Clarendon Press, Oxford) 1961. p. 73.
- [4] M. McCoy and W.S. Warren, *J. Chem. Phys.* 96 (1992) 1657.
- [5] D. Abergel, M.A. Delsuc and J.-Y. Lallemand, *J. Chem. Phys.* 96 (1992) 1657.
- [6] W.S. Warren, Q. He, M.A. McCoy and F.C. Spano, *J. Chem. Phys.* 96 (1992) 1659.
- [7] D. Abergel and J.-Y. Lallemand, *J. Magn. Reson.* A 110 (1994) 45.
- [8] A. Louis-Joseph, D. Abergel and J.-Y. Lallemand, *J. Biomol. NMR*, 5 (1995) 265.
- [9] X.-A. Mao, D.H. Wu and C.H. Ye, *Chem. Phys. Lett.* 204 (1993) 123.
- [10] X.-A. Mao, J.X. Guo and C.H. Ye, *Chem. Phys. Lett.* 218 (1994) 249.
- [11] X.-A. Mao, J.X. Guo and C.H. Ye, *Chem. Phys. Lett.* 222 (1994) 417.
- [12] D.H. Wu and C.S. Johnson, Jr., *J. Magn. Reson.* A 110 (1994) 113.
- [13] Q. He, W. Richter, S. Vathyam and W.S. Warren, *J. Chem. Phys.* 98 (1993) 6779.
- [14] W.S. Warren, W. Ritcher, A.H. Andreotti and B.T. Farmer II, *Science*, 262 (1993) 2005.
- [15] W. Ritcher, S. Lee, W.S. Warren and Q. He, *Science*, 267 (1995) 654.
- [16] X.-A. Mao and C.H. Ye, *J. Chem. Phys.* 99 (1993) 7455.
- [17] X.-A. Mao, J.X. Guo and C.H. Ye, *Chem. Phys. Lett.* 227 (1994) 65.
- [18] A.D. Bain, I.W. Burton and W.F. Reynolds, *Prog. NMR Spectr.* 26 (1994) 59.
- [19] For example, see H. Stark and F.B. Tuteur, *Modern Electrical Communications, Theory and Systems*, (Prectice-Hall, Englewood Cliffs), 1979.

Determination of the three-dimensional solution structure of the oxidised form of mesophilic thioredoxin from *Escherichia coli* and modelling by homology of the thermophilic thioredoxin from *Bacillus acidocaldarius*

Giuseppe Nicastro[□], Cesira de Chiara[□], Lorella Franzoni[□], Marco Tato^{1*}, Fabrizio Nozza[□]
 Enrico Carrara[□] and Claudio Nicolini [□]

[□] Institute of Biophysics, University of Genoa, Italy
¹Pharmacia, Viale Giovanni XXIII, Nerviano (MI), Italy

Abstract

The three-dimensional structures of oxidised thioredoxins from a mesophilic (*E. coli*) and from a thermophilic organism (*Bacillus acidocaldarius*) are estimated and analysed. The structure of *E. coli* thioredoxin has been determined on the basis of 1324 inter proton and 78 hydrogen-bonding distance restraints supplemented by 88 dihedral angle constraints derived from nuclear magnetic resonance (NMR) measurements¹, while that of *B. acidocaldarius* thioredoxin has been modelled by homology from the *E. coli* one. We have compared our structure to the structure obtained by NMR for the reduced form. The relationships between the structures are discussed. The 3D solution structure of *B. acidocaldarius* thioredoxin is actually in progress and the spin system identification is being carried out².

Thioredoxin is a protein that occurs in all living systems with many functions, particularly in thiol-dependent redox reactions^{3,4}. Thioredoxins are found in many organisms ranging from prokaryotes to eukaryotes and play a key role in maintaining the redox environment of the cell⁴, acting as potent reducing agents for disulphide bonds in many proteins⁵. Thioredoxin from *E. coli* contains 108 residues (Mr 11700). The active site of Thioredoxin has the sequence Cys32-Gly33-Pro34-Cys35-, contains a disulphide in the oxidised form and a dithiol in the reduced state. It is capable of catalysing thiol-disulphide exchange reactions and protein disulphide isomerization. Thermophilic thioredoxin has been isolated from *Bacillus acidocaldarius* a micro-organism which lives at high temperature and low pH. It is made of 105 residues (Mr 11800) and its active site has the sequence Cys29-Gly30-Pro31-Cys32-⁶. It's

well known that proteins and enzymes from thermophilic organisms are thermostable and exhibit an enhanced general stability if compared with mesophilic counterpart. These proteins can be very similar to mesophilics except for their general stability to heat, organic solvents, detergents, common protein's denaturing agents, and to proteolytic enzymes.

Therefore the mechanisms of thermal stability of proteins are of particular interest because of the benefits of using enzymes as practical catalysts at elevated temperature (e.g. enhanced rates of reaction). These biotechnological applications lay stress on the interest of thermophilic proteins.

In this work we present the experimental 3D solution structure of the oxidised form of mesophilic thioredoxin (from *E. coli*) and the theoretical 3D structure of the thermophilic one (from *B. acidocaldarius*) in the oxidised form, as modelled by sequence homology respect to the mesophilic protein. The 3D solution structure of *B. acidocaldarius* thioredoxin is actually in progress and the spin system identification is being carried out while its primary structure is being published separately⁶.

The three-dimensional X-ray structure of oxidised mesophilic form has been determined to 2.8 Å⁷ resolution and has been refined to 1.7 Å⁸. The structure of the reduced mesophilic protein could not be obtained by X-ray crystallography, because crystals of *E. coli* thioredoxin oxidised form were only obtained in the presence of Cu²⁺ ions⁹ which act to cross-link two molecules by co-ordination at Ser1, Asp2 and Asp10^{7,8}. This requirement for Cu²⁺ precludes crystallisation of reduced thioredoxin because Cu²⁺ is an oxidising substrate. The three-dimensional solution structure of reduced (dithiol) thioredoxin from *E. coli* has been determined¹⁰ and, during the

preparation of this work, has recently been achieved through the publication the high-resolution solution structures of both the reduced (Trx(SH)₂) and oxidised (Trx-S₂) forms¹¹.

Both mono- and two-dimensional ¹H-NMR were recorded on an Unity-600 Varian at 600 MHz spectrometer at Pharmacia (Nerviano, MI, Italy), equipped with a triple resonance probe, at the temperatures of 298 and 308 K and pH=5.7. All the chemical shift values reported are referenced to TSP localised at 0 ppm. The following experiments were recorded using standard methods: DQF-COSY^{12,13,14}, TOCSY^{15,16,17}, 2Q-2D^{13,18}, NOESY^{19,20} and E. COSY²¹.

In order to perform the calculation of the structure of the oxidised form of E. coli thioredoxin a set of 1324 approximate inter proton distance restrains, 55 ϕ backbone torsion angle restrains, 33 χ_1 side-chain torsion angle restrains and 15 stereo specific assignments have been derived from the NOESY, DQF-COSY, TOCSY, and E. COSY spectra.

These restrains, together with 78 backbone hydrogen bonds deduced from a qualitative interpretation of the NOEs and NH exchange rates, constituted the experimental data for the three-dimensional structure calculations using distance geometry and simulated annealing. A set of structures with only small residual violations of the n.m.r. and steric constraints was obtained as a result of calculations with the program DIANA²². Using the program DISCOVER INSIGHTII package these structures were then submitted to an initial energy minimisation, followed by molecular dynamics at high temperature, slow cooling phase and a final energy minimisation. The input for the DIANA calculations consisted of upper distance limits derived from NOESY (60, 90 ms) cross peak intensities with the program Felix 2.0 and dihedral angle constraints obtained by 55 ³J_{HN α} and 33 ³J _{$\alpha\beta$} spin-spin coupling constant measurements made on the DQF-COSY and E. COSY cross peaks. Initial structures were calculated with DIANA from a preliminary, incomplete input data set, using the default protocol suggested by the program. Additional NOESY cross peaks were assigned by analysing the resulting structures with small violations. The resulting new set of constraints was used as input for a second run of calculations, and this process was repeated several times until almost all NOESY cross peaks were assigned. During

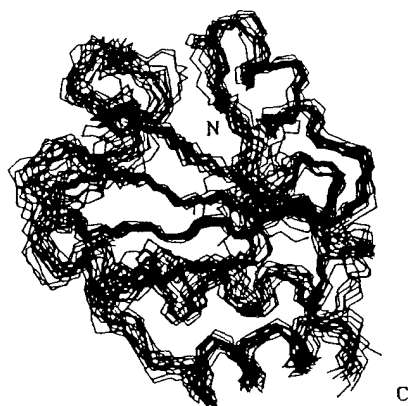
structure calculation we make use of redundant dihedral angle constraints (REDAC strategy)²³ derived from preliminary calculations of 80 complete structure. A set of 15 stereo specific assignments of β -methylene protons and other pairs of diastereotopic substituents were obtained with the program GLOMSA²². A total of 700 structure calculations were performed using the same input data but different starting conformations with random dihedral angles distributed uniformly between -180° and +180°. For each conformation, the target function was minimised at the levels (L in eqn (7) of reference 22) 0, 1, 2, 3, 4, 5, 6, 7, 8, 9, 10, 15, 20, 30, 40, 50, 60, 70, 80, 90, 100 and twice 108. Throughout the calculation, the weighting factors w_u and w_l for explicit upper and lower distance limits were set to unity, and the weighting factor w_a for dihedral angle constraints were set to 5 Å². For levels 0 to 108, the weighting factor w_v for van der Waals constraints was 0.2; for the first minimisation step at level 108, it was increased to 0.6, and for the final minimisation step at level 108 to 2.0. The 40 structures with lowest target functions resulting from the final input data set were used for the subsequent simulated annealing (SA) with INSIGHTII (Discover). The resulting best 40 structures had target functions ranging from 2.3 ± 0.2 Å and all residual violations of NOE distance constraints were less than 0.57 Å of dihedral angle constraints less than 5° and of van der Waals violations less than 0.52 Å. This set of 40 DIANA structures was first energy minimised and then subjected to simulated annealing (SA). The structures were first minimised with a maximum of 500 iterations using the conjugate gradient algorithm, rapidly heated to 1000° K, kept at this temperature during 4 ps, and cooled down slowly by decreasing the temperature in steps of 100° K during time intervals of 0.05 ps until 300° K was reached. Another molecular dynamics run of 1.5 ps at 300° K was added. Then the structures were again energy-minimised with 300 iterations using conjugate gradient algorithm to yield the final result. The best of 20 conformers obtained, resulting after simulated annealing and used to represent the solution conformation of the protein, are characterised by low energies in the range -985 to -1090 Kcal/mol and small residual violations of the conformational constraints residual. All the parameters characterising the structures are shown in Tab. 1

Table 1. Analysis of the 20 best thioredoxin structures obtained from DIANA before (B.M.) and after (A.M.) restrained simulated annealing with the program DISCOVER.

Quantity	Average value ±standard deviation	
	B.M.	A.M.
Target function (\AA^2)	2.3±0.2	
DISCOVER energy (Kcal/mol)	1024±32	-1030±25
Noe constraint violations:		
Number > 0.2 \AA	6.1±1.3	6.2±1.1
Sum (\AA)	4.1±0.18	4.7±0.7
Maximum (\AA)	0.57±0.10	0.47±0.01
Angle constraint violations:		
Number > 5°	2.64±0.8	2.4±1.5
Sum (deg.)	9.8±2.8	9.59±1.08
Maximum (deg.)	3.36±1.4	3.7±1.2
Pairwise r.m.s.d. (\AA):		
Backbone 3-108	1.84±0.87	1.10±0.12
Heavy atoms 3-108	2.42±0.44	1.80±0.17

All 20 SA structures satisfy the experimental restraints and display very small deviations from idealised covalent geometry. The overall polypeptide fold is illustrated in Fig. 1 which show the superposition of the backbone (N, C α , C') atoms of all 20 SA structures.

Figure 1.: Superimposition of the 20 best solution structures of oxidised thioredoxin after simulated annealing. The bonds connecting the backbone (N,C α ,C') atoms are shown.



The main secondary structure feature of thioredoxin consists of five stranded β -sheets surrounded by four α -helices arranged in the order $\beta\alpha\beta\alpha\beta\beta\alpha$ (Fig.1). The first strand of the β -sheet (residues 4 to 8) runs parallel to the second strand (22 to 29) and parallel to the third strand

(53 to 59). The third strand runs anti parallel to the fourth strand (76 to 81) and to the fifth strand (88 to 91). The helical region between residues 63-70 shows a number of similarities to both an α helix and a 3_{10} helix. The active site (residues - Cys 32-Gly 33-Pro 34-Cys 35-) forms a protruding loop from the end of the second β -strand to the start of the second α -helix. The regular secondary structure elements are well defined, while the loops between them have a much greater variation in conformation.

Oxidised versus reduced mesophilic thioredoxin.

Overall, the structure of oxidised thioredoxin in solution agrees closely with the previously determined structure of reduced thioredoxin¹¹. The structures are completely superimposable. Global r.m.s. values between the structures of the two proteins are given in table 2.

Table 2. Comparison between the solution structure of the oxidised and the reduced form of E. coli thioredoxin

Atom set	Average of the pairwise rmsd (\AA)
Backbone 0-108	6.12±1.45
Backbone 3-108	1.20±0.25
Backbone of residues: 3-29, 37-108	0.75±0.17
Backbone of residues: 11-18, 34-49, 95-108	0.40±0.12
Heavy atoms 3-108	1.82±0.34

The average was taken of all 200 pairwise comparisons between the 20 SA structures of thioredoxin for the oxidised form and the 10 thioredoxin for reduced form structures¹⁰. The structures are completely superimposable with an rmsd for residues 3-108 of 1.20±0.25 \AA (backbone atoms) and 1.82±0.34 \AA (all heavy atoms). There are apparent changes in the local structure of the active site region upon change of oxidation state.

Local variations of a few degrees are observed in the backbone dihedral angles. The side-chain conformations of the two cysteins are the same in Trx(SH)₂ and Trx-S₂: the observed χ_1 angles are the same for the two states.

The only noticeable difference between the backbone conformations of the two structures is found in residues Ala 29 to Lys 36, whose significance is also clearly confirmed by the small r.m.s.d. for residues 3 to 29 and 37 to 108 compared to that of the backbone atoms of residues 3 to 108 (table 2). Close similarity of the two structures is also supported by the near-identity of the ^1H chemical-shifts. We have also assigned from chemical shift of NH Asp 2 (8.61ppm), not identified previously. This resonance assignment was obtained through the spin system identification and the sequential assignment. A comparison of the close similarity of the structures of the two proteins is shown in Fig 2.

Figure 2.: Comparison of the reduced thioredoxin solution structure¹⁰ (thicker line) with the oxidised solution structure¹ (thin line). The two structures compared are those giving the smallest pairwise r.m.s.d.



Mesophilic versus thermophilic oxidised thioredoxin by homology.

The sequence alignment with *E. coli* thioredoxin used to model by homology the structure of *B. acidocaldarius* thioredoxin, has been obtained by using Clustal V²⁴, a program for the fast and sensitive multiple sequence alignment. The residues aligned were 77 (of which 49 identical and 28 homologue) corresponding to 73.33% of *E. coli* thioredoxin sequence. The second step has been the tertiary structure determination by using Homodel²⁵. Homodel is a system which models protein 3D structures, when only the amino acids sequence is known, on the bases of their similarity

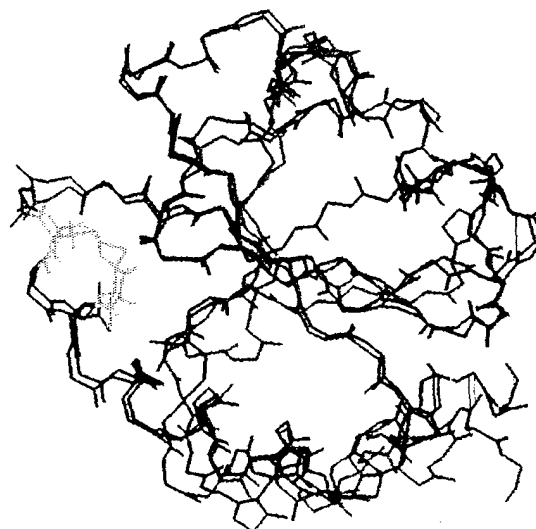
with other homologue proteins of known structure. Homodel generated for the thermophilic protein a set of structural constraints between residues within the regions aligned with the mesophilic one.

By using this set of constraints and the primary structure as input for Diana, a family of 10 3D structures of thermophilic thioredoxin was obtained.

The structures were first minimised with 1500 iterations of conjugate gradient, rapidly heated to 1000°K, kept at this temperature during 4 ps, and cooled down slowly by decreasing the temperature in steps of 100°K during time intervals of 0.05 ps until 300°K was reached. Another molecular dynamics run of 1.5 ps at 300°K was added. Then the structures were again energy-minimised with 3000 iterations of conjugate gradient to yield the final result. After minimisation the mean RMSD (calculated for backbone atoms of aligned regions) between each one of the 10 thermophilic structures and NMR mesophilic structure is $1.52 \pm 0.71 \text{ \AA}$.

Fig. 3 shows the superimposition of one of the thermophilic thioredoxin models with the mesophilic thioredoxin structures by NMR; active sites of both the proteins are in yellow.

Figure 3. Superimposition of one of the thermophilic thioredoxin structures obtained by modelling (blue line) with the mesophilic thioredoxin structures by NMR (green line; aligned residues are in red); active sites of both the proteins are in yellow



This preliminary study suggests that the two structures appear to have a similar global folding.

Active sites are included in a long aligned region and in the same way of mesophilic protein, forms a protruding loop from the end of the second β -strand through the start of the second α -helix. Most of differences are located in C-terminal region where less homology and alignment is observed (green region in Fig 3).

Acknowledgment

Part of this work was supported by research contract from PHARMACIA-Farmitalia Carlo Erba (Milano, Italy) within the framework of the National Program "Technology for Bioelectronics" sponsored by the Italian Ministry of Universities, Scientific and Technological Research.

Reference.

1. Nicastro, G., de Chiara, C., Franzoni, L., Tatò, M., Carrara, E.A., Carrara, S., Nicolini, C., NMR and Nanogravimetric comparative studies between oxidised and reduced form of Thioredoxin from *E. coli*. (in preparation) 1995.
2. de Chiara, C., Nicastro, G., Rossi, M., Nicolini C., Three-dimensional solution structure of thermophilic Thioredoxin from *Bacillus acidocaldarius*. (in preparation) 1995.
3. Holmgren, A. Thioredoxin. *Annu. Rev. Biochem.* 54:237-271, 1985.
4. Holmgren, A. Thioredoxin and glutaredoxin systems. *J. Biol. Chem.* 264:13963-13966, 1989.
5. Holmgren A 1984 Enzymatic reduction-oxidation of protein disulphides by thioredoxin. *Methods Enzymol.* 107, 295-300
6. Rossi, M. et al., (in preparation).
7. Holmgren, A., Soderberg B-O, Eklund, H., Branden C. I. Three-dimensional structure of *Escherichia coli* Thioredoxin to 2.8 Å resolution. *Proc. Natl. Acad. Sci. USA* 72:2305-2309, 1975.
8. Katti, S. K., LeMaster, D. M., Eklund, H. Crystal structure of thioredoxin from *Escherichia coli* at 1.68 Å resolution. *J. Mol. Biol.* 212:167-184, 1990.
9. Holmgren A & Soderberg B.O. 1970 Crystallisation and preliminary crystallographic data for thioredoxin from *Escherichia coli* *J. Mol. Biol* 54, 387-390)
10. Dyson, H.J., Gippert, G.P., Case, D.A., Holmgren, A., Wright, P.E. Three-Dimensional

Solution Structure of the Reduced Form of *Escherichia coli* thioredoxin determined by Nuclear Magnetic Resonance Spectroscopy. *Biochemistry* 29:4129-4136, 1990.

11. Jeng, M.-F., Campbell, A.P., Begley, T., Holmgren, A., Case, D.A., Wright, P.E. and Dyson, H.J. High-resolution solution structures of oxidised and reduced *Escherichia coli* thioredoxin *Structure* 2: 9, 853-867, 1994.
12. Muller, N., Ernst, R. R., Wüthrich, K. Multiple quantum-filtered two-dimensional correlated NMR spectroscopy of proteins. *J. Amer. Chem. Soc.* 108:6482-6492, 1986.
13. Rance, M., Wright, P. E. Analysis of ^1H NMR spectra of proteins using multiple-quantum coherence. *J. Magn. Reson.* 66:372-378, 1986.
14. Rance, M., Sorensen, O., Bodenhausen, G., Wagner, G., Ernst, R. R., Wüthrich, K. Improved spectral resolution in COSY ^1H NMR spectra of proteins via double quantum filtering. *Biochem. Biophys. Res. Commun.* 117:479-485, 1983.
15. Bax, A., Davis, G. D. MLEV-17 Based two-dimensional homonuclear magnetisation transfer spectroscopy. *J. Magn. Reson.* 65:355-360, 1985.
16. Rance, M. Improved techniques for homonuclear rotating-frame and isotropic mixing experiments. *J. Magn. Reson.* 74:557-504, 1987.
17. Griesinger, C., Otting, G., Wüthrich, K., Ernst, R. R. Clean TOCSY for ^1H spin system identification in macromolecules. *J. Amer. Chem. Soc.* 110:7870-7872, 1988.
18. Otting G., Wüthrich, K. Complete protein fingerprints by Double-quantum spectroscopy. *J. Magn. Reson.* 66:359-363, 1986.
19. Kumar, A., Ernst, R. R., Wüthrich, K. A two-dimensional nuclear Overhauser enhancement (2D NOE) experiment for the elucidation of complete proton-proton cross-relaxation networks in biological macromolecules. *Biochem. Biophys. Res. Commun.* 95:1-6, 1980.
20. Kumar, A., Wagner, G., Ernst, R. R., Wüthrich, K. Build-up rates of the nuclear Overhauser effect measured by two-dimensional proton magnetic resonance spectroscopy: implications for studies of protein conformation. *J. Amer. Chem. Soc.* 103:3654-3658, 1981.
21. Griesinger et al., *J. Am. Chem. Soc.* 107: 6394-6396, 1985
22. Guntert, P., Braun, W., Wüthrich, K. Efficient computation of three-dimensional protein structures in solution from nuclear magnetic resonance data using the program DIANA and the

- supporting programs CALIBA, HABAS and GLOMSA. *J. Mol. Biol.* 217:517-530, 1991.
23. Guntert, P., Wüthrich, K. Improved efficiency of protein structure calculations from NMR data using the program DIANA with redundant dihedral angle constraints. *J. Biomol. NMR* 1:447-456, 1991.
24. Higgins, D.G., and Sharp P.M. CLUSTAL: a package for performing multiple sequence alignments on a microcomputer. *Gene* 237-244, 1988.
25. Carrara, E.A., Nicolini, C., Protein structure by Homology, Biomedical Modelling and Simulation. J. Eisenfeld, D.S. Levine and M. Witten (Ed), Elsevier Science Publishers B.V. (North-Holland), 1992.

1. 5'-CAAAAATTTTG-3'
2. 5'-CGAAAATTTTCG-3'
3. 5'-CAGAAATTTCTG-3'
4. 5'-CAAGAATTCTTG-3'
5. 5'-CAAAGATCTTTG-3'
6. 5'-CAAAGCTTTTG-3'
7. 5'-CAGGAATTCCTG-3'
8. 5'-CGGGAATTCCTG-3'

Sequence 1 is a control which contains five consecutive adenine nucleotides and is known to have a narrow minor groove structure. In the other sequences, we were able to infer the effect of replacing an adenine with a guanine on the minor groove structure of the DNA molecule by measuring the minor groove distance at the adenine bases surrounding the substituted guanine(s) and comparing these distances to those in the control sequence. As shown in Figure 2 the measured distances indicate that the minor groove narrows significantly in the control sequence at the 3' end of the poly-A tract. Further examination of

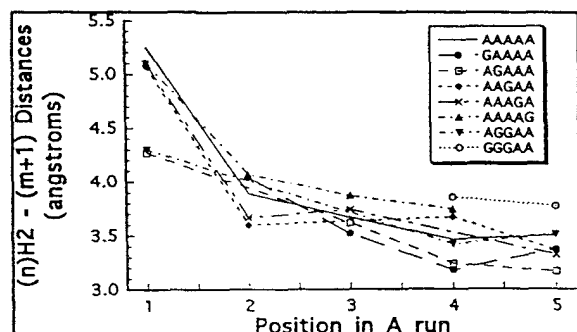


Figure 2. The cross-strand distances from the (n)A-H2 to (m+1)H1' distances are plotted as a function of the position of the adenine in sequences 1-8. The distances were determined from the initial build-up rate of NOESY crosspeaks taken at several mixing times and collected at 750 MHz. The determination of unknown distances was based on calibration compared to the cross-relaxation rates between the H5-H6 cytosine protons whose distance is fixed at 2.5Å.

Figure 2 shows that in all the sequences studied, the substitution of guanine for adenine did not alter the pattern of narrowing minor groove from 5' to 3' direction that was observed in the control sequence. Even in sequence 8, where three guanines are substituted for the first three adenine bases in the control sequence, the minor groove width at the two adenines, while $\sim 1\text{\AA}$ wider than the control, is still significantly narrower than in B-type DNA. Therefore, the pattern of compression of the minor groove width observed in poly-A DNA appears to be preserved in mixed poly-A:poly-G sequences. This helps to understand why BPDE adduction is greater at the 5' end of poly-G runs compared to the 3' end. At the 5' end of a poly-G tract, where the minor groove width is normal compared to B-type DNA, less perturbation to the secondary structure of the DNA would be required to accommodate the $\sim 3.7\text{\AA}$ widening of the minor groove upon formation of the BPDE adduct compared to the larger structural rearrangement that must occur at the 3' end where the minor groove structure is exceptionally narrow. Of more general interest, the results show that guanine can be accommodated in a relatively narrow minor groove topology in DNA. In order to determine structurally how guanine can be accommodated into narrow minor groove topologies, we determined the structure of sequences 4 and 8 by NMR spectroscopy. The structural models shown in Figure 3 clearly exhibit structural differences that are evident from observation of the kink in the ribbon representation of the DNA backbone that occurs at the GpA step. Structural details of these two sequences will be presented elsewhere. Visually, it is apparent that the minor groove is greater in the GGGAA sequence compared to the AAGAA sequence. Direct measurement of the minor groove width as (n+2)Phosphorous to (n-2)Phosphorous in the two model structures (Figure 4) shows that the minor groove width still reaches a

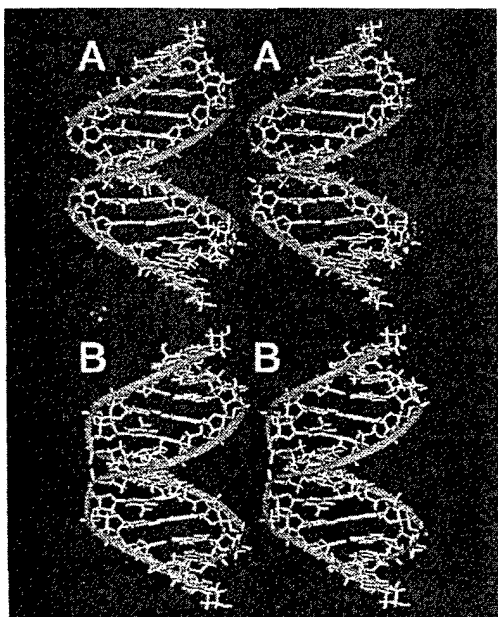


Figure 3. Structures derived from NMR data collected at 750 MHz for A) 5'-CAAGAATTCTTG-3' and B) 5'-CGGGAATTCCCG-3' shown in cross-eyed stereo representation. The DNA backbone is represented by a solid oval ribbon to illustrate how the minor groove varies with sequence and to illustrate the kink observed at the GpA step.

minimum value at the ApT step in both sequences. It is interesting to note that in the AAGAA sequence the minor groove width is compressed by $\sim 3\text{\AA}$ from $\sim 12\text{\AA}$ to $\sim 9\text{\AA}$ whereas in the GGGAA sequence the minor groove width is only compressed by 2\AA from $\sim 12\text{\AA}$ to $\sim 10\text{\AA}$. This indicates that while guanines can be accommodated into narrow minor groove topologies similar to those observed in poly-A DNA, the magnitude of the compression is not as great.

The observed compression of the minor groove in sequences containing multiple guanines helps to understand the ladder pattern of BPDE adduction but does not help explain the enhanced binding at the 5'-end of such sequences. The chemical reaction that occurs when BPDE forms a covalent DNA adduct

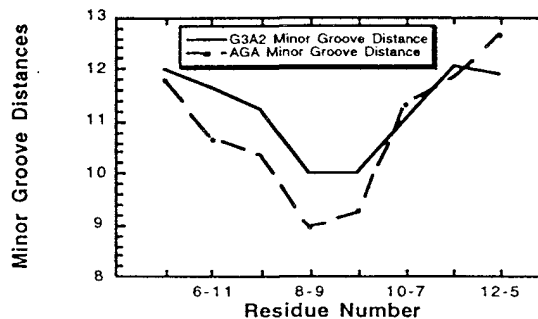


Figure 4. $(n+2)$ Phosphorous to $(n-2)$ phosphorous distance plotted as a function of residue number. The distances were measured from structures derived from NMR data collected at 750 MHz and refined using restrained molecular dynamics and back-calculation.

requires that the epoxide opens and a bond is formed between the C10 atom of the BPDE and the exocyclic 2-amino nitrogen atom of guanine. A potential competing reaction is the hydrolysis of the epoxide to an unreactive tetraol. Therefore, the presence or absence of water in the local microenvironment of the reaction could influence whether the fate of the epoxide proceeds to tetraol or adduct. Guanines in DNA have been shown by others to disrupt the spine of hydration in the minor groove, i.e. regions high in guanine content can be considered "dry". Therefore, in these "dry" regions of DNA, the formation of the covalent adduct would be favored compared to the hydrolysis that could occur in a more "wet" microenvironment such as occurs in poly:A DNA where a spine of hydration in DNA is thought to stabilize the secondary structure associated with exceptionally narrow minor groove topologies. This could explain the enhanced adduct yields in poly-G regions of DNA. We are currently investigating the extent of water of hydration in the sequences listed above and examining the role of water in BPDE adduction to DNA.

References

1. Thrall, B. D.; Mann, D. B.; Smerdon, M. J.; Springer, D. L.; *Biochemistry*, **1994**, *33*, 2210-2216.
2. Cosman, M.; De Los Santos, C.; Fiala, R.; Hingerty, B. E.; Singh, S. B.; Ibanez, V.; Margulis, L. A.; Live, D.; Geacintov, N. E.; Broyde, S.; *Proc. Natl. Acad. Sci. USA*, **1992**, *89*, 1914-1918.
3. (a) Chuprina, V. P.; Fedoroff, O. Y.; Reid, B. R.; *Biochemistry*, **1991**, *30*, 562-568. (b) Llanov, A. A.; Chuprina, V. P.; *Nucl. Acids Res.*, **1987**, *15*, 5833-5844.
4. Wüthrich, K. In *NMR of Proteins and Nucleic Acids*, Wiley, New York, 1986: Chapter 11.

STRUCTURAL STUDIES OF *o*-VANILLIN DERIVATIVES AND THEIR METAL COMPLEXES BY ONE AND TWO DIMENSIONAL NMRG.A. Naganagowda[†], S. Raghothama[†], B.V. Agarwala[§] and C.L.Khetrapal^{†*}[†] Sophisticated Instruments Facility,

Indian Institute of Science, Bangalore 560 012, India.

[§] Department of Postgraduate Studies and Research in Chemistry
Rani Durgavati Vishwavidyalaya, Jabalpur 481 001, India.**Abstract**

One and two dimensional NMR studies to investigate the structures of some *o*-Vanillin derivatives and their complexes with metals such as zinc and platinum are described. Some of the ligands and their metal complexes are found to exist as two or three species in dynamic equilibrium with one another. Unambiguous assignments of signals from the various species have been made by two dimensional experiments. The dynamic and structural aspects have been studied by NOE, exchange spectroscopy and molecular modeling.

Introduction

NMR spectroscopy is one of the most powerful techniques for obtaining information on the nature of complexation of the ligands with the metals, their structural and dynamical properties. The use of one dimensional NMR to study the structural and functional properties of metal complexes is very common. However, the employment of the multi-dimensional techniques which yield information that is otherwise difficult or impossible to obtain from the one dimensional experiments is not equally well exploited. Particularly, the dynamical and the structural aspects can be well studied by two

dimensional EXSY and NOE experiments. In this paper we report, the use of various two dimensional techniques, in addition to one dimensional NMR experiments to study some of the *o*-Vanillin derivatives and their metal complexes with zinc and platinum with emphasis on the information which otherwise cannot be easily obtained.

Experimental

The ligands *o*-Vanillin semicarbazone, *o*-Vanillin salicyloyl hydrazone, *o*-Vanillin phenylthiosemicarbazone and their complexes with zinc and platinum were prepared as reported in the literature (1,2).

About 0.05 M solutions of the ligands and their complexes in deuterated dimethyl sulphoxide solvent were used for the NMR experiments. ¹H, ¹³C and ¹⁹⁵Pt one dimensional NMR experiments along with the deuterium exchange studies were performed on an AMX-400 NMR spectrometer. Temperature variation experiments, one dimensional NOE experiments, phase sensitive double quantum filtered COSY (2QFCOSY) (3), rotating frame Overhauser and exchange spectra (ROESY) (4), Nuclear Overhauser enhancement (NOESY) (5) spectra, magnitude mode ¹H-¹³C heteronuclear COSY (HETCOSY) (6) and ¹H-¹³C correlations through long range couplings (COLOC)

^{1*} Author for correspondence

(7) were all recorded on the same spectrometer. For the zinc complex of *o*-Vanillin salicyloyl hydrazone, ^1H decoupled ^{13}C - ^{13}C NOESY experiment was also performed to assign the resonances.

For the 2QFCOSY, about 512 free induction decays with t_1 increments each of 1024 points and 16 scans were collected with a recycle delay of one second. Fourier transformation along both the dimensions was done after multiplying the data sets by sine square window function shifted by $\frac{\pi}{2}$ and with zero filling the t_1 -dimension to 1024 points. For the ROESY and NOESY spectra, spin lock time and mixing time of 250 ms and 300 ms, respectively were used. About 512 Free induction decays with t_1 incrementation each of 1024 data points, 64 scans and recycle delay of one second were collected. The t_1 -dimension was zero filled to 1024 points. Fourier transformation was performed along both the dimensions after multiplying by sine square window function shifted by $\frac{\pi}{2}$. For ^1H decoupled ^{13}C - ^{13}C NOESY, 128 scans, recycle delay of one second and mixing time of 400 ms were used. Fourier transformation was carried out after multiplying by Gaussian broadening function with the $\text{LB} = -0.96$ Hz and $\text{GB} = 0.01$ Hz. HETCOSY and COLOC experiments were performed collecting 512 t_1 points each of 1024 points, 128 scans and a recycle delay of 1 second, in both the cases. Fourier transformation was performed in magnitude mode with zero filling the t_1 points to 1024. The window function used was sine-square shifted by $\frac{\pi}{2}$ along both the dimensions in each of the cases. Spectral widths of 4500 and 17500 Hz were used for ^1H and ^{13}C respectively for the corresponding two dimensional experiments.

Results and Discussion

(1) *o*-Vanillin salicyloylhydrazone(*o*VSH)

The ^1H spectrum of *o*VSH shows two sets of signals referred to as the major and the minor sets, hereafter. The intensity of one of the sets

is about 3 % that of the other. Assignments of the major and the minor set of signals were made using deuterium exchange, 2QF-COSY and ROESY experiments. It may be noted that the two conformers are in dynamic equilibrium in dimethylsulphoxide solvent as observed by the presence of exchange cross peaks in ROESY spectrum as shown in figure 1. The observed signals from the minor conformer are found to be shifted upfield compared to those of the major conformer. The chemical shifts of the labile (NH and OH) protons vary differently with temperature indicating, thereby, the differential hydrogen bonding strengths of the two protons. The major component has the structure where the two hydroxyl protons are intramolecularly hydrogen bonded. In the minor set, the hydroxyl proton of the *o*-vanillin ring is hydrogen bonded to the S=O group of the solvent dimethyl sulphoxide- d_6 .

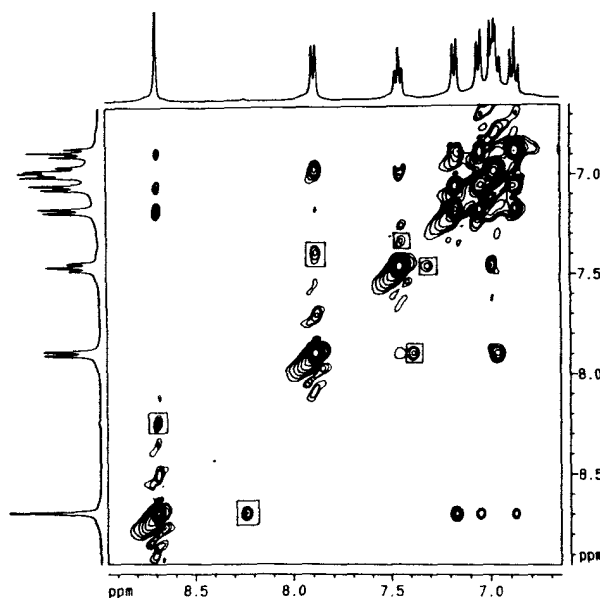


Figure 1: Aromatic region of ROESY spectrum of *o*VSH recorded on an AMX-400 spectrometer showing the exchange cross peaks between the major and the minor (marked with squares).

(2) Zinc complexes of *o*VSH

Like in the ligand two sets of signals were ob-

served in the NMR spectrum in the ratio 12:1 corresponding to two different complexes. Assignments of ^1H resonances were made by 2QF-COSY and ROESY spectra. ^{13}C signals from the major set were assigned by HETCOSY and COLOC experiments. The signals of the minor component which could not be analysed by the above techniques due to their low intensities, were analysed by ^1H decoupled ^{13}C - ^{13}C NOESY spectrum. In one of the complexes, zinc coordinates with phenolic oxygen of the *o*-vanillin group, azomethine nitrogen and carbonyl carbon. In the other, in addition to these, it also coordinates with the phenolic oxygen of the salicyloyl group. The coordination of this oxygen has been indicated by the drastic downfield shift of the carbon attached to this oxygen.

(3) *o*-Vanillin phenylthiosemicarbazone (oVPTSC)

The ligand oVPTSC showed only one set of signals in the dimethylsulphoxide solvent. ^1H and ^{13}C resonances were assigned by various one and two dimensional NMR experiments. It may be noted that NOE is observed between the protons labelled 1 and 8 which appear to be very far as seen in the structure (figure 2a) and it is also noticed from the temperature effect of the -OH proton chemical shift that this proton is hydrogen bonded. When the structure is determined by molecular modeling and energy minimization, it is still does not satisfy the constraints of the NMR parameters (figure 2b). Whereas the figure 2c shows the structure obtained after minimizing the energy with NOE and hydrogen bonding constraints.

(4) Platinum complex with oVPTSC and pyridine

Mixed ligand complex of Platinum with oVPTSC and pyridine has been studied by ^1H , ^{13}C and ^{195}Pt NMR spectra. Unambiguous assignments of various resonances have been made by two dimensional NMR experiments. It

is observed both from ^1H and ^{195}Pt NMR spectra that as a function of time, a second set of signals develops which is due to a second type of complex. The presence of inter-ligand NOE in the complex is also indicated by the NOESY experiment. Determination of the three dimensional structure of the complex using NOE and hydrogen bonding constraints, molecular modeling and the identification of the second type of complex are in progress.

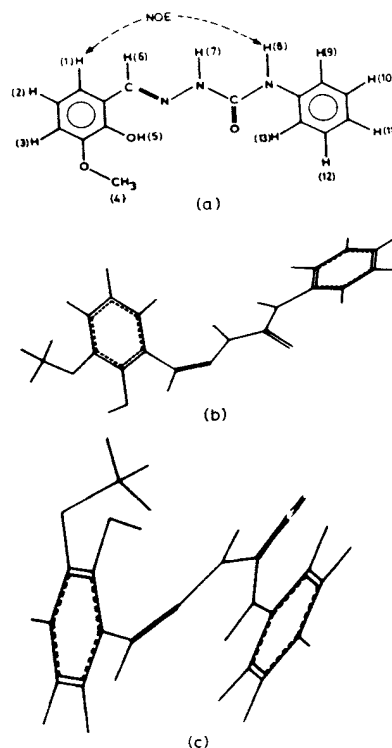


Figure 2: (a) Structure of oVPTSC indicating the observed NOE between the protons 1 and 8; (b) Structure obtained after minimizing the energy without the use of any constraints; (c) Structure obtained after minimizing the energy with NOE and hydrogen bonding constraints.

(5) Zinc complexes with *o*-vanillin semicarbazone (ZnoVSC)

^1H NMR spectrum of this complex in dimethylsulphoxide shows three sets of signals though the ligand shows only a single set. It is noticed from the two dimensional exchange

spectrum that all the three sets of signals are in dynamic equilibrium. Analysis of all the signals was made by 2QF-COSY and two dimensional exchange spectra. Chemical shift data reveal that the shifts of one of the set of signals are comparable with those of the uncomplexed ligand. As the temperature is raised, all the sets of signals move towards each other and at 368 K, they coalesce. Structures have been assigned for the different complexes.

Conclusions

Some o-vanillin derivatives and their metal complexes using multidimensional and multinuclear NMR experiments have been characterised. Two or three types of species in dynamic equilibrium with one another are observed. Structures of the ligands and complexes are assigned using NMR data and molecular modeling computations.

References

- ¹ B.V. Agarwala, V.Puri, G.A. Naganagowda and C.L. Khetrapal, *J. Mol. Struct.*, **327** 131 (1994).
- ² B.V. Agarwala, V.Puri, G.A. Naganagowda and C.L. Khetrapal, *J. Ind. Chem. Soc.*, **70** 967 (1993).
- ³ A. Wokaun and R.R. Ernst, *Chem. Phys. Lett.*, **52** (1977) 407.
- ⁴ A.A. Bothner-By, R.L. Stephens, J. Lee, C.D. Warren and R.W. Jeanloz, *J. Am. Chem. Soc.*, **106** 811 (1984).
- ⁵ S. Macura and R.R. Ernst, *Mol. Phys.*, **41** (1980) 95.
- ⁶ A. Bax and G.A. Morris, *J. Magn. reson.*, **42** 501 (1981).
- ⁷ H. Kessler, C. Griesinger, J. Zarbock and H.R. Loosli, *J. Magn. Reson.*, **57** 331 (1984).

Solid State NMR Characterization of Highly Conductive Lithium-Based Ceramics

K. M. Nairn¹, M. Forsyth¹, M. Greville¹, T. J. Bastow³, M. E. Smith^{3,4} and D. R. MacFarlane²Department of Materials Engineering¹ and Department of Chemistry²,
Monash University, Clayton, Victoria, 3168, Australia.Division of Materials Science and Technology³,
C.S.I.R.O., Clayton, Victoria, 3168, Australia.Physics Laboratory⁴, The University of Kent, Canterbury, Kent, CT2 7NR, U. K.

Solid lithium-ion conducting electrolytes are important as materials for use in devices such as lithium batteries. For battery use, high σ_{Li} (Li^+ ion conductivity) is important. Two families of ceramics which exhibit high σ_{Li} are $\text{Li}_{3x}\text{La}_{4-x}\text{TiO}_3$ ^{1,2} and $\text{Li}_{1+x}\text{Al}_x\text{Ti}_{2-x}(\text{PO}_4)_3$ ³.

Two of the more conductive ceramics reported for these systems have been prepared and studied using solid state NMR. $\text{Li}_{0.3}\text{La}_{0.57}\text{TiO}_3$ was prepared by dry ballmilling of stoichiometric amounts of Li_2O , La_2O_3 and TiO_2 , pressing pellets of the resultant powder, and calcining at 1100°C for 24 hours. The X-ray diffraction pattern for the final ceramic was similar to that reported by Kawai², indicating the presence of a single perovskite phase. $\text{Li}_{1.3}\text{Al}_{0.3}\text{Ti}_{1.7}(\text{PO}_4)_3$ was prepared by the ballmilling, in ethanol, of Li_2CO_3 , Al_2O_3 , TiO_2 and $(\text{NH}_4)_2\text{HPO}_4$, followed by calcining at 900°C for 2 hours³.

According to the literature, the bulk crystal ionic

conductivities (that is excluding the series resistance at the grain boundaries) for these ceramics at room temperature are $3 \times 10^{-3} \text{ S cm}^{-1}$ for the phosphate and $1.1 \times 10^{-3} \text{ S cm}^{-1}$ for the oxide. Inaguma et al.¹ studied the conductivity of a similar oxide as a function of temperature and reported a change in conductivity mechanism at around 380K, resulting in a decrease in activation energy from 0.40 eV to 0.15 eV. Aono et al.³ found that activation energy for conduction of the phosphate depended continuously on temperature, i.e. non-Arrhenius behaviour was observed. Inaguma's data could also be interpreted in this way. One of the aims of this study is to see if the mechanism of ion-motion in these ceramics changes with temperature, using solid state NMR to study the environments and motion of the ions.

⁷Li NMR static measurements were performed on a Bruker CXP-300 spectrometer (at 116 MHz) and a Bruker MSL-400 spectrometer (at 155 MHz). A 30° pulse was used for excitation, although the spectra appear to be independent of excitation pulse length.

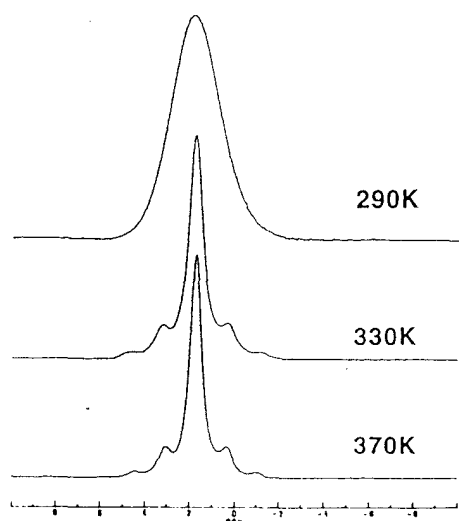


Figure 1: Static ⁷Li spectra of $\text{Li}_{0.3}\text{La}_{0.57}\text{TiO}_3$ at 155 MHz as a function of temperature.

Fig. 1 shows the ⁷Li static spectra of $\text{Li}_{0.3}\text{La}_{0.57}\text{TiO}_3$ as a function of temperature at 155 MHz. Quadrupolar satellites with C_Q around 900 Hz appear at temperatures greater than 310K. Both the singularities and the edges of the quadrupolar powder pattern are visible, while the splitting of the satellites decreases as temperature increases. Figure 2 shows the ⁷Li static spectra of $\text{Li}_{0.3}\text{La}_{0.57}\text{TiO}_3$ as a function of temperature at 116 MHz. These spectra used a much broader sweep and many more scans than the previous spectra. The central transition in these spectra appears as a single peak, unlike that at 155 MHz. A second set of satellite transition peaks is observed with a splitting of around 40 kHz. These peaks are not very intense, and might be attributed to a minority phase such as at the grain boundaries.

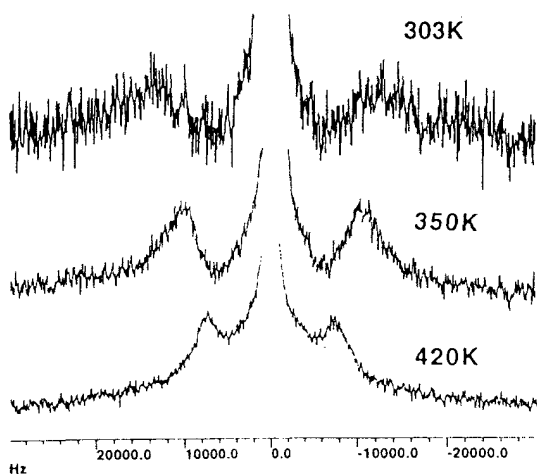


Figure 2: Static ${}^7\text{Li}$ spectra of $\text{Li}_{0.3}\text{La}_{0.57}\text{TiO}_3$ at 116 MHz as a function of temperature.

Similar quadrupolar structure has been observed at higher temperatures in less conducting ceramics by Vashman et al.⁴, Pronin et al.⁵ and by Xie et al.⁶. The appearance of quadrupolar structure appears to correlate with bulk conductivity in these systems (the higher the bulk conductivity, the lower the temperature at which quadrupolar structure appears). For quadrupolar structure to appear, the electric field gradient experienced by the lithium ions must be well defined. In systems with mobile ions this means that the ions must hop between equivalent sites in the lattice, with a long residence time and a short transit time on the NMR time-scale⁵.

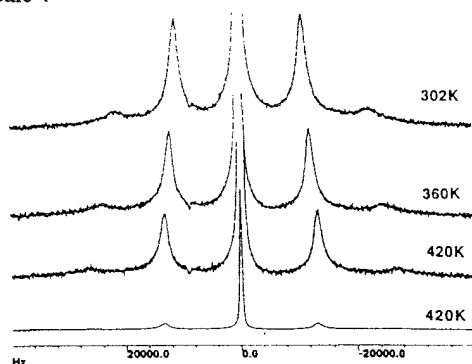


Figure 3: Static ${}^7\text{Li}$ spectra of $\text{Li}_{1.3}\text{Al}_{0.3}\text{Ti}_{1.7}(\text{PO}_4)_3$ at 116 MHz as a function of temperature.

Fig. 3 shows the ${}^7\text{Li}$ static spectra of $\text{Li}_{1.3}\text{Al}_{0.3}\text{Ti}_{1.7}(\text{PO}_4)_3$ as a function of temperature, measured at 116 MHz. Quadrupolar satellites are already strong at 302K, and both the $\theta=0^\circ$ and $\theta=90^\circ$ transitions are observable. Both ceramics have Lorentzian ${}^7\text{Li}$ lineshapes, indicating that the lithium ions are highly mobile in these materials.

Fig. 4 shows the ${}^7\text{Li}$ quadrupolar splitting as a function of temperature for both ceramics.

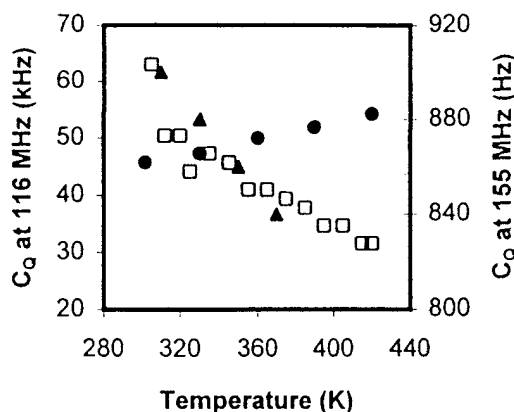


Figure 4: Quadrupolar coupling constant C_Q as a function of temperature. (\bullet) $\text{Li}_{1.3}\text{Al}_{0.3}\text{Ti}_{1.7}(\text{PO}_4)_3$ at 116 MHz, (\blacktriangle) $\text{Li}_{0.3}\text{La}_{0.57}\text{TiO}_3$ at 155 MHz, (\square) $\text{Li}_{0.3}\text{La}_{0.57}\text{TiO}_3$ at 116 MHz.

Results of relaxation time measurements on these systems, along with aluminium and phosphorus NMR spectra will be reported in a more detailed publication⁷. The effect of composition on the structure and mobility of these materials is currently being investigated as the next stage in this work.

1. Y. Inaguma, C. Liqun, M. Itoh, T. Nakamura, T. Uchida, H. Ikuta and M. Wakihara, *Solid State Commun.* **86**, 689 (1993).
2. H. Kawai and J. Kuwano, *J. Electrochem. Soc.* **141**, L79, (1994).
3. H. Aono, E. Sugimoto, Y. Sadaoka, N. Imanaka, and G. Adachi, *J. Electrochem. Soc.* **137**, 1023 (1990).
4. A. A. Vashman, I. S. Pronin and S. E. Sigaryov, *Solid State Ionics* **58**, 201 (1992).
5. I. S. Pronin, S. E. Sigaryov and A. A. Vashman, *Solid State Ionics* **38**, 9 (1990).
6. Z. H. Xie, M. E. Smith, J. H. Strange and C. Jaeger, *J. Phys.: Condens. Matter* **7**, 2479 (1995).
7. K. M. Nairn, M. Forsyth, M. Greville, D. R. MacFarlane and M. E. Smith, *Solid State Ionics*, to be published.

Acknowledgement:

The authors gratefully acknowledge the support of this work by the Australian Research Council and the Monash University Research Fund.

NMR Investigation of a New Semisynthetic Bioactive Compound

Claudio Rossi*, Alessandro Donati*, Debora Renzoni^o, Claudia Bonechi*,
Nadia Marchettini*

* Department of Chemistry, University of Siena, 53100 Siena Italy.

^o Department of Biochemistry, University of Oxford, Oxford OX1 3QU, UK.

1. Introduction

Rifaximin obtained from rifamycin SV¹ by chemical modification of the naphtho-furone moiety has antibiotic activity, inhibiting DNA-dependent RNA polymerase of bacteria² and reverse transcriptase of oncogenic RNA-viruses^{3,4}.

In this paper we report the NMR characterization and solution behaviour of a new class of ansamycin derivatives rifaximin OR (Open Ring) obtained by electrolytic reduction of rifaximin⁵. The electrolytic process causes selective reduction of the aliphatic chain of rifaximin,

forming an aldehyde group at C₂₉ without affecting the diene region at C₁₆-C₁₈.

Rifaximin protons show chemical shift dependence on concentration suggesting a self-association process by stacking interactions between aromatic residues of two molecules. In rifaximin OR the aromatic protons also show chemical shift dependence on concentration which is related again to intermolecular interaction. Nevertheless the aliphatic region in rifaximin OR is far enough from the planar aromatic ring not to be influenced by the dynamics of the anisotropic aromatic shielding contributions of the self-

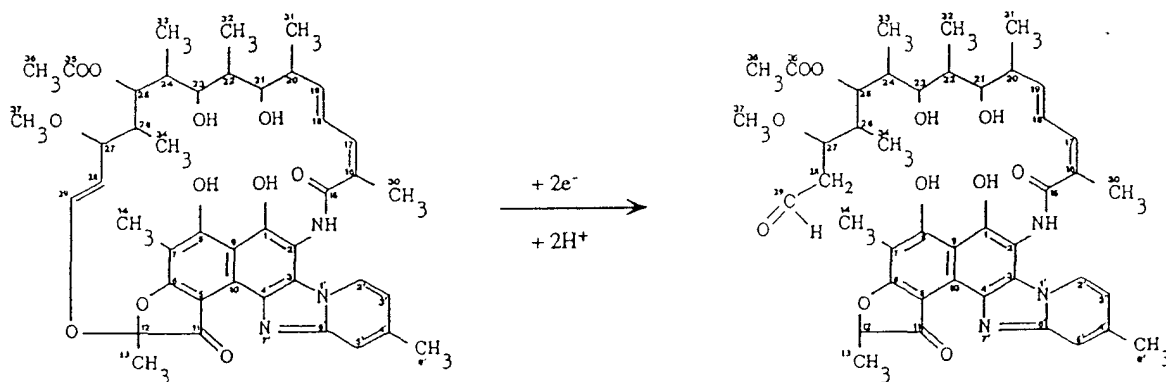


Figure 1. Pathway of the electrolytic reduction of rifaximin. Structures and numbering of rifaximin and rifaximin OR are also shown.

association process.

Preliminary structural information obtained by 2D-NOESY experiments and molecular mechanics calculations also suggests that a different molecular arrangements of the aliphatic region of the two molecules occurs. However the molecular conformation of rifaximin does not appear completely modified in rifaximin OR.

2. Experimental Methods

Electrolytic reduction of rifaximin was performed in a medium containing 0.83 mol.dm⁻³ KCl, 0.2 mol.dm⁻³ phosphate buffer at pH 7 and methanol in an electrolysis cell the anode compartment of which was separated from the solution by a Vycor partition. Electrolysis and the purity of the final product were checked by HPLC. The molecular weight of the product was determined by mass spectra with a VG70-250S double-focus spectrometer using the FAB ionization method.

NMR measurements were made with a Bruker AMX-600 spectrometer operating at 600 MHz. NMR solutions were prepared in 99.98% CDCl₃ in a nitrogen atmosphere. All measurements were at 300 K. The pure absorption phase NOESY spectra were obtained by the phase cycling routine suggested by States et al⁶.

3. Results and Discussion

The electrolytic reduction of rifaximin and the production of rifaximin OR is shown in Figure 1. As reported in this figure the reduction process caused a break in the aliphatic chain with the formation of an aldehyde group at C₂₉ and two diastereotopic protons at C₂₈. No other region of rifaximin was affected by the electrolytic process.

The 600 MHz proton spectrum of rifaximin OR with the complete assignment is shown in Figure 2. Table 1 reports the chemical shift values (ppm) of rifaximin OR and rifaximin.

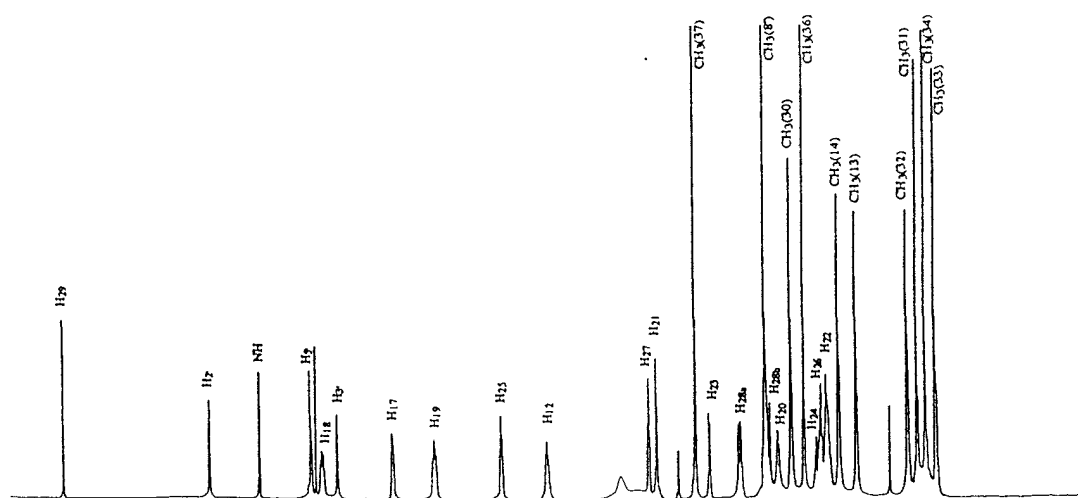


Figure 2. The 600 MHz proton spectra of rifaximin OR in CDCl₃ solution at 298 K.

Table 1
Proton chemical shift values of rifaximin and
rifaximin OR (0.2 mol.dm^{-3} at 298 K)

N. nucleus	Rifax. $^1\text{H } \delta$ (ppm)	Rifax. OR $^1\text{H } \delta$ (ppm)
2'	8.444	8.296
3'	7.058	6.945
5'	7.364	7.226
8'	2.585	2.466
12		4.782
13	1.919	1.530
14	1.984	1.719
17	6.302	6.392
18	6.745	7.130
19	6.000	5.967
20	2.228	2.390
21	3.557	3.637
22	1.525	1.859
23	2.815	3.094
24	1.252	1.938
25	4.851	5.304
26	1.052	1.885
27	3.253	3.723
28	4.943	
28a		2.773
28b		2.502
29	5.977	9.799
30	2.257	2.239
31	0.688	0.937
32	0.886	1.025
33	0.081	0.747
34	-0.662	0.851
36	1.925	2.098
37	2.936	3.224

These results confirm the structure of rifaximin OR obtained as described above. The main spectral differences between rifaximin OR and its parent precursor were: i) a 9.79 ppm aldehyde signal, ii) two non equivalent $\text{H}_{28\text{a}}$ and $\text{H}_{28\text{b}}$ protons at 2.77 and 2.50 ppm respectively, and iii) a down field shift of the $\text{CH}_3(34)$ from -0.66 to 0.85 ppm. The effect detected on the $\text{CH}_3(34)$ methyl is of particular importance as it is related to structural changes that occur during reduction.

This point was investigated by analysing the NOESY spectra of rifaximin and rifaximin OR. Figure 3 shows the NOESY spectrum of rifaximin OR. The cross peak between $\text{CH}_3(14)$ and $\text{H}_{28\text{b}}$ not present in rifaximin is diagnostic of the structural modification which occurred. The same conclusions are supported by molecular mechanics calculations

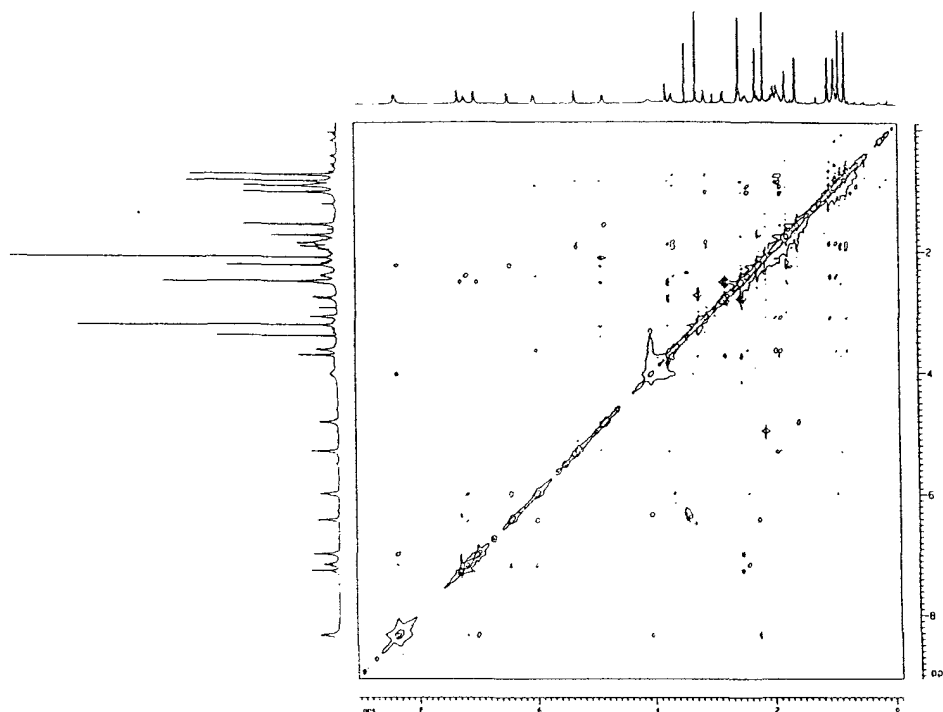


Figure 3. NOESY spectrum of 0.1 mol.dm^{-3} solution of rifaximin OR in CDCl_3 at 298 K.

(performed with the MacroModel package). The aliphatic chain in rifaximin OR is no longer symmetrical with respect to the aromatic naphtho-quinonic plane.

Although no dramatic structural rearrangements were detected, the aliphatic chain has now moved towards CH₃(14). The effect is a reduction of the aromatic shielding contribution with a generalized down field shift. In particular the CH₃(34) occurs at 0.85 ppm in rifaximin OR. The proposed structure of rifaximin OR is shown in Figure 4.

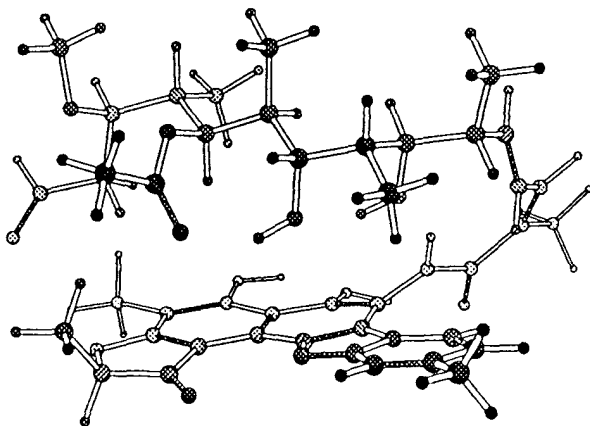


Figure 4. Solution structure of rifaximin OR obtained from NMR experimental constraints and subsequent energy minimization calculations.

References

- 1) M.Brufani, L.Cellai, E.Marchi and A.L.Segre; *J.Antibiotic* **37**, 1611 (1984).
- 2) L.Cellai, H.Heumann, G.Baer and W.Werel; *Eur.J.Med.Chem.* **24**, 105 (1989).
- 3) M.Brufani; "Topics in Antibiotic Chemistry" (Sammes P.G., ed.), Ellis Horwood Ltd., Chichester, 91-217 (1977).
- 4) G.Lancini and W.Zanichelli; "Structure Activity Relationships Among the Semisynthetic Antibiotics" (Perlmann D., ed.), Academic Press, New York 531-600 (1977).
- 5) C.Rossi, N.Marchettini, C.Bonechi, A.Donati, G.Corbini and P.Corti; *J.Chem.Research* (1995) submitted.
- 6) D.J.States, R.A.Haberkorn and D.J.Ruben; *J.Magn.Reson.* **48**, 286 (1982).

A COMPARISON BY NMR OF A *C-MYC* BINDING DNA OLIGOMER AND ITS
NON-BINDING METHYLATED ANALOGUE

Wendy Bicknell[†], Keith J. Cross[#] and Kevin J. Embrey[†]

[†]Victorian College of Pharmacy (Monash University), Melbourne, Vic. 3052, Australia

[#]42 Patrick Close, Greensborough, Vic. 3088, Australia

[†]Queensland Pharmaceutical Research Institute, Nathan, Qld. 4111, Australia

The oncogene *c-myc* is localized in the nucleus and is believed to contribute to the regulation of cell growth and differentiation. Two very similar high-affinity binding sites have been identified¹ as DNA dodecamers, both of which contain a central CpG step. Upon methylation at the C5 of this cytosine, binding of *c-myc* is precluded.

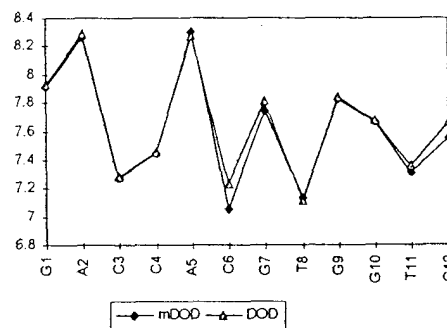
Two related DNA dodecamer duplexes were chosen for study by NMR. The non-methylated sequence, 5'-GACCACGTGGTC-3' is found to bind strongly to the *c-myc* protein, while its 5-methylated cytosine counterpart, 5'-GACCA^{5m}CGTGGTC-3', containing only one methylation site per strand does not bind at all to the protein.

¹H experiments were conducted on both oligomers using 1-D and 2-D NMR techniques under varying conditions of temperature, concentration, buffering and pH to investigate whether there were any conformational differences between the two DNA oligomers.

Only small differences were noted in chemical shifts and other indices and these changes were mainly limited to the base involved at the site of methylation. The dodecamer was dissolved in D₂O with a buffer consisting of 10mM phosphate, 50mM NaCl, 0.5mM EDTA and azide at a pH of 6.7 and was compared to its methylated counterpart under similar conditions. Most chemical shifts were within 0.03ppm of each other, with the exceptions falling within 0.2ppm.

A plot of the chemical shifts for the base protons purine H8 and pyrimidine H6 of each base is shown below. The

methylated sequence is labelled mDOD and the unmethylated sequence is DOD.



As expected, C6-H6 moved upfield on methylation as it is immediately adjacent to the methylation site at carbon-5 of residue C6. Interestingly, none of the deoxyribose sugar protons of the C6 residue were significantly changed. Other protons which moved upfield by >0.06ppm were G7-H8, C12-H6, C12-H5 and C12-H1'.

G7 is located on the 3' side of the methylated C6 residue and moves upfield on methylation, while A5, the base on the 5'-side of C6, does not show significantly altered chemical shifts. From molecular modelling, the closest approach of the C6-methyl to G7-H8 is ca. 2.7 Angstrom, while the distance to A5-H8 is ca. 6.3 Angstrom. This difference in proximity would explain the different responses in chemical shift. The terminal cytosine protons appear to be sensitive to oligomeric concentration and should not be affected by methylation at C6.

References:

1. G.C. Prendergast & E.B. Ziff, "A new bind for Myc", Trends in Genetics, 8(3), 1992.

Temperature dependence of ^7Li linewidth in poly(propylene oxide) complexed with LiClO_4 and LiBF_4 under different decoupling conditions

T.J. Bonagamba, N.C. Mello, L.H. Mattoso, H. Panepucci, and J.P. Donoso
 Instituto de Física de São Carlos - Universidade de São Paulo
 Caixa Postal 369, CEP 13560-970 - São Carlos, São Paulo, Brasil

Introduction

The study of ionic or molecular dynamics and structure is an usual application of solid state NMR. Much information about the mechanism of ionic conduction in alkali metal salt polymers complexes can be obtained from the temperature dependence of both T_1 and T_2 . In the present work we have studied the temperature dependence of ^7Li linewidth in solid polymer ionic conductors under different decoupling conditions in order to analyze dynamics of ionic motion.

Material and methods

Polymer electrolytes were prepared using high molecular weight poly(propylene oxide) (PPO) and commercial LiClO_4 and LiBF_4 . Appropriate amounts of polymer and salt were weighed and dissolved in distilled acetonitrile, to obtain the desired O/Li ratio, n . The solvent was allowed to evaporate slowly at 60°C . Two samples were prepared, PPO- LiClO_4 ($n=8$) and PPO- LiBF_4 ($n=8$). For the NMR experiments, the resulting dried samples were sealed in an NMR tube.

^1H and ^{19}F decoupling were used to separate the contribution of these nuclei to the ^7Li dipolar linewidth. This allows to evaluate the individual contribution arising either from the counterion or the protons in the polymeric chain. This helps to study contributions to the ion mobility not related to the polymeric segment motion.

The NMR spectrum of the ^7Li , consisting of only the central transition ($-1/2 \leftrightarrow +1/2$), was recorded as a function of the temperature between -120°C to 140°C at 32.9MHz using a TECMAG LIBRA system and a double resonance Doty probe. Linewidths were obtained with and without decoupling from the FIDs. Full widths at half maximum (FWHM) were obtained in both cases by fitting the lineshape by a lorentzian function above the glass transition temperature, T_g , and gaussian function below it. Special care was taken to avoid heating effects on the sample due to radiofrequency irradiation by using low duty cycle sequences.

Results and discussion

Figures 1 and 2 present results for the temperature dependence of the ^7Li linewidth using ^1H and ^{19}F decoupling for the case of LiClO_4 and LiBF_4 complexed poly(propylene oxide).

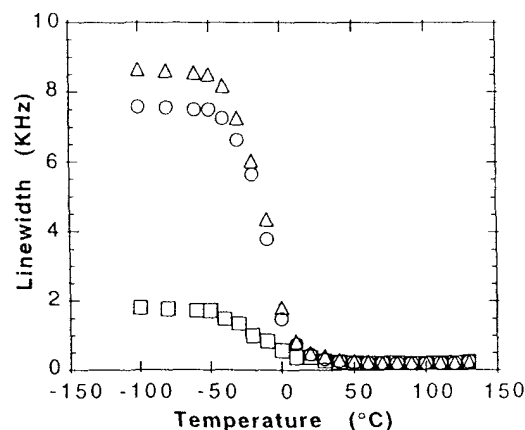


Figure 1: Temperature dependence of the ^7Li central transition linewidth in PPO- LiBF_4 ($n=8$). (Δ) Undecoupled linewidth, (O) linewidth with only ^{19}F decoupling and (\square) linewidth with only ^1H decoupling.

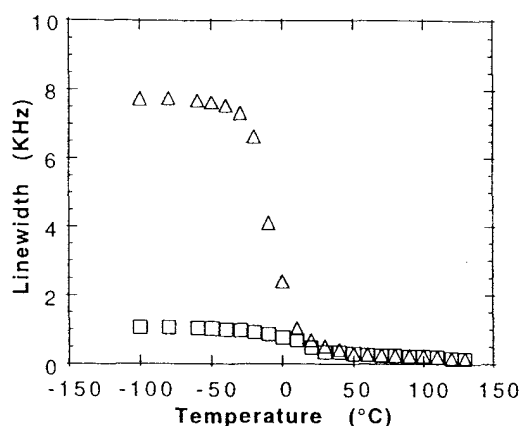


Figure 2: Temperature dependence of the ${}^7\text{Li}$ central transition linewidth in $\text{PPO-LiClO}_4(n=8)$. (Δ) Undecoupled linewidth and (\square) linewidth with only ${}^1\text{H}$ decoupling.

Both figures show that all contributions to the linewidth collapse at the glass transition temperature ($\sim -15^\circ\text{C}$). Since even the proton decoupled linewidth changes at this temperature one is forced to conclude that the ion and the counterion motion are controlled by the polymer segmental motion.

An additional reduction in the ${}^7\text{Li}$ linewidth at higher temperatures ($\sim 115^\circ\text{C}$) can be observed in figure 3, for the $\text{PPO-LiClO}_4(n=8)$.

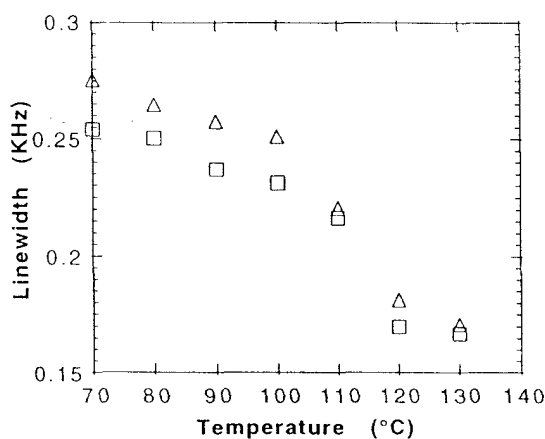


Figure 3: Detail of the high temperature region of figure 2 showing the additional narrowing in the ${}^7\text{Li}$ central transition linewidth in $\text{PPO-LiClO}_4(n=8)$ around 115°C . (Δ) Undecoupled linewidth and (\square) linewidth with only ${}^1\text{H}$ decoupling.

This extra narrowing could be attributed to the unbounded motion of Li^+ ions through a translational diffusion process [3]. In other polymeric electrolytes this extra narrowing in the linewidth is accompanied by an enhancement of the conductivity [3,4].

The linewidth data obtained at the lowest temperature attainable in our equipment ($\sim -100^\circ\text{C}$), under different decoupling conditions, allows to extract information on the rigid lattice structure which is summarized in table I. Special care has to be taken in the interpretation of the results shown in this table, because some motion might still be present at this temperature [1], and a residual second order quadrupolar enlargement might be broadening the ${}^7\text{Li}$ central transition linewidth, since we are using a magnetic field of only 2T.

Table I: Information about the ${}^7\text{Li}$ spectra under different decoupling conditions

	$\text{PPO}_8\text{LiBF}_4$	$\text{PPO}_8\text{LiClO}_4$
FWHM(KHz) ^(a)	8.66	7.70
(Without DEC)		
FWHM(KHz)	7.60	---
(${}^{19}\text{F}$ DEC)		
FWHM(KHz)	1.81	1.10
(${}^1\text{H}$ DEC)		
$\Delta\nu$ (Li-Li) ^(b) (KHz)	0.75	1.10
$\Delta\nu$ (Li-F) (KHz)	1.06	---
$\Delta\nu$ (Li-H) (KHz)	6.85	6.60

(a) FWHM - full width at half maximum, (b) $\Delta\nu$ - individual contribution to the dipolar linewidth.

Acknowledgments

This work was supported by the Brazilian agencies: FAPESP, FINEP, CNPq, PADCT and CAPES.

References

1. J.P. Donoso, T.J. Bonagamba, H. Panepucci, L.N. Oliveira, W. Gorecki, C. Berthier and M. Armand, *J. Chem. Phys.*, 98, 10026 (1993).
2. S. Panero, B. Scrosati and S.G. Greenbaum, *Electrochim. Acta*, 37, 1533 (1992).
3. S. Gupta, K. Shahi, N. Binesh, and S.V. Bhat, *Solid State Ionics*, 67, 97 (1993).
4. K. Dahmouch, M. Atik, N.C. Mello, T.J. Bonagamba, H. Panepucci, M. Aegerter, and P. Judenstein, *J. Sol. Gel. Sci. Technol.* (to be published).

^7Li NMR investigation of the Poly (ethylene glycol-400) distereate- LiClO_4 complex

T.J. Bonagamba, M.V. Giotto, H. Panepucci, A.L. de Oliveira†, and C.L. Sangiorge*

Instituto de Física de São Carlos, Universidade de São Paulo
Caixa Postal 369, CEP 13560-970 - São Carlos, São Paulo, Brasil

†Departamento de Física, ICEX, UFMG, Belo Horizonte, MG, Brasil

*Departamento de Química, CEFET, UFMG, Belo Horizonte, MG, Brasil

Introduction

Poly (ethylene glycol-400) distereate (PEGD) structure consists of a non-polar section associated with hydrocarbon chains, that have a fairly rigid structure, and a much more mobile phase composed of the polar ethylene oxide segments. It has the consistency of a soft wax at room temperature and melts to a viscous liquid around 35°C . The polar ethylene oxide segments can dissolve salts like LiClO_4 . NMR of the complexed Li^+ ion can give important structural and dynamical information about the resulting ionic conducting polymer. Since the electric conductivity and liquid viscosity depend strongly on the O/Li ratio, n [1], we studied the ^7Li NMR spectrum for different values of this ratio.

Material and methods

For the preparation of the samples we have used commercial poly (ethylene glycol-400) distereate (PEGD) and lithium perchlorate, both from Merck Chemicals. Appropriate amounts of polymer and salt were used to obtain the desired O/Li ratio. The complexes were obtained by direct salt dissolution at 80°C in PEGD[1].

The NMR spectrum of the ^7Li were recorded between -80°C to 90°C at 32.9MHz for samples having oxygen to lithium ratios, from 5 to 50, using a TECMAG LIBRA system and a double resonance Doty probe. The spectrum consists of the central transition ($-1/2 \leftrightarrow +1/2$) and in some cases also shows the typical quadrupolar powder spectrum associated to the satellite transitions ($-3/2 \leftrightarrow -1/2$ and $+1/2 \leftrightarrow +3/2$). The central transition linewidths were measured with and without ^1H decoupling from the Fourier transform of the Free Induction Decays [2,3]. Full widths at half maximum of the central transitions were

obtained in both cases by fitting the lineshape with a lorentzian function. Special care was taken to avoid the sample heating due to radiofrequency irradiation by using long repetition time pulse sequences and a small number of scans in the signal averaging process.

Results

At the lower temperatures the ^7Li spectra present a typical powder quadrupole pattern, as shown in figure 1.

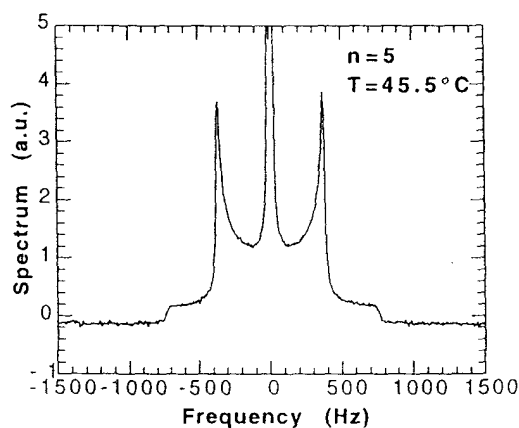


Figure 1: ^7Li spectrum showing the typical powder quadrupole pattern.

An interesting feature presented by the spectra is the fact that, for n less or equal to 9, the quadrupole powder structure is still observed even above the melting temperature. The satellite splitting, that has a low temperature average value of 1270 Hz for all n , suffers an abrupt reduction to 850 Hz at the melting point, as shown in figure 2. This reduced satellite splitting remains visible up to a higher temperature that depends on the particular value of n . Changes in the ^7Li central transition linewidth occur around -20°C , 35°C and 70°C for most samples, this behaviour is shown in figure 3 for $n = 5$.

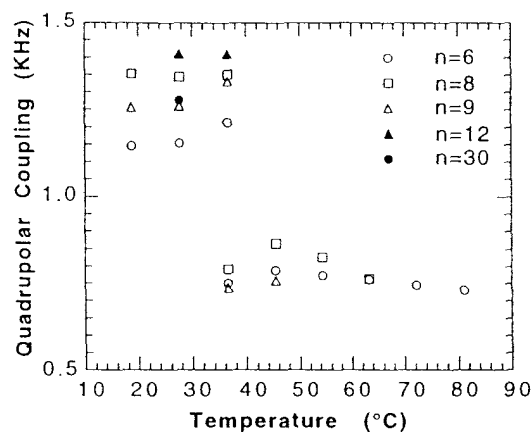


Figure 2: Quadrupolar coupling as a function of the temperature for different n .

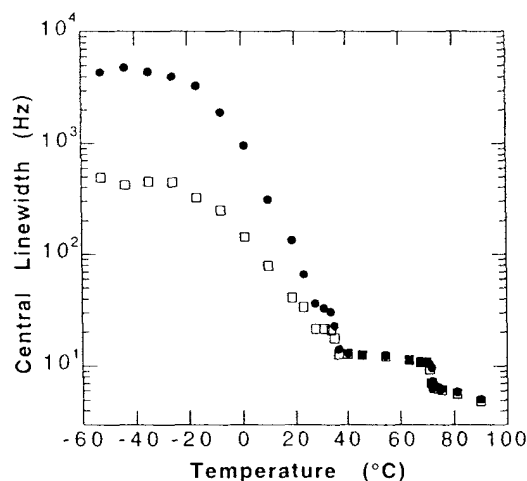


Figure 3: Central transition linewidth as a function of the temperature for $n=5$ (\square) with and (\bullet) without ^1H decoupling.

Discussion

The results for the temperature dependence of the ^7Li central transition linewidth, with and without ^1H decoupling, show that all spin interactions start to collapse around -20°C . The initial slow transition is probably related to the glass transition temperature ($T_g \approx -20^\circ\text{C}$ for $n=5$). While the second reduction in the ^7Li central transition linewidth around 35°C is associated to the sample melting. The extra narrowing in the ^7Li central transition linewidth occurring around 70°C could be related to an unbounded motion of Li^+ through a diffusion process [4,5]. The ^7Li central

transition linewidth is mainly due to magnetic dipolar interactions of Li-Li, Li-H and a residual second order quadrupolar enlargement, since we are using a magnetic field of only 2T. Analyzing the central transition under the two different decoupling conditions at the lowest temperatures, we can estimate that the magnetic Li-H dipolar interaction accounts for 90% of the linewidth and Li-Li and second order quadrupolar interaction to the remaining 10%.

The fact that the sharp reduction in the quadrupolar coupling is observed at the same temperature known to be the melting point of the pure polymer, suggests that the fusion mechanism is responsible for it. This might be due either to some configurational change affecting the Li-O distances, or to the rapid onset of a restricted motion that partially averages the interaction. Furthermore, the presence of a residual interaction above 35°C , indicates that the reorientation frequency in this temperature range is very low compared with the quadrupolar coupling. This is consistent with the high viscosities exhibited by the polymer complexes at these temperatures. Furthermore, the temperature, above which the quadrupolar powder pattern is no longer visible in the spectra, increases with decreasing O/Li ratio, n , which is consistent with the observed behavior of the viscosity.

Acknowledgments

We thank J. P. Donoso for the suggestion of this work. This research was supported by the Brazilian agencies: FAPESP, FINEP, CNPq, PADCT and CAPES.

References

1. A.L. de Oliveira, O. de O. Damasceno, P.R. Silva, C.L. Sangiorge, M. Armand, and M. Kleitz, *Solid State Ionics*, **60**, 99 (1993).
2. J.P. Donoso, T.J. Bonagamba, H. Panepucci, L.N. Oliveira, W. Gorecki, C. Berthier and M. Armand, *J. Chem. Phys.*, **98**, 10026 (1993).
3. S. Panero, B. Scrosati, and S.G. Greenbaum, *Electrochim. Acta*, **37**, 1533 (1992).
4. S. Gupta, K. Shahi, N. Binesh, and S.V. Bhat, *Solid State Ionics*, **67**, 97 (1993).
5. K. Dahmouch, M. Atik, N.C. Mello, T.J. Bonagamba, H. Panepucci, M. Aegerter, and P. Judenstein, *J. Sol. Gel. Sci. Technol.* (to be published).

ELIMINATION OF LONGITUDINAL AND TRANSVERSE MULTIPLE QUANTUM ARTEFACTS IN 2D COSY NMR SPECTRA

G J Bowden, T H Heseltine, G E Ball [†]
and M J Prandolini ^{††}
School Of Physics, University Of New South Wales
NSW 2052, Australia

[†]School Of Chemistry, University Of New South Wales
NSW 2052, Australia

^{††}Department Of Physics
University College, Australian Defence Force Academy
ACT 2600, Australia

It has been known for some time that multiple quantum (MQ) artefacts can be introduced into 2D COSY spectra if the repetition time between successive COSY rf-pulse sequences is not long enough to allow the nuclei to relax back to equilibrium (2,3,4). There are two types of MQ-artefacts, namely T₁ (or type 1) artefacts arising from incomplete relaxation of longitudinal nuclear order and T₂ (or type 2) artefacts arising from incomplete relaxation of transverse nuclear order. In a recent paper (1), a new pulse sequence was presented, which can be used to strip 2D COSY spectra of all even order type I MQ-artefacts. This method, known as ELMA-COSY (Elimination of Longitudinal MQ-Artefacts) involves adding the data from two separate COSY experiments prior to performing a Fourier transformation in the f₁ and f₂ dimensions. The two ELMA-COSY pulse sequences, A and B are shown schematically below.

$$A: \sum_{n=0,1}^N \left\{ \{x \sim t_1(n) \sim x, x_d\} \sim t_{rep} \right\}$$

$$B: \sum_{n=0,1}^N \left\{ \{x \sim t_1(n) \sim \bar{x}, x_d\} \sim t_{rep} \right\}$$

where (i) $t_1(n) = t_1 + n\delta t_1$ (with δt_1 being the small time increment in the f₁ dimension), (ii) x and \bar{x} refer to ± 90 degree rotations about the x axis, respectively, (iii) x_d (\bar{x}_d) refers to the phase of x detection in the f₂ dimension, and (iv) t_{rep} is the repetition time between successive COSY pulse sequences.

In this paper, we present a new pulse sequence which can be used to strip 2D NMR data sets of all even order type I and type II MQ-artefacts, simultaneously. The sequence, dubbed EMA-COSY, holds for a completely general Hamiltonian. To achieve elimination of both type I and type II MQ-artefacts, it is necessary to add the results from four separate COSY pulse sequences, prior to a 2D Fourier transformation.

The four EMA-COSY pulse sequences, A, B, C and D are shown below:

$$A: \sum_{n=0,2}^N \left\{ \{x \sim t_1(n) \sim x, x_d\} \sim t_{rep} \sim \{x \sim t_1(n+1) \sim x, x_d\} \sim t_{rep} \right\}$$

$$B: \sum_{n=0,2}^N \left\{ \{\bar{x} \sim t_1(n) \sim x, \bar{x}_d\} \sim t_{rep} \sim \{x \sim t_1(n+1) \sim x, x_d\} \sim t_{rep} \right\}$$

$$C: \sum_{n=0,2}^N \left\{ \{x \sim t_1(n) \sim x, x_d\} \sim t_{rep} \sim \{\bar{x} \sim t_1(n+1) \sim x, \bar{x}_d\} \sim t_{rep} \right\}$$

$$D: \sum_{n=0,2}^N \left\{ \{\bar{x} \sim t_1(n) \sim x, \bar{x}_d\} \sim t_{rep} \sim \{x \sim t_1(n+1) \sim x, x_d\} \sim t_{rep} \right\}$$

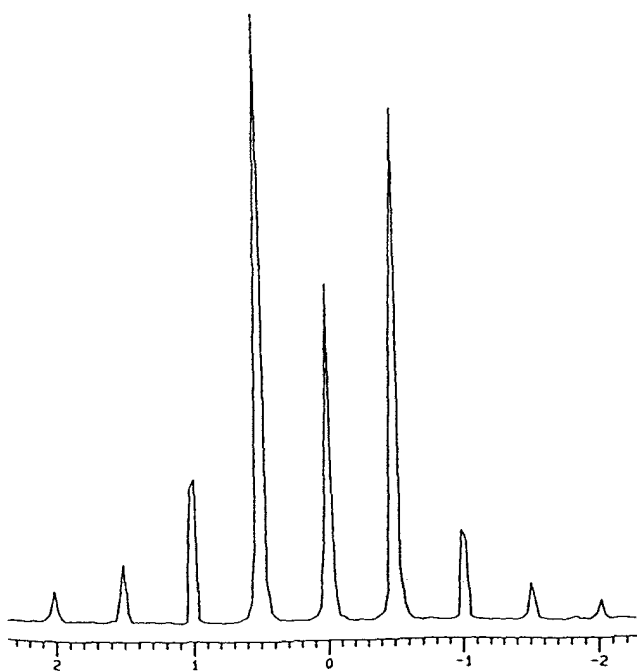
Note that unlike ELMA-COSY, the basic repeat unit now consists of two consecutive COSY rf-pulse sequences. Also within the EMA-COSY experiments B and C, the receiver phase is incremented by 180° from one COSY rf-pulse sequence to the next.

Using a compact matrix description of the pulse sequences, it is possible to show that unwanted modulation of either type I or type II is not passed between the first two COSY pulse sequences in either A+B or C+D sequences. Likewise, information is not passed between the second and third COSY pulse sequences in either A+C or B+D. For the third and fourth sequences, cancellation occurs between A+B and C+D thus completing the cycle. Consequently, if the four separate data sets are added together prior to Fourier transformation, unwanted modulation, in both the transverse and longitudinal sense, is not passed between successive COSY pulse sequences. This process removes all even order MQ-artefacts. However, triple (or in general, odd order) quantum

artefacts arising from information carried through three successive COSY pulse sequences are not suppressed by this procedure.

The EMA-COSY sequence was checked experimentally on a Bruker DMX 500 spectrometer. Measurements were made on the residual water signal of a sample of D₂O lightly doped with copper sulphate at 300K. Eight dummy scans were performed at the start of each series with one scan for each COSY pulse sequence; 256 data points were collected in the t_1 domain. The transverse and longitudinal relaxation times were measured using the CPMG sequence and inversion recovery and found to be $0.71s(T_2)$ and $1.01s(T_1)$, respectively. A repetition time of 300ms was used to ensure that both types of artefacts were present. Unfortunately, our spectrometer could not increment the receiver phases as required by sequences B and C. So all signals were detected with the same phase x_d and phase incrementation was subsequently accomplished computationally. The results, shown in figures 1 and 2, demonstrate a clear suppression of even order artefacts although a small amount of artefact signal does survive. We believe that the small amount of $\Delta m = \pm 2$ signal is due to (i) small drifts in the stability of the spectrometer, between the four separate A, B, C and D runs, and (ii) absence of phase cycling such as CYCLOPS.

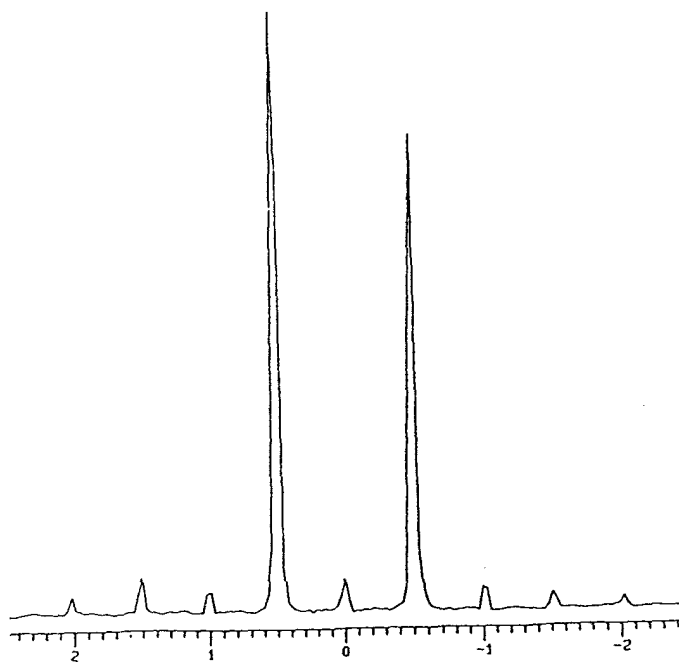
Figure 1.
Average Spectrum for COSY expts A, B, C and D



References

- [1] G.J. Bowden and M.J. Prandolini, *J.Mag.Reson. Series A* **107**, 32 (1994).
- [2] N. Murali and A. Kumar, *Chem. Phys. Lett.* **128**, 58 (1986).
- [3] S. Schäublin, A. Höhener, and R.R Ernst, *J.Mag.Reson.* **13**, 196 (1974).
- [4] C.J. Turner and S.L Patt, *J.Mag.Reson.* **85**, 492 (1989).

Figure 2.
Slice for A+B+C+D COSY resultant spectrum showing artefact suppression.



Application of Adaptive Simulated Annealing to Optimization of Transverse Gradient Coils with Concentric Return Paths

M.L. Buszko, M.F. Kempka⁺, E.Szczesniak⁺, D.C. Wang, and E.R. Andrew⁺

Departments of Microbiology & Cell Science, and Physics⁺ and Radiology⁺
University of Florida, Gainesville, FL 32611

Introduction

Simulated Annealing (SA) (1) is a well-known and widely used method of finding the global minimum of a function. It has been applied with great success to problems in many diverse areas including manufacturing of integrated circuits, designing communication systems, finance, pattern recognition, and computing global conformational minima of proteins. In magnetic resonance, applications of SA include designing magnetic field gradient coils (2), optimizing monochromatic (3) and band-selective radiofrequency pulses (4), and parametrically estimating time-domain signals (5). The underlying algorithm of SA may be described as being analogous to the thermodynamic process of slow cooling (annealing) of melts - new microscopic configurations of the system are being adopted with a probability given by the Boltzmann distribution function,

$$\text{Probability} \sim \exp(-(\text{energy change})/\text{temperature}).$$

Slow cooling results in the system finding the lowest-energy state. The system being annealed can temporarily adopt those configurations that correspond to higher-energy states. In actual systems being optimized, the energy change is replaced by an error function (*vide infra*). The error function is minimized by an iterative process of a) rearranging the system, b) evaluating the resulting error function and either accepting or denying the rearrangement, and c) lowering the temperature. The sequence of temperatures during the annealing process is called the annealing schedule.

One of the practical and most powerful implementations of the SA algorithm is Adaptive Simulated Annealing (ASA) (6). For ASA, the implemented rate of temperature changes is very fast - the temperature decreases exponentially in annealing time. To prevent being trapped in a local minimum, the program can periodically reanneal the system, i.e. the temperatures can be raised. Properly executed, the program ensures coarse global searching as well as fine and quick convergence in the final phases. Examples of applications of the ASA program include combat analysis, finance, and neuroscience.

The source code of the program is presently available on the Internet free of charge.

The optimization of magnetic-field gradient (MFG) coils remains one of the fundamental problems in designing magnetic resonance imaging systems. Coils of high efficiency, large volume of linear gradient, and low inductance are being sought. Particularly stringent requirements are imposed on coils designed for functional brain imaging (7) and microimaging of solid samples (8). Recently introduced coils with concentric return paths (9-12) present an interesting and promising alternative to classical transverse "Golay" coils that are currently in widespread use. They feature building blocks in which return paths are arranged as coaxial and co-planar arcs wound outside the primary arcs. The first practical realization of the idea of concentric return paths was described by Brey, Dougherty and Mareci (10) who demonstrated a numerically optimized coil composed of 10 equidistant building blocks with distributed currents. While featuring a relatively large volume of linear gradient, their coil posed some manufacturing difficulties resulting from the large number of turns required for some blocks. The alternative approach by Andrew and Szczesniak (11) featured equi-current building blocks with distributed positions of the blocks along the longitudinal axis of the coils. A simple-to-manufacture coil with eight blocks was demonstrated.

To numerically optimize gradient coils, the error function being minimized is usually expressed in terms of gradient-coil properties (10):

$$E = k_1 * S(G_0 - G_j)^2 + k_2/G_0 + k_3 * L \dots$$

where G_0 is the gradient at the center of the coil, G_j is the gradient at the j -th point, L is the inductance, and k 's are adjustable weighing factors. In our calculations, only the first term (i.e. gradient linearity) was included. To calculate G_j , Biot-Savart equation was solved for wire arrangement and distribution of the building blocks.

Results and discussion

Optimization was performed for a family of coils with 8-16 building blocks carrying equal

current. The radius of the inner arcs and the half-length of the coils were assumed to be unity. All coils were optimized with lower and upper limits on positions of the blocks equal to 0.01 and 1.0 respectively, with starting positions being 0.5 for all blocks. Number of points at which gradients were evaluated was selected to be 65 in one octant of the volume of interest. Such value was a compromise between accuracy of representation and computational time required. The time was 3.5 hours on a IBM's SP2 machine for the 8-block coil, increasing sharply for coils with larger number of blocks.

For the 8-block coil, the optimization procedure resulted in the distribution of blocks along the longitudinal axis (0.143, 0.428, 0.784, and 1.0) virtually identical to that given by Andrew and Szczesniak (11). For the 10-block coil, the optimized positions were 0.12, 0.37, 0.6, 1.0, and 1.0. For coils with larger number of blocks, the optimization resulted in "clustering" of positions of the two or three outer-most blocks, a situation equivalent to increasing current in a single block. Figure 1 presents the contours of constant MFG for the 10-block coil. The contours (in the xz plane) are plotted up to 45 % deviation from the value of the gradient at the center of the coil, at 5 % intervals.

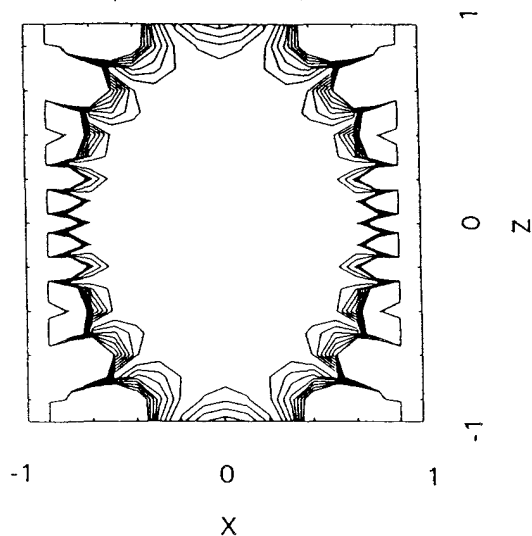


Fig. 1. Contours of constant magnetic field gradient for the 10-block coil in the xz plane.

The final value of the error function, if computed over the same set of points, can be used for comparison of different coils. This value is five times smaller for the 10-block coil than for the 8-block coil, indicating a better overall quality of the 10-block coil. Coils with larger number of blocks, while not providing smaller final value of the error function, do provide larger gradient strength.

Outer radius of individual building blocks is a variable that can also be utilized in optimization of

MFG coils with concentric return paths. The ASA program was adapted to such optimization. In our calculations, the outer radii were allowed to be adjusted from 1.2 to 1.7 of the inner radius. As with the previous case, a distribution of building blocks was obtained along the longitudinal axis. The analysis reveals that the final values of the error function are smaller for coils with optimized radii than for the fixed ones. These coils provide greater gradient uniformity than the coils where only positions of the blocks are optimized. The uniformity, combined with greater gradient strength provided by coils with greater number of blocks, may be important factors in implementing such coils in new higher-precision and higher-resolution imaging and spectroscopic applications.

Acknowledgments

The authors would like to thank Dr. Lester Ingber for his computer code. The use of the following computing facilities of the University of Florida is greatly acknowledged: Center for Structural Biology, Parallel Research Lab, IFAS Computer Lab, and North-East Regional Data Center (award rci082).

References:

1. a) S. Kirkpatrick, C. D. Gelatt Jr., and M. P. Vecchi, *Science* **220**, 671 (1983). b) P. J. M. van Laarhoven and E. H. L. Aarts, "Simulated Annealing: Theory and Applications", Reidel, Dordrecht, 1987.
2. D. M. Dodrell and S. J. Crozier, *J. Magn. Reson.* **A103**, 354 (1993).
3. J. Shen and L.E. Lerner, *J. Magn. Reson.* **A114**, 116 (1995).
4. H. Geen and R. Freeman, *J. Magn. Reson.* **93**, 93 (1991).
5. F. S. DiGennaro and D. Cowburn, *J. Magn. Reson.* **96**, 582 (1992).
6. L. Ingber, Lester Ingber Research, P.O.Box 857, McLean, VA, 1993.
7. a) A.M. Abduljalil, A.H. Alertan, and P.M.L. Robitaille, *Magn. Reson. in Medicine* **31**, 450 (1994). b) S. Crozier, L.K. Forbes, and D.M. Dodrell, *J. Magn. Reson.* **A107**, 126 (1994).
8. M.L. Buszko and G.E. Maciel, *J. Magn. Reson.* **A107**, 151 (1994).
9. G. Frese and E. Stetter, US Patent 5,198,765, March 30, 1993.
10. W.W. Brey, J.L. Dougherty, and T.H. Mareci, *Abstracts SMRM, 12th Annual Meeting*, 1038 (1993).
11. E.R. Andrew and E. Szczesniak, *Magn. Reson. Imag.* (in press).
12. P. Mansfield, B. L. W. Chapman, R. Bowtell, P. Glover, R. Coxon, and P. R. Harvey, *Magn. Reson. in Medicine* **33**, 276 (1995).

NMR and the Information Superhighway: What's on the Net?

Marian Lech Buszko

University of Florida, Department of Microbiology and Cell Science
Gainesville, FL 32611, USA

In recent years, an unprecedented shift in internetworking paradigm has been observed - the shift is from the centralized model of networking, exemplified by the mainframe systems, to an open, decentralized, client-server architecture. On decentralized systems, any of the internetworked computers can provide services or content, as opposed to the mainframe system. At least 6.6 million computers have been interlinked world-wide (as of July, 1995), and it is estimated that 2.5 million actually do provide various services (1). This vast network of computers is called the Internet. It can be viewed as a firm basis for future deployment of the Information Superhighway, spanning computer, telephone, cable, and television networks.

Numerous information services have been developed to make use of the open architecture of the Internet. The major tools include electronic mail (e-mail), Gopher, File Transfer Protocol (ftp), Usenet, and World-Wide Web (WWW) (2). With recent commercialization of the Internet and development of easy-to-use browsers, e.g. Mosaic and Netscape, the majority of the Internet traffic is currently due to the World-Wide Web.

In decentralized systems, each individual site is responsible for its own content, and anyone can make any kind of information available. Magnetic Resonance is a ubiquitous tool of chemistry, structural biology, and many other scientific disciplines. Its presence on the Internet dates back to the early 90's when dedicated mailing lists (Bruker Users Mail, VarNet, etc.) and subsequently, Usenet newsgroups (Bionet.structural-nmr, Sci.techn.magnetic-reson), had become popular among practitioners of NMR. Later, in the early 1993, the first WWW NMR Information Server was launched at the University of Florida (3). It was followed by the recent deployment of MAGNET, the WWW NMR Guide, at the University of Akron (<http://atlas.chemistry.uakron.edu:8080/cdept.docs/nmr/sites.html>).

Originally, the NMR Information Server was deployed as a Gopher server. It incorporated existing, scattered sources of information pertinent to Magnetic Resonance onto a single page. The sources included the gopher server of the NMR Facility at Madison,

Wisconsin, the NMR software archives maintained at the University of California, the gopher archives of the Association of Managers of Magnetic Resonance Labs, and others (for current URL links to those resources, see reference 3). Although with limited support, the Gopher server is still in service at the original site (gopher://micro.ifas.ufl.edu).

The NMR Information Server was established for the world-wide community of those who are interested in magnetic resonance. Each time the server is accessed, a log file is updated. Hundreds of connections are made every day, from all-over the world. The server provides a focal point and access to information pertinent to NMR, MRI, ESR, etc., as well as links to the sciences of physics, chemistry and biology. The following major categories were selected: NMR Journals, Facilities, Archives, Meetings, Jobs, Organizations, Software, Vendors, and Who's Who in Magnetic Resonance.

Numerous initiatives have been undertaken at the site of the NMR Information Server, for example the Internet Edition of Magnetic Resonance and the NMR Gallery. The Internet Edition of Magnetic Resonance is an experiment. Its hypertext formula allows one to access resources that are distributed across the Internet. However, we would like to open this forum for electronic publishing. Such publishing is increasingly used as a powerful alternative to print media. The NMR Gallery can be a perpetual exhibit of photographs of people, events, hardware, etc. It can also accommodate video and audio files. The success of such initiatives depends largely on willingness to participate and share information.

The future of NMR on the Information Superhighway is likely to bring interactive, hypermedia access to NMR lectures, events, and perhaps even NMR experiments.

References:

1. C. Bournellis, *Internet World*, Nov. 1995, p.47.
2. Ed Krol, *The Whole Internet Users' Guide & Catalog*, 2nd edition, O'Reilly & Associates, 1994.
3. M. Buszko, NMR Information Server, available on the Internet at URL <http://micro.ifas.ufl.edu>.

Mechanochemical Reduction of Haematite – The Effect of NaCl Electrolyte

S.J. Campbell[#], W.A. Kaczmarek^{}, E. Wu[#] and G-M. Wang[#]*

[#] School of Physics, University College, University of New South Wales,
Australian Defence Force Academy, Canberra ACT 2600, Australia.

^{*} Research School of Physical Sciences and Engineering, Australian National
University, Canberra ACT 0200, Australia.

Abstract

The effects of milling α -Fe₂O₃ in a range of NaCl solutions (0.1 M, 0.5 M, 1.0 M and 2.0 M) as investigated by x-ray diffraction and Mössbauer effect spectroscopy are reported. Similar to the effects of milling in water, the 0.1 M solution exhibits complete transformation to off stoichiometric Fe_{3- ν} O₄ with vacancy concentration $\nu \sim 0.1 - 0.2$. Higher NaCl molar concentrations are found to retard the transformation with only $\sim 40\%$ transformation to Fe_{3- ν} O₄ occurring at 1.0 M NaCl.

I. Introduction

Ball milling and related methods are long standing techniques in metallurgy which are used primarily for particle size reduction with a view to, for example, sintering or further materials processing. The past two or three decades have seen increasing application of mechanical alloying and mechanochemical treatments as methods of preparing new phases and materials. Indeed materials prepared by mechanochemical synthesis often exhibit a combination of useful physical properties compared with materials prepared by conventional means (see reference (1) for a recent review of the fundamentals of mechanical alloying). Given the continuing importance of iron oxides in a number of fields of magnetic materials technology such as magnetic recording and magnetic field devices (2), ball milling techniques have been applied increasingly in the study of iron oxides with a view to refining and improving their structural and magnetic properties (see eg 3,4).

Of particular interest is the transformation from haematite, α -Fe₂O₃, to magnetite, Fe₃O₄, which occurs on milling. Matteazzi and Le Cäer (3) synthesized nanocrystalline Fe₃O₄ on dry-milling α -Fe₂O₃ in nitrogen whereas Kaczmarek and Ninham (5) demonstrated that complete transformation of α -Fe₂O₃ to Fe₃O₄ could be obtained on wet-milling α -Fe₂O₃ in vacuum. This reduction transformation is considered to occur mainly as a result of the breaking of the oxygen bonds in oxide layers, leading to release of oxygen.

Graig et al (6) have recently reported a comprehensive investigation of the effects of a series of common electrolytes on the rate of bubble coalescence in water. Whereas little or no change in bubble coalescence was observed in 14 of the salts, NaCl, in common with 19 others, exhibited a marked dependence in the fraction of bubble coalescence on the molar concentration. For example NaCl exhibited reduced coalescence (only $\sim 5\%$) above ~ 0.078 M, rising to 100%, below ~ 0.01 M NaCl. As part of an exploratory investigation of the influence of different electrolytes on the transformation of haematite to magnetite on milling in water, we have investigated the

effects of wet-milling α -Fe₂O₃ in NaCl solution over the range 0.1–2.0 M. Here we present the main structural and magnetic effects resulting from wet-milling haematite in NaCl electrolyte as measured by x-ray diffraction and Mössbauer effect spectroscopy.

II. Experimental

The samples were wet milled in NaCl solutions 0.1 M, 0.5 M, 1.0 M and 2.0 M under the general conditions described previously (5). Briefly, the ~ 8 g charges of α -Fe₂O₃ (99.99% purity, particle size ~ 20 – 70 μ m, Koch-Light Laboratories) were milled in a vertical stainless steel mill with four hardened stainless steel balls (each of mass ~ 66 g) containing ~ 5 ml solution. The mill was evacuated to $\sim 10^2$ – 10^3 Pa and the material milled for a period of 125 h in the low energy mode found to be most appropriate for transforming haematite to magnetite (5). The x-ray diffraction patterns were obtained using a Phillips diffractometer with CoK α radiation, and the Mössbauer effect measurements were carried out on a standard spectrometer. The spectrometer was calibrated using a standard α -Fe foil and isomer shift values are quoted relative to the centre of the α -Fe spectrum.

III. Results and Discussion

The x-ray diffraction patterns for α -Fe₂O₃ milled in 0.1 M, 0.5 M, 1.0 M and 2.0 M NaCl solutions are shown in Figure 1. Also shown in Figure 1 are the patterns for the α -Fe₂O₃ starting material and a haematite sample milled in water (0.0 M NaCl) for 144 h as a reference material for comparison with the haematite milled in NaCl electrolyte. As expected the sample milled in water exhibits the diffraction pattern characteristic of the spinel structure Fe₃O₄, consistent with the reduction transformation reported previously (5). Similar behaviour is observed for the 0.1 M sample although both the α -Fe₂O₃ and Fe₃O₄ phases are found to be present in the patterns of the 1.0 M and 2.0 M samples. Also evident in the patterns of the strongest NaCl molar concentration is the presence of NaCl in the dried powders.

The room temperature Mössbauer spectra of the milled samples (Figure 2) show good agreement with the x-ray data. As observed previously (7), the sample milled in water is well described in terms of the well established hyperfine interaction parameters of Fe₃O₄ (e.g. 8) with two subspectral sextets of magnetic hyperfine field values $\mu_0 H_{hf}^A \sim 48.9$ T (fractional area $\sim 50.4\%$) and $\mu_0 H_{hf}^B \sim 45.5$ T (area $\sim 49.6\%$), representing the tetrahedral Fe³⁺ A site and the octahedral Fe²⁺ / Fe³⁺ B site respectively. The spectrum for the 0.1 M sample is also well described

by 2 sextets characteristic of Fe_3O_4 although, in agreement with the x ray pattern, subspectral contributions due to the characteristic sextet $\mu_0 H_{\text{hf}} \sim 51.5 \text{ T}$ of $\alpha\text{-Fe}_2\text{O}_3$ are evident in the 1.0 M sample ($\sim 53.4\%$ $\alpha\text{-Fe}_2\text{O}_3$) and the 2.0 M sample ($\sim 30.42\%$ $\alpha\text{-Fe}_2\text{O}_3$). The optimum fit to the spectrum for the sample milled in 0.5 M (Figure 2) is obtained with a subspectral fraction of $\sim 7\%$ of $\alpha\text{-Fe}_2\text{O}_3$ present. This is consistent with the x-ray pattern which also reveals traces of $\alpha\text{-Fe}_2\text{O}_3$ present in this sample (Figure 1).

The spectra for the 1.0 M and 2.0 M samples show clear evidence for an additional component present in these milled materials. The spectra of both samples exhibit a central resonance absorption which can be characterised by a doublet of quadrupole splitting $QS \sim 0.8 \text{ mm s}^{-1}$ and isomer shift $IS \sim 0.3 \text{ mm s}^{-1}$ and of subspectral fractional areas $\sim 5\%$ and $\sim 10\%$ for the 1.0 M and 2.0 M samples respectively. Given the corrosive nature of such concentrated NaCl solutions, these components may well be associated with the formation of iron oxide Fe_{1-x}O which has paramagnetic hyperfine interaction parameters

generally similar to those observed in Figure 2 (see reference (9) for a review of wüstite Fe_{1-x}O). The Fe_{1-x}O is likely to form as a result of the enhanced wear on the balls and mill resulting from milling in the concentrated NaCl solution. A further possibility, however, is that the central absorption feature is due to superparamagnetic relaxation resulting from fine $\alpha\text{-Fe}_2\text{O}_3$ particles which are known to exhibit similar hyperfine parameters (10). Related micrograph studies of the present 1.0 M and 2.0 M milled samples indicate particle sizes in the range $\sim 0.2 - 0.5 \mu\text{m}$ (11) although analysis of the broadening of the x-ray diffraction lines using the Scherrer formula indicate minimum grain sizes of $\sim 35 \text{ nm}$ and 45 nm respectively. These fine grain sizes suggest that the relatively large particles observed in the micrographs are due in part to the clumping together of fine particles in the milling process.

The main conclusion from the spectral analysis, however, is that the reduction transformation of $\alpha\text{-Fe}_2\text{O}_3$ to Fe_3O_4 is retarded significantly on wet milling in NaCl solution $\geq 0.5 \text{ M}$. The spectra for the 0.5 M, 1.0 M and 2.0 M solutions exhibit subspectral $\alpha\text{-Fe}_2\text{O}_3$ fractions

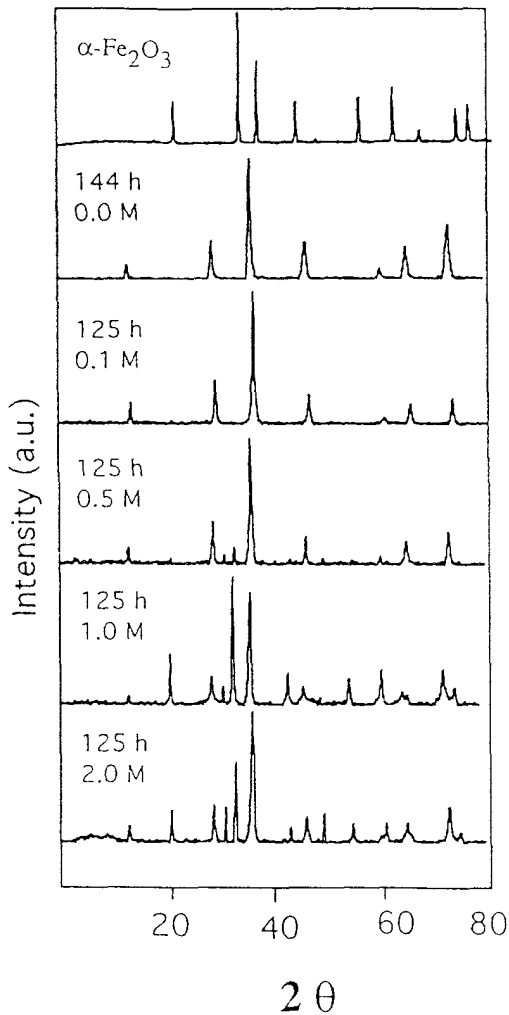


Fig.1 X-ray diffraction patterns ($\text{CoK}\alpha$ radiation) of $\alpha\text{-Fe}_2\text{O}_3$ milled in the molar NaCl solutions indicated for 125 h. The pattern for the $\alpha\text{-Fe}_2\text{O}_3$ starting material and haematite milled in water (0.0 M) for 144 h are shown for comparison.

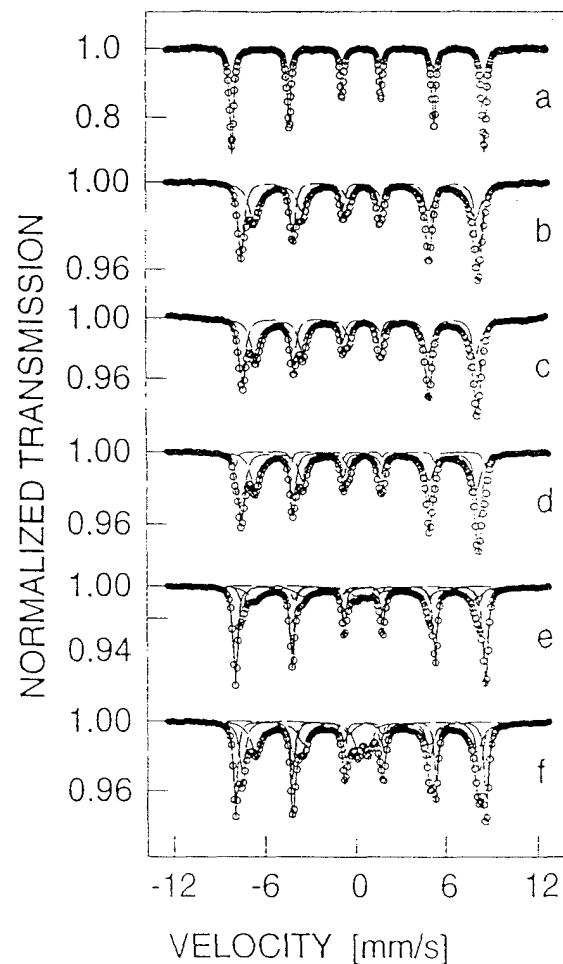


Fig.2 Room temperature Mössbauer spectra for $\alpha\text{-Fe}_2\text{O}_3$ wet milled in the presence of NaCl solution: (a) Fe_2O_3 starting material, (b) 0.0 M 144 h, (c) 0.1 M 125 h, (d) 0.5 M 125 h, (e) 1.0 M 125 h and (f) 2.0 M 125 h. The fits to the spectra are discussed in the text.

of ~ 7 %, ~ 53 % and ~ 30 % respectively, indicating clearly that the reaction rate of transformation to Fe₃O₄ has decreased significantly, with the lowest reaction rate occurring around ~ 1.0 M NaCl solution.

The relative areas of the sextets associated with the octahedral B and tetrahedral A sites, normally around F_B:F_A ~ 2:1 for stoichiometric Fe₃O₄, are around F_B:F_A ~ 1:1 in the present milled samples. This spectral behaviour is consistent with the occurrence of vacancies which are distributed predominantly over the octahedral sites (e.g. 12, 13). Further evidence of vacancies occurring on the octahedral sites is given by the increased linewidth exhibited by the sextet describing octahedral site B (FWHM $\Gamma^B \sim 0.8 - 1 \text{ mm s}^{-1}$) compared with the linewidth for the tetrahedral site, $\Gamma^A \sim 0.5 \text{ mm s}^{-1}$. This line broadening indicates the increased relaxation time of the electron hopping in the Fe²⁺/Fe³⁺ octahedral site which occurs in off stoichiometric Fe_{3- ν} O₄ of vacancy concentration ν compared with that obtained in stoichiometric Fe₃O₄ (13,14). The increasing vacancy concentration with milling time is likely to contribute to the fracture of the oxide bonds in the oxide layers on milling, leading to the reduction transformation to Fe_{3- ν} O₄ on release of the oxygen. Further information on the spectral and structural analysis, particularly with regard to the behaviour of the hyperfine interaction parameters leading to detailed information on the vacancy concentration and site occupancies, will be presented elsewhere (11).

IV Conclusions

Wet milling of α - Fe₂O₃ in NaCl electrolyte has been found to retard the reaction rate of transformation to Fe₃O₄ compared with milling in water. More specifically, milling in NaCl solutions above the molar concentration ~ 0.078 M reported recently for reduced bubble coalescence in water (6), shows similar results at 0.1 M to those obtained in water with ~ 100 % transformation to Fe_{3- ν} O₄. On the other hand higher molar concentrations lead to a reduced reaction rate with only ~ 40 % of the original α - Fe₂O₃ transforming to Fe_{3- ν} O₄ on milling in 1.0 M NaCl solution. The extended low energy milling for ~ 125 h leads to vacancy distributions, primarily in the octahedral

sites, with resultant off - stoichiometric Fe_{3- ν} O₄ and, on the basis of the present Mössbauer analysis and recent neutron diffraction studies (14), vacancy concentrations around $\nu \sim 0.1 - 0.2$.

Acknowledgments

GMW acknowledges the support of a University College Postgraduate Research Scholarship. SJC and WAK acknowledge the support of the ANU-UNSW Research Collaborative Scheme.

References

- ¹J.S. Benjamin, *Mater.Sci.Forum*, **88-90** (1992).
- ²Q.A. Pankhurst and R.J. Pollard, *J.Phys. Cond. Matter*, **5**, 8487 (1993).
- ³P. Matteazzi and G. Le Càer, *Mater.Sci.Eng.*, **A149**, 135 (1991). Y. Uehara, *Bull.Chem.Soc. Japan*, **48**, 3383 (1975).
- ⁴T. Kosmac and T.H. Courtney, *J.Mater.Res.*, **7**, 1519 (1992).
- ⁵W.A. Kaczmarek and B.W. Ninham, *IEEE Trans. Magn.*, **30**, 732 (1994).
- ⁶V.J. Craig, B.W. Ninham and R.M. Pashley, *J.Phys. Chem.* **97**, 10192, (1993).
- ⁷S.J. Campbell, W.A. Kaczmarek and G-M Wang, *Nanostructured Mater.*, **6**, 735 (1995).
- ⁸E. De Grave, R.M. Persoons, R.E. Vandenberghe and P.M.A. de Bakker, *Phys.Rev. B*, **47**, 5881 (1993).
- ⁹G.J.Long and F.Grandjean in *advances in Solid State Chemistry*, Vol.2 (JAI press Ltd, 1991) p187
- ¹⁰W.Kundig, H.Bömmel, G.Constabaris and R.H.Lindquist, *Phys. Rev.*, **142**, 327 (1966)
- ¹¹S.J.Campbell, W.A.Kaczmarek, G.M.Wang and B.W.Ninham (in preparation 1995).
- ¹²J.M.D. Coey, A.H. Morrish and G.A. Sawatzky, *J.Phys*, **32**, C1-271 (1971).
- ¹³H. Annersten and S.S. Hafner, *Z. Kristallogr., Bd* **137**, 321 (1973).
- ¹⁴M. Hofmann, S.J. Campbell and W.A. Kaczmarek, *Proc. of the European Powder Diffraction Conference*, Chester, UK, July 1995.

Powder ESR Spectra of Specific Alkyl Radicals: Selective ESR Observation of Specific Alkyl Radicals in γ -Irradiated cis-Decalin-d₁₈/Chloroalkane and Bromoalkane Systems at Cryogenic Temperatures.

Dominique Stienlet and Jan Ceulemans

*Department of Chemistry, K.U.Leuven
Celestijnenlaan 200-F, B-3001 Leuven, Belgium*

I. Introduction

A number of methods have been described in the literature for generating specific alkyl radicals in solution, allowing the recording of their isotropic ESR spectrum (1-4). None of these methods offers much promise for obtaining specific alkyl radicals in solid systems, however, because in rigid systems the radicals produced by photolysis are kept together by the surrounding molecules thus greatly increasing the probability of mutual reaction, and/or because reactants and reactive intermediates responsible for the formation of the alkyl radicals are immobilized in solid systems thus largely preventing them from reacting. The liquid phase spectra cannot be utilized to predict the shape and appearance of powder spectra of alkyl radicals in solid systems, either. In the liquid state, anisotropies of g and hyperfine coupling tensors are averaged out and very narrow ESR lines are observed. As a result of the averaging, however, the information on the anisotropic interactions in alkyl radicals is lost and liquid phase spectra cannot as a rule be utilized as a basis for simulating powder ESR spectra of alkyl radicals. There thus appears to be a real need for the development of an independent method for the selective formation of specific alkyl radicals in solid systems, which would allow the recording of their powder ESR spectrum.

II. Outline of the Method

The method outlined below offers a convenient and versatile technique for generating specific alkyl radicals, whose identity is fully determined by the choice of the haloalkane solute utilized. It consists in the γ -irradiation at 77 K of the appropriate chloro- or bromoalkane (5) at low concentration in solid cis-decalin-d₁₈ (perdeuterated decahydronaphthalene). In such systems, irradiation mainly leads to excitation and ionization of the decalin matrix. Alkyl radicals are formed by dissociative electron attachment to the chloro- or bromoalkane solute.



Excitation energy transfer, if occurring, also yields this radical, but radical formation and trapping as a result of this process is certainly very limited. Paramagnetic species associated with the chloro- or bromoalkane solute are restricted very strictly to the corresponding alkyl radicals because, due to the low ionization energy (9.40 eV) of cis-

decalin with respect to that of chloro- and bromoalkanes, no hole transfer to these compounds can take place. Chromatographic analyses, on the other hand, clearly demonstrate that the identity of the alkyl radicals is fully determined by the chloro- and bromoalkane solute and that no radical isomerization occurs (6).

The use of perdeuterated cis-decalin as matrix results in a very considerable contraction of the ESR spectrum of matrix radicals. This is illustrated in Figure 1, in which the ESR spectrum obtained after irradiation of neat cis-decalin-d₁₈ is shown. The spectrum simply consists of a broad unresolved absorption, which extends over about 75 G.

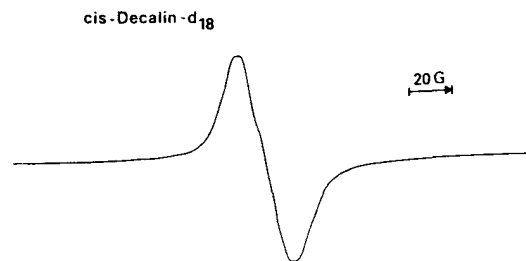


Figure 1: First-derivative ESR spectrum obtained after irradiation of neat cis-decalin-d₁₈.

This absorption can be attributed to deuterated decalyl radicals, the hyperfine structure becoming unresolved by the contraction resulting from deuteration. As a result of this contraction, a large part of the powder ESR spectrum of the specific alkyl radicals can be observed without interference from other paramagnetic absorptions in the lateral regions of the spectrum. Those lateral regions are sufficient for analyzing other spectra and identifying radicals in systems where the identity of the radicals formed is under investigation. This is illustrated in Figure 2, in which the spectrum obtained after irradiation of cis-decalin-d₁₈, containing 1 mol% 1-chloroheptane is shown. In addition to the central unresolved absorption, which is greatly distorted by spurious lines and by an additional underlying ESR absorption, a number of features are also observed in the more lateral region of the spectrum. Quite similar results are obtained by irradiation of 1-bromoheptane in cis-decalin-d₁₈. In view of the method employed, the lateral features can unambiguously be attributed to 1-heptyl radicals. Characteristic features in the ESR spectrum of 1-alkyl radicals are a double-humped curve situated at both sides of the spectrum and relatively

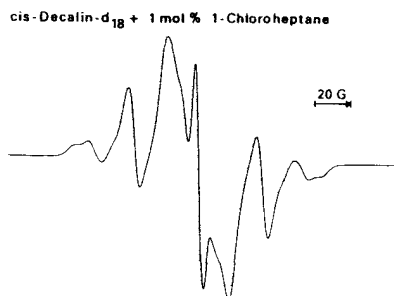


Figure 2: First-derivative ESR spectrum obtained after irradiation of cis-decalin- d_{18} containing 1 mol% 1-chloroheptane; ● indicates a background signal.

sharp intense hyperfine lines, which make the spectrum easily recognizable. Both features are very clearly discernible in the ESR spectrum shown in Figure 2. These features are predicted by theoretical calculations on the hyperfine interactions in the ESR spectrum of alkyl radicals (7). In such radicals one has both isotropic and anisotropic hyperfine interactions with the α -protons, but only an extensive isotropic interaction with the β -protons. When in 1-alkyl radicals the two α -protons are antiparallel, the hyperfine anisotropy largely cancels and relatively sharp intense hyperfine lines result. The double-humped curve is due to the outermost absorption, which is anisotropically broadened. Other, more centrally situated, anisotropically broadened transitions are as a rule less easily observable.

In secondary alkyl radicals, there is an odd number of α -hydrogens with no possibility of cancellation of the anisotropic hyperfine interaction. Consequently, all transitions are expected to be broad and this is what is observed experimentally. ESR spectra obtained after irradiation of 1 mol% 2-bromoheptane and 3-bromoheptane in cis-decalin- d_{18} are shown in Figures 3 and 4, respectively. The lateral region of these spectra differs drastically from that of the spectra obtained by irradiation of 1-chloroheptane and 1-bromoheptane in cis-decalin- d_{18} ,

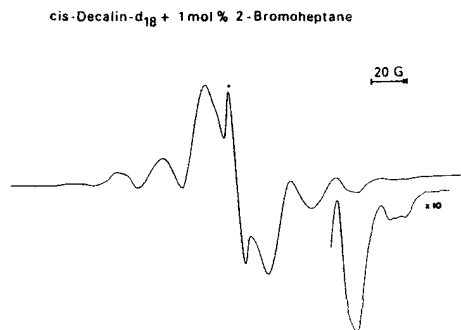


Figure 3: First-derivative ESR spectrum obtained after irradiation of cis-decalin- d_{18} containing 1 mol% 2-bromoheptane; ● indicates a background signal.

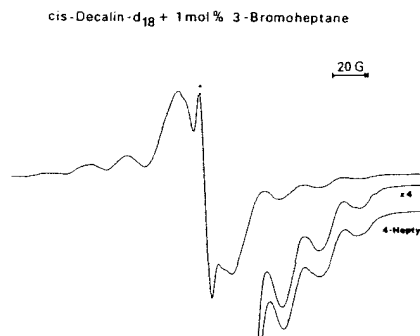


Figure 4: First-derivative ESR spectrum obtained after irradiation of cis-decalin- d_{18} containing 1 mol% 3-bromoheptane; ● indicates a background signal; the right lateral part of the ESR absorption obtained after irradiation of 4-bromoheptane in cis-decalin- d_{18} is also shown.

making it easy to differentiate chain-end *n*-alkyl radicals from other types of *n*-alkyl radicals. *n*-Alkyl radicals essentially can belong to three general types, viz. chain-end ($\text{CH}_2\text{-CH}_2\text{-CH}_2\text{-...}$), penultimate ($\text{CH}_3\text{-CH-CH}_2\text{-...}$) and internal ($\text{CH}_3\text{-CH}_2\text{-CH-...}$) radicals, which are characterized by different ESR spectra. The difference between ESR spectra of penultimate and internal radicals is not as pronounced as their difference from ESR spectra of chain-end radicals, but is still sufficient to differentiate between these two types of radicals. Interior *n*-alkyl radicals have a more contracted spectrum and the different ESR absorptions are less resolved.

III. Assessment of the Method

The main merit of the method described consists in the fact that it provides a general technique for generating specific alkyl radicals in solid systems. Though this may appear simple in principle, in practice it is far from trivial. As a matter of fact, the only alternative method for the generation of specific alkyl radicals in solid systems, which is described in the literature, appears to be the photolysis of iodoalkanes in argon matrices at 4 K (7,8). The primary, radical-generating event in this case is simple rupture of the C-I bond and abstraction reactions are prevented by use of the argon matrix. It has been reported, however, that even with this method paramagnetic species other than the expected alkyl radicals are observed under certain wavelength conditions. Also, attempts to observe secondary alkyl radicals by this method appear to have been unsuccessful. This is due to the fact that (i) ESR lines of such radicals are broad and consequently relatively weak as a result of anisotropic hyperfine interaction and (ii) the quantum yield for alkyl radical trapping is very low (10^{-3}), because of the cage effect. This cage effect prevents the separation of the alkyl radical from the iodine atom, thus promoting recombination and disproportionation.

IV. Acknowledgment

The authors thank the national fund for scientific research (NFWO) of Belgium for financial support.

V. References

- ¹A. G. Davies and B. P. Roberts, *Chem. Commun.* 699 (1969).
- ²A. Hudson and R. A. Jackson, *Chem. Commun.* 1323 (1969); A. Hudson and H. A. Hussain, *Mol. Phys.* **16**, 199 (1969); D. J. Edge and J. K. Kochi, *J. Am. Chem. Soc.* **94**, 7695 (1972); K. U. Ingold and J. C. Walton, *J. Am. Chem. Soc.* **104**, 616 (1982); K. U. Ingold, D. C. Nonhebel and J. C. Walton, *J. Phys. Chem.* **90**, 2859 (1986).
- ³J. N. Kirwan and B. P. Roberts, *J. Chem. Soc. Perkin Trans. 2* 539 (1989); P. Kaushal, P. L. H. Mok and B. P. Roberts, *J. Chem. Soc. Perkin Trans. 2* 1663 (1990).
- ⁴J. K. Kochi and P. J. Krusic, *J. Am. Chem. Soc.* **91**, 3940 (1969); A. L. J. Beckwith and R. O. C. Norman, *J. Chem. Soc. (B)* 400 (1969).
- ⁵D. Stienlet and J. Ceulemans, *J. Radioanal. Nucl. Chem.* **173**, 67 (1993).
- ⁶D. Stienlet, A. Vervloessem and J. Ceulemans, *J. Chromatogr.* **475**, 247 (1989).
- ⁷E. L. Cochran, F. J. Adrian and V. A. Bowers, *J. Chem. Phys.* **34**, 1161 (1961).
- ⁸F. J. Adrian, E. L. Cochran and V. A. Bowers, *J. Chem. Phys.* **59**, 3946 (1973); C. A. McDowell and K. Shimokoshi, *J. Chem. Phys.* **60**, 1619 (1974).

Alkane Aggregation and Proton Transfer from Alkane Radical Cations to Alkane Molecules in γ -Irradiated CCl_3F /Alkane Systems at Cryogenic Temperatures: a Summary of ESR Evidence

Geert Luyckx and Jan Ceulemans

Department of Chemistry, K.U. Leuven
Celestijnenlaan 200-F, B-3001 Leuven, Belgium

I. Introduction

The question whether hydrogen and/or proton transfer between higher alkanes and their cations widely takes place in condensed phases has long been an important unsolved problem. In the gas phase, hydrogen and proton transfer occurring in electron-irradiated methane was among the first ion-molecule reactions observed in mass spectrometers with elevated ion-source pressure (1). The reaction has been observed mass-spectrometrically only for the lower alkanes, however (2). Alkane radical cations have been studied by ESR spectroscopy in various matrices at cryogenic temperatures and thermal conversion to alkyl radicals has been observed in SF_6 and $\text{CCl}_2\text{FCF}_2\text{Cl}$ (3). Such studies do not clearly differentiate between ion-molecule reactions, unimolecular dissociation and neutralisation, however, nor do they provide conclusive evidence as to the identity of the reacting molecule in an ion-molecule reaction process. Reaction of alkane radical cations with alkane molecules is firmly indicated by fluorescence-detected magnetic resonance (FDMR) experiments (4), but this technique can provide no information on the reaction products of the hydrogen/proton-transfer process, *i.e.*, alkyl radicals (which are paramagnetic but nonionic) and protonated alkanes (which are ionic but diamagnetic).

II. ESR Evidence for Proton Transfer from Alkane Radical Cations to Alkane Molecules

Evidence for, and detailed information on, proton transfer from alkane radical cations to alkane molecules has been obtained in CCl_3F matrices at cryogenic temperatures (5). The evidence is derived from comparison of ESR spectra obtained after irradiation of alkanes at different concentrations in CCl_3F , with spectra obtained at identical concentrations in CCl_3CF_3 , $\text{CCl}_2\text{FCF}_2\text{Cl}$ and $\text{CF}_2\text{ClCCl}_3$. Chemical properties of these different chlorofluorocarbons are very similar. Yet, ESR spectra obtained at higher alkane concentrations differ drastically. Upon γ -irradiation of alkanes at both low and high concentration in CCl_3CF_3 , $\text{CCl}_2\text{FCF}_2\text{Cl}$ and $\text{CF}_2\text{ClCCl}_3$ and at low concentration in CCl_3F only the ESR spectrum of alkane radical cations is observed. At high concentration in CCl_3F , alkyl radicals also appear and the relative contribution of these alkyl

radicals to the ESR spectrum increases with increasing alkane concentration. ESR results obtained after irradiation of heptane in CCl_3F can be considered typical in this regard and are briefly discussed below.

First-derivative ESR spectra obtained after irradiation of heptane at various concentrations in CCl_3F are shown in Figure 1. The spectrum at low concentration only consists of a triplet with an hyperfine splitting constant of 30 G, which can be attributed to heptane radical cations. The triplet spectrum indicates that the radical cations are in the extended *all-trans* conformation. In the extended conformation, the unpaired electron is delocalized over the carbon-carbon σ -bonds as well as the two in-plane end carbon-hydrogen bonds. This results in a characteristic three-line spectrum with relative intensities 1 : 2 : 1, arising from coupling with the end protons. Increasing the heptane concentration in CCl_3F causes the spectrum to change gradually. From *ca.* 2 mol% typical alkyl radical features also appear, being clearly discernible only in the lateral parts of the spectrum. The alkyl radical spectrum becomes very prominent at higher concentrations. In contrast, only a triplet is observed after irradiation of 4 mol% heptane in CCl_3CF_3 , $\text{CCl}_2\text{FCF}_2\text{Cl}$, $\text{CF}_2\text{ClCCl}_3$ and perfluorohexane, a typical ESR spectrum is shown in Figure 2.

The intensity of the alkyl radical absorptions is *proportionally* much higher in irradiated CCl_3F /alkane systems than in the corresponding neat alkanes. Results obtained with undecane illustrate this well. The first-derivative ESR spectrum obtained after irradiation of 1 mol% undecane in CCl_3F is shown in Figure 3. Typical alkyl radical features are very prominent in the lateral region of this spectrum. As is evident from the right lateral part of the spectrum, in which matrix absorption is virtually absent, a double-humped absorption and a more centrally-situated narrow ESR absorption are the most prominent features in this spectral region, features which are quite characteristic for 1-alkyl radicals (6). In the lateral region of the spectrum, ESR absorptions correspond closely with those in the spectrum observed after irradiation of neat undecane (see Figure 4). The intensity of the alkyl radical spectrum in neat undecane is somewhat higher (but in view of the much higher alkane concentration *proportionally* much lower) than in CCl_3F containing undecane. As a matter of fact, taking into account the respective signal gain and accumulation settings, a ratio of 2.8 : 1 is obtained with

respect to the intensity in CCl_3F containing 1 mol% undecane.

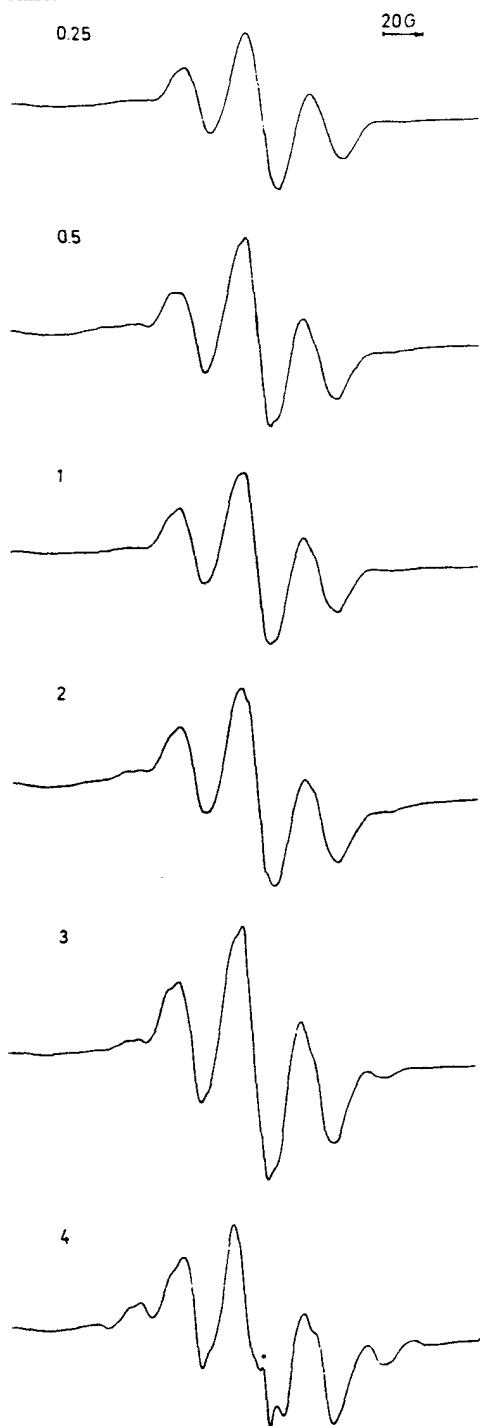


Figure 1: First-derivative ESR spectra obtained after irradiation of heptane at various concentrations in trichlorofluoromethane; ● shows a background signal; the number indicates the concentration (in mol%) of heptane.

At identical alkane concentrations, intensities of the alkyl radical absorptions increase quite considerably with

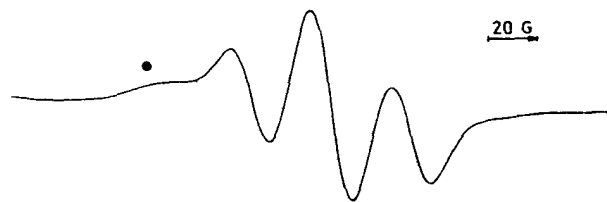


Figure 2: First-derivative ESR spectrum obtained after irradiation of 4 mol% heptane in 1,1,1-trichlorotrifluoroethane; ● shows an ESR absorption due to the irradiated matrix.



Figure 3: First-derivative ESR spectrum obtained after irradiation of 1 mol% undecane in trichlorofluoromethane; ● shows a background signal.

increasing chain length of the alkane solute. This can be illustrated nicely by comparison of the ESR spectrum obtained after irradiation of 2 mol% hexane in CCl_3F shown in Figure 5, with the spectrum obtained after irradiation of 1 mol% undecane in this matrix; (see above). The ESR absorption obtained after irradiation of hexane in CCl_3F mainly consists of a triplet spectrum, which can firmly be attributed to hexane radical cations in the extended all-*trans* conformation. Considerable additional hyperfine structure is observable in the spectrum, which is due to hyperfine interaction with the CH_2 -protons; it has been established that the out of plane protons in the CH_3 -groups give unresolvably small splittings (7). From the lateral region of the spectrum, it is obvious that alkyl radical absorptions are only barely discernible, which is in sharp contrast with ESR observations made after irradiation of 1

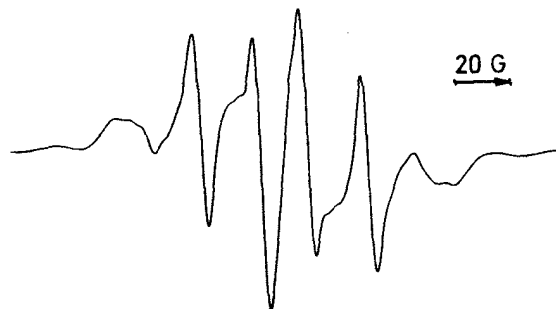


Figure 4: First-derivative ESR spectrum obtained after irradiation of neat undecane.

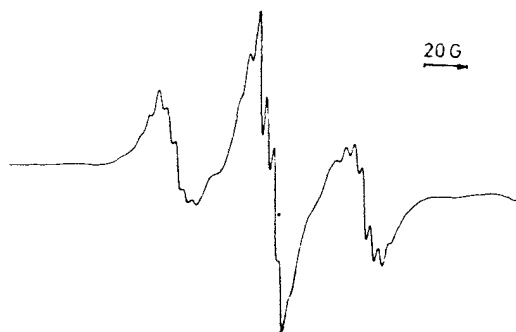


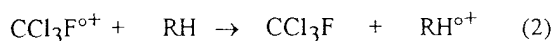
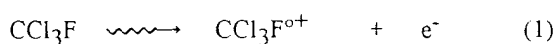
Figure 5: First-derivative ESR spectrum obtained after irradiation of 2 mol% hexane in trichlorofluoromethane; ● shows a background signal.

mol% undecane in CCl_3F (see above), indicating proportionally much higher alkyl radical formation in the latter case. Quite in general, the 'onset' of alkyl radical formation decreases and the intensity of the alkyl radical absorption increases with increasing chain length of the alkane solute.

III. Conclusion

In summary, the following ESR observations were made relating to γ -irradiated CCl_3F /alkane systems at 77 K. (i) After γ -irradiation of decane and lower n-alkanes ($n_C > 5$) at low concentration in CCl_3F only the ESR spectrum of the corresponding radical cations is observed, whereas at higher concentrations -(the onset decreasing with chain length)- the spectrum of alkyl radicals also appears. With higher n-alkanes alkyl radicals were observed even at quite low alkane concentrations. (ii) For all n-alkanes, the signal intensity and relative contribution of neutral alkyl radicals to the observed ESR spectra increases with increasing alkane solute concentration and at equal concentrations increases with increasing chain length of the alkane solute. (iii) Alkane radical cations but no alkyl radicals are observed after irradiation of n-alkanes in CCl_3CF_3 and other matrices at concentrations where alkyl radicals are already quite prominent in CCl_3F . (iv) The formation of neutral alkyl radicals in irradiated CCl_3F /alkane systems is proportionally much higher than in irradiated neat alkanes.

From these observations, it is concluded that alkanes form small aggregates in CCl_3F matrices at cryogenic temperatures and that the extent of aggregation increases both with increasing alkane concentration and with increasing chain length of the alkane solute. It is further concluded that upon γ -irradiation positive-hole transfer from matrix cations to the alkane clusters still takes place efficiently and that alkane radical cations react with alkane molecules in such clusters by proton transfer. The alkyl radicals in irradiated CCl_3F /alkane systems are therefore formed by the following sequence of reactions:



Various less plausible alternative mechanisms for alkyl radical formation, *viz.* direct radiolysis of the alkane solutes, formation as a result of electronic excitation energy transfer and formation from the corresponding alkane radical cations by unimolecular deprotonation or charge neutralization by electron tunnelling, may be ruled out as a major source for alkyl radical formation on different grounds on the basis of the experimental results obtained. The distinction between hydrogen abstraction by and proton transfer from alkane radical cations may be made from a careful examination of the nature of the alkyl radicals formed in the process and from its relation to the electronic structure of the reacting alkane radical cations (5).

IV. Acknowledgment

The authors thank the National Fund for Scientific Research (N.F.W.O.) of Belgium for financial support.

V. References

- ¹V. L. Talroze and A. K. Lyubimova, *Dokl. Akad. Nauk SSSR* **86**, 909 (1952).
- ²S. G. Lias and P. Ausloos, "Ion Molecule Reactions, Their Role in Radiation Chemistry", ERDA/ACS Research Monographs in Radiation Chemistry, American Chemical Society, Washington D.C., 1975.
- ³See for instance and for further references: K. Toriyama, K. Nunome and M. Iwasaki, *J. Phys. Chem.* **85**, 2149 (1981); M. Iwasaki, K. Toriyama and K. Nunome, *J. Am. Chem. Soc.* **103**, 3591 (1981); G. Dolivo and A. Lund, *J. Phys. Chem.* **89**, 3977 (1985); G. Dolivo and A. Lund, *Z. Naturforsch.* **40A**, 52 (1985); K. Toriyama, K. Nunome and M. Iwasaki, *J. Phys. Chem.* **90**, 6836 (1986).
- ⁴D. W. Werst and A. D. Trifunac, *J. Phys. Chem.* **92**, 1093 (1988); D. W. Werst, M. G. Bakker and A. D. Trifunac, *J. Am. Chem. Soc.* **112**, 40 (1990).
- ⁵G. Luyckx and J. Ceulemans, *J. Chem. Soc., Chem. Commun.* 988 (1991); G. Luyckx and J. Ceulemans, *J. Chem. Soc., Faraday Trans.* **87**, 3499 (1991); D. Stienlet and J. Ceulemans, *J. Phys. Chem.* **96**, 8751 (1992); D. Stienlet and J. Ceulemans, *J. Chem. Soc., Perkin Trans.* **2** 1449 (1992).
- ⁶E. L. Cochran, F. J. Adrian and V. A. Bowers, *J. Chem. Phys.* **34**, 1161 (1961).
- ⁷K. Toriyama, K. Nunome and M. Iwasaki, *J. Chem. Phys.* **77**, 5891 (1982).

In vivo non-invasive determination of abnormal water diffusion of EAE in the rat by diffusion-weighted NMR Imaging.

M.R. Verhoye^{1,2}, E.J.'s-Gravenmade³, E.R. Raman^{1,2}, J. Van Reempts⁴, R. Dommissie^{1,5} & A. Van der Linder¹

¹ Bio Imaging Lab, ² BIMEF, ⁵ Applied NMR: University of Antwerp, RUCA, Belgium, ³ Dept of Neurology: University Hospital Groningen, The Netherlands, ⁴ Dept Life Sciences, Janssen RF, Beerse, Belgium

PURPOSE

Experimental Allergic Encephalomyelitis (EAE) in the rat is a well established animal model of Multiple Sclerosis (MS). Both diseases show a complicated set of pathological features which are accompanied by changes in free and restricted diffusion of water. In this study we determined the ADC (Apparent Diffusion Coefficient) in different areas in the brain (gray and white matter) before, during and after the first exacerbation. We hoped to find ADC changes preceding the clinical signs.

MATERIALS AND METHODS

Chronic Experimental Allergic Encephalomyelitis (CrEAE) was induced in four Lewis rats with an emulsion of guinea pig spinal cord tissue in complete Freund's adjuvant enriched with Mycobacterium Tuberculosis H37 RA. On alternate days, from day 0 to day 23 post-immunization, the animals were treated with Cyclosporin A. The EAE rats were weighted and clinically scored daily.

To confirm the pathological changes in the EAE rats, the brains of two EAE rats, one recovered and one still sick, were submitted to an histological examination at the end of the NMR experiment.

MR-imaging was performed at 300 MHz on a SMIS MR microscope with a horizontal 7 Tesla wide bore magnet and 8 cm aperture self shielded gradient coils (Oxford Instruments).

The EAE rats were submitted to the MRI protocol, every 3 or 4 days during a complete pathological cycle (starting after induction and up to 37 days after EAE induction).

A multi slice spin echo sequence was used with diffusion sensitizing gradients on both sides of the 180° RF pulse as described by Stejskal and Tanner (1965). The orientation of the diffusion sensitizing gradients was along the (1,1,1) direction of the magnet by applying diffusion gradients with equal strength and at the same time in the X, Y and Z direction which ensured an intersection of all fiber directions. Imaging of the complete brain took 16 transverse slices of 1 mm with a gap of 0.6 mm between adjacent slices. A (256 x 256) acquisition matrix was used resulting in an in-plane resolution of 98x98 µm. The acquisition parameters of the diffusion-weighted images were: TE 56 ms, TR

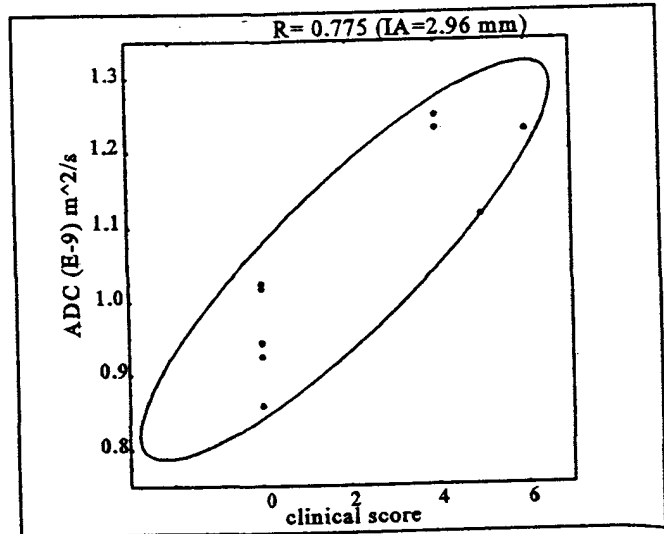


Fig. 1. The figure shows, for one rat, the ADC of white matter in the external capsule, of the specific stereotactical position for which a significant correlation was found with the clinical score, versus the clinical score. The Spearman Rank coefficient R is given together with the 95 % confidence ellipse.

2400 ms, the diffusion gradient duration 10 ms, the diffusion gradient separation 27 ms. Sets of five diffusion-weighted images (b -values: $b_0=53$, $b_1=92$, $b_2=342$, $b_3=805$ and $b_4=1480$ s/mm²) were used to calculate diffusion maps at different time intervals of pathology.

We studied changes in the ADC values of white and gray matter during the progression of the pathology. Therefore ADC values were determined in different regions of interest assigned in different diffusion maps from slices positioned from IA 3.7 to 10.1 mm.

RESULTS

The clinical signs appeared eleven days after the induction in all rats. Three rats had a similar clinical evolution during the complete experimental period (variation from score 4 to score 0 over a period of 33 days after induction). One rat kept severe EAE signs and was not yet recovered at the time it was sacrificed.

For the group of control rats we obtained $\langle \text{ADC} \rangle$ values of $(474 \pm 15) 10^{-12}$ m²/s for gray matter and $(920 \pm 30) 10^{-12}$ m²/s for white matter, measured in

the external capsule.

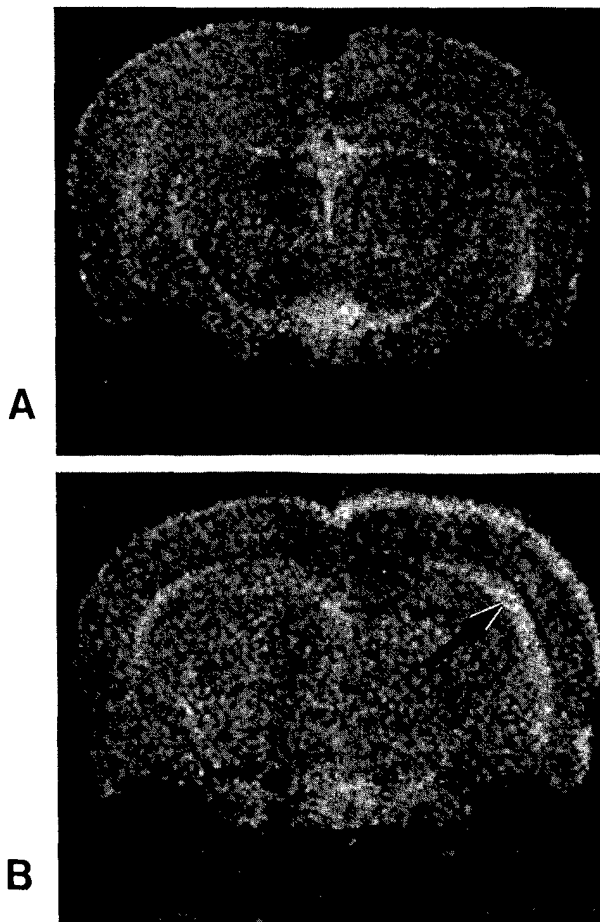


Fig. 2. Diffusion map of the brain at IA 4.48 mm corresponding to clinical score 0 (A) and clinical score 4 (B), demonstrating a higher grey level of white matter in the part of the external capsule, for which the direction of the myeline fibers is perpendicular to the direction of the diffusion sensitizing gradient, when the rat is clinically scored non-zero.

For each region, grey matter as well as white matter, the Student t-test showed that the ADC values of the control group were not significantly different from those of the induced rats corresponding to a clinical score 0 before clinical signs occurred.

A Spearman Rank correlation test revealed no significant correlation between the ADC values of the gray matter and the clinical score.

On the other hand, in each rat a significant correlation was found between the clinical score and the ADC values of white matter in the external capsule: the ADC value increased with increasing clinical score (Fig. 1).

This means that as the EAE pathology develops there is a rise in the water diffusion of white matter in the external capsule. The diffusion maps demonstrated a higher grey level for white matter in the external capsule when the animal was clinically scored non-zero in comparison with the grey levels of diffusion maps corresponding to a clinical score 0, before and after the EAE phase (Fig. 2).

CONCLUSION

- Diffusion-weighted imaging with sensitizing gradients in a direction intersecting the external capsule may be used to monitor changes of water diffusion properties during the first exacerbation of EAE.

- There were no alterations in the ADC of gray matter surrounding the external capsule with increasing clinical score. Concerning white matter, as determined in the external capsule, there were no significant differences in ADC values between controls and EAE rats before clinical signs occurred.

However, as soon as clinical signs were observed, we could demonstrate a significant positive correlation between the ADC values and the clinical score. As the clinical signs became more severe, we measured a rise in water diffusion (increase in ADC) in the external capsule which was accompanied by the occurrence of interstitial edema as revealed by a complementary histological study.

The IA positions for which a positive correlation was found, were different from rat to rat. This reflects the fact that the position of the EAE injury is unpredictable.

REFERENCES

1. Stejskal E.O., Tanner J.E., *J. Chem. Phys.*, 42,1,288-292,1965.

In vivo and non invasive measurement of temperature stress induced changes in the energy metabolism of the common carp, by ^{31}P -NMRS

R. Borger^{1,2}, J. Van Audekerke², R. Blust¹, R. Domnisse³ and A. Van der Linden²

¹Ecophysiology and Biochemistry, ²Bio Imaging Lab, ³Applied NMR, University of Antwerp (RUCA), Belgium

Purpose

In this study we aim to analyse the effects of environmental stressors, such as temperature changes, on the energy metabolism of common carp, *Cyprinus carpio*. Furthermore we wish to distinguish the effects of sudden temperature changes versus acclimation.

The rationale behind this is that stress reduces the energy resources of an organism, resulting in less energy available for normal energy requiring processes such as growth and reproduction. Studying the energy metabolism, as a bioindicator for stress, would allow on-line monitoring of the physiological condition of an animal.

In vivo ^{31}P -NMR spectroscopy allows the consecutive measurement of different phosphorous compounds in the same living organism. It therefore allows to monitor changes in the energy metabolism as the result of exposure or adaptation to certain stressors.

This paper reports on changes in the dynamics of high-energy phosphate compounds and pH_i of the muscle of common carp during anoxia and recovery of anoxia under different conditions of temperature. The recovery from a standardised anoxia stress was used as a method to define the physiological fitness of an animal after being submitted to an acute sublethal temperature shock.

Material and Method

Common carp, *Cyprinus carpio*, (length 17 to 18 cm) were used. *In vivo* ^{31}P -NMR spectra of the muscle of the carp were obtained on a 7 Tesla SMIS (U.K.) NMR spectrometer, with a horizontal (8 cm diameter) accessible bore. The signal of the fish muscle was picked up with a surface coil of 20 mm diameter, which was double tuned to the hydrogen and phosphorus frequencies (300 MHz and 121 MHz, respectively). A glass capillary tube filled with a solution (180 mg/ml) of methylene diphosphonate (MDP) was mounted on the surface of the coil at the opposite side to the fish and served as standard. FID signals were acquired under the following conditions: 60° pulse of 100 μs , 10 kHz spectral width, 3750 ms repetition time, 2048 sample points, averaging over 48 scans. A line broadening factor of 10 Hz was used to process the spectra.

Relative quantification was obtained by normalising peak intensities to those of the external standard (MDP).

The B_0 field was optimised by shimming on the ^1H signal, until the full width at half maximum was less than 0.2 ppm.

In a first series of experiments, the energy metabolism of the lateral muscle of common carp ($n=3$), acclimated at 25°C, was studied. Under anaesthesia, the carp was mounted in a flow cell (Van den Thillart *et al.*, 1989). When the flow cell was positioned in the centre of the magnet, the carp was allowed to recover from the handling stress during 2 hours. Hereafter a continuous acquisition of FID signals was established, during the next 9 hours. The energy metabolism was followed under normoxic water conditions for the first two hours. Subsequently the carp was exposed to anoxia, until the height of the inorganic phosphate peak reached half-height of the phosphocreatine. Similar experiments were performed on fish ($n=3$) acclimated at 25°C but exposed to a temperature shock (from 25°C to 33°C) at the beginning of the experiment (shortly after the acquisition of FID signals was started). Furthermore, the experiments were repeated on carp ($n=3$) acclimated at 33°C. The necessity of using an anoxia load to visualise changes in the energy metabolism, originated from the fact that the temperature shock, performed in these experiments, only induced a minor and short influence on the PCr/ P_i ratio.

Results

A number of preliminary experiments showed us that carp acclimated at 25°C could withstand temperature shocks up until 35°C. The shock to 33°C was defined as a sublethal stressor. The time-course of the changes of pH_i , P_i , PCr and α -ATP observed in the muscle of common carp, under different conditions of temperature, before, during and after exposure to anoxia are shown in fig. 1. The resting levels of pH_i was 7.3 in carp acclimated at 25°C and evolved to 6.8 under anoxia. Anoxia caused a steep decline of PCr and an increase of inorganic phosphates in all three cases, while ATP remained constant. The level of recovery of PCr, P_i and pH_i after the anoxia was complete within 2 hours.

The resting levels of pH_i in carp acclimated at 33°C was 7.2 (fig. 1C), due to the anoxia a drop to 6.6 occurred. The level of recovery of PCr, P_i and pH_i after the anoxia was complete and within 2 hours.

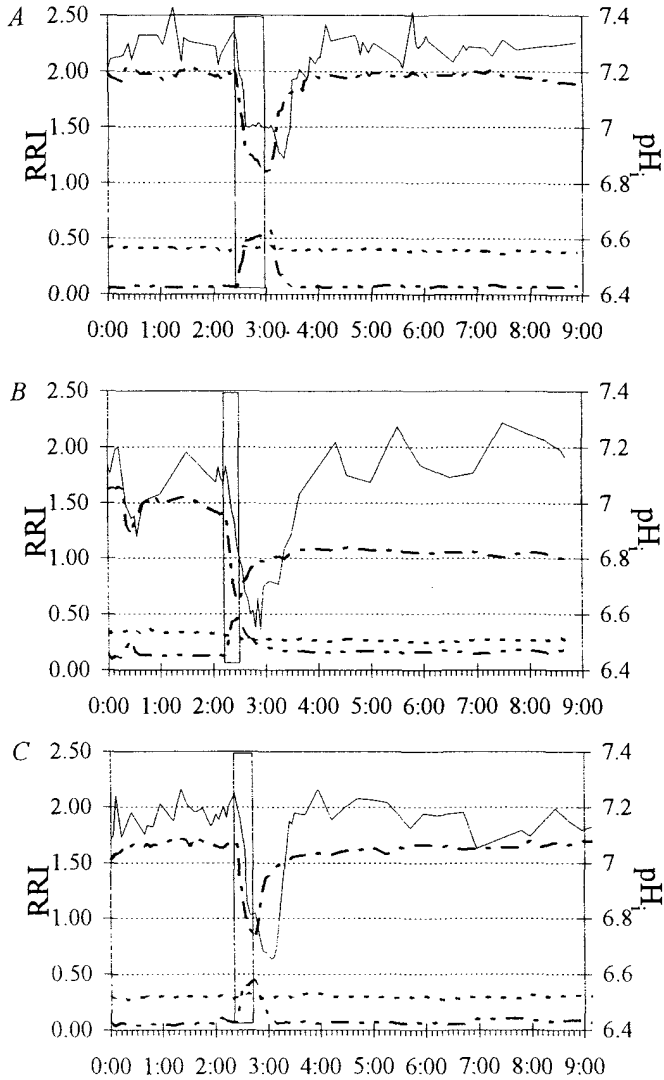


Fig. 1 : Time-course of the changes in relative resonance intensities (RRI) of PCr , P_i and α -ATP, and in pH_i of the muscle of carp before, during and after anoxia. A=acclimated at 25°C, B=exposed to a temperature shock (25°C-33°C) and C=acclimated at 33°C. The marked area indicates the anoxia period.

In carp exposed to the temperature shock, the resting levels of pH_i were 7.2 (fig. 1B). Due to the anoxia load a pH_i drop to 6.6 occurred. The level of recovery of PCr and P_i after the anoxia was not complete within the duration of the experiment. The level of recovery of the pH_i on the other hand was complete within 2 hours.

Table 1 indicates the level of recovery of the different compounds and pH_i in the muscle of carp. This table shows the significant differences in level of recovery of P_i and PCr in the muscle of the carp between the 25°C acclimated group and the temperature shock group on one hand, and between the temperature shock group and the 33°C acclimated group on the other hand. This table

indicates significant differences between the 25°C acclimated and the temperature shock group and between the temperature shock and the 33°C acclimated group. No significant differences in the level of recovery were found between the 25°C and the 33°C acclimated groups.

Table 1 : The level of recovery of different phosphorous compounds and pH_i in the muscle of carp (n=3).

	25°C	Temp. shock	33°C
PCr/MDP	96%	68% ^{*2}	104%
P_i /MDP	98%	90% ^{*1,2}	99%
PCr/ P_i	88%	57% ^{*1,2}	95%
pH_i	101%	100% ^{*1,2}	98%

^{*1}= significant difference between 25°C and temperature shock group, ^{*2}= significant difference between temperature shock and 33°C group. The significance was tested using the Mann-Whitney U test (p<0.05).

Conclusions

The lack of recovery from anoxia (fig. 1B & table 1) of carp exposed to a temperature shock indicate that they have a lower capacity to compensate this anoxia load. The energy metabolism of the muscle of carp acclimated at 33°C does recover from anoxia in a similar manner as that of carp acclimated at 25°C (cf. fig. 1A&C). These results omit the possibility that the lower energy state was caused by the changed temperature, but instead they indicate that an acclimation process is active. The reduced capacity to deal with the anoxia load, in carp exposed to a temperature shock, shows that the carp didn't acclimate to the changed temperature, within the measured time (9h). These observations open perspectives to evaluate when and how fast acclimation to a changed environmental condition occurs. The changes of the intracellular pH showed similar time-courses when comparing the results from the temperature shock and the 33°C acclimated group. A significant difference of the resting level was found when comparing the 25°C acclimated group with the two other groups. This difference is caused by a different temperature, but the pH_i experiences no effect from the temperature shock.

Acknowledgement

We acknowledge support by contract n° GC/05/029: Impulse programme "Global Change" supported by the Belgian State-Prime Minister's service for Scientific, Technical and Cultural affairs.

Literature

Van den Thillart, G., Körner, F., Van Waarde, A., Erkelens, C. and Lugtenburg, J. (1989). A flow-through probe for *in vivo* ³¹P-NMR spectroscopy of unanesthetized aquatic vertebrates at 9.4 Tesla. *J. Magn. Res.* 84, 573-579.

Parahydrogen: the means to see the unseen. NMR studies of metal complexes with parahydrogen.

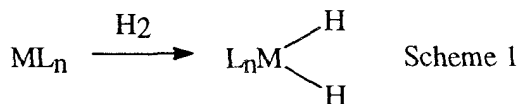
Simon. B. Duckett^{*}, Graham. K. Barlow, Martin. G. Partridge, Roger. J. Mawby
and Barbara. A. Messerle.[‡]

Department of Chemistry, University of York, Heslington, York YO1 5DD UK.

[‡]Department of Organic Chemistry, University of Sydney, Sydney. Australia.

Enhanced absorption and emission signals have been observed in NMR spectra from nuclei that originate from, or are connected to nuclei originating from parahydrogen.¹ Parahydrogen is dihydrogen in the nuclear singlet state $\alpha\beta\text{-}\beta\alpha$, and is restricted to symmetric rotational levels. There are three other spin permutations, the symmetric ortho states $\alpha\alpha$, $\beta\beta$ and $\alpha\beta\text{+}\beta\alpha$, and these are restricted to antisymmetric rotational levels. The presence of a paramagnetic agent relaxes the selection rule that stops inter-conversion between spin isomers and enables their populations to move, rapidly, to equilibrium even at low temperatures. At equilibrium at 77 K, 50% of the molecules present in a sample of H_2 are in the lower energy, para state. This is the means by which the para-enriched-hydrogen (p- H_2) used in this study was obtained.

Dihydrogen commonly enters the coordination sphere of a transition metal complex via a concerted oxidative addition process (Scheme 1). If, in this reaction, the spin state populations of protons in the product are similar to those found in dihydrogen then signals for NMR transitions between levels can be enhanced. This phenomenon was initially termed PASADENA by Weitekamp² and later parahydrogen induced polarisation (PHIP) by Eisenberg.¹ Such transformations are common in catalytic hydrogenation reactions, and enhancements of signal intensity in the ^1H spectra of the hydrogenation products are often large. This approach allows the detection of intermediates, such



as $\text{Rh}(\text{H})_2\text{Cl}(\text{alkene})(\text{PPh}_3)_2$, through observation of their PHIP-enhanced hydride signature.³ The enhancement of signals for ^{31}P and ^{13}C nuclei through cross relaxation can also be very impressive.⁴ In addition, NMR sequences such as INEPT⁺ which facilitate population transfer can be used to increase the intensity of heteronuclei signals still further.⁵

In this paper we describe how a series of rhodium and ruthenium complexes can be probed by NMR spectroscopy in conjunction with p- H_2 . It was of interest to determine whether p- H_2 and two-dimensional indirect experiments could be used to detect low γ nuclei, such as ^{103}Rh , ^{31}P and ^{13}C , in transition metal complexes, in samples that contain less than 1 mmol of complex. We were also curious to see whether these experiments could be repeated with magnetic field gradient methods without affecting p- H_2 derived signal enhancements.

The dihydride complexes examined here were selected because their hydride ligands undergo exchange with free hydrogen, an essential requirement if p- H_2 enhancement is to be maintained during the whole observation period.

When a solution of the complex $\text{Rh}(\text{PMe}_3)_3\text{Cl}$ ⁶ **1** (< 1 mg) is placed under 3 atm of p- H_2 at 300 K, the two polarised hydride resonances of $\text{Rh}(\text{H})_2(\text{PMe}_3)_3\text{Cl}$ **2** can be observed in the ^1H NMR spectrum: in CD_2Cl_2 these are at δ -9.79 (H_a) and -19.50 (H_b). Fig. 1 shows the PMe_3 proton resonances and the H_a hydride resonance in a corresponding solution in C_6D_6 at 343 K. The coupling, $J(\text{HH})$, can be measured directly from the separation between the antiphase peaks, and the emission absorption profile confirms that $J(\text{HH})$ is negative. The enhanced antiphase character is a result of the p- H_2 derived populations of the $\alpha\beta$ and $\beta\alpha$ levels of the coupled dihydride spin system.

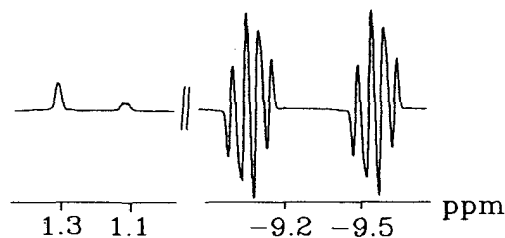
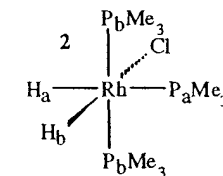


Fig 1. ^1H NMR spectrum of $\text{Rh}(\text{H})_2(\text{PMe}_3)_3\text{Cl}$ **2** obtained with p- H_2 at 343 K in C_6D_6 . The antiphase components arise in transitions involving protons that originate from p- H_2 . The right section illustrates the resonance H_a which when compared with the 18 protons of the PMe_3 ligands (left section) is 200 fold enhanced.

The maximum initial transverse magnetization obtainable from the two-spin order $|z_1z_2\rangle$ product state formed in the p- H_2 derived product **2** arises when a $\pi/4(1\text{H})$ pulse is applied to the sample. In this case, a 100 fold increase in signal strength over that expected from reaction with normal H_2 can be obtained.

A heteronuclear multiple quantum correlation experiment (HMQC)⁷ in which the first $\pi/2(1\text{H})$ pulse is also replaced by a $\pi/4$ pulse^{1,8} can be used to measure the chemical



1. R. Eisenberg. *Acc. Chem. Res.* 1991, 24, 110.

2. C. R. Bowers and D. P. Weitekamp. *J. Am. Chem. Soc.* 1987, 109, 5541.

3. S. B. Duckett, C. L. Newell and R. Eisenberg. *J. Am. Chem. Soc.* 1994, 116, 10548.

4. J. Barkenmeyer, M. Haake and J. Bargon. *J. Am. Chem. Soc.* 1995, 117, 2927.

5. S. B. Duckett, C. L. Newell and R. Eisenberg. *J. Am. Chem. Soc.*, 1993, 115, 1156.

6. R. A. Jones, F. M. Real, G. Wilkinson, A. M. R. Galas, M. B. Hursthouse and K. M. A. Malik. *J. Chem. Soc., Dalton Trans.* 1980, 511.

7. A. Bax, R. H. Griffey and B. L. Hawkins. *J. Mag. Resonance*, 1983, 301. M. H. Frey, G. Wagner, M. Vasak, O. W. Sorensen, D. Neuhaus, E. Worgotter, J. H. R. Kagi, R. R. Ernst and K. Wuthrich. *J. Am. Chem. Soc.*, 1985, 107, 6847

8. O. W. Sorensen, G. W. Eich, M. H. Levitt, G. Bodenhausen and R. R. Ernst. *Progress in NMR Spect.* 1983, 16, 163. G. Wagner, G. Bodenhausen, N. Muller, M. Rance, O. W. Sorensen, R. R. Ernst and K. Wuthrich. *J. Am. Chem. Soc.* 1985, 107, 6440.

shifts of the two inequivalent phosphorus nuclei of **2** [Fig. 2a].⁹ This approach makes optimal use of the p-H₂ enhancement seen in the hydride signature of the complex and employs the most receptive nucleus, ¹H, to obtain ³¹P chemical shift information. The remainder of the sequence, [$-\tau \cdot \pi/2(X) - t_1 - \pi(1H) - t_1 - \pi/2(X) - \tau \cdot \pi/2(X)$ -detect (¹H)], is identical to the standard HMQC experiment in which the magnetization created by the initial pulse evolves during the fixed delay τ by way of heteronuclear couplings, enabling the generation of heteronuclear multiple quantum coherence. Phase-sensitive acquisition was achieved using TPPI¹⁰ by incrementing the phase of the first pulse to the heteronucleus (X) by $\pi/2$ for each slice of the 2D data set, and t_1 , the evolution period, was incremented in the usual way to produce the 2D data matrix. Data measurement is extremely rapid because the optimum scan-scan repetition time is determined by the dihydride/dihydrogen exchange rate; temperatures were selected where this process is rapid.

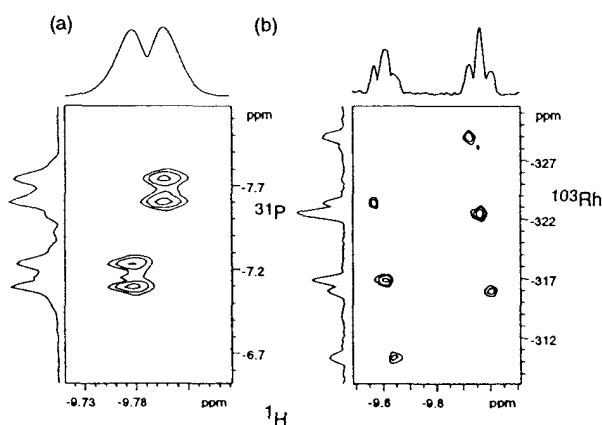
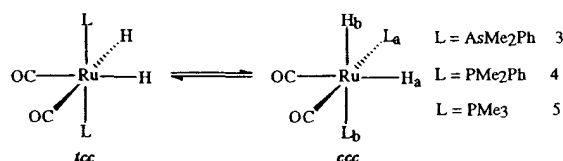


Fig 2. Selected cross peaks (positive contours) and projections from ¹H-³¹P and ¹H-¹⁰³Rh correlation spectra of Rh(H)₂(PMe₃)₃ **2** obtained with p-H₂ in CD₂Cl₂ at 313 K. (a) ¹H-³¹P correlation spectrum, ³¹P decoupled, showing only the cross peak connecting H_a to P_b. (b) ¹H-¹⁰³Rh correlation spectrum, ¹⁰³Rh decoupled, acquired using $\tau = 1/2J(\text{RhH}_a)$ for multiplet selection, showing correlated transitions between H_a and ¹⁰³Rh in **2**.

The p-H₂ enhanced ¹H-³¹P correlation spectrum of **2** shows four cross peaks that connect the phosphorus centres, P_a and P_b, to their proton coupling partners, the hydrides H^a and H^b [Fig. 2a]. The relative intensities of the cross peaks depend critically on the value of τ , which when based on $J_{P^aH^a}$, produces a strong cross peak connecting the hydride at $\delta_{1H} -9.79$ (H^a) to the phosphorus centre at $\delta_{31P} -21.3$ (P^a, dt, $J_{RhP^a} = 89$, $J_{PP} = 30$ Hz). The magnitude and sign of the heteronuclear coupling constants can be measured directly from these spectra. The transitions are separated by J_{PH} and J_{RH} in the ¹H dimension and J_{PP} and J_{RHP} in the ³¹P dimension, and the sign of the slope between connected transitions within the cross peak framework determines the sign of the product $J_{PH} \times J_{PP}$ and $J_{RH} \times J_{RHP}$. Upon examination, these data reveal that J_{RH^a} , J_{RH^b} , J_{RHP^a} and J_{RHP^b} all have the same sign, and have opposite sign to $J_{P^bH^a}$.

The corresponding ¹H-¹⁰³Rh correlation spectrum of **2** shown in Fig. 2b illustrates the cross peak connecting the resonance due to the rhodium nucleus, $\delta_{103Rh} -319$ (dt, $J_{RhP^a} = 103$, $J_{RhP^b} = 88$ Hz) to those of its hydride coupling partner, H_a, $\delta_{1H} -9.79$ (dt, $J_{P^aH^a} = 176$, $J_{P^bH^a} = -19$ Hz) and possesses a slope that is dependent on $J_{PH} \times J_{PRh}$. Spectral analysis confirms that $J_{P^bH^a}$ is of negative sign while the remaining coupling constants are positive [the sign of $J(PP)$ is unknown]. These experiments reveal that p-H₂ facilitates the rapid, indirect observation of highly insensitive nuclei such as ¹⁰³Rh.



It has also proved possible to observe similar enhancements in a series of ruthenium complexes. Here we describe how the complexes [RuL₂(CO)₂(H)₂] (L = AsMe₂Ph, PMe₂Ph) behave with p-H₂.¹¹ When a C₆D₆ solution containing an equilibrium mixture of *trans,cis,cis*-[Ru(AsMe₂Ph)₂(CO)₂(H)₂] *tcc*-**3** and *all-cis*-[Ru(AsMe₂Ph)₂(CO)₂(H)₂] *ccc*-**3** (< 1 mg) is placed under 3 atm of p-H₂ and monitored by ¹H NMR spectroscopy at 343 K the spectrum shown in Fig. 3a is obtained.¹² The two polarised hydride resonances at $\delta -6.89$ and -8.82 are easily assigned to the hydride ligands H_a and H_b of *ccc*-**3** respectively. In this case, the enhanced antiphase character shown by each of these signals corresponds to a 1035 fold increase in signal strength over that normally expected.

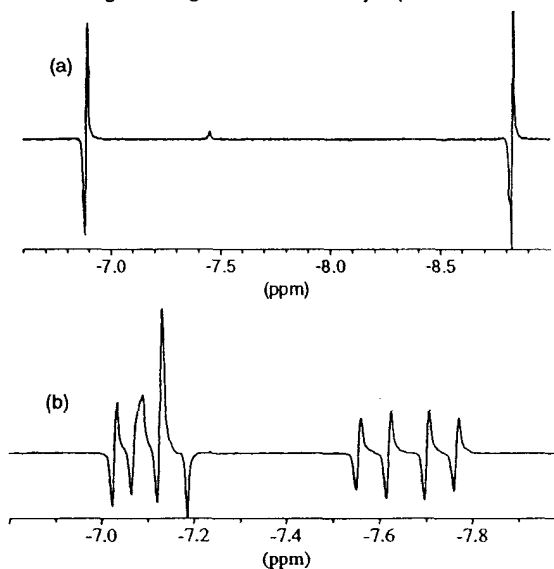


Fig 3. NMR spectra of Ru(L)₂(CO)₂(H)₂, obtained with p-H₂ in C₆D₆ showing the hydride region only. The antiphase components arise in transitions involving protons that originate from p-H₂. (a) ¹H spectrum of **3** at 343 K (the small peak at $\delta -7.46$ is due to *tcc*-**3**); (b) ¹H spectrum of **4** at 333 K.

The phosphine analogue of **3**, [Ru(PMe₂Ph)₂(CO)₂(H)₂] **4** was originally reported to exist in C₆D₆ solution as the *trans,cis,cis* isomer *tcc*-**4**, but when this system is examined at 500 MHz, the *cis,cis,cis*

9. S. B. Duckett, G. K. Barlow, M. G. Partridge and B. A. Messerle, *J. Chem. Soc., Dalton Trans.*, 1995, 3427.

10. G. Drobny, A. Pines, S. Sinton, D. Weitekamp and D. Wernmer. *Faraday Div. Chem. Soc. Symp.* 1979, 13, 49. G. Bodenhausen, R. L. Vold and R. R. Vold. *J. Mag. Reson.* 1980, 37, 93.

11. J. M. Bray and R. J. Mawby, *J. Chem. Soc., Dalton Trans.*, 1987, 2989. J. M. Bray, R. J. Mawby, *J. Chem. Soc., Dalton Trans.*, 1989, 589. R. J. Mawby, R. N. Perutz and M. K. Whittlesey. *Organometallics*, 1995, 14, 3268.

12. S. B. Duckett, R. J. Mawby and M. G. Partridge, *J. Chem. Soc., Chem. Commun.*, In press.

isomer *ccc-4* can also be detected ($[tcc-4]/[ccc-4] = 24$). The presence of *ccc-4* becomes obvious when a ^1H NMR spectrum of a C_6D_6 solution of **4** (<1 mg) under a $p\text{-H}_2$ atmosphere is collected. The 4 scan spectrum shown in Fig. 3b, obtained at 333 K, shows two sets of antiphase multiplets at δ -7.08 and δ -7.66, assigned to the hydride ligands H_a and H_b of *ccc-4* respectively. The H_b resonance of *ccc-4* appears in an otherwise clear spectral region and shows one large phosphorus splitting [$J(\text{P}_b\text{H}) = 74$ Hz] and one smaller splitting [$J(\text{P}_a\text{H}) = 32$ Hz]. Unfortunately, values of $J(\text{P}_a\text{H}_a)$ and $J(\text{P}_b\text{H}_a)$ for *ccc-4* cannot be determined directly from this spectrum because the resonance due to H_a overlaps with the triplet signal, δ -7.13 [$J(\text{PH}) = 29$ Hz], due to the hydride ligands of the major isomer *tcc-4*. However, the corresponding ^1H - ^{31}P correlation of *ccc-4* contains four, well separated, cross peaks that connect the phosphorus nuclei, P_a , δ (^{31}P) 8.8, and P_b , δ (^{31}P) 0.2, to their proton coupling partners, H_a and H_b [Fig. 4]. Analysis of the cross peaks yields values for $J(\text{P}_a\text{H}_a)$, $J(\text{P}_b\text{H}_a)$ and $J(\text{P}_a\text{P}_b)$.

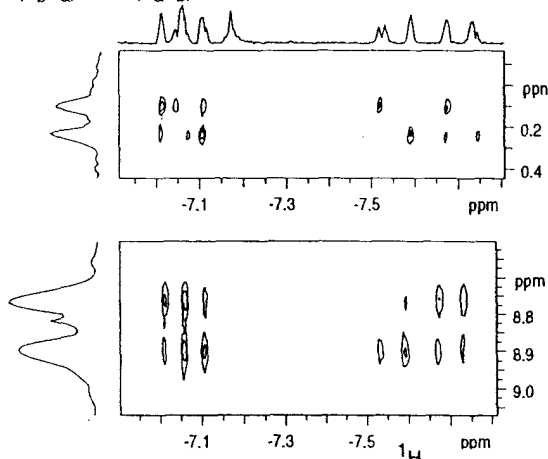


Fig. 4. ^1H - ^{31}P correlation spectrum of **4**, obtained with $p\text{-H}_2$ in C_6D_6 at 333 K, showing the cross peaks and projections connecting H_a and H_b to P_b and P_a in *ccc-4*.

The large $p\text{-H}_2$ enhanced hydride signals observed for the hydride resonances of **2** and *ccc-4* mean that ^1H NMR spectra only require one scan. However, the $p\text{-H}_2$ present in solution is not affected by this process because this molecule has no magnetic moment. These reactions can therefore be monitored by NMR experiments that use z -field gradients to reduce phase cycling requirements. Application of this procedure allows the spectral resolution obtained in the second dimension of the indirect experiments to be quadrupled without changing the time taken to complete them. This result is of critical importance because data measurement can now be completed before relaxation leads to significant depletion of the $p\text{-H}_2$ spin state population. In the case of ^{13}C , where parent ^1H signals which show no $J(^1\text{H}^{13}\text{C})$ scalar coupling yield 99 % of the detected signal intensity, gradient filtering is essential. The corresponding ^1H - ^{13}C gradient assisted correlation spectrum shown in Fig. 5 illustrates the cross peak connecting the hydride and carbonyl carbon resonances of $[\text{Ru}(\text{PMe}_3)_2(^{13}\text{CO})(^{12}\text{CO})(\text{H})_2]$, *tcc-5*.

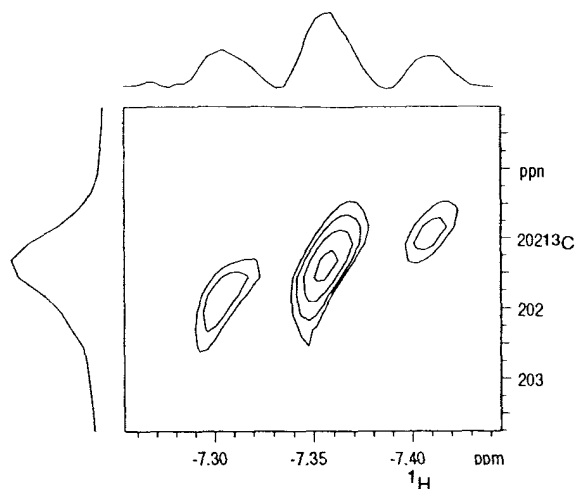


Fig. 5. ^1H - ^{13}C gradient assisted correlation spectrum of **5**, obtained with $p\text{-H}_2$ in C_6D_6 at 323 K, showing the cross peaks and projections connecting the hydride and carbonyl carbon resonances in *tcc-5*.

It is clear that the study of transition metal hydride complexes benefits from coupling the resolving power of indirect two dimensional methods with the signal enhancements associated with $p\text{-H}_2$ derived species.

Acknowledgements

We are grateful to the University of York (for MGP) and the Royal Society for financial support (field gradient unit and a study visit grant for Australia to SBD). Generous loans of ruthenium and rhodium trichlorides from Johnson Matthey and the loan of a low frequency probe from Bruker (UK) are gratefully acknowledged. We appreciated helpful discussions with Prof. R. Eisenberg and Prof. R. N. Perutz. Dr. M. K. Whittlesey and Mr. J. M. Lynam are thanked for providing some of the ruthenium complexes used in this study.

Footnotes

Selected spectroscopic data for compound **2**, **3**, **4** and **5** with ^1H 500.13 MHz, ^{31}P 202.45 MHz, ^{13}C 125.03 MHz and ^{103}Rh 15.77 MHz. ^{31}P and ^{13}C spectra recorded on 5 mm samples in a 5 mm geometry probe with gradient coil. ^{103}Rh spectra, recorded on 5 mm samples in a 10 mm inverse geometry probe, were referenced relative to 3.16 MHz, δ 0. Compound **2**, (CD_2Cl_2) ^1H (312 K) δ -9.79 (H_a , $J(\text{P}_a\text{H}) = 176$ Hz, $J(\text{P}_b\text{H}) = -19$ Hz, $J(\text{RhH}) = 15$ Hz, $J(\text{HH}) = -8$ Hz), δ -19.50 (H_b , $J(\text{RhH}) = 27$ Hz, $J(\text{P}_a\text{H}) = 13$ Hz, $J(\text{P}_b\text{H}) = 20$ Hz, $J(\text{HH}) = -8$ Hz). ^{31}P (312 K); δ -7.4 (P_b , dd, $J(\text{P}_b\text{Rh}) = 103$ Hz, $J(\text{PP}) = 28$ Hz), δ -21.3 (P_a , dt, $J(\text{P}_a\text{Rh}) = 88$ Hz, $J(\text{PP}) = 28$ Hz). ^{103}Rh (312 K) δ -319 (dt, $J(\text{P}_a\text{Rh}) = 88$, $J(\text{P}_b\text{Rh}) = 103$ Hz). *ccc-3* (C_6D_6) ^1H (343 K) δ -6.89 (H_a , $J(\text{HH}) = -7$ Hz), δ -8.82 (H_b , $J(\text{HH}) = -7$ Hz). *ccc-4* (C_6D_6): ^1H (333 K) δ -7.08 (H_a , $J(\text{P}_a\text{H}) = J(\text{P}_b\text{H}) = 23$ Hz, $J(\text{HH}) = -6$ Hz), δ -7.66 (H_b , $J(\text{P}_b\text{H}) = 74$ Hz, $J(\text{P}_a\text{H}) = 32$ Hz, $J(\text{HH}) = -6$ Hz). ^{31}P (333 K); δ 8.8 (P_a , d, $J(\text{PP}) = 28$ Hz), δ 0.2 (P_b , d, $J(\text{PP}) = 28$ Hz). *tcc-5* (C_6D_6): ^1H (333 K) δ -7.38 (2H, $J(\text{PH}) = 26$ Hz), ^{31}P (333 K); δ -2.6 (s), ^{13}C (323 K); δ 202.7 (t, $J(\text{PC}) = 10$ Hz).

MAGIC-ANGLE-SPINNING TWO-DIMENSIONAL NMR
FOR THE STUDY OF CONFORMATION OF LEUCINE ENKEPHALIN
ORIENTED IN LYOTROPIC LIQUID CRYSTAL

Atsuomi Kimura*, Naohito Kuni, Takahiro Jikihara and Hideaki Fujiwara

Faculty of Pharmaceutical Sciences, Osaka University 1-6 Yamadaoka, Suita, Osaka 565, Japan

Conformation of a leucine enkephalin(Tyr-Gly-Gly-Phe-Leu) has been determined by liquid crystal NMR spectroscopy after exploiting magic-angle(MAS) and near-magic-angle-spinning(NMAS) two-dimensional methodology. The solvent used for this investigation is cesium perfluorooctanoate(CsPFO) lyotropic liquid crystal. Analysis of the conformation of Leu-enkephalin dissolved in anisotropic environment is based on a measurement of ^1H - ^1H homonuclear dipolar couplings obtained under NMAS and a measurement of space proximity of ^1H - ^1H spin pairs from ROESY experiment under MAS conditions. By these approaches, preferred conformations of Leu-enkephalin and their orientation in liquid crystal membrane were determined successfully.

The NMR ROE data(Table 1) were obtained from MAS-ROESY experiments on a Varian VXR-200 spectrometer. ROESY spectra were recorded at four mixing times (60ms, 100ms, 120ms, 150ms) after the sample was checked to form the nematic phase at 298K from 2D-NMR spectra. Table 1 shows intrabackbone ROEs of Leu-enkephalin dissolved in CsPFO lyotropic liquid crystal at 298K obtained from the 100ms mixing time ROESY spectrum. The rate of sample rotation was 2.3kHz. The r.f. field strength used for spin locking was 2.0kHz and the carrier frequency was positioned at one end of the spectrum to avoid a Hartman-Hahn match. Interproton distances were calculated by making a correction for the effect of resonance offset¹⁾ and using the internal calibration distance between Gly² α methylene protons as 1.77 Å.

Table 1. Experimental Backbone Interproton Distances

residue	ROE type	Å	residue	ROE type	Å
Tyr ¹	$\alpha\text{H}_1\text{-NH}_2$	2.30	Leu ⁵	$\alpha\text{H}_5\text{-NH}_5$	2.49
Gly ²	$\alpha_1\text{H}_2\text{-NH}_2$	2.12			
	$\alpha_2\text{H}_2\text{-NH}_3$	2.65		$\text{NH}_2\text{-NH}_3$	2.60
Gly ³	$\alpha\text{H}_3\text{-NH}_3$	2.08		$\text{NH}_4\text{-NH}_5$	2.71
Phe ⁴	$\alpha\text{H}_3\text{-NH}_3$	2.74			

From these experiments, numerous ROEs could be detected, *i.e.*, 18 interresidue ROEs were obtained among a total of 37 ROEs. In a flexible system consisted of a small linear peptide such as enkephalin, long range NOEs

will be weak. Liquid crystal system is thought to be in such an intermediate flexibility condition. However, ROE is still sensitive to slow motions that induce unfavorable correlation time for the occurrence of NOE. Therefore MAS-ROESY is thought to be a powerful technique for the structural study in liquid crystal system.

Homonuclear dipolar couplings observed in liquid crystal NMR are known to give precise informations on molecular geometry. This technique, however, turns out to be helpless for complexed molecules containing, for example, more than 9 spins in a molecule because of the complexity of their NMR spectra.

Then the authors here intended to scale down such anisotropic interactions and obtain homonuclear dipolar couplings by means of sample spinning at an angle different from just the magic-angle. Direct coupling constants listed in Table 2 were obtained successfully from homo 2DJ experiment measured under sample rotating at the magic-angle $+1.0^\circ$, that is, at an angle of $+55.7^\circ$. These direct couplings can be expressed as follows²⁾:

$$D_{ij} = -\frac{\hbar\gamma_i\gamma_j}{4\pi^2r_{ij}^3} S_{ij} \quad (1)$$

where γ_i and γ_j are the gyromagnetic ratios of the interacting nuclei i and j separated by a distance r_{ij} , and S_{ij} is degree of order of the i - j vector. S_{ij} is defined as

$$S_{ij} = \sum_{p,q} \cos\alpha_p^{ij} \cdot \cos\alpha_q^{ij} \cdot S_{pq} \quad p, q = x, y, z \quad (2)$$

where α_q are angles between i - j vector and molecule fixed-coordinate system. S_{pq} are defined as

$$S_{pq} = \frac{1}{2} \langle 3\cos\theta_p \cos\theta_q - \delta_{pq} \rangle \quad p, q = x, y, z \quad (3)$$

where $\delta=1$ for $p=q$ and 0 otherwise.

To introduce direct couplings into conformational search, the pseudo potential energy represented by eq.4 was considered.

$$E_{DD} = W\{(D_{\text{calc}})^2 - (D_{\text{exp}})^2\}^2 \quad (4)$$

where E_{DD} is the pseudo energy composed of dipole couplings and W is a weighting factor.

Table 3. Direct Couplings observed and calculated at 298K

vectors	observed ^{a)}	calculated			order parameters	
		conformer 1	conformer 2		conformer 1	conformer 2
Tyr ¹ α -Tyr ¹ β_1	17.3	-17.5	-17.4	S _{XX}	-0.02144	-0.01991
Tyr ¹ α -Tyr ² β_1	17.3	-18.0	-18.5	S _{YY}	-0.02121	-0.02165
Gly ² α_1 -Gly ² α_2	11.4	-11.4	-11.4	S _{ZZ}	0.04264	0.04156
Gly ³ NH-Gly ³ α_1	4.22	4.24	4.34	S _{XY}	-0.00110	-0.00239
Gly ³ NH-Gly ³ α_2	4.22	4.18	4.34	S _{XY}	-0.00110	-0.00239
Leu ⁵ NH-Leu ⁵ α	8.44	8.42	8.50	S _{XZ}	0.00803	0.01488
Tyr ¹ Ar ₂ -Tyr ¹ Ar ₃	16.9	16.9	16.4	S _{YZ}	-0.00892	-0.01043
Tyr ¹ Ar ₅ -Tyr ¹ Ar ₆	16.9	16.9	16.4	S _{YZ}	-0.00892	-0.01043

a) absolute value

In the conformational search, 256 initial conformations were generated randomly and among these 2 energy minimum conformers were obtained with build-up method³⁾ using all ROE restraints. Then for each of these two conformers, 128 magnetic field directors were generated randomly and the pseudo potential energy(eq.4) defined by internal variables θ_X , θ_Y and θ_Z is minimized with Powell's conjugate gradient method using the experimental direct coupling data shown in Table 3. As a result, a set of magnetic field direction and order parameters was obtained successively from calculated values of penalty function. In the end, a conformational search was continued for both ROE and direct coupling restraints using a set of internal variables for the initial values that were obtained by the above mentioned procedures.

Thus obtained conformers and field directions are shown in Fig. 1. The orientation of Leu-enkephalin is also understood in Fig. 1 from the fact that CsPFO bilayer normal axis is parallel relative to the magnetic field direction⁴⁾. The results suggest 5 \rightarrow 2 β turn structure as a preferred conformation of Leu-enkephalin in anisotropic environment. And the side chain substituents of Tyr, Phe and Leu are deduced to be embedded in membrane matrix while the Leu carboxylate is just below the head groups of membrane.

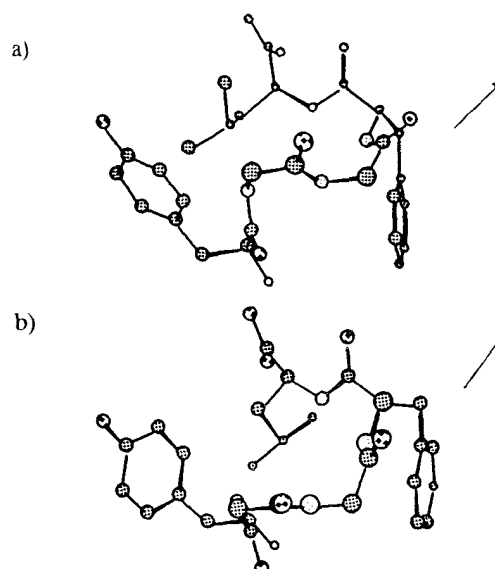


Fig. 1. Conformation and orientation of Leu-enkephalin. (a) Conformer 1, (b) conformer 2. The vector shown at the left side represents direction of the magnetic field direction.

References

1. C. Griesinger and R. R. Ernst, *J. Magn. Reson.* **75**, 261(1987).
2. C. L. Khetrapal, A. C. Kunwar, A. S. Tracey and P. Diehl, *Nuclear Magnetic Resonance Studies in Lyotropic Liquid Crystals*, in *NMR Basic Principles and Progress*, ed. by P. Diehl, E. Fluck and R. Kosfeld, Vol. 9, Springer, Heidelberg(1975).
3. W. Braun and N. Go, *J. Mol. Biol.*, **186**, 611(1985).
4. N. Boden, P. H. Jackson and K. McMullen, *Chem. Phys. Lett.*, **65**, 476(1979).

Tertiary Structure Determination of a Potent C5a Semi-synthetic Antagonist in Solution by Nuclear Magnetic Resonance Spectroscopy

Xiaolu Zhang, William Boyar, Matthew Toth, Nicholas Galakatos¹ and Nina C. Gonnella
Ciba-Geigy Corporation, Pharmaceuticals Division, 556 Morris Ave., Summit, N.J. 07901, USA.

Introduction:

The C5a protein is an inflammatory mediator implicated as a causative or aggravating agent in a variety of diseases including rheumatoid arthritis, adult respiratory distress syndrome (ARDS), pulmonary disease, psoriasis, select forms of renal disease, necrotizing vasculitis, lupus erythematosus, burn, adverse dialysis reactions, and ischemia (1). The generation of C5a can occur through a diverse number of mechanisms however its biological effect can only be initiated when C5a binds to its receptor on target cells. Because induction of a biological effect is dependent on the formation of a C5a-receptor complex, inhibition of C5a binding to the C5a receptor constitutes a therapeutic approach for modifying the course of these inflammatory diseases.

The tertiary structure of human recombinant (hr)-C5a (M^0) has been determined by NMR spectroscopy (2). This protein was found to exist as an anti parallel bundle of four helices stabilized by three disulfide linkages. The protein was also shown to possess a structurally undefined C-terminus from residue 64-74. Functional studies have been carried out which suggest that the regions of C5a that interact with the C5a receptor are widely dispersed in the core of the protein and at the C-terminus (2). Based on these results, two independent binding sites for the C-terminus and core region with the receptor were proposed.

As part of our drug discovery effort, a potent and selective semi-synthetic analog of C5a was prepared, having properties of a C5a receptor antagonist with no appreciable agonist response. Structural NMR studies were carried out on this protein and comparisons were made with the structure of hr-C5a (M^0) (2). The results showed a remarkable structural difference for the C-terminus of the semi-synthetic, not found in hr-C5a (M^0).

Here we report the three dimensional structure of this semi-synthetic C5a receptor antagonist in solution. The structure was generated using over 800 NOE distance constraints. Ensembles of 20 structures were calculated using molecular dynamics and simulated annealing algorithms. The unique structure of the C5a receptor antagonist was correlated with internally derived mutagenesis data (3) for hr-C5a (T^1M), showing the formation of a highly charged contiguous contact surface exclusively located in the core region of the protein. Implications of these findings in receptor binding and structure based drug design are discussed.

Experimental:

Preparation of Protein Samples: Human r-C5a(T^1M) and C5a 1-71 (T^1M , C^{27S} , Q^{71C}) were prepared as

glutathione adducts using procedures that were previously described (3). Uniform ^{15}N label (>98%) was incorporated into C5a 1-71 (T^1M , C^{27S} , Q^{71C}) using $^{15}NH_4Cl$ as the sole nitrogen source. Approximately 10 mg of protein was prepared which was 93% pure by HPLC analysis. ES-MS analysis of semi-synthetic protein found a mass of 8476 daltons; theoretical mass is 8477 daltons. The NMR samples were prepared by dissolving ^{15}N labeled or unlabeled protein in 0.5 ml of 90% H_2O and 10% D_2O or 100% D_2O under nitrogen gas. Samples were adjusted to pH 5.2 with dilute NaOH or HCl. Final sample concentrations were about 1-2 mM.

NMR: The NMR spectra were recorded at 303 °K on Bruker AMX 500 and DMX 600 spectrometers. All 2D spectra were acquired in the phase-sensitive absorption mode with quadrature detection in both dimensions using the time-proportional phase-incrementation method (4). Solvent suppression was achieved by low-power irradiation during the recycle delay (1.0-1.6 s). Proton resonances were assigned with the following experiments: COSY (5), Relayed-COSY (6), DQF and TQF COSY (7,8), TOCSY (9) and NOESY (10). NOESY experiments were also performed using a jump and return water suppression pulse sequence: [$t_0 - 90^\circ - t_1 - 90^\circ - t_m - (90^\circ_x - D - 90^\circ_x) - t_2$]_n. The NOESY spectra were recorded with 100, 150, and 200 ms mixing times. The NOEs were classified as strong (1.9-2.7 Å), medium (1.9-3.5 Å), and weak (1.9-5.0 Å) based on the cross peak integration. Hydrogen bonding constraints in the α -helical regions were derived from the observed slowly exchanging amide protons in the $^1H/^{15}N$ HMQC experiment in D_2O at pH 5.2, and 303 °K, as well as other NOEs which define α -helical structure. Data processing was carried out on a Silicon Graphics Onyx workstation using the Felix program (Biosym, Inc.). The FIDs for the initial t_1 value in each 2D data set were multiplied by 0.5 in order to eliminate t_1 ridge artifacts (11). For each spectrum both time domain signals were apodized with a 0-70° phase-shifted sine bell window function and then zero filled to 2048 or 4096 data points before Fourier transformation.

Structure Calculations: Structure calculations were carried out on a SG Onyx workstation using XPLOR 3.1. (12). The random set of linear starting structures was refined by simulated annealing to obtain good local geometry. Distance constraints used in the calculation of the semisynthetic antagonist structure consisted of three disulfide bonds between cystine residues 21-47, 22-54 and 34-55 (13), plus the core-tail disulfide linkage between Cys⁷¹ and Cys⁷², 31 hydrogen bonding constraints and 843 inter-proton distance constraints. Randomly sampled structures were subjected to the following simulated annealing protocol. Initial Minimization: $K_{bonds} = 1000$

¹Present Address: Venrock Associates, Rm. 5508, 30 Rockefeller Center, New York, N.Y. 10112, USA.

kcal/(mol Å²), K_{angles} = 500 kcal/(mol rad²), K_{planar} = 500 kcal/(mol rad²), K_{repel} = 1.0 kcal/(mol Å²), K_{NOE} = 50 kcal/(mol Å²), Asymptote = 0.1, van der Waals = 0.002, Simulation time = 50 steps; High Temperature: Temperature 2000 °K, Masses = 100 a.m.u., K_{bonds} = 1000 kcal/(mol Å²), K_{angles} = 200 → 500 kcal/(mol rad²), K_{planar} = 50 → 500 kcal/(mol rad²), K_{repel} = 1.0 kcal/(mol Å²), K_{NOE} = 50 kcal/(mol Å²), Asymptote = 1.0, van der Waals = 0.002, Timestep = 0.005 psec, Simulation time = 75 psec; Cooling: Temperature 2000 → 100 °K, Masses = 100 a.m.u., K_{bonds} = 1000 kcal/(mol Å²), K_{angles} = 500 kcal/(mol rad²), K_{planar} = 500 kcal/(mol rad²), K_{repel} = 0.9 → 0.75 kcal/(mol Å²), K_{NOE} = 50 kcal/(mol Å²), Asymptote = 1.0, van der Waals = 0.003 → 4.0, Timestep = 0.005 psec, Simulation time = 30 psec; Final Minimization: K_{bonds} = 1000 kcal/(mol Å²), K_{angles} = 500 kcal/(mol rad²), K_{planar} = 500 kcal/(mol rad²), K_{repel} = 0.75 kcal/(mol Å²), K_{NOE} = 50 kcal/(mol Å²), Asymptote = 1.0, van der Waals = 4.0, Simulation time = 1000 steps.

Results and Discussion:

The sequences for the core portions (residues 1-64) of both hr-C5a (T¹M) and the semi-synthetic are virtually identical with the exception of a mutation at residue 27 where the Cys glutathione adduct in hr-C5a (T¹M) is converted to serine. The antagonist's C-terminus however is quite different from that of hr-C5a (T¹M). In the semi-synthetic, residue 71 is converted from glutamine to cysteine and a synthetic portion, [Cys-Leu-Gly-(D-Arg)], is attached via a disulfide bond.

The NMR studies were carried out using either unlabeled or uniformly labeled (¹⁵N 1-71) semi-synthetic protein. Complete proton chemical shift assignments and analyses were made. Sequential assignments of proton resonances were carried out using the standard assignment procedures developed by Wüthrich (14). Stereospecific assignments were determined for 5 Valine methyl groups based on ³J_{αβ} coupling constants and NOE intensities (15). The ³J_{αβ} coupling constants for Valine residues 17, 18, 28, 56 and 57 were found to be greater than 9.4 Hz. These large ³J_{αβ} coupling constants indicate a g⁺ conformation where the α and β protons are in the *trans* conformation. Because the g⁺ conformation necessitates a shorter distance between NH and C^γH₃ than between NH and C^γH₂, a much stronger NOE intensity will exist between NH and C^γH₃. Stereospecific assignments could then be determined from NOE intensities between the amide protons and the γ-methyl protons. Stereospecific assignments were also made for β protons on residues Tyr¹³, Cys²², Tyr²³, Asp²⁴, Asn³⁰, Cys⁴⁷, Phe⁵¹, Cys⁵⁴, Cys⁵⁵, Asn⁶⁴ using a similar method described by Bundi and Wüthrich (16). Rotation states χ₁ about the αC-βC bond were established

based on ³J_{αβ} coupling constants and NOE intensities between intraresidue amide and β protons. Residues 22, 23, 24, 30 and 64 had χ₁ rotation states of -60 while residues 13, 47, 51, 54, and 55 had χ₁ rotation states of 180 which allowed unambiguous assignment of C^βH¹ and C^βH².

A total of 843 NOE distance constraints for the semi-synthetic antagonist were assigned from the NOESY spectra. Approximately 43% were intra-residue, 24% were sequential and the remaining 33% were medium to long range NOE interactions. The NOESY spectra contained a large number of amide-amide proton NOEs d_{NN(i,i+1)}, indicating a significant amount of secondary helical structure (17). Deuterium exchange experiments also showed slow exchange of amide protons on residues 10-12, 22-27, 37-39, 48, 50-58 and 60-63. Based on this data, four helical bundles were identified for residues 4-12, 17-25, 33-39, and 46-64. These results were virtually identical to that reported for C5a (M⁰) (2).

Published studies on the solution structure of hr-C5a (M⁰) revealed no conformational definition of the C-terminus (2). For the semi-synthetic however, the results were quite different. The amide region of the NOESY spectrum contained two unexpected resonances from the C-terminus to the core. These resonances were identified as amide-amide cross peaks between Val⁵⁷-Cys⁷¹ and between Lys¹⁴-Gly⁷⁴, consistent with the association of the tail with the core of the protein. Further analysis uncovered nineteen additional NOE constraints between the C-terminus and the core portion of the molecule.

Structure calculations were carried out using the NOE derived distance constraints. Twenty of the lowest energy tertiary structures of the semi-synthetic antagonist were selected and superimposed with a combined backbone r.m.s. deviation of 0.6 Å for all helices. All experimental distance constraints were satisfied with no violations greater than 0.5 Å.

The tertiary backbone structure of the core portion of the semi-synthetic antagonist, involving residues 1-64, was similar to that of hr-C5a (M⁰). Like hr-C5a, the antagonist consists of an antiparallel bundle of four helices connected by three flexible loop regions. One minor difference between the two proteins was observed in the orientation of the first helix. Unlike hr-C5a (M⁰), the first helix of the semi-synthetic is pushed away from the core, most likely to accommodate the folded back C-terminus. However the major difference between the two proteins resides in the C terminus which is conformationally restricted in the case of the semi-synthetic antagonist but remains conformationally undefined for hr-C5a (M⁰). Our results show that the C terminus portion of the C5a semi-synthetic antagonist is folded back and aligns itself in a groove between the first and fourth helix. The result was quite surprising considering prior structural studies of hr-C5a (M⁰) and other C5a analogs showed no definition of the tail portion of the protein (2, 18, 19). This conformationally restricted tail phenomenon may, in part, be attributed to a hydrophobic association between the core and the extended synthetic C-terminus. Examination of the tertiary structure has also

revealed the possibility of weak hydrogen bonding interactions between Tyr¹³ and Cys⁷¹, Glu⁵³ and Cys⁷² and Arg⁴⁶ and Arg⁷⁵.

This semi-synthetic compound represents the first potent C5a receptor antagonist discovered in this series of compounds. In vitro activities for hr-C5a (T¹M) and the semi-synthetic analog in human neutrophils are given below.

In Vitro Activities for C5a (T¹M) and the Semi-Synthetic Analog in Human Neutrophils

	Semi-synthetic analog	C5a (T ¹ M)
Mem. ^a Binding (nM)	0.7	0.007
<u>Ca Rise</u> ^b		
IC ₅₀ (nM) ^c	400	-----
EC ₁₀ (nM) ^d	13,300	0.01

a) Membrane binding assay was performed as described by Braunwalder et. al. (20).

b) Calcium Rise assay was performed as described by Seligmann et. al. (21).

c) IC₅₀ values are defined as the concentration of antagonist needed to reduce the calcium rise response of the 100 pM C5a challenge by 50%.

d) EC₁₀ values are defined as that concentration of compound needed to elicit 10% of the maximum calcium rise response produced by the compound.

Extensive random mutagenesis studies were carried out on hr-C5a (T¹M)(3). Membrane and whole cell binding assays, performed on the individual mutant analogs, suggested that the core contact residues involved in receptor binding include His¹⁵, Leu⁴³, Arg⁴⁶ and Lys⁴⁹, while Arg⁷⁴ was identified as a single contact residue in the tail domain (3). When these contact residues were mapped onto an internally derived three dimensional structure of hr-C5a (T¹M), a highly charged contact surface was formed from residues His¹⁵, Arg⁴⁶ and Lys⁴⁹ in the core of the protein however the position of terminal Arg⁷⁴ remained undefined. The key contact residues were subsequently mapped on to the tertiary

structure of the C5a semi-synthetic antagonist. A contiguous highly charged contact surface was formed involving residues His¹⁵, Arg⁴⁶, Lys⁴⁹ and DArg⁷⁵. As illustrated in Figure 1, the conformational restriction of the C-terminus situates the terminal DArg⁷⁵ in a wedge between His¹⁵ and Arg⁴⁶.

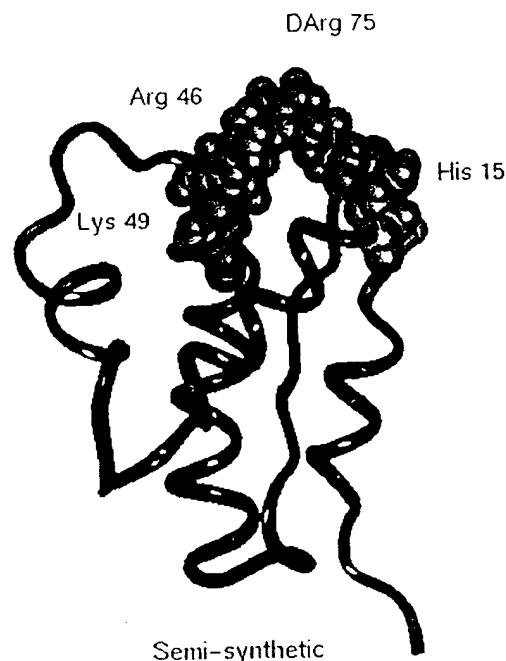


Figure 1. Structure of the semi-synthetic antagonist with key contact residues displayed as a van der Waals surface.

The unique structural features of this antagonist may be quite significant with respect to its interaction with the C5a receptor. In the absence of structural data for the C5a-receptor complex, several hypotheses have been proposed invoking a two-site receptor-ligand model for C5a, where the core binds to receptor site 1 and the C-terminus binds to receptor site 2 (22, 23). These hypotheses were based on the knowledge that removal of the C-terminal arginine diminishes agonist activity whereas the biologically inactive derivative C5a (1-69) is still capable of binding to the receptor (22). Other studies involving N-terminal truncation of the C5a receptor have shown a loss of C5a binding but not C-terminal peptide binding. These results suggest that the initial site of binding is between the extracellular N-terminus of the receptor and the core of C5a, and that it is this interaction that can be disrupted by antagonists (23).

The N-terminus of the C5a receptor is known to contain seven aspartic acid residues hence binding energy can be attributed to contact between negatively charged residues on the receptor and positively charged residues on the ligand. Since the restriction of the semi-synthetic's C-terminus places the terminal DArg⁷⁵ in the vicinity of the other core contact residues, this orientation results in the formation of a positively charged contiguous surface clustered at the top

of the protein. Based on what is currently known, it is likely that the antagonist properties exhibited by the semi-synthetic are the result of the interaction of this ligand's positively charged surface with the N-terminus of the receptor. Thus while the two site model may explain the relationship of C5a with its receptor, our results suggest the formation of a single binding site between the semi-synthetic antagonist and the extracellular N-terminus of the C5a receptor.

From the standpoint of structure based drug design, this cationic surface presents intriguing possibilities. Since these contact residues possess only a 6 Å separation, smaller peptidic structures may be modeled to mimic both the size, shape, and charge distribution of the contact surface with the ultimate goal of producing a nonpeptidic mimic of the contact surface. Our results provide a surface template for incorporating these features which may ultimately lead to a small selective mediator to effectively block the activity of C5a.

In summary, the tertiary structure of a potent C5a antagonist has been determined. Unlike C5a, this structure was shown to possess a conformationally restricted C-terminus. The structural information combined with mutagenesis data revealed the formation of a positively charged contiguous surface which suggests a single binding site with the C5a receptor. This charged contact surface can serve as a template for structure based drug design.

References:

1. T. Hugli, *Crit. Rev. Immunol.* **1**, 321 (1981).
2. E.R.P. Zuiderweg, D.G. Nettesheim, K.W. Mollison, G.W. Carter, *Biochemistry* **28**, 172 (1989).
3. M. Toth, L. Huwyler, W. Boyar, A. Braunwalder, D. Yarwood, J. Hadala, W. Haston, M. Sills, B. Seligmann, and N. Galakatos, *Protein Science* **3**, 1159 (1994).
4. D. Marion, and K. Wüthrich, *Biochem. Biophys. Res. Commun.* **113**, 967 (1983).
5. W. P. Aue, E. Bartholdi, and R. R. Ernst, *J. Chem. Phys.* **64**, 2229 (1976).
6. G. Eich, G. Bodenhausen, R. R. Ernst, *J. Am. Chem. Soc.* **104**, 3731 (1982).
7. I. Braunschweiler, G. Bodenhausen, R. R. Ernst, *Mol. Phys.* **48**, 535 (1983).
8. M. Rance and P. E. Wright, *J. Magn. Reson.* **66**, 372 (1986).
9. D. G. Davis and A. Bax, *J. Am. Chem. Soc.* **107**, 2820 (1985).
10. J. Jeener, B. H. Meier, P. Bachmann, and R. R. Ernst, *J. Chem. Phys.* **71**, 4546 (1979).
11. G. Otting, H. Widmer, G. Wagner, and K. Wüthrich, *J. Magn. Reson.* **66**, 187 (1986).
12. A.T. Brünger, *X-PLOR Version 3.1: A System for X-ray Crystallography and NMR* (Yale Univ. Press, New Haven, CT, 1993).
13. B. Zimmerman and W. Vogt, *Hoppe Seyler's Z. Physiol. Chem.* **365**, 151 (1984).
14. K. Wüthrich, *NMR of Proteins and Nucleic Acids* (John Wiley & Sons, New York, 1986).
15. E.R.P. Zuiderweg, R. Boelens and R. Kaptein, *Biopolymers* **24**, 601 (1985).
16. A. Bundi and K. Wüthrich, *Biopolymers* **18**, 285 (1979).
17. M. Billeter, W. Braun, and K. Wüthrich, *J. Mol. Biol.* **155**, 321 (1982).
18. M.P. Williamson and V.S. Madison, *Biochemistry* **29**, 2895 (1990).
19. J. Zarbock, R. Gennaro, D. Romeo, G.M. Clore, and A.M. Gronenborn, *FEBS. Letters* **238**, 289 (1988).
20. A.F. Braunwalder, D. Musmanno, N. Galakatos, R. Garlick, W. Haston, J. Rediske, L. Wennogle, B. Seligmann, and M. Sills, *Mol. Immunol.* **29**, 1319 (1992).
21. B. Seligman, K. Patel, W. Haston, J.J. Rediske, *Agents and Actions* **21**, 375 (1987).
22. D.E. Chemoweth and T.E. Hugli, *Mol. Immunology* **17**, 151 (1980).
23. S.J. Siciliano, T. Rollins, J. DeMartino, Z. Konteatis, L. Malkowitz, G. Van Riper, S. Bondy, H. Rosen and M. Springer, *Proc. Natl. Acad. Sci. USA* **91**, 1214 (1994).

Proton Magnetic Resonance Study of High Resolution Solution Structure of
Hordothionin- α

Kyou-Hoon Han*§, Kyu-Hwan Park*, Hyun-Ju Yoo*, Hoon Cha†, Se Won Suh†,
Fairwell Thomas‡, Tae-Sung Moon*, and Seung-Moak Kim*

* Laboratory of Biological Analysis, Korea Research Institute of Bioscience and
Biotechnology, KIST, Yusong P.O. Box 115
Taejon, 305-600, Korea

† Department of Chemistry, Seoul National University, Seoul, 151-742, Korea

‡ Molecular Disease Branch, National Heart, Lung and Blood Institute, NIH, Bethesda,
Maryland 20892 U. S. A.

The high resolution three-dimensional solution structure of hordothionin- α obtained from Korean barley was determined using two-dimensional nuclear magnetic resonance techniques combined with distance geometry and restrained molecular dynamics. Combined use of TOCSY, DQF COSY and NOESY spectra according to the sequential resonance assignment procedure has allowed a complete resonance assignment for this 45-residue plant toxin protein. Total of 292 interproton distance restraints measured from NOE experiments were supplemented, at the second stage of distance geometry calculations, by the skewed biharmonic potential terms representing the 16 hydrogen bond restraints, 4 disulfide bridge restraints for distance geometry and restrained molecular dynamics calculations. Also included in the calculations were 36 ϕ and 17 χ^1 torsion angles obtained from $^3J_{HN\alpha}$ and $^3J_{\alpha\beta}$ coupling constants in DQF COSY and P.E. COSY experiments, respectively. Restrained molecular dynamics calculations followed an annealing strategy which included 1000 cycles of initial energy

minimization, 5 ps of restrained molecular dynamics at 1000 K, 25 ps of cooling down to 300 K, additional dynamics calculation for 5 ps followed by the final 500 cycles of energy minimization. The overall protein fold is similar to crambin or purothionin- α 1 which maintains a very stable structure through 3 or 4 disulfide bridges. Two α -helices running in opposite direction are found based upon $^3J_{HN\alpha}$ and $^3J_{\alpha\beta}$ and deuterium exchange rates for backbone NH protons and encompass the residues 7T-18V and 22Q-28V. These two helices are connected by a turn and form a *helix-turn-helix* motif. A short stretch of an anti-parallel β -sheet exists between the residues 1K-4C and 31C-34T. The two protein termini of hordothionin- α are "well-anchored": the N-terminus of the protein is immobilized by this short β -sheet whereas the C-terminus is "pasted" to the carbonyl group of 4C by a very stable hydrogen bond. A homodimeric model of hordothionin- α can be proposed based upon the very slow deuterium exchange rates for the amide protons of L15-V18. In such a model the dimeric interface is stabilized

by hydrophobic interactions between the side chains of these residues. This model can favorably account for the initial binding mode of thionins to membranes. The average *rms* differences for the backbone and heavy atoms after the restrained molecular dynamics calculations are 0.62 and 1.16

Å respectively. These numbers represent a significant improvement over the corresponding values for the previous NMR structures of other thionins. The distance violation from the experimental interproton distances for the final structures is 0.14 Å for all atoms.

Nuclear Magnetic Resonance Solution Structure of Calciseptine, a Small Protein with Ca²⁺ Channel Blocking Activity from Black Mamba (*Dendroaspis polylepis polylepis*)

H. Haruyama, T. Takayama and H. Hanzawa

Anal. and Metabolic Res. Lab., Sankyo, Co., 2-58 Hiromachi 1-chome, Shinagawa-ku, Tokyo 140 Japan

Introduction

Calciseptine is a small protein isolated from the venom of the black mamba (*Dendroaspis polylepis polylepis*), containing 60 amino acid residues with four disulfide bridges⁽¹⁾. In spite of its moderate sequence homology with short neurotoxins and cardiotoxins, including disulfide bridging resemblance, calciseptine exhibits no biological activities associated with these related toxins, but is a specific antagonist of L-type calcium channel. For understanding the three dimensional structural basis of the observed differences in biological activity, solution structure of calciseptine was determined.

Result and Discussion

The concentration of calciseptine used for recording homonuclear and heteronuclear 2D experiments were 4.0mM and 8.0mM, respectively, in 90% H₂O/ 10% D₂O or 100% D₂O at pH 5.5. The spectra were recorded on JEOL GSX-500 or A-500 spectrometer at 20 °C and 35 °C. Almost complete sequential assignments summarized in Fig. 1 was achieved by the combination of the well-established strategy based on homonuclear 2D-NMR spectra and the analysis of natural abundance ¹H - ¹³C HSQC and HSQC - NOESY spectra.

The heteronuclear experiments were used in cases where the homonuclear 2D-NMR based strategy failed, the failure being due to ¹H signal overlapping and unexpected chemical shift values. For example, the overlapping α CH and δ CH₂ of Pro 47 around 3.16 ppm were clearly resolved in the ¹H - ¹³C HSQC spectrum due to the well dispersed chemical shifts of the corresponding C α and C δ carbons. The presence of sequential NOE between α CH (Trp 46) and α CH (Pro 47) was unambiguous in the HSQC-NOESY spectrum, indicating a cis - peptide linkage between Trp 46 and Pro 47.

β - strands identified by stretches of strong sequential d _{α N} (i, i + 1) NOEs and large ³J_{NH α} coupling constants could be arranged in a short double - stranded (I and II in Fig. 1) and triple - stranded β - sheet (III, IV and V) according to the long range backbone - backbone NOEs, d _{α N} (i, j) and d _{$\alpha\alpha$} (i, j). A β - bulge between Ser 35 and Glu 36 was suggested by the presence of a strong NOE between NH (Ser 35) and NH (Glu 36). A backbone fold was obtained by the distance geometry calculation with DIANA followed by a simulated annealing refinement with XPLOR, in which 480 distance constraints (433 derived from by NOEs, 24 from disulfide bonds and 23 from dihedral angle constraints) were used (see Fig. 2). The average pairwise RMSD among 15 structures was 1.62 Å for the backbone region.

As expected from the primary sequence homology, the resulting overall fold comes close to that of other neurotoxins and cardiotoxins. Three loops extend from a core region consisting of invariant residues including four disulfide bridges. The short double - stranded β - sheet corresponds to the middle part of loop I. The β - strands III and IV corresponding to the middle part of loop II were connected by a turn comprising Arg 28 - Ile 34 which is followed by a β - bulge at Ser 35 - Glu 36. Consequently, the tip of loop II becomes longer and rather similar to that of cardiotoxins. The β - strand V, which corresponds to the inner strand of loop III, forms hydrogen bonds with the β - strand IV in loop II and completes the well defined triple stranded β - sheet. The tip of loop III (45 - 48) is a type VI turn characterized by cis - Pro at the third position. Here, Trp - cis Pro - Tyr is reported to be in favor of inducing this type of turn. Apart from the fact that this portion does not have any sequential homology with the neurotoxins nor cardiotoxins, the observation that the similar type VI turn is also observed in leualacin, a

depsipeptide isolated from *Hapsidospora irregularis*, with Ca^{2+} channel blocking activity suggests the possibility that this is responsible for its activity as a L type Ca^{2+} channel blocker (2). Studies to examine this possibility is presently ongoing in our laboratory.

References

- (1) De weille, J. R., Schweitz, H., Maes, P., Tartar, A. and Ladzdunski, M. (1991) Proc. Natl. Acad. Sci. USA **88**, 2437-2440
 (2) Yoda, K., Haruyama, H., Hamano, K. and Tanzawa, K., Tetrahedron **50**, 6537-6548 (1994)

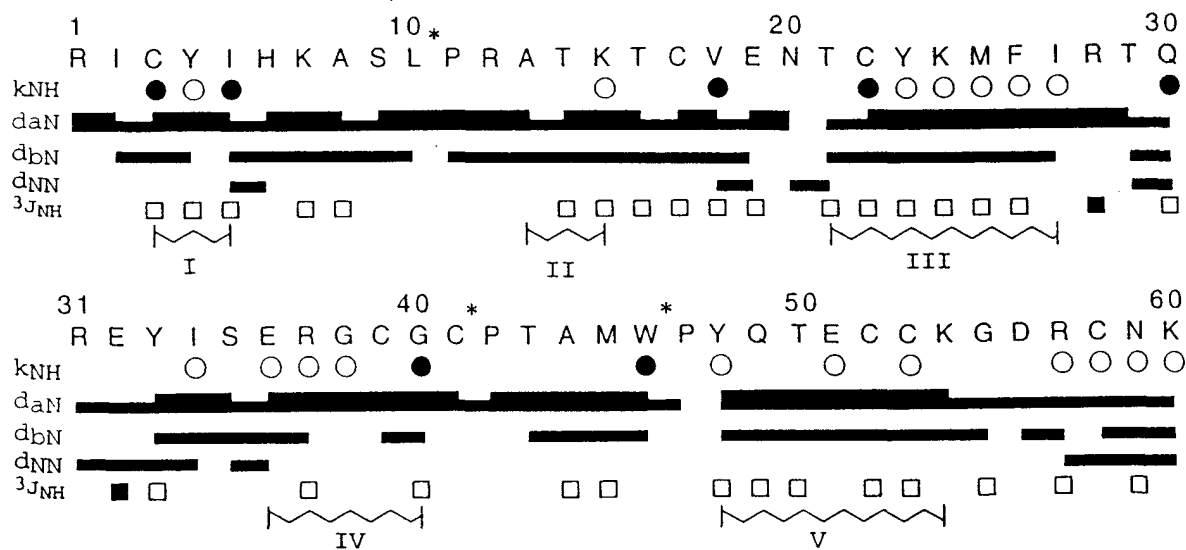


Fig. 1. Amino acid sequence of Calciseptine and a summary of the sequential NOE connectivities ($d_{\alpha N}$, $d_{\beta N}$, d_{NN} ; thickness of the bars reflecting NOE intensities. *: $d_{\alpha\delta}$ for Leu 10 - Pro 11 and Cys 41 - Pro 42, $d_{\alpha\alpha}$ for Trp 46 - Pro 47), slowly exchange protons (k_{NH} ; ●: $k_{NH} < 10^{-5} \text{ min}^{-1}$, ○: $10^{-5} \text{ min}^{-1} < k_{NH} < 10^{-2} \text{ min}^{-1}$), and NH - αCH coupling constants ($^3J_{NH}$; ■: $^3J_{NH\alpha} < 7.0 \text{ Hz}$, □: $^3J_{NH\alpha} > 8.0 \text{ Hz}$).

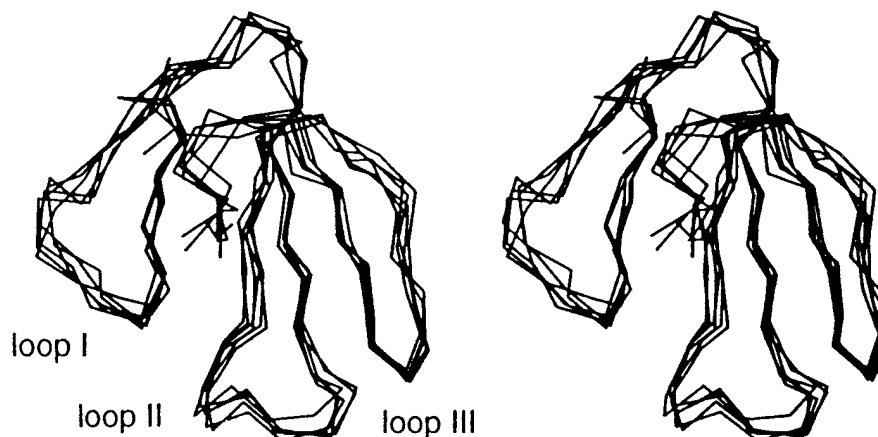


Fig. 2. stereopair of the superpositions of the 6 converged structures of Calciseptine.

Are NMR Chemical Shift Calculations of Small Molecules Inexpensive You Get What You Pay For!

*J.F. Hinton, K. Wolinski, P. Kozlowski, and P. Pulay
Department of Chemistry, University of Arkansas
Fayetteville, Arkansas 72701 USA*

The calculation of NMR chemical shielding parameters using the ab initio quantum mechanical method, GIAO (1,2), can produce quite accurate values. However, there are a number of factors that one must consider in order to obtain reliable results. Even the calculation of the chemical shielding parameters of small molecules can be very computer intensive when these factors are taken into account. The GIAO calculation of the ^{13}C chemical shift parameters of glycine ($^+\text{NH}_3\text{CH}_2\text{COO}^-$), the smallest of the amino acids, is presented to illustrate how computer intensive the calculation can become to obtain accurate results. For glycine a relatively high level of basis set, electron correlation, hydrogen bonding, and a large molecular system are required to obtain chemical shielding parameters that are in agreement with experimental results.

The molecular geometry and crystal structure of glycine ($^+\text{NH}_3\text{CH}_2\text{COO}^-$) used for the theoretical calculations were those obtained by neutron diffraction (3). The experimental chemical shift parameters for glycine were obtained using solid state NMR spectroscopy (4).

A careful study of the effect of basis set on the chemical shift parameters revealed that above the 6-31G(d,p) level, all basis sets gave about the same results. For example, the values of the principal components of the chemical shift tensor for the carboxy carbon, δ_{11} ppm, δ_{22}

ppm, and δ_{33} ppm relative to TMS obtained with the basis sets 6-311G(d,p); 6-311G⁺(d,p); 6-311G⁺(2d,p); 6-311G⁺⁺(df,pd); and gc-TZP(spdf/sp) are 283.22, 128.38, 108.36; 285.71, 136.22, 106.50; 284.75, 136.81, 109.20; 285.14, 136.70, 106.17; and 284.54, 135.62, 109.69, respectively. The experimentally determined values are $\delta_{11} = 246 \pm 1$ ppm, $\delta_{22} = 179 \pm 1$ ppm, and $\delta_{33} = 106 \pm 1$ ppm. The theoretical isotropic chemical shift, $1/3(\delta_{11} + \delta_{22} + \delta_{33})$, given by each basis set is in excellent agreement with the experimentally determined value. However, the chemical shift anisotropy agreement is poor. Consequently, one should never use the isotropic chemical shift value as a criterion for the accuracy of the theoretical calculation.

For heavy atoms, particularly those involved in multiple bonding or lone electron pairs, electron correlation must be considered when performing a chemical shielding calculation. The effect of inclusion of electron correlation on the chemical shielding parameters of glycine is quite significant. The values of the tensor components obtained with the basis set 6-311G^{**} with electron correlation (density functional theory) are $\delta_{11} = 273.63$, $\delta_{22} = 137.00$, and $\delta_{33} = 113.44$. These values are in better agreement with the experimental values, but are still not satisfactory.

One must now confront a particularly important problem with the calculations.

Is the molecule in the computer the same as that in the NMR spectrometer? The unit cell of glycine contains two hydrogen bonded dimers. Consequently, one can not perform a calculation on a monomer and expect to reproduce experimental results. If one considers five unit cells and selects a glycine molecule that is hydrogen bonded to four other glycine molecules, not all from the same unit cell, and performs a chemical shielding calculation for the carboxyl and C_α carbons on it better agreement is obtained with the experimental values. The 6-311G⁺(d,p) basis set was used for these calculations. For the carboxyl carbon, $\delta_{11}=269.16$ ppm, $\delta_{22}=188.55$ ppm, and $\delta_{33}=97.44$ ppm. These values indicate the importance of considering the molecular system and not just the single molecule when comparing the theoretical and experimental values. For the C_α carbon the calculated values of the tensor components are $\delta_{11}=63.85$ ppm, $\delta_{22}=45.84$ ppm, and $\delta_{33}=21.75$ ppm. The experimental values for the C_α carbon are $\delta_{11}=61 \pm 3$ ppm, $\delta_{22}=46.1 \pm 1$ ppm, and $\delta_{33}=24 \pm 5$ ppm. For the C_α carbon the theoretical results are in exceptionally good agreement with the experimental values; however, the chemical shift anisotropy calculated for the carboxyl carbon is still too large. This would suggest the necessity of including electron correlation in the calculation for the pentamer based upon the results obtained with the monomer.

In summary, ab initio quantum mechanical calculations of the chemical shielding parameters of even small molecules can be very computer intensive. To obtain accurate results one must use a relatively large basis set and in some cases electron correlation. The molecule in the computer must be similar to the molecule or molecular system in the NMR

spectrometer. With care, very accurate chemical shielding parameters can be obtained. In the near future parallel processing, new electron correlation methods and faster computer workstations will enable one to perform such calculations for large molecules efficiently and accurately.

REFERENCES

- ¹R. Ditchfield, *Mol. Phys.* **27**, 789 (1974).
- ²K. Wolinski, J. F. Hinton and P. Pulay, *J. Amer. Chem. Soc.* **112**, 8251 (1990).
- ³P.-G. Jösön and A. Kvick, *Acta Cryst.* **B28**, 1827 (1972).
- ⁴C.Y. Ye, R. Fu, J. Hu, L. Hou and S. Ding, *Magn. Reson. Chem.* **31**, 699 (1993).

A Method for Removing Geminal Proton Resonances from Oligonucleotide Spectra: 1D and 2D Applications

Hilary A. Berthon and Max A. Keniry

Research School of Chemistry, The Australian National University,
Canberra, ACT 0200, Australia

While ^1H NMR methods have proven invaluable in the determination of the conformation and dynamics of small oligonucleotides in solution, the situation is less favorable when there is a substantial bend in the DNA backbone, when bases are displaced from the helix axis, or when an aromatic drug binds to the DNA. In these cases, aromatic ring currents shift resonances out of their well-defined regions in the NMR spectrum, or drug proton resonances may overlap with DNA proton resonances.

This poster illustrates two closely related methods for suppressing geminal proton resonances in the NMR spectra of DNA. Both methods use J-modulation of the large geminal $\text{H}2'\text{-H}2''$ coupling in DNA to edit the spectrum. The HAL experiment was previously used to suppress the two-spin cytosine H5-H6 doublets in DNA spectra (1). We show that when the J-modulating delay is set to match the DNA $\text{H}2'\text{-H}2''$ geminal coupling, these multispin systems can be suppressed in the spectra of large fragments of DNA. We also show that a gradient analog of the SQF experiment (2), previously used to edit the spectra of small molecules (3) can also be employed to suppress geminal proton resonances. This latter experiment is superior at retaining the other deoxyribose resonances and requires no phase cycling. By employing the gradient experiment as a NOESY detection pulse (Figure 1), we are able to detect internucleotide methyl-H1' crosspeaks that are concealed by several overlapping crosspeaks involving $\text{H}2'$ and $\text{H}2''$ resonances in the NOESY spectrum of a DNA quadruplex.



Figure 1: A two dimensional NOESY experiment which employs gradients to suppress multiplets. The delay τ is set to $1/(2J_{2'2''})$. The delay δ was set to the duration of the gradient G_2 . The durations and strengths of the gradients are as follows: G_1 , 500 μs and 20 G/cm; G_2 , 50 μs and 30 G/cm; G_3 , 500 μs and 10 G/cm. The phase cycling is $\phi_1 = x, -x, y, -y, -x, x, -y, y$; $\phi_2 = 2(x), 2(y), 2(-x), 2(-y)$; $\phi_3 = 8(x), 8(y), 8(-x), 8(-y)$; $\phi_4 = 8(-x), 8(-y), 8(x), 8(y)$; $\phi_{\text{rec}} = 4(y, -y)$; the phase of ϕ_1, ϕ_2 and ϕ_{rec} is incremented by 90° every eight scans.

Both the HAL pulse sequence (1) and the gradient pulse sequence (3) use a Hahn spin echo to refocus the chemical shift terms while allowing the scalar coupling terms to evolve. In the experiment of Figure 1, gradient pulses are applied during the refocusing period to eliminate the effects of imperfections in the 180° pulse (4). At the end of the refocusing period, a spin-locking pulse is used to dephase the unwanted magnetization but retain the desired magnetisation in the HAL experiment, whereas in the gradient experiment the desired magnetisation is stored along the z axis by applying a 90_x pulse. All remaining transverse and multiple quantum components in the latter experiment are then dephased by the pulsed field gradient and the previously stored I_z magnetisation is converted into observable magnetisation by a 90_x pulse.

In the presence of Na^+ , two d(GGGTTTGGG) strands associate to form a G-quadruplex with three G-quartets (5). Each d(GGGTTTGGG) strand is folded into a highly-structured hairpin loop at the T_4 segment. Analysis of the NMR spectra is complicated by the magnetic inequivalence of the two strands and substantial ring current shifts of some of the $\text{H}2'$, $\text{H}2''$, $\text{H}4'$ and thymine methyl resonances. As a consequence, there is considerable spectral overlap of all these resonance groups.

An expansion of a NOESY spectrum of the quadruplex is given in Figure 2A. When the modified NOESY experiment (Figure 1) is employed, all the broad crosspeaks involving $\text{H}2'$ or $\text{H}2''$ resonances in the F2 dimension are suppressed and only methyl-base and methyl-H1' crosspeaks remain (Figure 2B). This effect is most easily seen at the $T_4\text{H}2'$ resonance position (1.36 ppm) where all three crosspeaks to $T_5\text{H}6$, $T_4\text{H}6$ and $T_4\text{H}1'$ are no longer observed in the modified NOESY experiment (Figure 2B). The benefits of the experiment are most easily seen by focusing on the boxed regions in Figure 2. In the normal NOESY spectrum (Figure 2A), the boxed region encloses the very intense $T_6\text{H}2'\text{-T}6\text{H}1'$ and the less intense $T_16\text{H}2'\text{-T}15\text{H}1'$ and $T_6\text{H}2'\text{-T}5\text{H}1'$ crosspeaks which overlap and conceal the non-sequential internucleotide $T_7\text{Me-T}5\text{H}1'$ and $T_17\text{Me-T}15\text{H}1'$ crosspeaks. The latter four crosspeaks arise because there are sharp turns in the backbone of the quadruplex at $T_5\text{pT}6$ and $T_15\text{pT}16$. In the equivalent region of the modified NOESY experiment optimised for the $\text{H}2'\text{-H}2''$ J coupling (Figure 2B), the $T_6\text{H}2'\text{-T}6\text{H}1'$, $T_6\text{H}2'\text{-T}5\text{H}1'$ and $T_16\text{H}2'\text{-T}15\text{H}1'$

crosspeaks are suppressed and the T7Me-T5H1' and T17Me-T15H1' crosspeaks are selectively observed.

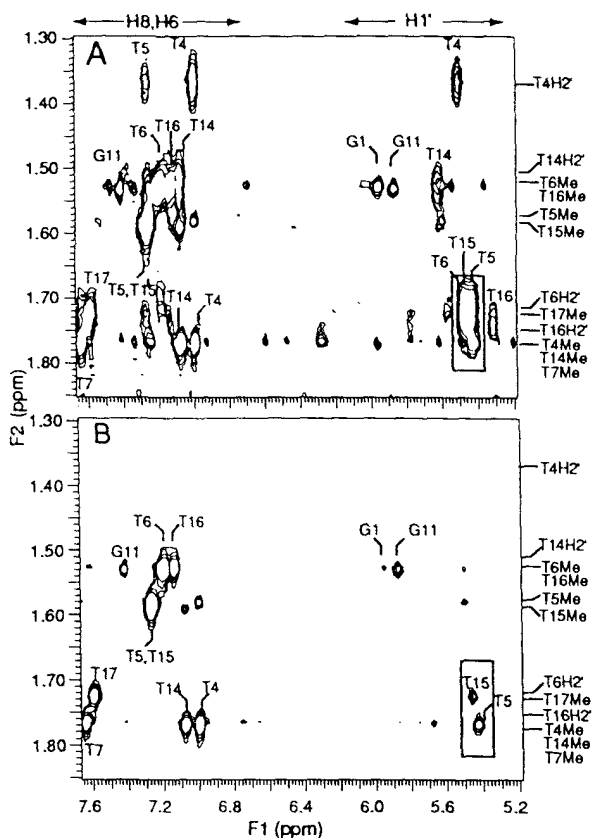


Figure 2: Expansions of (A) NOESY spectrum and (B) edited NOESY spectrum of $[d(\text{GGGTTTTGGG})]_2$ obtained with the pulse sequence given in Figure 1. Spectra were obtained at 20 °C on a Varian VXR 500S NMR spectrometer fitted with pulsed field gradient apparatus and probe. The sample was 1.9 mM $[d(\text{GGGTTTTGGG})]_2$ in 400 μl of 10 mM phosphate buffer (100% $^2\text{H}_2\text{O}$; 100 mM NaCl; pH 6.5). 4096 complex points, 2×352 t1 increments, 32 transients per increment, a 200 ms mix time and a 3 s recycle delay were used. The delay τ was 40 ms. Phosphorus decoupling in F2 was achieved by WALTZ-16 decoupling at a field strength of 625 Hz during the acquisition time. The F2 assignments are labelled at the edge of the spectrum and the F1 assignments are labelled adjacent to each crosspeak.

We have also applied the modified NOESY pulse sequence with success to a drug-oligonucleotide complex, mithramycin- Mg^{2+} - $d(\text{ACCCGGGT})_2$, that has a total molecular weight in excess of 10 kDa. The 7-methyl protons of mithramycin(1) and (2) resonate in the same region as the H2' and H2'' protons of the

oligonucleotide (6) causing this region of the unedited NOESY spectrum to appear quite complex. In such extreme cases, it is advisable to shorten the τ delay and accept less than perfect suppression of the H2' and H2'' resonances; we found $\tau \approx 24$ ms gave acceptable suppression of the H2' and H2'' resonances for this sample. Alternatively, the τ delay in a constant-time NOESY experiment (7) may be adjusted to selectively remove protons with a given coupling constant. The modified NOESY experiment (Figure 1) is best suited for slowly tumbling macromolecules larger than 5 kDa, for which the antiphase crosspeaks that arise from coherences that have followed the zero quantum pathway are most attenuated by the broader lines in these spectra.

In conclusion, we are able to selectively suppress the H2' and H2'' proton resonances in NMR spectra of non-linear DNA and drug-DNA complexes, enabling us to identify other resonances that are overlapped or to reveal NOESY crosspeaks that are concealed by intense crosspeaks that involve H2' and H2'' resonances. Because the gradient experiment utilises evolution under the influence of J coupling to suppress the undesired resonances, it can be employed in any macromolecule where the undesired resonances have a much larger J coupling constant than that of the desired resonances. It is anticipated that this technique might also be used to suppress the H5', H5'', H3' and H4' resonances in RNA. The technique, however, works optimally when the desired resonances are protons with little or no J coupling.

Acknowledgments

The contribution of E.A. Owen in the purification of the oligonucleotide is gratefully acknowledged.

References

- 1C. Kojima and Y. Kyogoku, *J. Magn. Reson., Ser. B* 102, 214-217 (1993).
- 2C. Kojima and Y. Kyogoku, *J. Biomol. NMR* 4, 181-191 (1994).
- 3G. A. Naganagowda, *J. Magn. Reson., Ser. A* 113, 235-237 (1995).
- 4A. Bax and S. S. Pochapsky, *J. Magn. Reson.* 99, 638-643 (1992).
- 5F. W. Smith, F. W. Lau and J. Feigon, *Proc. Natl. Acad. Sci. USA* 91, 10546-10550 (1994); G. D. Strahan, R. H. Shafer and M. A. Keniry, *Nucleic Acids Res.* 22, 5447-5455 (1994); M. A. Keniry, G. D. Strahan, E. A. Owen and R. H. Shafer, *Eur. J. Biochem.* 233, 631-643 (1995).
- 6M. A. Keniry, D. L. Banville, P. M. Simmonds and R. Shafer, *J. Mol. Biol.* 231, 753-767. (1993).
- 7A. Bax and R. Freeman, *J. Magn. Reson.* 44, 542-561 (1981); J. Santoro, M. Bruix, C. González, J. L. Nieto and M. Rico *J. Biomol. NMR* 2, 647-653 (1992).

^1H , ^{13}C , ^{15}N , and ^{31}P NMR methods for studying metabolites in an N_2 -fixing root nodule symbiosis, *Alnus incana* \times *Frankia*.

Peter Lundberg ^{α} , Per-Olof Lundquist ^{β} , and Kerstin Huss-Danell ^{γ}

^{α} Department of Physical Chemistry, University of Umeå, S-901 87 Sweden;

^{β} Dept of Agronomy and Plant Genetics, University of Minnesota, St Paul, MN 55108, USA;

^{γ} Dept of Crop Science, Swedish University of Agricultural Sciences, PO Box 4097, S-904 03 Umeå, Sweden.

I. Introduction

Alnus incana is a tree which benefits from a symbiotic relationship with the actinomycete *Frankia*, a filamentous Gram-positive soil bacterium in root nodules. The nodules contain both uninfected and *Frankia* infected plant cells (an infected cell can contain ~10–15% (v/v) bacteria). *Frankia* has the ability to reduce gaseous nitrogen to ammonium, which can be assimilated through the nitrogen metabolism of the plant. All *Alnus* specimens in nature have been found to have root nodules. The symbiosis makes it possible for *Alnus* to occupy habitats which would otherwise be unsuitable because of low nitrogen availability in soil (1–3).

We have used ^{31}P and ^{15}N NMR (5–7, 9) to investigate the metabolic processes controlling assimilation of ammonium in root nodules of *Alnus incana*. We have also attempted to identify the major metabolites (using NMR (4)), involved in the metabolism of the root nodules, that are markers for the symbiotic relationship between *Alnus incana* and *Frankia*.

II. Material and Methods

1. Samples

We used *Alnus incana* plants (0.5–1 m tall specimens) which had been infected with a local source of *Frankia* bacteria. The nitrogen fixing nodules produced on the roots were used for perfusion experiments, as well as for extracts. The specimens were kept in a growth chamber with controlled temperature and light period for several weeks prior to the experiments.

2. In vivo NMR

We have used ^{31}P NMR (at 11.8 T) to investigate levels of 'energy carrying metabolites' in intact perfused root nodules. Also we perfused the samples with a medium containing ^{15}N labeled ammonium and followed the assimilation of nitrogen, and formation of amino acids using ^{15}N NMR (at 11.8 T). A perfusion system according to (8) was used in these experiments, in order to maintain the extracellular conditions.

3. Extract analysis

$^1\text{H}/^{13}\text{C}$ -13 NMR was used to identify the metabolites (carbohydrates, amino acids, organic acids, etc) in extracts of *Alnus incana* leaves (young and old), stems, roots, root nodules. One dimensional ^1H NMR spectra were acquired (1-pulse and 1D TOCSY), as well as 2D double quantum filtered COSY, DQ2D, and TOCSY spectra. In addition, heteronuclear $^1\text{H}\{^{13}\text{C}\}$ 2D NMR spectra were used to disperse the signals even more and to identify the various metabolites. We used 2D HMQC, as well as 2D HMQC-TOCSY with various mixing times, for the heteronuclear correlations.

III. Results

Phosphomonoesters, cytoplasmic Pi, extracellular Pi, phosphodiester, ATP, UDPG, and polyphosphate were observed by ^{31}P NMR in the perfused root nodules. The ATP concentration was constant throughout the perfusion. Polyphosphate is a metabolite which is stored in the bacterial component (*Frankia*).

Labeled ammonium (^{15}N) was taken up by the root nodules and the label entered glutamine amide, then glutamate amine, and citrulline δ and ω . The nitrogen label was subsequently transferred to alanine by the action of a transaminase, as well as into GABA.

In the presence of MSO (methionine sulfoximine, a GS inhibitor) no ammonium was metabolized in the root nodules. The N-15 ammonium signal showed an intensity which was the function of its location in the perfused sample. The extracellular signal contributed with 'negative intensity', while the intracellular signal added a 'positive intensity' under these experimental conditions.

HPLC analysis together with 2D NMR data showed that the main soluble metabolites were citrulline, glutamate, malate, and citrate, in addition to sucrose, fructose, and glucose. A number of metabolites were identified only in the root nodules and not in other parts of the plant. Some of these were nitrogen containing compounds of a high concentration.

IV. Discussion and Conclusions

We have studied the assimilation of ammonium in root nodules of *Alnus incana* \times *Frankia* using N-15 NMR. N-15 labeled glutamine is formed — then sequentially glutamate, citrulline, arginine, alanine, and GABA. The concentration of ATP, Pi, and UDPG remained constant in these experiments. MSO inhibited the assimilation of

ammonium suggesting that the GS/GOGAT pathway is exclusively used under the conditions used in the perfusions. Combined H-1/C-13 NMR analysis of extracts was used to identify and localize metabolites involved in the nitrogen assimilation process. The present work shows that it is possible to maintain a sample of root nodules under constant conditions in an NMR tube, and that the metabolism is stable up to at least ~15 h.

V. References

- ¹KR. Schubert, GT. Coker, RB. Firestone *Plant Physiol.* **67**, 662 (1981).
- ²J. Blom, W. Roelofsen, ADL. Akkermans *New Phytol.* **89**, 321 (1981).
- ³PR. McClure, GT Coker, KR. Schubert *Plant Physiol.* **71**, 652 (1983),
- ⁴TW-M. Fan, RM. Higashi, AN. Lane *Arch Biochem Biophys.* **266**, 592 (1988).
- ⁵DB. Rolin, RT. Boswell, C. Sloger, SI. Tu, JS. MacFall, JH. Schmidt PE. Pfeffer *Plant Physiol.* **89**, 1238 (1989).
- ⁶P. Lundberg, E. Harmsen, C. Ho, HJ. Vogel *Anal Biochem.* **191**, 193 (1990).
- ⁷PE. Pfeffer, DB. Rolin, TF. Kumosinski, JS. MacFall, JH. Schmidt *Plant Physiol.* **100**, 1682 (1992).
- ⁸P. Lundberg, S. Roy, PW. Kuchel *Immunomethods*, **4**, 163 (1994).
- ⁹Y. Shachar-Hill, PE. Pfeffer, D. Douuds, SF. Osman, LW. Doner, RG. Ratcliffe *Plant Physiol.* **108**, 7 (1995).

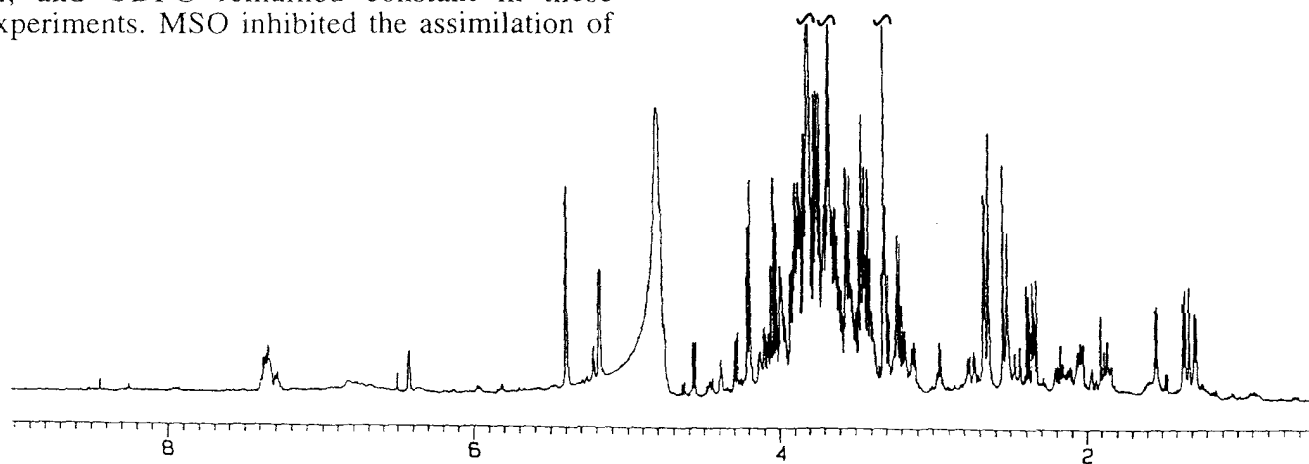


Figure 1: ^1H NMR spectrum (at 500 MHz, pH ~7.3, and 298 K) of an extract of the symbiotic root nodules of *Alnus incana* \times *Frankia*. The chemical shift scale is referenced to DSS at 0.00 ppm.

In vivo NMR monitoring of the metabolism of [1-¹³C] glucose in the sophorose lipid producing yeast *Candida (Torulopsis) apicola*

R. Meusinger¹⁾, R. K. Hommel²⁾ and U. Himmelreich³⁾

1) University of Leipzig, Institute of Analytical Chemistry, Linnestr. 3, Leipzig, D-04103, Germany;

2) CellTechnologie, Leipzig, Fontanestr. 21, Leipzig, D-04289, Germany;

3) present address : University of Sydney, Department of Biochemistry, Sydney, NSW-2006, Australia

Introduction

The metabolism of [1-¹³C] glucose was monitored in whole cells of the obligate aerobic *Candida (Torulopsis) apicola*, a sophorose lipid producing yeast, using *in vivo* ¹³C NMR. The ability of some microorganisms to form extracellular surface active compounds like sophorose lipids (see Figure 1) is predominantly considered in close connection with the uptake and metabolism of hydrophobic carbon sources. However, it has been shown that sophorosides are also produced by cells grown on carbohydrates as the sole source of carbon and energy [2, 3].

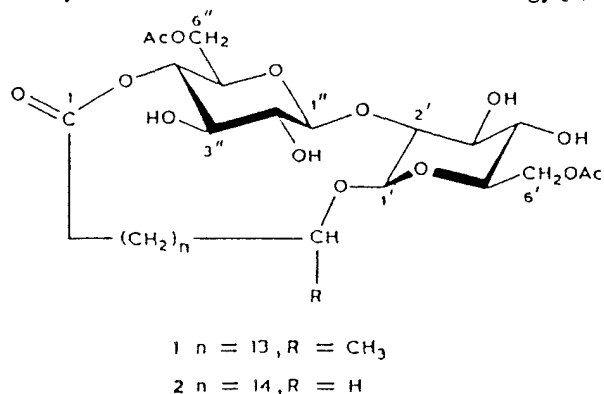


Figure 1 : Sophorose lipid [1]

In vivo ¹³C NMR spectroscopy is an excellent experimental method for the detection and quantification of labelled metabolites *in vivo*, the measurement of carbon flow through glycolysis, and the analysis of label-partitioning between different metabolic pathways. By ¹³C NMR the determination of independent carbon fluxes is possible which may in turn contribute to further advanced process development of metabolic engineering by directed modifications. The present study was undertaken with cells obtained from different growth phases (logarithmic [A], late logarithmic [B] and stationary [C] growth phases; see Figure 3). In this way it was possible to detect assumed growth-phase dependent differences in the flux of ¹³C label into the different metabolic pathways of this obligate aerobic yeast and to elucidate and understand the critical junctions in the metabolic network that impact directly on the formation of the sophorose lipid.

Experimental

Sample preparation for NMR experiments.

Cells of *C. apicola* grown on glucose were harvested after 8 h (logarithmic cells), 24 h (late logarithmic cells), 36 h (early stationary cells) and 72 h (stationary cells). The cells were then spun down and washed with water and cold potassium phosphate buffer. D₂O (1 ml) was added to 3 ml of the cell suspension to provide a lock signal. NMR measurements were performed with 4 ml volumes of this suspension in a 10 mm NMR tube.

NMR procedures and parameters.

Cells were aerobically incubated using a modified aeration system according to the method of Santos and Turner [4]. D-[1-¹³C] glucose (99 % isotopically labelled) diluted in buffer was added via the aeration system. The sample temperature was set to 24°C for all NMR experiments. In order to supply the yeast with air, we used the apparatus shown in Figure 2.

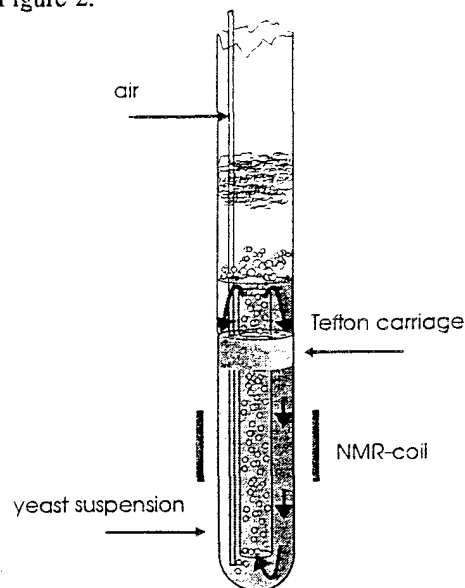


Figure 2 : Flow apparatus for *in vivo* NMR measurements on samples in 10 mm NMR tubes.

All spectra were obtained with a Varian UNITY 400 spectrometer operating at 100.577 MHz for ¹³C. A pulse width of 10 μs (pulse flip angle ~60°), a repetition time of 3.2 s and a sweep width of 20 000 Hz were used for

experiments performed. $[1-^{13}\text{C}]$ glucose was used as an internal standard for chemical shifts. To follow the dynamic behaviour of the process eight to sixteen spectra were recorded sequentially. NMR resonances were assigned on the basis of chemical shift information obtained from the spectra of samples of known composition in the same buffer.

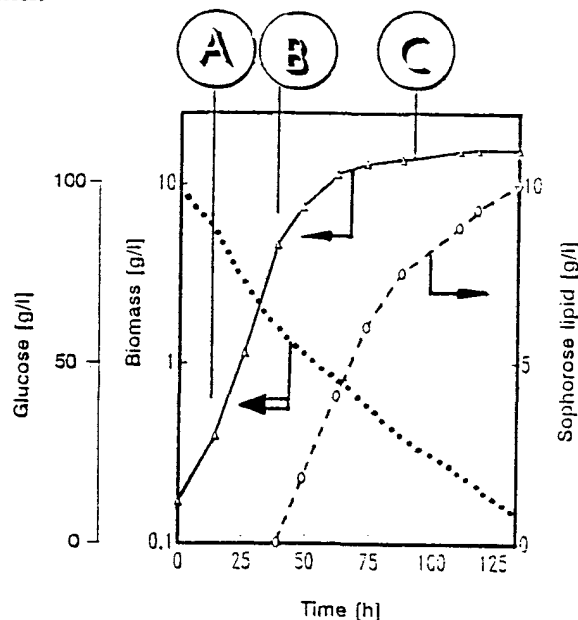


Figure 3 : The study was undertaken with cells obtained from the different growth phases to monitor assumed growth phase dependent differences in the flux of glucose into the different metabolic pathways ([A] logarithmic, [B] late logarithmic, [C] stationary growth phase).

Results

Figure 4 shows the time courses of the glucose signal in a suspension of stationary glucose-grown cells.

The label of $[1-^{13}\text{C}]$ glucose in cells of the logarithmic growth phase was incorporated predominantly into the C-2 of ethanol. Minor amounts of dihydroxyacetone phosphate (DHAP) ($\delta = 65.0$ ppm) and $[1-^{13}\text{C}]$ fructose-6-phosphate (F6P) ($\delta = 63.8$ ppm) accumulated.

In contrast, cells harvested from the late logarithmic growth phase showed significantly reduced rates of ethanol formation which became detectable only after remarkable glucose consumption. Immediately after the addition of glucose, the intensity of the signal of $[6-^{13}\text{C}]$ fructose-1,6-bis-phosphate (FDP) ($\delta = 64.4$ ppm) decreased within a period of 10 minutes. In parallel, the signal intensity of the F6P steadily increased. The DHAP signal intensity remained at a constant but higher value than with early logarithmic cells. The signal of $[1, 3-^{13}\text{C}]$ glycerol ($\delta = 63.6$ ppm) became dominant. Additional signals at 126 ppm (olefinic carbons of fatty acids) and 14.8 ppm (methyl group of fatty acids) indicated incorporation of the label into fatty acids by late logarithmic cells.

In stationary cells ethanol formation could not be detected. Glycerol was produced in large amounts. Whereas FDP and

F6P reached steady state concentrations within 20 and 60 minutes, respectively, the concentration of glycerol increased continuously. Also, low intensities of broad signals were obtained in the region of the C-1' and C-1'' carbon atoms of the sophorose lipid (101 to 105 ppm, [5]). Incorporation into the C-6 and C-3 of the two glucose residues of the sophorosides could not be detected. That might be due to interference with high intensities caused by the high concentration of glucose added.

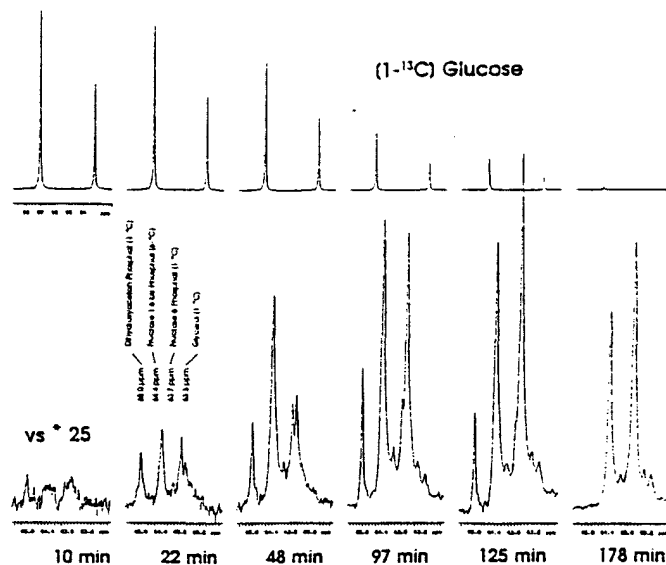


Figure 4 : ^{13}C -NMR spectra of $[1-^{13}\text{C}]$ glucose metabolism in a suspension of stationary glucose grown cells of *C. apicola* at different times after addition of $[1-^{13}\text{C}]$ glucose.

The ^{13}C NMR experiments with *C. apicola* document the fatty acid synthesis by incorporating the label into the terminal methyl group of fatty acids and additionally into different fatty acid carbons by late logarithmic cells. The presented results stress the assumption that carbohydrate metabolism is central in the regulation of sophorose lipid biosynthesis. The fate of glucose depending on the growth phase of *C. apicola* is different to the commonly accepted view of yeast metabolic regulation. Further studies are necessary to clarify this complex behaviour.

References

- [1] R. K. Hommel, L. Weber, A. Weiss, U. Himmelreich, O. Rilke and H. P. Kleber, *J. Biotechnol.* **33**, 147 (1994)
- [2] U. Gobbert, S. Lang and S. Wagner, *J. Biotechnol. Lett.* **6**, 225 (1984)
- [3] R. K. Hommel and K. Huse, *J. Biotechnol. Lett.* **15**, 853 (1993)
- [4] H. Santos and D. L. Turner, *J. Magn. Reson.* **68**, 345 (1986)
- [5] L. Weber, C. Doge, G. Haufe, R. K. Hommel and H.P. Kleber: *Biocatalysis* **5**, 267 (1992)

Phosphoryl Group - Metal Ion Interactions Probed by ^{17}O NMR Spectroscopy

M. P. Belciug, A. M. Modro, T. A. Modro and P. L. Wessels

Centre for Heteroatom Chemistry, Department of Chemistry,
University of Pretoria, Pretoria 0002, South Africa

I. INTRODUCTION

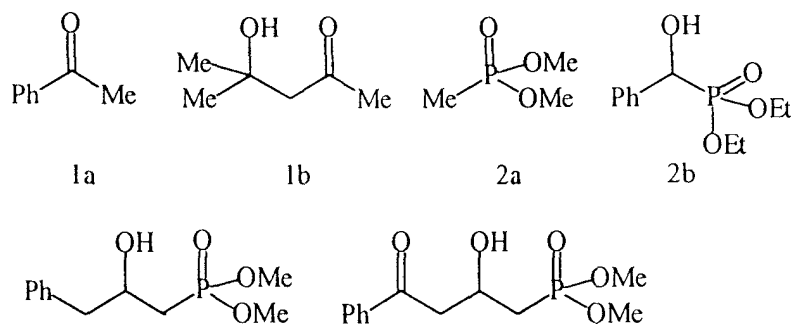
Our previous NMR (^1H , ^{13}C , ^{31}P) spectroscopic studies on esters of β,γ -disubstituted propylphosphonic acids, $\text{YCH}_2\text{CHXCH}_2\text{PO}_3\text{R}_2$ (**1**), demonstrated attractive interactions between the phosphoryl group and the oxygen containing substituent X (**1**). The effect is enhanced by metal ions, presumably *via* chelation. Since for the substrates containing both, the phosphoryl, and the carbonyl group, some of the results were ambiguous, we decided to study the effect of metal ions on the ^{17}O NMR spectra of some hydroxyalkylphosphonates (**1**, X = OH), and related carbonyl derivatives (**2**). It is known (2) that ^{17}O NMR spectra proved very successful in identifying the nature of the interactions between various organic systems and metal ions.

RESULTS AND DISCUSSION

Two carbonyl compounds, three phosphoryl compounds, and one trifunctional compound were selected as substrates, and the effect of Na^+ and Mg^{2+} ions on their ^{17}O NMR spectra were determined in acetonitrile. The following ranges of the ^{17}O NMR chemical shifts (rel to H_2O) were obtained for **1** and **2**: P=O, 91 - 104; OH and OR, 35 - 65; C=O, 543 - 567 ppm. Upon the addition of

metal ions both low-field signals (P=O and C=O) undergo significant upfield shifts (up to -18 and -25 ppm, respectively), whereas the high-field signals of the sp^3 oxygens (OH, OR) are little affected by the addition. The effect of Mg^{2+} ions is always stronger than that of Na^+ . The negligible shifts observed for the OH groups are taken as an evidence against any chelating effects by the 2-hydroxy group in the alkylphosphonic or keto systems. It was also found that the phosphoryl (or carbonyl) oxygen - metal ion interactions, easily detected by the ^{17}O NMR shift, have no effect on the IR spectra of those substrates; the values of $\nu_{\text{P=O}}$ and $\nu_{\text{C=O}}$ were approximately constant irrespective of the excess of the ions.

Substrate **2d** contains, in addition to the OH group, two donor groups (phosphoryl and carbonyl) that may compete for an added metal ion. IR spectroscopy showed that it is the P=O group, and not the C=O group, that is involved in the intramolecular hydrogen bonding with the equidistant OH function. The effect of metal ions on the ^{17}O NMR spectrum of **2d** is very distinctive: strong high-field shift for the P=O signal, strong high-field (with significant broadening) shift for the C=O signal, and the negligible shift for the OH/OMe signal. The IR spectroscopy demonstrated the existence of the intramolecular P=O...H-O bonding (five-membe-



red ring) unaffected by the addition of the metal ions. The conclusion is that in the presence of a M^+ ion, **2d** exists as an eight-membered chelate structure, incorporating at the same time the 1,5-hydrogen bonded ring. The model of such structure, involving the most stable boat-chair (BC) conformation of an eight-membered ring (3), is shown in Figure 1.

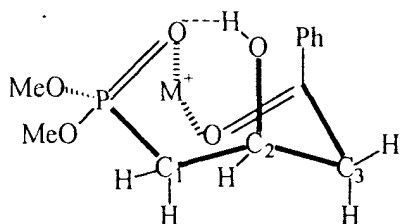


Figure 1. Proposed structure of the metal complex of **2d**

A Dreiding model of the structure revealed the features that remain in full agreement with the experimental results. Firstly, the $P=O \cdots HO$ distance is of the order of 2.5 \AA , perfectly well within the usual range observed for the distance in the hydrogen bonded $P=O \cdots H-O$ system. Secondly, the trigonal geometry of the carbonyl carbon resulted in some distortion of the BC conformation, in which the bonds at C_2 (C-H and C-OH) are forced into an almost eclipsed relationship with respect to the bonds at C_1 . In consequence, the torsion angles between the two hydrogens at C_1 and the hydrogen at C_2 approach the values of 0° and 120° rather than the values of 60° and 180° postulated for the most stable, staggered conformation of **2d** (4). According to the Karplus equation, the calculated values of the proton - proton vicinal coupling constants for the torsion angles of 0° and 120° are 8.2 and 2.1 Hz, respectively, while for the *anti/gauche* relation the respective values are 9.2 and 1.8 Hz. Since the experimental values of the vicinal J_{AC} and J_{BC} observed for **2d** upon the addition of Na^+ or Mg^{2+} ions are 8.4 and 4.4 Hz, it is not possible to distinguish between the usual staggered (60° and 180°) and the eclipsed conformations on the basis of the

vicinal coupling constants involving hydrogens of an ABX system. ^{17}O NMR spectroscopy, on the other hand, offers a much more specific and selective approach for monitoring any electronic changes that occur at the potential binding sites when metal ions are added to the system. The metal ion - organic substrate interactions occurring in systems **1** and **2** are too weak to be detected by IR spectroscopy, but they are strong enough to be conveniently monitored by ^{17}O NMR spectroscopy.

REFERENCES

- ¹ M. P. Belciug, T. A. Modro, and P. L. Wessels, *Magn. Reson. Chem.*, **31**, 1024 (1993), and the preceding papers of this series.
- ² J. Schulte and J. Lauterwein, *Magn. Reson. Chem.*, **30**, 344 (1992); T. A. Powers and S. A. Evans, *Heteroatom Chem.*, **3**, 41 (1992).
- ³ E. L. Eliel and S. H. Wilen, in *Stereochemistry of Organic Compounds*, J. Wiley, New York, 1994, ch. 11.5.d.
- ⁴ M. P. Belciug, T. A. Modro, and P. L. Wessels, *J. Phys. Org. Chem.*, **6**, 523 (1993).

Comparison of Counterion Effects in Ionomer Membranes Using ^{14}N NMR Spectroscopy

Mallika Rankothge, Jim Hook and Grainne Moran
School of Chemistry, The University of New South Wales, Sydney 2052, Australia

Introduction

Nafion and other perfluoroulfonate ionomer membranes have important applications in the chlor-alkali industry. This is due to their chemical inertness and in particular to their high permselectivity which allows efficient transport of counter-ions with rejection of co-ions even at high electrolyte concentration [1,2]. The structure and properties of these ionomers have been studied extensively using physical, chemical and spectroscopic methods but the detailed cluster morphology of the membranes is the subject of ongoing investigation. Cluster formation, due to aggregation of ion pairs, is also important in determining the properties of polystyrenesulfonate ionomers, which find applications in electrodialysis [3,4].

The perfluorinated cation-exchange membranes typified by Nafion also have particularly high selectivities for large organic counterions [5]. We have previously investigated perfluorinated and polystyrene-based ionomers using ^{14}N NMR spectroscopy with NH_4^+ and NO_3^- as probe ions [6,7]. Here we extend the study to compare the counterion effects of NH_4^+ with tetraalkylammonium ions in these membranes.

Experimental

Nafion 117 (Aldrich) and Neosepta CMX (Tokuyama Soda) cation exchange membranes were pretreated as described previously [6]. Deionized water was used in all experiments and other reagents were analytical grade. Membranes were equilibrated separately in solutions containing an excess volume of 1% w/v $\text{R}_4\text{N}^+\text{X}^-$ (where R = H, Me, Et and X = Cl or Br) and then washed to remove excess electrolyte. All measurements were made on fully hydrated membranes at 300 K unless otherwise specified. Detailed sample preparation procedures for recording membrane spectra have been described in detail elsewhere [6].

^{14}N NMR spectra were recorded at 21.67 MHz on a Bruker ACP 300 NMR spectrometer using a 10 mm broad band probe. ^{14}N chemical shifts, δ_{N} are referenced externally to CH_3NO_2 in DMSO-d_6 (= 0 ppm). Relaxation times, T_1 , were obtained with the inversion-recovery sequence and analysed using Bruker software.

Results and Discussion

^{14}N NMR Spectra

Fig. 1 shows the ^{14}N NMR spectra of NH_4^+ , $\text{N}(\text{CH}_3)_4^+$ (TMA $^+$) and $\text{N}(\text{C}_2\text{H}_5)_4^+$ (TEA $^+$) ion-exchanged Nafion membranes at 300 K. The membranes are fully hydrated, being immersed in water while the

spectra are measured. At this temperature a quadrupolar splitting is clearly observed only in the NH_4^+ exchanged membranes. Broader lines (250 - 600 Hz) are observed in TMA $^+$ and TEA $^+$ exchanged membranes with the linewidths increasing in the order $\text{NH}_4^+ < \text{TEA}^+ < \text{TMA}^+$. Similar spectral lineshapes were observed for TMA $^+$ and TEA $^+$ ion-exchanged Neosepta CMX at 300 K. However the quadrupolar splitting in Neosepta- NH_4^+ is smaller than in Nafion due to the lower level of orientational anisotropy in this membrane [6,7].

Also shown in Figure 1 are the spectra of TMA $^+$ in Nafion and Neosepta at 355 and 340 K respectively. In both cases the linewidths are much narrower at the higher temperature as expected. However for Neosepta-TMA $^+$ a quadrupolar splitting can also be resolved, which decreases with increasing temperature. This trend is in contrast to the results for NH_4^+ in Nafion where an increase in quadrupolar splitting with increasing temperature was found [6].

Table 1. ^{14}N spin lattice relaxation times for NH_4^+ , TMA $^+$, and TEA $^+$ ions in membranes and in solution. $T_1/T_{1,s}$ is the ratio of T_1 in the membrane to that in solution. E_a values are from Arrhenius plots in the range 290-340 K.

Nafion			
Cation	T_1 (ms)	$T_1/T_{1,s}$ $\times 10^3$	E_a (kJ mol $^{-1}$)
	300 K		
NH_4^+	72 ± 2 ?	44	20
TMA $^+$	58	4.2	-
TEA $^+$	43	5.9	22
Neosepta			
NH_4^+	67 ± 5	41 ± 3	31
TMA $^+$	73	5.3	-
TEA $^+$	49	6.7	29

Solution			
	T_1 (s)		E_a (kJ mol $^{-1}$)
	300 K		
NH_4Cl	1.64	-	6.5
TMACl	13.7	-	9.0
TEA Br	7.29	-	14.9

Relaxation Times

Spin-lattice relaxation times for the three counter-ions in Neosepta and Nafion are compared with the solution state values at 300 K (Table 1). At this temperature the mobility of the tetraalkylammonium ions is more restricted in Nafion than in Neosepta as reflected

in the lower T_1 values for both ions. To allow easy comparison of the effects of ion-exchange on the rotational mobility of the ions, the ratios of the relaxation rates in the membranes compared to solution, $T_1/T_{1,s}$, were calculated. It is clear that the reduction in T_1 for the membrane-exchanged ions is an order of magnitude greater for the alkylammonium ions compared to NH_4^+ . Secondly, TEA^+ is more mobile than TMA^+ in both membranes. This is consistent with dynamic mechanical measurements on dry samples, which showed that alkylammonium ions act as plasticisers for the cluster regions in ionomers [4].

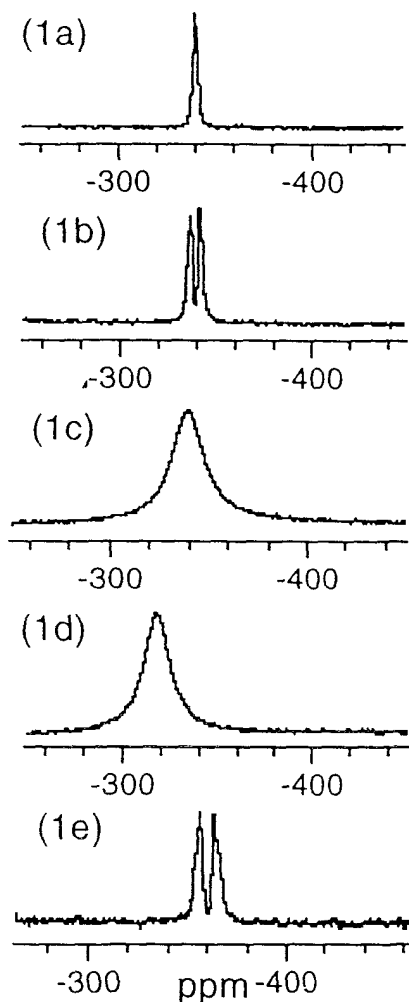


Fig. 1 ^{14}N NMR spectra of 1(a) Nafion TMA^+ , 355K, 1(b) Neosepta TMA^+ , 340K, 1(c) Nafion TMA^+ , 300K, 1(d) Nafion TEA^+ , 300K, 1(e) Nafion NH_4^+ , 300K.

The temperature dependence of the T_1 values is shown in Figure 2. Arrhenius-type plots are linear for all ions in solution and for NH_4^+ and TEA^+ over the temperature range 290–340 K. However plots for TMA^+ in Nafion and Neosepta are non-linear even over this narrow temperature range, so activation energies are not derived in these cases. Instead it is clear from Figure 2 that the correlation time for reorientation of TMA^+ in the membranes is increased to the point where $1/\tau_c \sim$

$\nu(^{14}\text{N})$, as seen from the minimum in the plot of T_1 versus T . The higher activation energies for ion reorientation in Neosepta may be attributed to smaller ionic multiplets and a more rigid chain structure. We also note that all temperature dependent effects will include a contribution from the degree of membrane swelling since the samples are immersed in water throughout the measurements.

Conclusion

The higher reorientational mobility of TEA^+ in the ionomers compared to TMA^+ is consistent with its ability to plasticise the cluster regions of the membranes. There is no simple correlation between ion mobility and selectivity coefficients for cation exchange. Further work is being carried out on the interactions of large plasticising ions in ionomer membranes.

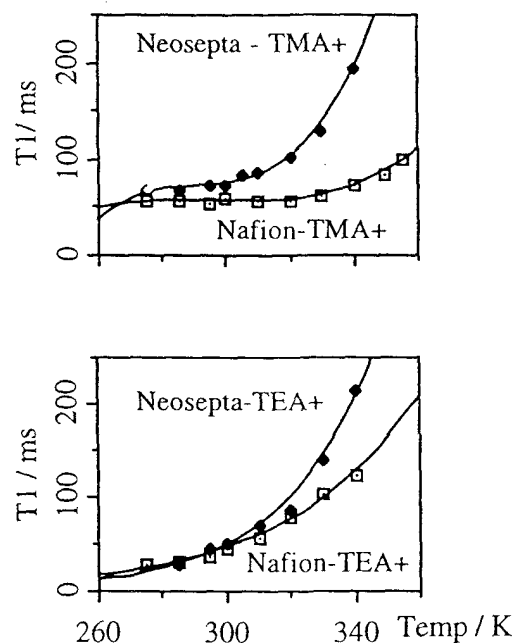


Fig. 2 Temperature dependence of T_1 .

References

- [1] 'Structure and Properties of Ionomer Membranes', M. Pineri and A. Eisenberg Eds., NATO ASI, D. Reidel Dordrecht, 1986.
- [2] 'Perfluorinated Ionomer Membranes' A. Eisenberg and H.L. Yeager Eds., ACS Washington, 1982.
- [3] A. Eisenberg, B. Hird and R.B. Moore, *Macromolecules*, 23 (1990) 4098.
- [4] J-S. Kim, S.B. Roberts, A. Eisenberg and R.B. Moore, *Macromolecules*, 26 (1993) 5256.
- [5] M.N. Szintermay and C.R. Martin, *Anal. Chem.*, 48 (1984) 1898.
- [6] Haryadi, M. Rankothge, J. Hook, L. van Gorkom and G. Moran, *Magn. Reson. in Chem.*, 32 (1994) 446.
- [7] G. Moran, J. Hook and M. Rankothge, 20th Australian Polymer Symposium, Adelaide, Australia, Feb. 1995.

NMR as a Tool for Understanding Fundamental Dynamic Properties of Solid Polymer Electrolytes.

Ng, S.¹, Smith, M.E.³, Garcia, M.³, MacFarlane, D.² and Forsyth, M.¹

¹Department of Materials Engineering, Monash University, Clayton, Victoria, Australia, 3168.

²Department of Chemistry, Monash University, Clayton, Victoria, Australia, 3168.

³Physics Laboratories, University of Kent, Canterbury, Kent, United Kingdom, CT2 7NR.

INTRODUCTION

As a class of materials, Solid Polymer Electrolytes (SPEs) are relatively young, with a substantial portion of the advances taking place over the last 15 to 20 years. These materials conduct current via the motion of a solvated ionic species, the charge carrier, through a solid polymer medium, the host¹⁻³. The exact nature of the interaction between solvated ions and the polymer host is not understood³. It is known that cations form coordinate bonds with the polymer, and that these act as transient crosslinks, limiting polymer mobility and thereby increasing T_g . But a range of other interactions between anion, cation and polymer are also possible, and the extent to which these influence the properties of the SPE is merely conjecture^{1,3,4-5}. In addition, the popular use of low molecular weight diluents in an effort to enhance polymer mobility has added a further dimension to this problem⁶⁻⁷. Elucidating the nature of the polymer-cation-anion interactions is of primary concern to all researchers in this field.

Multinuclear Solid State NMR is a tool which allows investigation of the dynamics of relaxation of specific ionic species within the SPE^{4,7,8}. Measurement of the T_1 relaxation process for both the ^7Li and ^{19}F nuclei has provided some insight into the effects that salt concentration and plasticiser addition have on the environment of the cation and the Triflate anion. Further, Pulsed Field Gradient (PFG) NMR for the ^{19}F species has allowed measurement of the diffusion coefficient (\mathcal{D}) for the Triflate anion as a function of temperature - \mathcal{D} being related to conductivity via the Nernst-Einstein equation.

EXPERIMENTAL METHOD

A 5000 molecular weight trifunctional polyethylene glycol (3PEG5000), and two suitable salts, LiCF_3SO_3 and LiClO_4 , were dried under vacuum at 60°C for 72 hours to remove all moisture. Tetraglyme (a low molecular weight polyether analogue) was vacuum distilled. Samples containing varying molal (m) concentrations (mole kg^{-1}) of salt and plasticiser were crosslinked using hexamethylene diisocyanate to produce a fully networked SPE. T_1 measurements over a range of temperatures were made for

the ^7Li nuclei on a Bruker CPX series spectrometer at a frequency of 29.86 MHz, using the inversion-recovery method. T_1 and \mathcal{D} measurements for the ^{19}F nuclei were made using an inversion-recovery and $90^\circ\text{-}\tau\text{-}180^\circ$ pulse sequence respectively on a homebuilt spectrometer operating at 13.65 MHz.

RESULTS AND DISCUSSION

It is well known that the cations in a SPE form transient crosslinks both inter- and intra-molecularly. It is not known which of these forms is prevalent, but the end result is reduction of the polymer mobility, and consequently, hindrance of the conductivity process. An understanding of the cationic environment is essential to understanding the mechanisms of interaction. Figure 1 shows the T_1

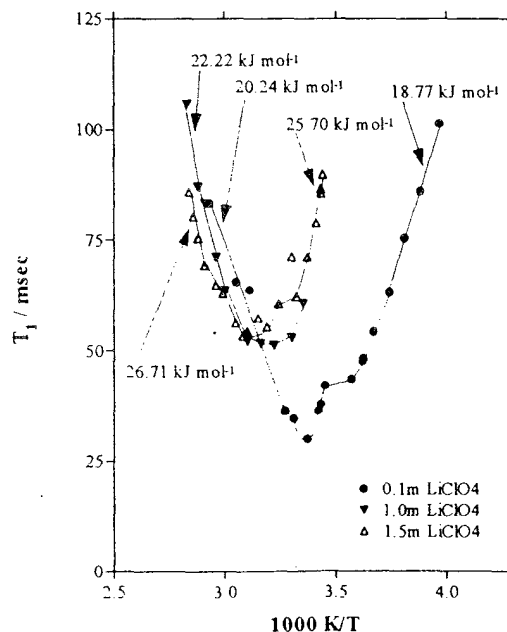


Figure 1: T_1 plotted against $1000\text{K}/T$ for samples containing 0.1, 1.0 and 1.5 molal lithium perchlorate salt, with ΔE_a for samples included where possible (sight lines placed for convenience)

relaxation process for ^7Li as a function of temperature and salt concentration. With increasing salt concentration there is an upward shift in the value of T_1 at the minimum. Previous work has provided evidence that the relaxation

mechanism for ^7Li involves an interaction with the polymer chain. The upward shift in the minimum is therefore consistent with a reduced interaction between cation and polymer, and previously observed increases in the level of ion aggregation as salt concentration increases⁶.

Increasing salt concentration also produces a shift in the position of the T_1 minimum to higher temperatures, indicating a decreasing mobility of the ^7Li as salt concentration increases. When plotted against reduced temperature ($T-T_g$), the shift seems to be consistent with the change in T_g for the 0.1m and 1.0m samples. For the 1.5m sample, however, the minimum occurs at lower values of $T-T_g$, consistent with an inherently more mobile ^7Li nuclei. As in Figure 1 above, this may be explained by the presence of a cation that is less strongly bound to the polymer.

Activation Energies (ΔE_A) calculated from the relaxation data are shown in Figure 1. Where possible, ΔE_A were determined for both the low and high temperature portions of the relaxation curves. BPP theory predicts a symmetrical T_1 relaxation curve, built on the assumption of a single correlation time (τ_c). In reality, it is unlikely that a single τ_c exists. The Cole-Davidson theory models the effect of a distribution of τ_c , predicting no affect on the motionally narrowed region of the relaxation curve, but a diminished slope for the low temperature portion of the curve⁹. ΔE_A calculated for the low temperature portions of Figure 1 are consistently smaller than those calculated for the motionally narrowed regime, suggesting that in all of our samples the ^7Li nuclei experience a range of environments. The ΔE_A from conductivity measurements, included in Figure 1 for comparison, are considerable larger than those from the ^7Li NMR relaxation measurements. This is not surprising given that conduction is a long range phenomenon involving not only cations, but anions and aggregates.

Figure 2 shows T_1 measurements made for two 1.0m LiClO_4 samples, one of which contains 30 wt% tetraglyme. There is a shift in the minimum to lower temperatures upon addition of plasticiser, consistent with the plasticising effect. There is also an increase in the value of the T_1 minimum with addition of tetraglyme. It is thought that low molecular weight tetraglyme, which has a dielectric constant similar to that of the polymer host itself, will be a poor solvator. The upward shift in the minimum is only slight, suggesting that addition of tetraglyme may cause a small increase in the level of aggregation, but not a significant one. The fact that the shift in the temperature position of the minimum seems consistent with the change in T_g also precludes any large changes in the level of aggregation, which would be expected to cause changes in the mobility of the ^7Li unrelated to T_g decreases. A comparison of activation energies shows higher values for the sample containing tetraglyme.

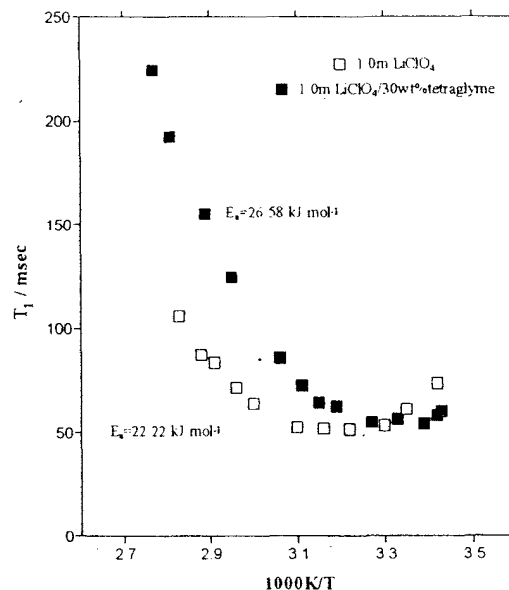


Figure 2 : T_1 against reciprocal temperature for a 1.0m lithium perchlorate sample with and without tetraglyme.

Calculation of \mathcal{D} for the triflate anion (^{19}F) in a 1.0m LiCF_3SO_3 containing 50wt% tetraglyme revealed a value of $2.71 \times 10^{-11} \text{ m}^2 \text{ sec}^{-1}$ - comparable to values calculated by other investigators^{10,11} ($3.16 \times 10^{-12} \text{ m}^2 \text{ sec}^{-1}$ for PF_6^- in oxymethylene-linked PEO with an ethylene oxide to anion ratio of 20:1, and $9.5 \times 10^{-11} \text{ m}^2 \text{ sec}^{-1}$ for CF_3SO_3^- in PEG (mw 400) with an ethylene oxide to anion ratio of 10:1).

ACKNOWLEDGMENTS

This research was made possible through funding provided by a British Council Bursary and an Australian Postgraduate Award.

REFERENCES

- [1] Watanabe, M. and Ogata, N. *British Polymer Journal*. **20**, 1988, 181-192.
- [2] Gray, F. M. "Solid Polymer Electrolytes". VCH Publishers Inc., NY, 1991.
- [3] Bruce, P.G. and Vincent, C.A. *J. Chem. Soc., Faraday Trans.* **89**(17), 1991, 3187-3203.
- [4] Greenbaum, S. G., Pak, Y. S., Wintersgill, M.C. and Fontanella, J.J. *Solid State Ionics*. **31**, 1988, 241-245.
- [5] Torell, L. M., Jacobsson, P. and Petersen, G. *Polymers for Advanced Technologies*. **4**, 1993, 152-163.
- [6] Bishop, A. G., MacFarlane, D.G., MacNaughton, D. and Forsyth, M. 1995, (*submitted to Solid State Ionics*).
- [7] Forsyth, M., Meakin, P., MacFarlane, D. R., Bulmer, G. and Reid, M. *J. Mater. Chem.* **4**(7), 1994, 1149-1151.
- [8] Greenbaum, S.G., Pak, Y.S., Adamic, K.J., Wintersgill, M.C. and Fontanella, J.J. *Polymer Chem.* **31**, 1993, 1687-1695.
- [9] Connor, T.M. *Trans. Faraday Soc.* **60**, 1963, 1574-1591.
- [10] Arungum, S., Shi, J., Tunstall, D.P. and Vincent, C.A. *J. Phys. Condens. Matter*. **5**, 1993, 153-160.
- [11] Johansson, A., Gogoll, A. and Tegenfeldt, J. 1995, (*submitted to Polymer*).

EPR Investigation of Unstable Intermediates in Photoinduced Reactions at CdS Semiconductor Particles Dispersed on CdO

Y. Nakaoka and Y. Nosaka

Nagaoka University of Technology, Nagaoka, Niigata, 940-21, Japan

Semiconductor photocatalysis attracts special attentions in view of chemical storage of solar energy, detoxification of waste water, organic synthesis, and so on (1). In the initial stage of photocatalysis, electrons and holes are produced in the semiconductor powders by photoirradiation and trapped at their surface. The trapped electrons and holes form paramagnetic radicals through which photocatalysis takes place. Therefore, it is important to know the properties of the radicals photoproduced on the semiconductor surface. Although numerous studies have been reported with respect to the photocatalysis on CdS particles (2-7), there is little information on the surface structures of them. In this study, we prepared high dispersed CdS at the surface of the CdO powders by contacting them with H_2S in gaseous phase. The CdO powders were dispersed on the fine particulate SiO_2 . EPR spectroscopy is an effective method for direct observations of the radicals photoproduced on semiconductors. We applied this method to CdS particles dispersed on CdO and presumed the structures of the surface radicals formed by the photoirradiation.

In the sample preparation, CdO/ SiO_2 powder was obtained as follows; 2.5 mol % of CdO (Nacalai Tesque, GR) was dispersed in the aqueous suspension of fine SiO_2 particles (Nippon Aerosil) and this suspension was dried in vacuum. A half aliquot of this powder was exposed to H_2S (Seitetsu Chemicals) and consequently CdS was formed on the CdO surfaces (CdS/CdO/ SiO_2). Both samples were placed in quartz tubes and they were evacuated and sealed. EPR measurements were carried out with an X-band EPR spectrometer (JEOL, ES-RE2X) at 77 K under the irradiation of the light from a 500-W high pressure mercury lamp (Ushio, USH-500D) through a band pass filter (Toshiba, UV-D36C). The spectra obtained were read in a personal computer, converted into a g value scale, and simulated.

Without irradiation, no EPR signals were observed for both samples. Under the irradiation, CdO/ SiO_2 gave the spectrum a in Figure 1. For SiO_2 alone, however, a similar signal to a was observed under the irradiation, but for CdO alone, no signal appeared. Therefore, the signal of spectrum a originates from SiO_2 in CdO/ SiO_2 . CdS/CdO/ SiO_2 gave the spectrum b in Figure 1 under the irradiation. For CdO exposed to H_2S without SiO_2 , a weak signal which is similar to spectrum b was observed. Since the surface area of the

CdO becomes large by dispersing on SiO_2 , the large signal for CdS was observed. The subtraction of the spectrum for CdO/ SiO_2 (spectrum a) from that for CdS/CdO/ SiO_2 (spectrum b) gave the spectrum of radicals produced on the CdS (spectrum c). This spectrum was simulated with the computer as shown in spectrum d. This is the summation of the two fundamental spectra having $g_1 = 2.0035$, $g_2 = 2.009$ and $g_3 = 2.042$ (spectrum e), and $g_{\parallel} = 2.005$ and $g_{\perp} = 2.032$ (spectrum f). Thus, it is revealed that two kinds of radicals were photoproduced on this CdS. We reported previously that on the irradiated CdS powder the EPR signals of trapped holes appeared in the range of $g = 2.004 - 2.035$ (8). Moreover, the reported g values of sulfur radicals lay in the range of $g = 2.00 - 2.05$ (9-12). Based on these evidences, the radicals observed are attributable to the trapped holes on

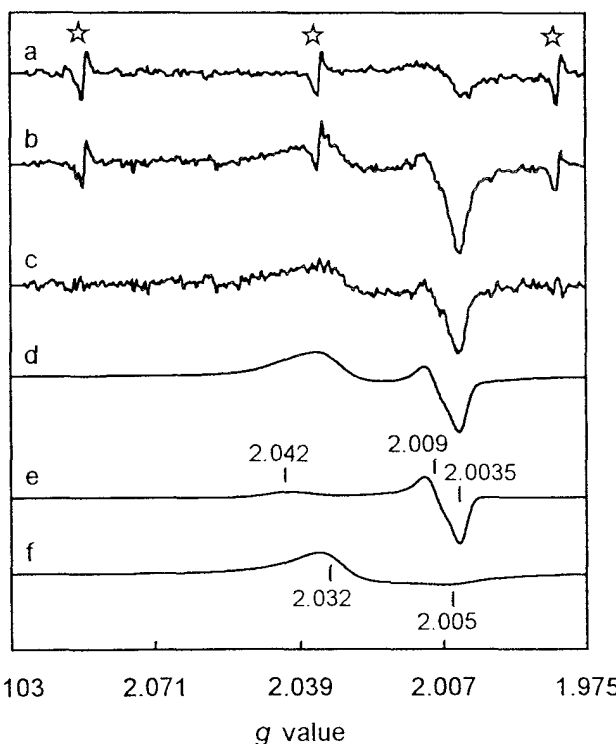
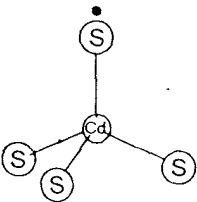
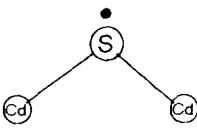
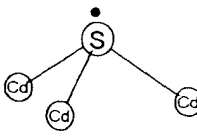


Figure 1: EPR spectra obtained for irradiated (a) CdO/ SiO_2 and (b) CdS/CdO/ SiO_2 at 77 K. (c); subtraction of a from b. (d); simulated spectra for c. (e) and (f); components of spectrum d. Stars indicate Mn^{2+} marker.

Table 1: g values calculated for three possible structures and obtained in the experiment.

assumed structures of radicals	g values	
	calculated	experimentally observed
	$g_{xx} = g_e \left\{ 1 + \frac{\zeta}{4\Delta\epsilon_b} + \frac{\zeta}{2\Delta\epsilon_n} \right\}$ $g_{yy} = g_e$ $g_{zz} = g_e$	
	$g_{xx} = g_e$ $g_{yy} = g_e \left\{ 1 + \frac{\zeta}{\Delta\epsilon_b} \right\}$ $g_{zz} = g_e \left\{ 1 + \frac{\zeta}{6\Delta\epsilon_b} + \frac{2\zeta}{3\Delta\epsilon_n} \right\}$	$g_1 = 2.0035$ $g_2 = 2.009$ $g_3 = 2.042$
	$g_{xx} = g_e$ $g_{yy} = g_e \left\{ 1 + \frac{3\zeta}{8\Delta\epsilon_b} \right\}$ $g_{zz} = g_e \left\{ 1 + \frac{3\zeta}{8\Delta\epsilon_b} \right\}$	$g_{\parallel} = 2.005$ $g_{\perp} = 2.032$

$\Delta\epsilon_b$ and $\Delta\epsilon_n$ indicate the energy differences from unpaired electron orbital for bonding and non-bonding orbitals, respectively.

sulfur atoms.

Since the crystal structure of CdO is zinc-blende, the CdS produced on it likely has the same crystal structure. As the radicals on the surface sulfur atoms, we may assume three types of structures which are classified in the coordination number of the sulfur radical center to the cadmium atoms attached. Based on the molecular orbital expression of the electronic structures of radicals, anisotropic g values can be calculated with the following Pryce's equation (13,14).

$$g_{ii} = g_e \left\{ 1 + \zeta \sum_{m \neq p} \frac{\left| \langle \psi_m | L_i | \psi_p \rangle \right|^2}{\epsilon_p - \epsilon_m} \right\}, \quad i = x, y, z.$$

Where x , y and z are the molecular axis, g_e is the g value of free electron, ζ is the spin-orbital coupling constant of sulfur atom, ψ are wave functions of the orbitals, p indicates the orbital of unpaired electron, L_i are the angular momentum operator around the i axis, ϵ are the energies of the orbitals. The g values were calculated based on the

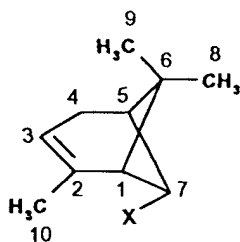
valence bond approximation for the radicals having the coordination numbers of 1–3, where the hybrid orbitals of sp , sp^2 , and sp^3 were assumed for the sulfur atoms (9). The calculated result was listed in Table 1. Since the exact values of $\Delta\epsilon$ were unknown, only the orders of the three g values could be estimated. By comparing the orders of the g values with that of the experimentally obtained, the radicals which gave the spectrum d and e correspond to the structures having the coordination number of 2 and 3, respectively. Therefore, at the surface of irradiated zinc-blende CdS, the sulfur atoms having the coordination number of 2 and 3 are suggested to be trapping sites of hole radicals. We reported previously that, for wurtzite CdS, the radicals of $g_{\perp} = 2.005$ and $g_{\parallel} = 2.035$ was produced and attributed to the trapped holes (8). From the results of the present calculations, the radicals produced on the wurtzite CdS is suggested to have the structure of coordination number of 1.

Since the structure at particle surface reflects the crystal structure of the bulk, different structures of surface radicals arise for different crystal structures. This may be one of the reasons why the differences in the photocatalytic activity exist between wurtzite and zinc-blende CdS (6,7).

References

- ¹Photocatalysis - Fundamentals and Applications; N. Serpone, and E. Pelizzetti (Eds.), Wiley, New York, 1989.
- ²B. Ohtani, J. Kawaguchi, M. Kozawa, Y. Nakaoka, Y. Nosaka, and S. Nishimoto, *J. Photochem. Photobiol., A: Chem.* in press.
- ³T. Shiragami, C. Pac, and S. Yanagida, *J. Phys. Chem.* **94**, 504-506 (1990).
- ⁴S. Kodama, A. Matsumoto, Y. Kubokawa, and M. Anpo, *Bull. Chem. Soc. Jpn.* **59**, 3765-3770 (1986).
- ⁵N. Bühler, K. Meier, and J.-F. Reber, *J. Phys. Chem.* **88**, 3261-3268 (1984).
- ⁶A. W.-H. Mau, C.-B. Huang, N. Kakuta, A. J. Bard, A. Campion, M. A. Fox, J. M. White, and S. E. Webber, *J. Am. Chem. Soc.* **106**, 6537-6542 (1984).
- ⁷M. Matsumura, S. Furukawa, Y. Saho, and H. Tsubomura, *J. Phys. Chem.* **89**, 1327-1329 (1985).
- ⁸Y. Nakaoka, and Y. Nosaka, *J. Phys. Chem.* **99**, 9893-9897 (1995).
- ⁹Y. Kurita, and W. Gordy, *J. Chem. Phys.* **34**, 282-288 (1961).
- ¹⁰A. Taylor, G. Filipovich, G. K. Lindeberg, *Solid State Commun.* **9**, 945-947 (1971).
- ¹¹Y. Shono, *J. Phys. Soc. Jpn.* **47**, 590-598 (1979).
- ¹²W. Giggenschach, *J. Inorg. Nucl. Chem.* **30**, 3189-3201 (1968).
- ¹³M. H. L. Pryce, *Proc. Phys. Soc. A* **63**, 25-29 (1950).
- ¹⁴M. Abragam, and M. H. L. Pryce, *Proc. R. Soc. (Lond.) A* **205**, 135-153 (1951).

Günther reported a parametrised Karplus type equation for adamantanes (5). They considered the effect of carbon substituents in the $^{13}\text{C}_\alpha\text{-C}_\beta\text{-C}_\gamma\text{-H}$ fragment as additive constants. Parella *et.al.* (6) reported the effect of hydroxy and carbonyl substitution on the $^3J_{\text{C,H}}$ couplings, Beuzekom *et.al.* (7) calculated the effect of the orientation of substituents of the C_α atom.



I : X=H : α -pinene

II : X=OAc : trans-chrysanthenyl acetate

Table 3.: Measured and calculated vicinal $J_{\text{C,H}}$ coupling constants in α -pinene and in trans-chrysanthenyl acetate

	ϕ	J(I)	J(II)	J(calc)
$J_{\text{C}1,5\text{-H}}$	143	7.2	8.0	2.3
	146			2.7
$J_{\text{C}2,7\text{-H}}$	-164	5.6	3.9	7.8 (5.8)
$J_{\text{C}3,5\text{-H}}$	179	7.3	7.3	7.4
$J_{\text{C}4,7\text{-H}}$	162	5.9	3.7	7.6 (5.6)
$J_{\text{C}5,1\text{-H}}$	148	8.0	8.4	3.0
	148			3.0
$J_{\text{C}6,7\text{-H}}$	85	1.3	≈ 0	0.5
	-85			0.5
$J_{\text{C}8,1\text{-H}}$	34	3.2	2.9	5.3
$J_{\text{C}8,5\text{-H}}$	-32	3.6	3.3	5.3
$J_{\text{C}9,1\text{-H}}$	-94	≈ 0	≈ 0	0
$J_{\text{C}9,5\text{-H}}$	96	≈ 0	≈ 0	0
$J_{\text{C}10,1\text{-H}}$	1	4.4	4.1	7.7

in paranthesis: calculated for trans-chrysanthenyl acetate

Were measured the $^3J_{\text{C,H}}$ coupling constants in two natural products, in strictosidine and in 5- β -hydroxy-8-O-acetyl-myoporoside (8) and we compared the measured coupling constants with calculated values obtained by Ayring and Günther's Karplus equation using the correction terms indicated in refs. 5-7. A good agreement between the measured and calculated coupling constants were observed for this two compounds which contains only 6 and 5 membered rings. Denisov *et.al.* reported the $^3J_{\text{C,H}}$ coupling constants of α -pinene (9), and we in collaboration with others reported these constants of

trans-chrysanthenyl acetate (10) (Table 3.). The decrease of $J_{\text{C}2,7\text{H}}$ and $J_{\text{C}4,7\text{H}}$ in trans-chrysanthenyl acetate compared to the measured values in α -pinene is in agreement with the observation of Parella *et.al.* (6) that an oxygen substituent on a γ -carbon decrease the coupling constant with about 2 Hz in a transoid arrangement in a $^{13}\text{C}_\alpha\text{-C}_\beta\text{-C}_\gamma\text{-H}$ fragment. Column 5 shows the calculated coupling constants based on Ayring and Günther's equation. The significant deviations between the measured and the calculated coupling constants suggests that for 4-membered rings further contributions has to be considered.

References

1. A. Bax: *J. Magn. Reson.*, **57**, 314, (1984).
2. A. Bax and M. F. Summers: *J. Am. Chem.Soc.*, **108**, 2093 (1986).
3. M. Eberstadt, G. Gemmecker, D.F. Mierke and H. Kessler: *Angew. Chem.Int.Ed.Engl.* **34**, 1671 (1995).
4. B. Mulloy, T.A. Frenkiel and D.B.Davies: *Carbohydr. Res.*, **184**, 39 (1988).
5. R. Aydin and H. Günther: *Magn. Res.Chem.* **28**, 448 (1990).
6. T. Parella, F. Sanchez-Ferrando and A. Virgili: *Magn. Res. Chem.* **32**, 657 (1994).
7. A.A. van Beuzekom, F.A.A.M. de Leeuw and C. Altona: *Magn.Reson. Chem.*, **28**, 68, (1990).
8. B. Podányi, M. Morvai: to be published
9. A. Y. Denisov, E.A Tyshchishin, A. V. Tkachev and V. I. Mamatyuk: *Magn. Res.Chem.* **30**, 886, (1992).
10. A. Neszmélyi, G.W.A. Milne, B. Podányi, I. Koczka, and É. Héthelyi: *J. Essent.Oil Res.*, **4**, 243 (1992).

¹³C Relaxation in Natural Diamond

E.C. Reynhardt and C.J. Terblanche
Department of Physics, University of South Africa,
P.O. Box 392, Pretoria, South Africa.

1 Introduction

¹³C spin-lattice relaxation times (T_1) in the laboratory frame have been measured for one Ia diamond and one IIa diamond. T_1 for polarisation in a field of 4.7 T is shorter than T_1 associated with the depolarisation in a field of 4.7 T after dynamic nuclear polarisation (DNP) in a field of 0.34 T. If the ¹³C spins are inverted after DNP, T_1 is shortened, but it is still longer than T_1 for polarisation in a field of 4.7 T. It is suggested that spin-lattice relaxation via paramagnetic impurities is the main spin-lattice relaxation mechanism. A qualitative explanation is offered for the observed relaxation times.

2 Relaxation Mechanism

Natural diamonds contain small concentrations of paramagnetic impurities which play an important role in the spin-lattice relaxation of ¹³C nuclei. The average distance between impurities is

$$R = 0.55 N_S^{-1/3}, \quad (1)$$

where N_S is the concentration of paramagnetic impurities. Similarly, the average distance between ¹³C nuclei (1.1% natural abundance) is

$$a = 0.55 N_I^{-1/3}. \quad (2)$$

In an external field the dipolar coupling

$$C = -\frac{3}{2} \sin \theta \cos \theta \exp(-i\phi) S_z I_+ \quad (3)$$

induces a flip of a nuclear spin unaccompanied by an electron flip. For this process [1]

$$\frac{1}{T_1} = \frac{2}{5} \gamma_S^2 \gamma_I^2 \hbar^2 S(S+1) \frac{\tau}{1 + \omega_I^2 \tau^2}, \quad (4)$$

where, if $\hbar \gamma_S H_0 / 2kT \leq 1$ [2],

$$\frac{1}{\tau} = \frac{1}{\tau_e} + \frac{1}{\tau_S}. \quad (5)$$

Here τ_S is the electron spin-spin relaxation time and τ_e the electron spin-lattice relaxation time. The order of magnitude of τ_S can be estimated from

$$\frac{1}{\tau_S} \simeq \frac{\pi}{6} N_S \gamma_S^2 \hbar. \quad (6)$$

If the concentration of impurities is sufficiently high $\tau_S \ll \tau_e$, $\tau = \tau_S$ and the relaxation of the nuclei is caused by the time-varying local magnetic field and the time dependence of the local field is brought about by the spin-spin relaxation of the impurities. Nuclei inside a sphere of radius b_0 , the diffusion barrier, execute flips and relax quickly via the electron to the lattice, but due to the large distribution in local fields inside the sphere, the resonance frequencies of neighbouring spins are not sufficiently close and spin diffusion cannot take place. For $\tau \ll T_{2I}$ and $\gamma_S \hbar H_0 < 2kT$ [3] we have

$$b_0 = \left[\frac{\gamma_S^2 \hbar H_0}{\gamma_I 2kT} \right]^{1/3} a. \quad (7)$$

¹³C spins on the surface of the sphere relax reasonably fast and also take part in spin diffusion via flip-flop transitions with neighbouring spins inside the shell $R > r > b_0$. The time required to cool/heat the spins inside this shell via spin diffusion is proportional to the volume of the shell and the degree of polarisation inside the shell. The distance

$$\beta = 0.68 \left[\frac{C}{D} \right]^{1/4}, \quad (8)$$

where

$$C = \frac{2}{5} \gamma_S^2 \gamma_I^2 \hbar^2 S(S+1) \frac{\tau}{1 + \omega_I^2 \tau^2} \quad (9)$$

and

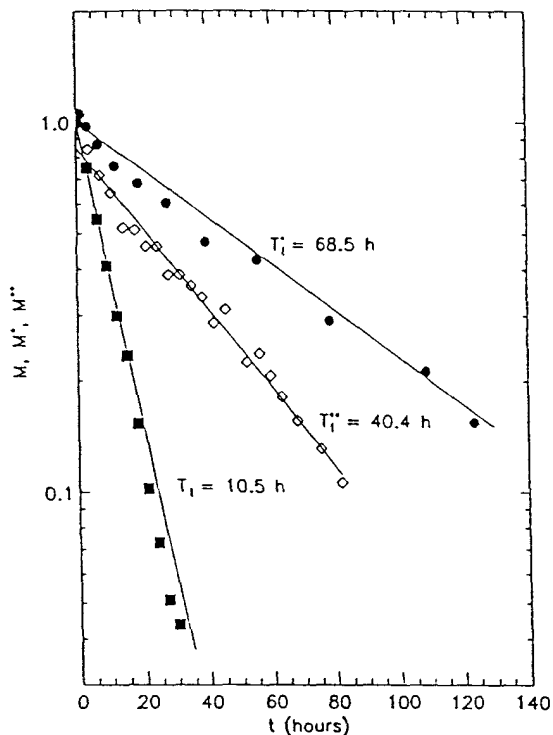
$$D = \frac{a^2}{50T_{2I}}, \quad (10)$$

the diffusion coefficient, determines the radius at which direct relaxation ($r \leq \beta$) is faster than spin diffusion. For $H_0 \geq 1$ T, we expect $\beta < b_0$. The spin-lattice relaxation rate is given by

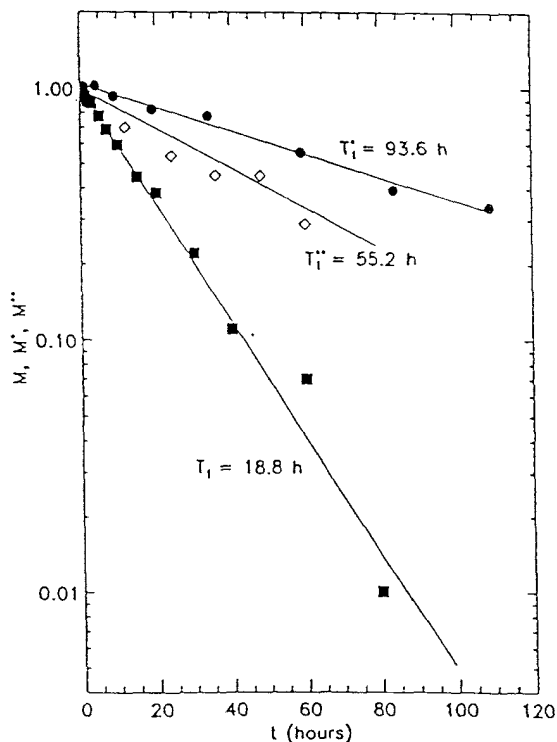
$$T_1^{-1} = \frac{4\pi N_S C}{3b_0^3}. \quad (11)$$

3 Results

Type Ia Diamond (3.5 ct): Spin-Lattice Relaxation In External Field



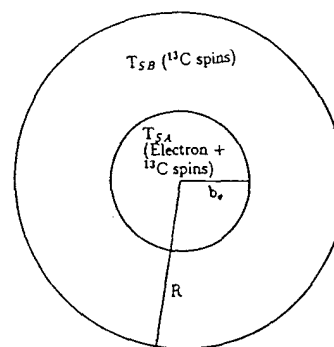
Type IIa Diamond (3.4 ct): Spin-Lattice Relaxation In External Field



4 Discussion

4.1 Polarisation in Zeeman Field (T_1)

When the unpolarised sample is placed in the 4.7 T magnetic field, the electrons cool down quickly via spin-lattice relaxation. The ^{13}C nuclei inside the radius b_0 relax fast and reach a low spin temperature (T_{SA}) quickly. Spins on the surface of the sphere with radius b_0 are involved in flip-flop transitions with neighbouring spins in the shell $R > r > b_0$, which in turn execute flip-flop transitions with spins further away. Since the spins in the shell have a high spin temperature (T_{SB}) (unpolarised), they are cooled at a relatively fast rate ($(T_1)^{-1}$).



4.2 Depolarisation After DNP (T_1^*)

After DNP at 0.34 T, the sample is transferred to a field of 4.7 T. Now both T_{SA} and T_{SB} are low and the relaxation rate $(T_1^*)^{-1}$ should be very low. If $T_{SA} \approx T_{SB}$, direct relaxation of the ^{13}C spins to the lattice would be the only relaxation mechanism. Therefore $(T_1)^{-1} > (T_1^*)^{-1}$.

4.3 Depolarisation After DNP and Spin Inversion (T_1^{**})

After transfer from 0.34 T to 4.7 T the ^{13}C spins in the shell with $R > r > b_0$ are inverted by applying a 180° pulse. Now $T_{SB} \rightarrow \infty$ and since T_{SA} is low, the spins on the surface of the sphere, with radius b_0 , are cooled down and the probability that they will be involved in flip-flop exchange with neighbouring hot spins T_{SB} in the shell is high. The diffusion process is therefore expected to be relatively fast, but on the other hand, the shell contains a large number of spins oriented antiparallel to the external field. It is expected that the relaxation rate $(T_1^{**})^{-1}$ will be faster than $(T_1^*)^{-1}$ but slower than $(T_1)^{-1}$.

5 References

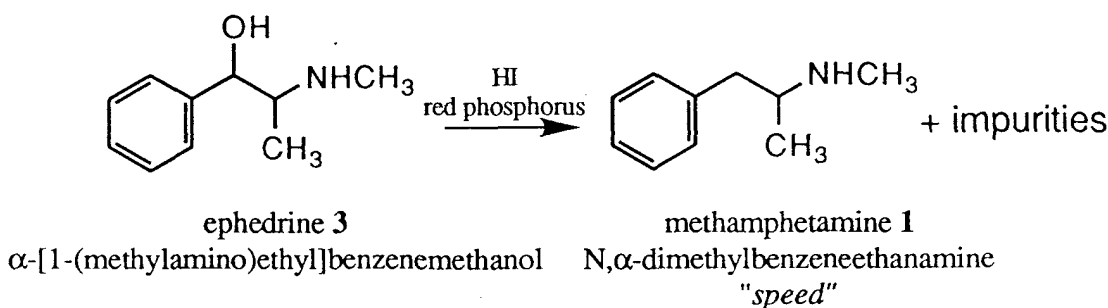
- [1] A Abragam, The Principles of Nuclear Magnetism, (Oxford) 1961, Ch IX.
- [2] GR Khutsishvili, Sov. Phys. USPEKHI, 8, 743 (1966).
- [3] M Goldman, Spin Temperature and Nuclear Magnetic Resonance in Solids, (Oxford) 1979, Ch. 3.

NMR Solves Drug Problems with "Speed"

M.J. McTigue, R.T.C. Brownlee, J.R. Pearson*, S.J. Pratt,
J.E. Rowe, M. Sadek and E.M. Sear

School of Chemistry, La Trobe University, Bundoora, Victoria, 3083, Australia

**Victoria Forensic Science Centre, MacLeod, Victoria, 3085, Australia*



Introduction

The strength of NMR spectroscopy has been illustrated by the structural elucidation of impurities found in illicitly manufactured amphetamines.

The synthesis of methamphetamine ("speed") **1** from pseudoephedrine **3** via reduction with hydriodic acid and red phosphorus was studied. The impurities that contaminated the product were isolated and investigated. Some of the impurities had been reported previously (1), while diastereomers of N-methyl-N-(α -methylphenethyl)amino-1-phenyl-2-propanone **8** and **9** and the cis-cinnamoyl derivative of methamphetamine **10** were identified for the first time (2).

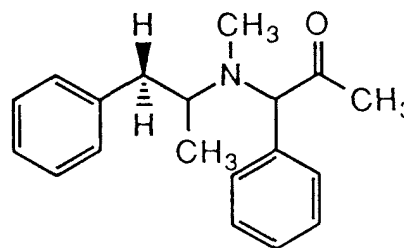
Background

Currently the most popular method for the production of "speed" in Victoria (Australia) is by the reduction of pseudoephedrine **3** with hydriodic acid and red phosphorus to yield methamphetamine **1**. Impurities in the product originate from:

1. inadequate purification procedures,
2. impurities already found in the starting materials,
3. unreacted intermediates or incomplete reactions, and
4. polycondensation reactions.

Identification of these impurities can be used as a guide in determining which synthetic method has been used. This in turn helps with identification of the particular laboratory from where the sample has originated. Structural elucidation of these impurities is essential. This information allows the design of straightforward analytical techniques for rapid characterisation of samples that will not be disrupted by unknown species. It also allows the toxicity of the impurities to be determined which can be of importance for the treatment of drug overdose and addiction.

NMR spectroscopy and mass spectrometry were the analytical techniques that were used to determine the structures of the unknown impurities.



diastereomers of
N-methyl-N-(α -methylphenethyl)-
amino-1-phenyl-2-propanone
8 and **9**

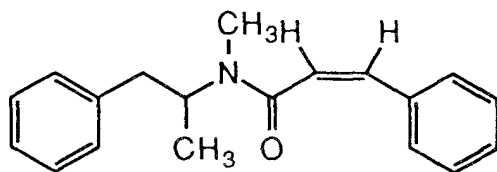
Identification of 8 and 9

Isomers **8** and **9** were inseparable by TLC and reverse phase HPLC. Mass spectra indicated that each isomer had a molecular mass of 281. These isomers were also known to contain nitrogen from GC analysis using a nitrogen-phosphorus detector. NMR spectroscopy was used to determine the structural formulae of the two diastereomers.

NMR data were collected on a Bruker AM300 NMR spectrometer. Assignment of the isomeric species was performed with a variety of NMR experiments. The experiments performed included double quantum filtered COSY, INEPT, HETCOR and FUCOUP. The full assignment required successful long range correlation of ^1H with ^{13}C nuclei. As inverse experiments were plagued with artefacts the assignment was performed using the robust ^{13}C acquired FUCOUP experiment (4).

Identification of 10

Species **10** was found to have a molecular mass of 279 from its mass spectrum. The compound was also found to contain nitrogen from GC analysis with a nitrogen-phosphorus detector.



cis-cinnamoyl derivative
of methamphetamine
(Z)-N-methyl-N-(α -methylphenethyl)-
3-phenylpropenamide
10

Magnitude COSY and HETCOR data were adequate to determine the chemical structure of **10**. The compound was found to be the cis-cinnamoyl derivative of methamphetamine ($^3J_{\text{HH}}=12.6\text{Hz}$). NMR spectra indicated the presence of two rotational isomers. Further chemical analyses required the synthesis of **10** and the corresponding trans-cinnamoyl derivative of methamphetamine. The trans-isomer was dissolved in DMSO- d_6 and NMR

data were acquired at a variety of temperatures. The ^1H NMR assignment was determined from magnitude COSY data. Variable temperature experiments substantiated claims that both the trans and cis isomers existed as a pair of rotational isomers in solution.

Conclusions

All the impurities from the synthetic scheme under analysis were identified. Impurities **8**, **9** and **10** were reported for the first time (2). Their structural formulae were determined by utilising homo- and heteronuclear NMR techniques and mass spectrometry. A distinctive trace was recorded by GC which now enables forensic scientists to identify when a similar synthetic scheme has been adopted. Relative proportions of the different impurities in the GC trace can now be used to aid further identification of clandestine laboratories. Impurities **8** and **9** have already been reported in street samples of "speed" in N.S.W. (Australia) (1) and California (U.S.A.) (3).

References

- ¹P.A. Donkin and H. Dinh. Chemical profile of liquid methyl-amphetamines. Report, Division of Analytical Laboratories, N.S.W. Dept. Health (May 1989).
- ²K.L. Windahl, M.J. McTigue, J.R. Pearson, S.J. Pratt, J.E. Rowe and E.M. Sear. An investigation of the impurities found in methamphetamine synthesised from ephedrine by reduction with hydriodic acid and red phosphorus. *Forensic Science International* (in press 1995).
- ³D. Christian and R. Schneider. Methyl-amphetamine via the pressure cooker. Presented at the first technical meeting of the Clandestine Laboratory Investigating Chemists Association, San Diego (September 1991).
- ⁴A.L. Waterhouse, I. Holden and J.E. Casida. Ryanoid Insecticides: Structural examination by fully coupled two-dimensional ^1H - ^{13}C shift correlation nuclear magnetic resonance spectroscopy. *J. Chem. Soc. Perkin Trans. II*, 1011 (1985).

INEPT NMR of Paramagnetic Compounds.

M. Sadek, R.T.C. Brownlee, S.D.B. Scrofani* and A.G. Wedd*

School of Chemistry, La Trobe University, Bundoora, Victoria, 3083, Australia

*University of Melbourne, Parkville, Victoria, 3052, Australia

NMR of paramagnetic compounds

A major difficulty in the study of paramagnetic proteins by NMR methods is the observation of ^1H resonances associated with the hydrogen atoms located close to the paramagnetic active sites. Identification of these protons is important to establish secondary and tertiary structure.

^1H NMR based experiments form the core of structural studies, however, protons (having a large magnetogyric ratio) are more susceptible to excessive line broadening (≥ 100 Hz) due to electron and nuclear dipole interactions. In paramagnetic proteins broad resonances from the paramagnetic parts of the protein, resonating within the same chemical shift region as narrow resonances from the diamagnetic part of the molecule, are almost impossible to detect. Protons less than 4 Å from the paramagnetic centres are unobservable by ^1H NMR, whereas protons between 4 -7 Å are difficult to detect.

In contrast, all 61 nitrogens of the NH backbone in the paramagnetic protein CpFd (ferredoxin from *Clostridium pasteurianum*) can be easily identified by ^{15}N NMR (1). Thus ^{15}N may provide a route to the indirect identification of protons.

Relaxation in ferredoxin from *C. pasteurianum*

The NH...S hydrogen bonds between the backbone NH groups and the iron-sulfur clusters, together with the effect of protein folding, modulate the redox potential and hence the efficiency of electron transfer. Detection of the proton resonances associated with these nitrogens is therefore important in defining the effect that the NH...S hydrogen bonds have on the properties of the active sites and on the protein as a whole.

The linewidths of hyperfine shifted proton coupled nitrogen resonances are broad (30-40 Hz), however decoupling reduces them to 3-10 Hz. The difference can be interpreted in terms of a substantial contribution to ^{15}N relaxation from *scalar relaxation of the second kind*, which is removed by decoupling (1). This also confirms the predominance of nuclear dipole-dipole interactions in the relaxation processes affecting ^{15}N nuclei.

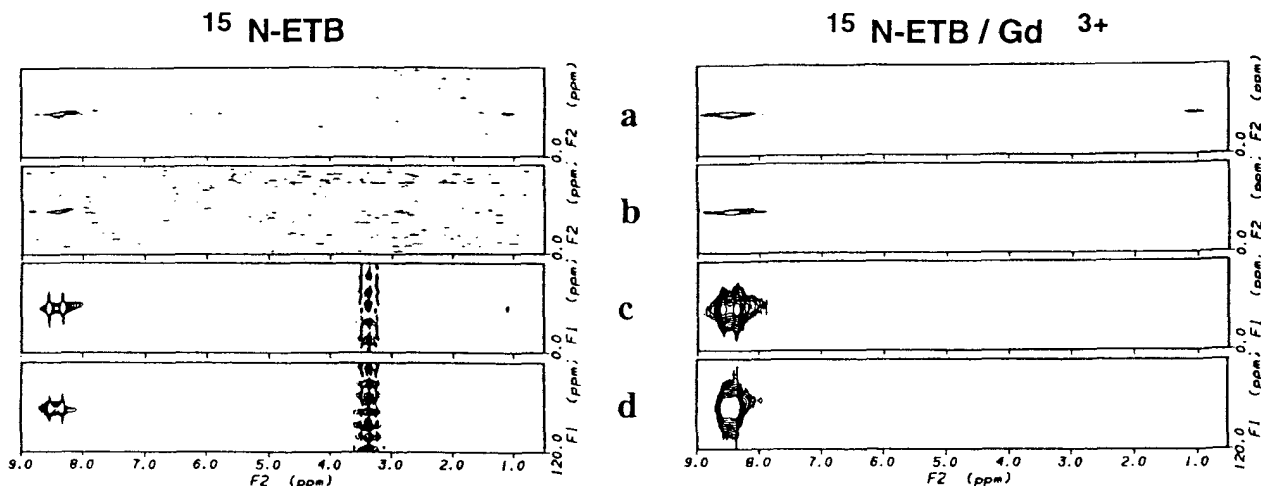
Relaxation of proton and nitrogen nuclei

Dipole-dipole interactions (proportional to the product of parameters which include the second power of magnetogyric ratios of the interacting species) involving electrons ($\gamma_e \equiv 657 * \gamma_H$) are especially large for hydrogen. Relaxation processes are very fast and ^1H resonance lines are broad ($\equiv 100\text{Hz}$).

The low magnetogyric ratio of ^{15}N ($\gamma_N \equiv \gamma_H / 10$) makes it far less vulnerable to line broadening. Thus ^{15}N is expected to give relatively narrow resonance lines, even when affected directly by electron-induced (paramagnetic) relaxation.

Since the problem of low natural abundance of ^{15}N is effectively removed by labeling, both ^1H - and ^{15}N -detected NMR methods are accessible for these proteins. The paramagnetic properties of the protein determine which of these methods is more suitable, rather than the theoretical sensitivities of the methods.

A simple test sample of 0.1 M ^{15}N labeled ethylbenzamide in DMSO- d_6 spiked with paramagnetic gadolinium nitrate was used for the comparison of related proton / nitrogen correlation experiments with either ^1H or ^{15}N detection (2).



a) proton decoupled ^{15}N -detected 2D INEPT (coupling evolution delay of 2.73 ms ($1/4J$)). b) proton decoupled ^{15}N -detected 2D INEPT (delay of 1.5 ms). c) ^{15}N coupled ^1H -detected 2D HMQC (delay of 5.46 ms ($1/2J$)). d) ^{15}N coupled ^1H -detected 2D HMQC (delay of 3 ms).

The relative sensitivity of ^{15}N - and ^1H -detected correlations in paramagnetic compounds

All experiments for ^{15}N -ETB (diamagnetic) and ^{15}N -ETB / Gd^{3+} (paramagnetic) samples were obtained on a Bruker AM-400 with comparable settings (experimental time of 2 hours each).

The figures above show that for paramagnetic compounds ^{15}N -detected experiments have better signal to noise, improved possibilities of resolving overlapped crosspeaks, and the absence of troublesome artefacts resulting from water presaturation.

^{15}N -detected 2D TOCSY-INEPT

A ^{15}N -detected 2D TOCSY-INEPT experiment with a short spin-lock time of approximately 10 ms is suggested as a better alternative to long range heteronuclear correlations (HMBC), which often fail in paramagnetic proteins because of the necessary inclusion of long delays (> 30 ms).

This sequence was derived from the standard ^{15}N -detected 2D INEPT experiment for Bruker AM spectrometers by insertion of an MLEV-17 spin-lock after t_1 . This type of an experiment was first described by Kessler *et al.* (3).

The spin-lock duration of 10-20 ms is usually sufficient to allow significant magnetization transfer within the coupled spin systems (2).

Conclusions

In the experiments that have been described both relaxation-induced coherence transfer and scalar coupling may contribute to the cross-peaks. However, both effects arise from the existence of scalar coupling, thus making it unnecessary for assignment purposes to differentiate between them.

This work has shown that ^{15}N -detected heteronuclear correlation experiments are more successful than the ^1H -detected versions in detecting paramagnetically broadened proton resonances. The advantage for paramagnetic compounds is further enhanced by reducing the coupling related delays in these pulse sequences by up to 50%.

References

- 1M. Sadek, S. D. B. Scrofani, R. T. C. Brownlee and A. G. Wedd, *J. Chem. Soc. Chem. Comm.*, 105-106 (1995).
- 2M. Sadek and R. T. C. Brownlee, *J. Magn. Reson., Series B* **109**, 70-75 (1995).
- 3H. Kessler, G. Gemmecker, M. Kock, R. Osowski and P. Schmieder, *Magn. Reson. Chem.*, **28**, 62 (1990).

The Voids Analysis of the Refractories Using NMR Micro-imaging Method

* KOJI SAITO, MASAOKI SHINOHARA, HISAYUKI TSUNO and KENICHI HASEGAWA

*Advanced Technology Research Laboratories NIPPON STEEL CORPORATION
1618 ida nakahara-ku Kawasaki City 211 JAPAN*

1. INTRODUCTION

Refractories, which have voids, are very important for the steel-making industries. Huge and many kinds of refractories are used to cope with very high temperature environments which are produced from the iron and steel making process. But there are no suitable methods for the void analysis. Only potentiometer method with mercury has been conventionally used. In this paper, we demonstrate a voids analysis of refractories using NMR micro-imaging method.

2. EXPERIMENT

We prepare the MgO sample for converters, which is important for process of steel-making. This is the typical sample for measurement, 5 mm sample tubes, MgO refractories, methanol solvents. We sometimes use ultrasonic treatments to permeate solvents into refractories. The imaging experiments were recorded JEOL A-400 (9.45T Oxford type SCM) NMR spectrometer with imaging units. The active shielded gradient coils were equipped, of which max. gradient strength is 120 gauss/cm. Its probe has exchangeable RF insert type ϕ 5, 10 mm diameter sample size. We were used mainly 3D spin echo sequence because 2D spin echo method is not sensitive. The measurement conditions mainly were 128*128, echo time ; 2msec, pulse delay time; 0.5sec. The used gradient strength were 60 gauss/cm.

3. RESULTS AND DISCUSSION

It is well-known that the factor of refractories, for example heat, shock, and slag-resistant, have relationship with not only total volumes of the voids but also the distribution, size three dimensional void structure. We think the suitable solvents are like these for the voids analysis of micro-imaging method. 1) permeate easily, 2) cheap, 3) sharp and strong single peak in NMR spectroscopy, 4) not poison, not harmful, 5) not react with refractories, 6) easy to use. So we select methanol (MeOH), silicon oil, acetone etc. The void

image of refractories are shown in Fig.1. The part of white colors showed the voids. Upper column showed the slice section on the line of image. In Fig.2 there was the voids images which were continuous slices. We can easily understand the voids size and those distribution maps from statical calculation programs. Fig.3 showed the voids of refractories with diameters versus its existence rates. The voids distribution were not Gaussian distribution, like parson rate distribution. It is surprisedly data. Table 1 is the comparison between the results of potentiometer and that of micro-imaging data. The results are consistent.

4. CONCLUSION

- 1). The results of NMR micro-imaging method, which reflected completely the voids image contrast, were very clear and consistent with the results of the potentiometer method.
- 2). We could easily understand those size and distribution maps from some statistical calculation.
- 3). We are sure that NMR micro-imaging method is powerful and useful method for the voids analysis of the refractories in the steel industries. Probably in Japanese iron and steel committee, they become to approve that the standard method of the voids analysis of the refractories is NMR micro-imaging method instead of the potentiometer, 1996. We think it is first case that NMR micro-imaging method spread the industries areas.

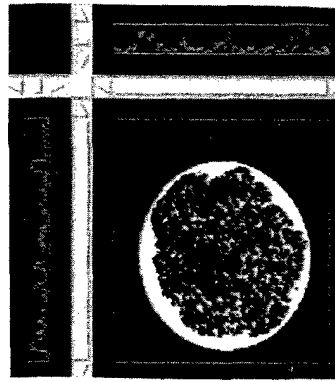


Fig.1 One slice image obtained by 2D spin echo image

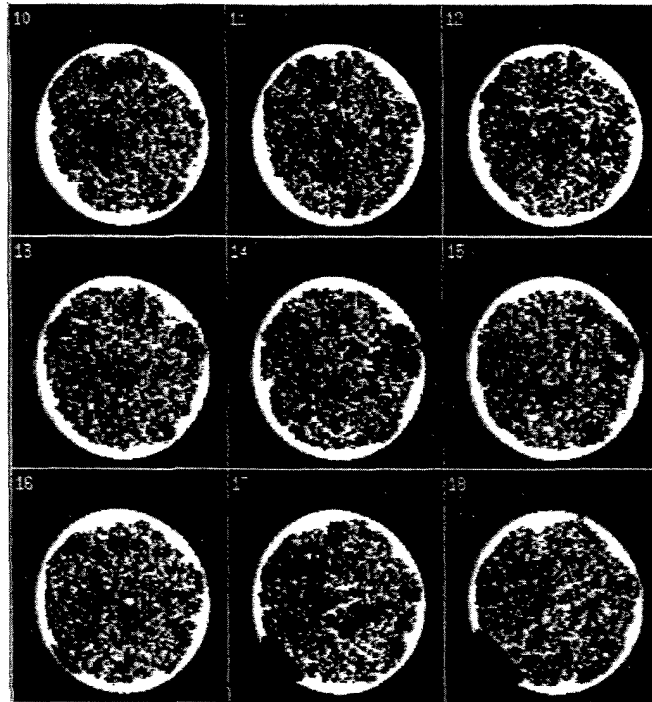


Fig.2 Some slice images of refractories obtained by 3D spin echo method

Table 1 The comparison between void fractions (%) measured by potentiometer and that of micro-imaging method

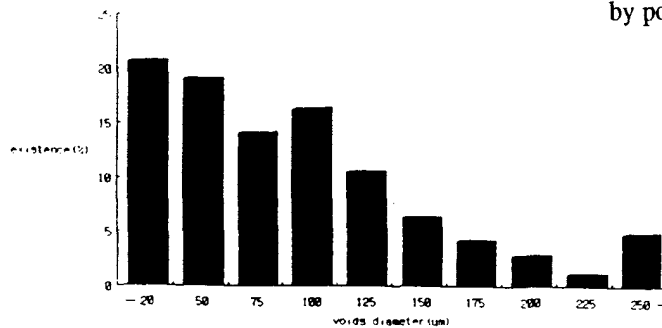


Fig.3 Relationship between void diameter and its existing rate

	apparent porosity (%)	
	MgO-C	SiO ₂ -Al ₂ O ₃
potentiometer	20.4	26.5
micro-imaging method	21.3	25.0

Oxygen Permselective Hollow Fiber Membrane of Fluoren-based Polyimides <studies on structural analysis and its mechanisms>

* KOJI SAITO, MORIAKI HATAKEYAMA, MASAOKI SHINOHARA and KOUICHI FUJISHIRO

Advanced Technology Research Laboratories NIPPON STEEL CORPORATION
1618 ida nakahara-ku Kawasaki City 211 JAPAN

1. INTRODUCTION

It is well-known that polymers containing fluorene moiety, <CARDO-TYPE POLYMER> have high thermal stability. In addition, we found these polymer had a high oxygen permselective property. We analyzed these polymer structures by solid-state ^{13}C and ^{15}N CPMAS and clarified the mechanisms of gas separation.

2. EXPERIMENT

The representative structures of cardo-polyimides were shown in Fig.1. All NMR experiments were performed on a JEOL EX-400 spectrometer using 5000-6000Hz of spinning rate. In the ^{15}N CPMAS experiments, we used long contact time (=20msec) for the improvement of the S/N because of natural abundance measurements.

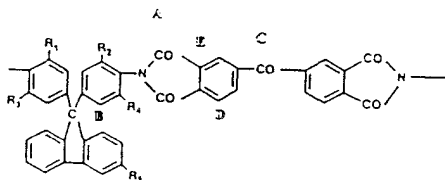


Fig.1 The chemical structure of cardo-polyimides

3. RESULTS AND DISCUSSION

<the correlation of the forms of cardo-polyimides>

The ^{13}C and ^{15}N CPMAS spectrum of cardo-polyimides in the forms of powder, hollow fiber and film were shown in Fig.2, respectively. There were no differences in ^{13}C CPMAS. But there were significant difference among the three forms, powder: 151, 153, 159ppm, hollow fiber: 153, 159ppm, film: 153ppm in ^{15}N CPMAS. It was reason that ^{15}N chemical shift were wider in chemical shift range and more sensitive to the structure of polymer caused by polymer array. The results of SEM image (Fig.3) showed there were two phase, an active phase (outer parts) and an inactive phase (inner parts) for gas separation in the form of the hollow fiber.

So, it was clear that the results of NMR studies were consistent with the results of SEM. And then, the structure of an active phase for gas separation, which of peak of chemical shift was 153ppm, was not the same structure of an inactive phase, which of that was 159ppm. Because the form of film had only an active phase and there was only one peak at 153ppm. After all, cardo-polyimides had a various kinds of structure about imide parts respectively.

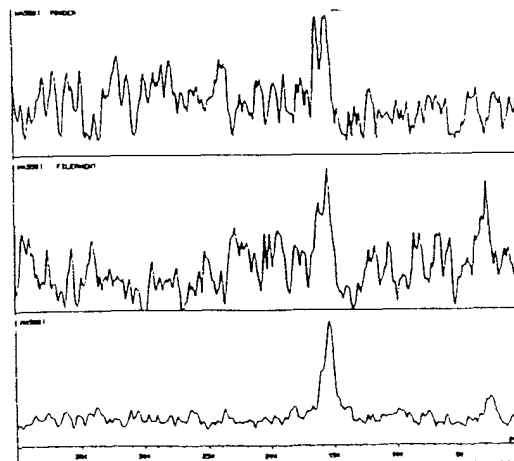
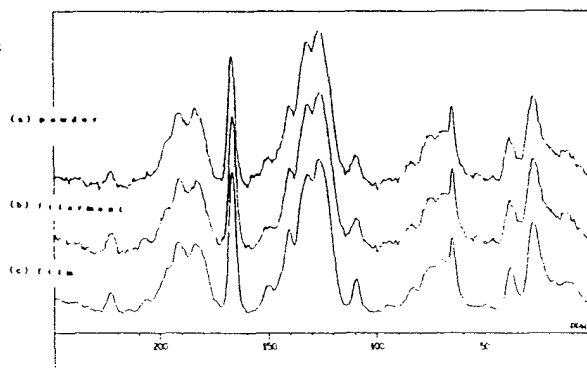


Fig.2 The ^{13}C and ^{15}N CPMAS spectrum of cardo-polyimides in the form of powder, hollow fiber and film



Fig.3 The SEM image of the form of hollow fiber

<the mechanisms of gas separation>

It was well-known that the NMR relaxation time parameters were depend on the molecular motion of polymer. So we measured and analyzed the relaxation parameters (T_{1C} , T_{1Cp} , T_{CH}) with CP methods. Fig.4 showed that the correlation between the NMR relaxation parameters and gas separation permeabilities. $1/T_{1C}$ (relaxation rate) at imide carbonyl carbon and cardo center carbon has a good correlation to the permeabilities of cardo-type polyimides, respectively. But $1/T_{1Cp}$ had not good correlation. So, it was meant that gas permeabilities depend on the local molecular motion (correspond to mainly T_{1C}) of these polymer. Especially, $1/T_{1C}$ at the other carbons (for example, aromatic carbons, alkyl group carbons etc.) had not so good correlations, and then gas permeabilities were mainly performed in imide carbonyl and cardo center regions and subject to the local motion of these polymer about 10^{-8} sec of time scale.

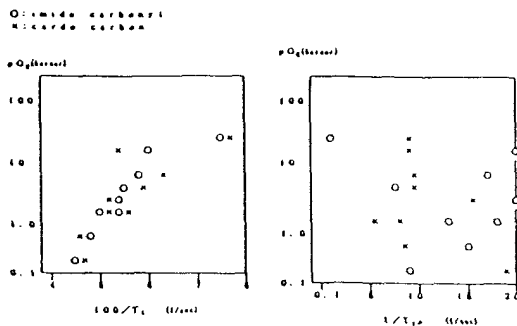


Fig.4 The relationship between $1/T_{1C}$ or $1/T_{1Cp}$ and gas permeabilities

And then, how about gas separation? In general, gas separation permselective property were depend on chemical structure, so we checked the relationship between structural parameters and permselective property. NMR parameters, especially chemical shift, are sensitive to the chemical structure. But ^{13}C chemical shift at imide carbonyl had not good relation. Already we discussed ^{15}N chemical shift were more sensitive and wider chemical shift to the chemical structure. Fig.5 showed the relationship between ^{15}N chemical shift and gas permselective property. There was a good correlation. ^{15}N chemical shift were depend on three dimensional structure in which imides nitrogen regions were produced by polymer array.

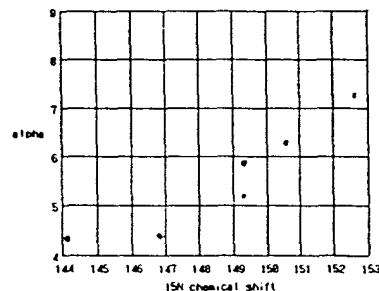


Fig.5 The relationship between ^{15}N chemical shift and gas permselective property

4. CONCLUSION

We clarified the mechanisms of gas separation by solid state ^{13}C and ^{15}N CPMAS. The mechanisms were followed: (a) The gas permeability depend on the molecular motion about 10^{-8} sec of time scale, which subjected to T_{1C} at imide carbonyl carbon and cardo center carbons. (b) The gas permselective property mainly depend on the three dimensional structures of these polymer, especially in imides nitrogen regions. (c) We will propose "the rotational doors at the hotel" model as the mechanisms of gas separation (Fig.6).

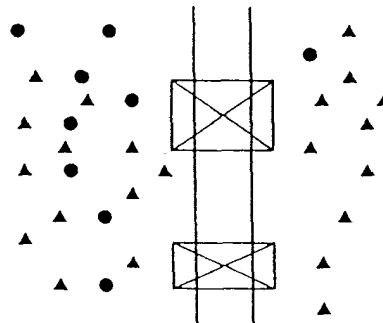


Fig.6 The rotational doors at the hotel model

**FT Pulsed EPR of Exchange-coupled Spin Systems
in Transition Metal Clusters and Low-dimensional Magnets**

Daisuke Shiomi,¹ Kazunobu Sato,² Takeji Takui,² and Koichi Itoh¹
¹Department of Material Science and ²Department of Chemistry, Faculty of Science,
Osaka City University, Sumiyoshi-ku, Osaka 558, Japan

In chemistry and biochemistry, Fourier transformed (FT) pulsed EPR has been one of the most powerful tools particularly in investigating isolated paramagnetic centers. We have proposed time-domain EPR as a new spectroscopic technique for investigating molecule-based magnetic materials in which paramagnetic centers are exchange-coupled in a solid state.^{1,2)} This report deals with a peculiar magnetic resonance phenomenon which has been found during such studies of FT pulsed EPR.

The main topic of the present pulsed EPR study is electron spin transient nutation. Using the relation between the nutation frequency ω_n and the spin quantum numbers S and m_s of allowed EPR transitions,

$$\omega_n = \gamma B_1 [S(S+1) - m_s(m_s-1)]^{1/2}, \quad (1)$$

(γ : gyromagnetic ratio, B_1 : field amplitude of pulsed microwave), in the weak B_1 limit,^{3,4)} we can discriminate between different spin multiplicities in the frequency domain. The identification of the spin quantum number S on the basis of eq. (1) has been reported for randomly oriented systems of some paramagnetic molecules.^{1,2)} In order to establish the methodology of the nutation technique for studying solid state magnetism, particularly the system characterized by the exchange interactions comparable to the thermal energy $k_B T$, we adopted a powder sample of zinc-doped cupric acetate monohydrate as a minimal model for the exchange-coupled molecular spin systems. The compound has two kinds of paramagnetic species in a solid state; one is a two-spin system with $S=0$ and $S=1$ equilibrium in the Cu acetate dimeric structure and the other an only apparently isolated $S=1/2$ on the Cu²⁺ ion in the Zn-doped heterobimetallic site.

Pulsed and cw EPR spectra were recorded on a Bruker ESP380 FT EPR spectrometer equipped with a dielectric cavity with a tunable Q of 100–5000. The temperature was controlled by using a Bruker helium-flow cryostat and an Oxford ITC4 temperature controller. The microwave pulse was amplified by a 1 kW travelling wave tube amplifier. The Zn-doped Cu acetate crystal was prepared by recrystallization from a water solution of $\text{Cu}(\text{CH}_3\text{CO}_2)_2 \cdot \text{H}_2\text{O}$ and $\text{Zn}(\text{CH}_3\text{CO}_2)_2 \cdot 2\text{H}_2\text{O}$ (about 8:2 molar ratio). The crystal was ground finely before the EPR measurements. The doping ratio was found to be 1 mol % from a static susceptibility measurement on a Quantum Design SQUID magnetometer MPMS2.

Continuous-wave EPR spectra measured for the powder sample of the compound are depicted in Fig. 1. The spectra consist of both the signal from the doublet ($S=1/2$) of the Zn-doped site and that of the fine structure from the thermally excited triplet ($S=1$) of the dimer. The doublet as well as

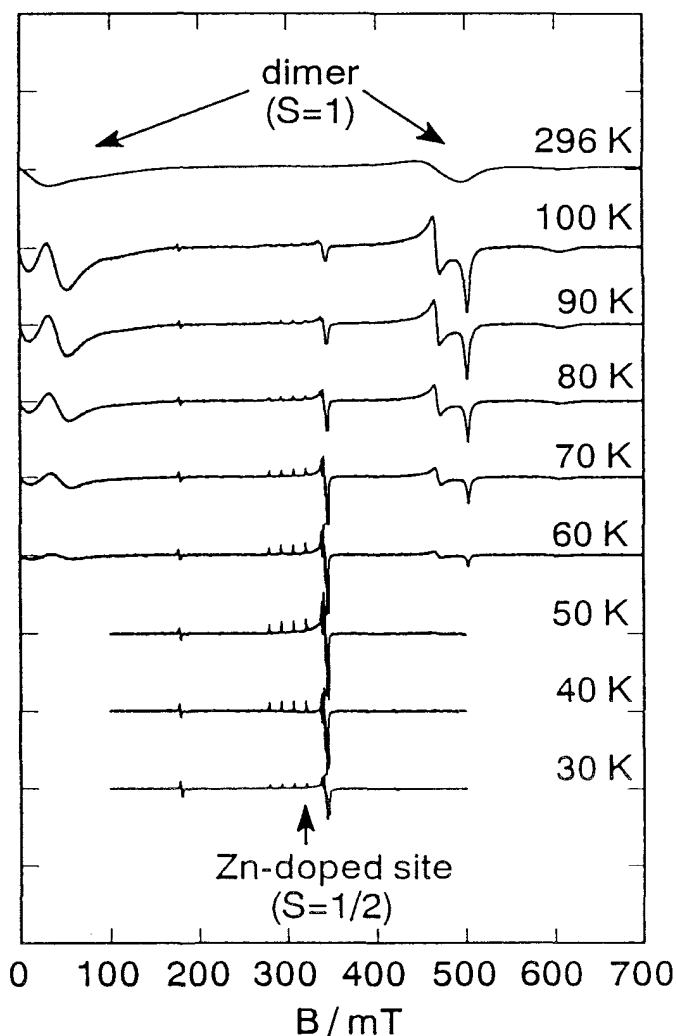


Fig. 1. CW EPR spectra of the Zn-doped cupric acetate powder. The DPPH reference has been removed in the cw measurements.

the triplet signal has been reproduced well by using the reported EPR parameters⁵⁾ (the g value, the hyperfine coupling constant for the $I=3/2$ nucleus of Cu and the fine structure constants), indicating that the observed signals can be assigned to Zn-doped Cu acetate in the crystalline solid and not to impurities or lattice defects.

Two-pulse Hahn echo experiments ($\pi/2$ - π -echo) were made for the powder sample in the whole static field range examined in the cw measurements. The compound was found to be echo-silent except for the $g=2$ region where the

cw EPR signal from the doublet was observed. Figure 2 shows the field-swept echo-detected EPR spectrum in the $g \sim 2$ region recorded by monitoring the echo-peak intensity with sweeping the static field. The spectral profile in Fig. 2 reproduces the cw signal from the doublet (Fig. 1), indicating that the echo signal reflects the spin magnetization from the doublet species at the Zn-doped site.

For identification of the spin quantum number S on the basis of eq. (1), it is crucial to calibrate the microwave amplitude B_1 applied to the sample. In the present nutation experiments, a single crystal of an organic radical DPPH was mounted on the quartz tube in the vicinity of the Cu acetate powder as an $S=1/2$ reference ($\omega_n(\text{DPPH}) = \omega_{1/2} = \gamma B_1$). The nutation of DPPH was measured by monitoring the FID signal, serving as a standard for ω_n .

The transient nutation of Cu acetate was detected by monitoring the intensity of the echo signal with incrementing the excitation pulse ($\pi/2$ -pulse) length. The static magnetic field was fixed at 320.4 mT in order to suppress the influence of the FID from DPPH after the π -pulse on the detection of the echo intensity. Fourier transformation of the nutation signals to the frequency domain yielded nutation spectra exhibiting two peaks as shown in Fig. 3. The peak at 14 MHz is not intrinsic but of apparatus-origin; these peaks are independent of the microwave power. On the other hand, the frequency of the broader peak varies in the range from 21 to 16 MHz as the microwave power varies. The broader peaks are thus ascribable to Cu acetate.

The arrows in Fig. 3 denote the nutation frequency of the DPPH reference, $\omega_{1/2}$. According to eq. (1), the observed ω_n value for the above power-dependent peak, $\omega_n \sim 1.4\omega_{1/2}$, is indicative of triplet species instead of doublet. It should be noted that the microwave pulse excited the doublet more efficiently than the triplet under the present static field: In the $g \sim 2$ region, the triplet species should have small intensity in the cw spectra as compared with the doublet. Any experimental artifact due to the reference can be ignored since the nutation experiments without the reference have given the same result.

Considering that the triplet species was found to be echo-silent, a possible explanation of the finding described above is given in terms of cross-polarization between the doublet and triplet species; the apparent discrepancy can be solved by taking account of a transfer of the Zeeman energy in the rotating frame from the doublet excited by the microwave pulse to the triplet. The observed phenomenon is thus regarded as "pseudo-double resonance" associated with the molecules with different spin multiplicities, suggesting the potentiality of FT pulsed EPR spectroscopy for examining the microscopic environments of the magnetic centers which are subject to exchange interactions.

The cross-polarization rate in the present system should be governed by the concentration of the triplet and doublet molecules in the solid. For expounding the findings, pulsed EPR experiments on the single crystal samples are now in

progress with varying the concentration ratio of the $S=1/2$ and $S=1$ species.

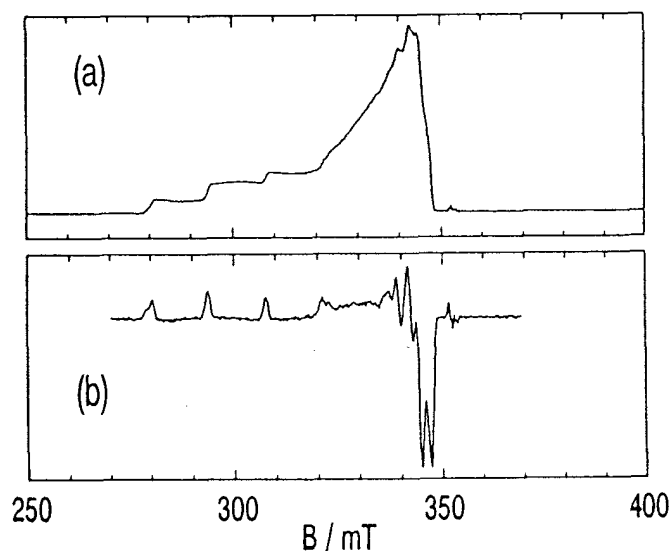


Fig. 2. (a) Field-swept echo-detected EPR spectrum measured at 15 K. The signal from the DPPH reference has not been detected since DPPH was echo-silent. (b) First derivative curve obtained from the spectrum in (a).

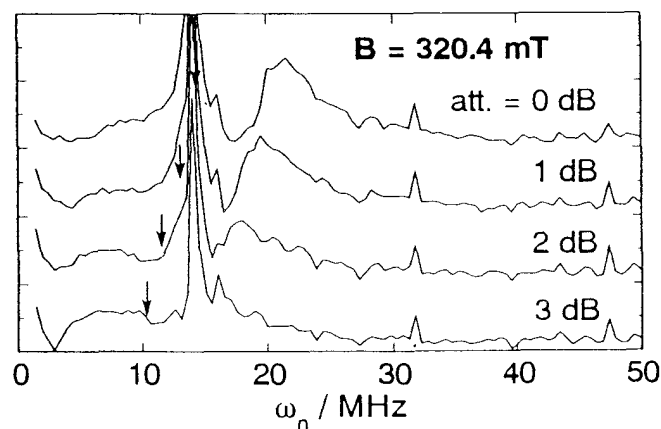


Fig. 3. Fourier transformed nutation spectra recorded at 15 K. The arrows denote the nutation frequency of the DPPH reference measured by the FID-detected method.

References

- 1) K. Sato, D. Shiomi, T. Takui, K. Itoh, T. Kaneko, E. Tsuchida and H. Nishide, *J. Spectrosc. Soc. Jpn.*, **43**, 280(1994).
- 2) D. Shiomi, K. Sato, Y. Teki, T. Takui, K. Itoh, K. Tanaka and F. Toda, *Mol. Cryst., Liq. Cryst.*, **271/272**, in press.
- 3) J. Isoya, H. Kanda, J. R. Norris, J. Tang and M. K. Bowman, *Phys. Rev. B*, **41**, 3905(1990).
- 4) A. V. Astashkin and A. Schweiger, *Chem. Phys. Lett.*, **174**, 595(1990).
- 5) P. Sharrock and M. Melnik, *Can. J. Chem.*, **63**, 52(1985).

NMR studies of the active site of the HIV-1 protease by site-specific labelling.

Ross Smith, Ian M. Brereton¹, Richard Y. Chai² and Stephen B. H. Kent²

*Department of Biochemistry and ¹Centre for Magnetic Resonance
University of Queensland, Queensland 4072, Australia*

*²The Scripps Research Institute, 10666 N. Torrey Pines Road
La Jolla, California 92037, U.S.A.*

The human immunodeficiency virus-1 contains a proteolytic enzyme, HIV-1 protease (HIV-1 PR), which is expressed as part of the gag-pol polyprotein primary translation product. It is responsible for specific cleavage of the gag and gag-pol translation products to yield the structural proteins and enzymes required for assembly of new virions (1). Inhibition of HIV-1 PR action has been shown to prevent formation of mature viral particles. For this reason, the HIV-1 PR is currently one of the most intensively studied targets of drug design, with the aim of developing specific inhibitors as candidate anti-AIDS therapeutics (2).

HIV-1 PR is a homodimeric protein formed from two identical 99-residue polypeptides (3). Substrate-derived inhibitors are bound in a 22Å-long tube at the dimer interface, with both subunits contributing a catalytically-essential aspartic acid side chain to the active site.

The currently accepted mechanism (4) for HIV-1 PR involves a sidechain -COOH donating a proton to the carbonyl of the scissile peptide bond, increasing the electrophilic character of the carbonyl carbon; nucleophilic attack by a water molecule is then catalyzed by a -COO⁻ carboxylate sidechain, leading to the formation of a neutral gem-diol intermediate. The rate-determining collapse of this tetrahedral intermediate is catalyzed by the same two sidechains, playing inverse roles, to yield the cleaved products.

Despite the widespread acceptance of this mechanistic proposal, several aspects of the mechanism remain unclear. In this report we describe the use of site-specific labelling with NMR probe nuclei to establish fundamental properties of the catalytically-essential aspartyl side chains in complexes with the prototypical

peptide inhibitor, pepstatin A, which are considered to mimic the catalytic tetrahedral intermediate.

Total chemical synthesis was used to prepare fully active enzyme with 96% ¹³C enrichment of the Asp²⁵ side chain carboxyls. The enzyme was prepared by ligation of two long, unprotected peptides assembled using solid-phase peptide synthesis (5). The amino acid sequence was altered at two residues to decrease its susceptibility to autolysis. The enzyme showed full activity in the standard fluorogenic assay.

The dependence of the enzyme activity on pH is shown in Fig. 1. The existence of a maximum implies that the activity is dependent on the deprotonation of a group with a pK below 6 and is diminished by deprotonation of another with a pK above 6. It has been generally

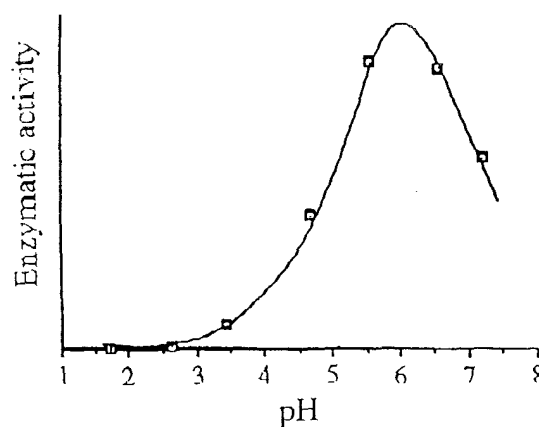


Fig 1 HIV-1 PR pH-activity profile. The kinetic characteristics of the chemically synthesized enzyme did not differ from those of the native enzyme or that from cellular expression systems.

assumed that these two titrating groups are the catalytically essential Asp²⁵ residues. The results of our experiments suggest otherwise.

Two ¹³C resonances of equal intensity were observed in the carbonyl region of the spectrum of protease•pepstatin complex, at 178.80 and 172.40 ppm. These peaks were unaltered in chemical shift over the pH range from 2.5 to 6.5 (Fig. 2). Only the downfield peak shifted in ²H₂O, indicating that it is associated with a protonated carboxylate and the other peak with a charged side chain.

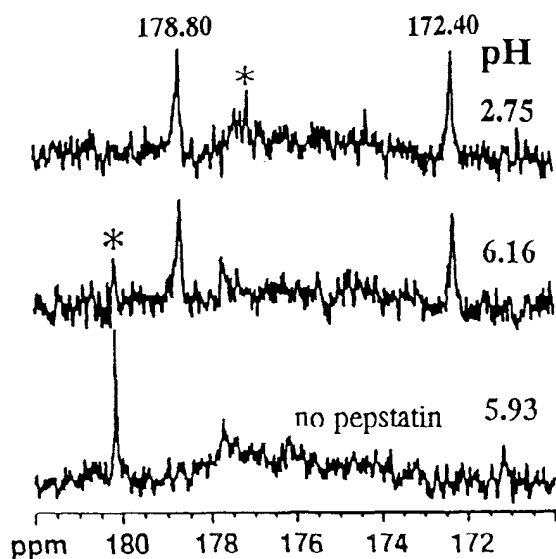


Fig. 2. 125 MHz ¹³C NMR spectra for HIV-1 PR at 303 K. Spectra of freshly prepared enzyme complexed with pepstatin at pH 2.75 and 6.16 showing the two peaks at 178.80 ppm and 172.40 that do not titrate, along with small resonances (asterisked) that arise from protein fragments. For comparison, the bottom spectrum was recorded at pH 5.93 from enzyme that had never been exposed to pepstatin.

¹H/¹³C heteronuclear single- and multiple-quantum correlation spectra were employed to follow the titration behaviour of the carboxyl carbon atoms via their weak (5-8 Hz), three-bond coupling to the magnetically inequivalent Asp β protons. However, a sole pair of peaks

appeared in the relevant region of the spectrum: these resonances titrated with a pK near 4.0, and were shown to arise from protease breakdown products. The absence of a peak corresponding to the non-titrating peaks seen in the direct ¹³C spectra of the intact enzyme•pepstatin complex is attributable to the short transverse relaxation times of the β protons.

The properties of the kinetically-identified groups do not match those of Asp²⁵ as revealed in the NMR experiments. This suggests that although the Asp²⁵ residues are essential for catalysis they may not be the principal determinants of the rate of proteolysis catalysed by this enzyme.

It has been widely assumed that the catalytic Asp residues in the inhibitor- and substrate-free enzyme are hydrogen bonded to each other with one protonated and the other not, thus providing the proton donor and proton acceptor required by the general acid/general base mechanism. In contrast, in the absence of the inhibitor at pH 5.93 there was only a single, intense ¹³C resonance which appeared at the chemical shift of the Asp²⁵ in a small model peptide at the same pH (Fig. 2). These data are consistent with both solvent-exposed Asp side chains in the inhibitor-free enzyme being in the carboxylate form near pH 6, and hence being unprotonated at the pH optimum of the enzyme. Under these circumstances the initial nucleophilic attack on the substrate carbonyl cannot involve the postulated proton transfer from these residues.

References

- ¹C. Debouck et al., *Proc. Natl. Acad. Sci. U.S.A.* **84**, 8903-8906 (1987).
- ²J.R. Huff, *J. Med. Chem.* **34**, 2305-2314 (1991).
- ³A. Wlodawer et al., *Science* **245**, 616-621 (1989).
- ⁴K. Suguna, E.A. Padlan, C.W. Smith, W.D. Carlson, and D.R. Davies, *Proc. Natl. Acad. Sci. U.S.A.* **84**, 7009-7013 (1987).
- ⁵M. Schnoltzer and S.B.H. Kent, *Science* **256**, 221-224 (1992).

Towards TOCSY - free ROESY

T. Kanthimathi and S. Subramanian*

Regional sophisticated Instrumentation centre
Indian Institute of Technology, Madras 600 036, INDIA

High resolution NMR spectroscopy in liquids has proved to be a powerful technique for the analysis of structure and dynamics of large molecules through the investigation of relaxation. The elucidation of three dimensional structure of large molecules depends on the fact that the major mechanism for relaxation in solution is through fluctuating dipolar coupling brought about by random Brownian motion and that the dipolar cross relaxation depends on the internuclear distance. The two types of 2D experiments which are used to derive the internuclear distance information and hence molecular structure are the NOESY and ROESY (or CAMELSPIN),¹ the former depends on the laboratory frame longitudinal cross relaxation rates, while the latter deals with cross relaxation between spins that are locked in the rotating frame close to resonance. The reason for the development of ROESY is that for an isolated pair the cross relaxation rates in NOESY which depends on the rotational correlation time, τ_c , and the frequency of measurement, ω , goes from positive to negative through zero at $\omega\tau_c = 1.13$. The rotating frame cross relaxation on the other hand is always positive even in the "spin diffusion" limit ($\omega\tau_c \gg 1$). With the use of high field supercon NMR many molecules of intermediate size fall in the zero NOE regime and are to be addressed by ROESY for structural elucidation.

The major problem in ROESY is the coherent transfer of magnetization between J-coupled networks that is facilitated under the spin locked condition through TOCSY or Homonuclear Hartmann Hahn mechanism. This complicates the interpretation of

ROESY. Although TOCSY cross peaks are of opposite sign from those of ROESY,² relay effects can produce false positive peaks in ROESY and mislead interpretation.

In order to avoid the use of strong continuous rf power which is needed to effectively lock the magnetization in the transverse plane, composite pulses have been used. But these also do not completely suppress TOCSY artifacts.

To understand the working of multiple pulse sequences and to find the sequences which are effective for ROESY, it is better to resort to the "Average Hamiltonian" theory and use numerical simulation of the evolution of coherences. The sequences which are good for offset independent TOCSY are not good for performing ROESY.

Recently Hwang *et al*³ have used repetitive pairs of phase alternated π pulses (PAPS) with only moderate power and have shown that the chemical shift scale factor is 0.63 and TOCSY artifacts are suppressed. A simulation of coherence transfer frequencies under the PAPS sequence shows that TOCSY transfer is significant close to resonance, but it performs much better at larger offsets.

Recently Desvaux *et al*⁴ have suggested that a continuous spin lock applied at a large offset leads to suppression of TOCSY artifacts as well as effects of chemical shift distribution among the dipolar coupled partners.

We have tested a new pulse sequence which is called a spiral lock ROESY

* Author for correspondence

consisting of a cyclic sequence consisting of a pair of six pulses each of flip angle 30° and progressively phase shifted by 30° .

$$[30^\circ_0 - \tau - 30^\circ_{30} - \tau - 30^\circ_{60} - \tau - 30^\circ_{90} - \tau - 30^\circ_{120} - \tau - 30^\circ_{150} - \tau - 30^\circ_{-30} - \tau - 30^\circ_{-60} - \tau - 30^\circ_{-90} - \tau - 30^\circ_{-120} - \tau - 30^\circ_{-150} - \tau - 30^\circ_{180}]_n$$

This sequence of cyclic pulses form the mixing segment of the ROESY sequence.

Average Hamiltonian theory, assuming perfect pulses gives a chemical shift scale factor of 0.95 on resonance (compared to 0.63 for the PAPS sequence) and the magnetization is locked farther away from the transverse plane.

A numerical simulation of the PAPS and the spiral lock sequences to examine the TOCSY transfer shows that the PAPS has a significant coherence transfer on resonance and behaves well off resonance. The spiral lock sequence on the other hand shows no significant coherence transfer of magnetization even close to resonance.

We have tested the sequence on a few small molecules, and have found almost complete suppression of the TOCSY artifacts. (Figs. 1 and 2.)

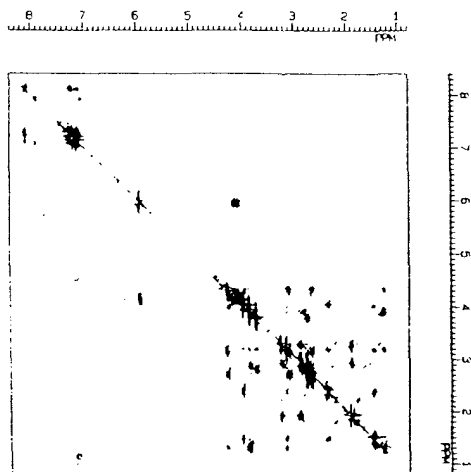


Fig.1. Spiral lock ROESY spectrum of Strychnine with mixing time 200 ms.

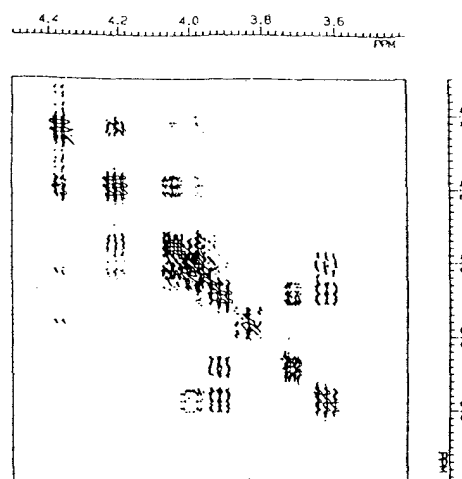


Fig.2. Spiral lock ROESY spectrum of Sucrose with mixing time 200 ms.

Our results show that at low rf power almost complete suppression of TOCSY can be achieved even on resonance. The present scheme at moderate power simulates the effect of a combination of PAPS of Hwang *et al* and the large offset CW lock of Desvaux *et al*.

Acknowledgment: Thanks are due to Professor J. S. Waugh for kindly providing the ANTIPOE program. T.K. thanks Indian Institute of technology for a fellowship.

REFERENCES:

1. A.A. Bothner-By, R.L. Stephens, J-M. Lee, C.D. Warren and R.W. Jeanloz, *J.Amer. Chem. Soc.* **106**, 811 (1984).
2. A. Bax and D.G. Davis, *J. Magn. Reson.* **63**, 207 (1985)
3. T-L. Hwang and A.J. Shaka, *J. Magn. Reson.* **B102**, 155 (1993).
4. H. Desvaux, P. Berthault, N. Birlirakis and M. Goldman, *J. Magn. Reson.* **A108**, 219 (1994).

Structural Elucidation of Calmodulin Fragments using NMR and CD studies

L. Gomathi[†], Thomas Fairwell*, Gopal A. Krishna*, James A. Ferretti* and S. Subramanian^{†#}
[†]Department of Chemistry, Indian Institute of Technology, Madras 600 036 INDIA, *National Heart, Lung and Blood Institute, National Institutes of Health, Bethesda, MD 20892 USA

Calmodulin (CaM) occupies a special position among Calcium binding proteins because of its high affinity and specificity for calcium binding¹. It serves as an intracellular Ca²⁺ receptor, mediates calcium levels in nucleotide and glycogen metabolism, secretion, motility and calcium transport.

The native CaM exists as a monomer of MW 16,700D and resists denaturation in the calcium bound state. X-ray structure² and NMR³ have established the presence of four calcium binding sites. These sites have the characteristic helix-loop-helix motif (EF hand). All the four binding sites have different calcium affinities and there is considerable controversy in the literature regarding the relative magnitudes of the same. It is also known that the exchange of loops between helices of different calcium binding sites modifies the calcium binding affinity in a marked way.

We have undertaken a study of a number of individual synthetic CaM fragments corresponding to the various helix-loop-helix sites as well as their loop exchanged analogs to look at the secondary structural contents by CD, 2D NMR and FT IR techniques. The CaM fragments were synthesized using modified Merrifield solid phase method⁴. These are the peptide 1-1-1 (A E F K E A F S L F D K D G D G T I T T K E L G T V M R S L G Q), 1-4-1 (A E F K E A F S L F D I D G D G Q V N Y E E L G T V M R S L G Q), 4-1-4 (V D E M I R E A D K D G D G T I T T K E F V Q M M T A K) and 4-4-4 (V D E M I R E

A D I D G D G Q V N Y E E F V Q M M T A K) respectively.

CD studies show that the native fragment 4-4-4 has the highest ellipticity in the absence of calcium. The binding sites IV and III are supposed to have higher affinity than sites I and II. Only qualitative trends could be derived from CD studies.

The fragments 1-1-1 and 1-4-1 were examined by FT IR in DMSO with and without calcium. The peptide 1-1-1 was also investigated in TFE. These show that the fragments do not have a preponderance of helical structure in DMSO and that there is not much of calcium induced helicity. CD and IR studies, however, have shown an increase in helical content in TFE.

The fragments 1-1-1 and 1-4-1 were studied in detail using a BRUKER AMX 600 MHz spectrometer. They were studied in DMSO at 40 °C. Two dimensional DQF COSY, TOCSY and NOESY were undertaken for these fragments and a complete analysis of cross peaks were carried out⁵. Schematic diagrams showing the various through space connectivities are shown in Fig. 1.

The overall conclusions of our study on CaM fragments can be stated as follows. The dissection of the protein into its individual binding sites has drastically altered the secondary structural features of the otherwise EF hand motif of the sites. The calcium binding affinity as well as the effect of calcium on the induction of secondary structural features could not be unequivocally quantified because of the

Author for correspondence

possible fact that the presence of all the sites together is important for the protein to adopt its native structure and that allsoteric effects, such as progressive changes in the affinity of one site depending upon whether the other sites are calcium bound or free is important. The observation that the fragments 1-1-1 and 1-4-1 adopt a folded structure with very little helical content is somewhat surprising. Many large proteins do have a tendency to retain their active site conformation to a large extent even when they are fragmented. Our NMR results indicate that although the structures of the fragments 1-1-1 and 1-4-1 do differ in their secondary structural content as brought about by CD and NMR, the latter clearly indicates that there is considerable conformational interconversion between helical and extended structures.

Acknowledgment: Thanks are due to IIT, Madras for a fellowship to L.G.

References

1. J.R. Dedman, B.R. Brinkley and A.R. Means, *Adv. Cyclic Nucleotide Res.* **11**, 131 (1979).
2. Y.S. Babu, C.E. Bugg and W.J. Cook, *J. Mol. Biol.* **204**, 191, (1988).
3. M. Ikura, S. Spera, G. Barbato, L.E. Kay, M. Krinks and A. Bax, *Biochemistry* **30**, 9216 (1991).
4. R. B. Merrifield, *Adv. Enzymol.*, **32**, 221 (1969).
5. K. Wüthrich, *NMR of Proteins and Nucleic Acids*, J. Wiley, New York (1986).

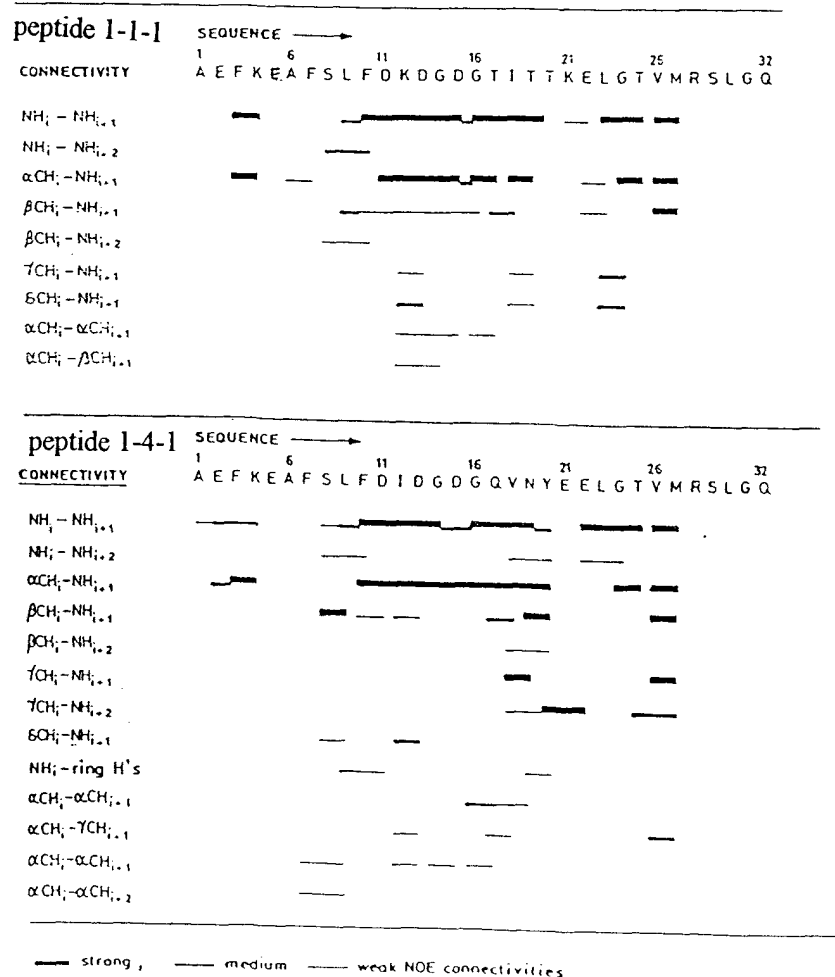


Fig. 1 Schematic diagram showing the various throughspace connectivities derived from NOE data for the peptides 1-1-1 and 1-4-1

Pattern Recognition of specific dipolar networks

C. Seetharaman and S. Subramanian*

Regional Sophisticated Instrumentation Centre

Department of Chemistry

Indian Institute of Technology, Madras 600 036, INDIA

Dynamic aspects of macromolecules such as proteins and polypeptides, especially internal motions can in principle be unravelled by the interpretation of NMR relaxation times T_1 and T_2 of nuclei in specific locations in the molecule.¹ Although measurement of T_1 and T_2 and relaxation of higher order coherences can be made accurately, the precise interpretation is rather difficult because of the complexity of the problem. We report here a new two dimensional NMR strategy, namely DQRF-COSY (Double Quantum Relaxation Filtered Correlated Spectroscopy) which distinguishes different secondary structural elements based on their relative structural dynamics. As a demonstration of this method we show that in the 58 residue polypeptide Basic Pancreatic Trypsin Inhibitor (BPTI) the β -sheets can be discriminated from α -helices and other random structured residues by using DQ relaxation as the distinguishing factor. Previous studies have dealt with the single quantum relaxation times T_1 and T_2 ² as well as molecular modelling studies³ of back bone C_α atoms.

Some examples of local dynamics in biomolecules are movements of groups in small segments that allow fast recognition and binding, specific structures that aid surface / surface recognition (e.g. of antigen / antibody as well as drug / protein interactions), relative motion of helices within domains, swinging arm motions associated with specific sequences etc. It is important to understand the correlation between structure, dynamics and function to

appreciate specific bioactivity.

Several authors have tried to derive information on the structural fluctuations and the dynamics of folded proteins using the measured dispersion of spin lattice and spin spin relaxation times of ^{13}C on the back bone as well as molecular dynamics simulations. These studies reveal the presence of large fluctuations in structure and energy components in many proteins. Because of the presence of multiple degrees of freedom of motion in a macromolecule it is not correct to assume a unique molecular correlation time. Thus, owing to intrachain steric interactions a given dipole-dipole vector may not assume all possible orientations. Therefore the spectral densities $J(\omega)$ will be a function of an effective correlation time of the dipolar vector under consideration as well as a generalized order parameter which is a measure of degree of spatial restriction of the local motion.⁴

Here we describe the possible use of DQ relaxation as a tool for discriminating different motional regimes in a given macromolecule. Since multiple quantum relaxation (unlike single quantum relaxation) is more sensitive to an external perturbation when the partners in coupling undergo a concerted motion we would expect that DQ relaxation will be able to bring about a better discrimination between different secondary structural elements. The pulse sequence of DQRF-COSY is as follows:

$$\pi/2 - t_1 - \pi/2 - \tau/2 - \pi - \tau/2 - \pi/2 - t_2(\text{Acq.})$$

* Author for correspondence

It differs from DQF-COSY in that, a relaxation delay τ has been introduced, after the second pulse. During the delay τ the double quantum coherences that are created relax with a decay constant $T_2(DQ)$. The π -pulse in the middle of the delay τ , removes the inhomogeneity effects. The reasons for choosing BPTI as the molecule of study are manifold. BPTI has been extensively studied by both X-ray⁵ and NMR.⁶ In addition, it possesses two important secondary structural elements, a large antiparallel β -sheet (residues 18 to 35) and an α -helix (47 to 55).

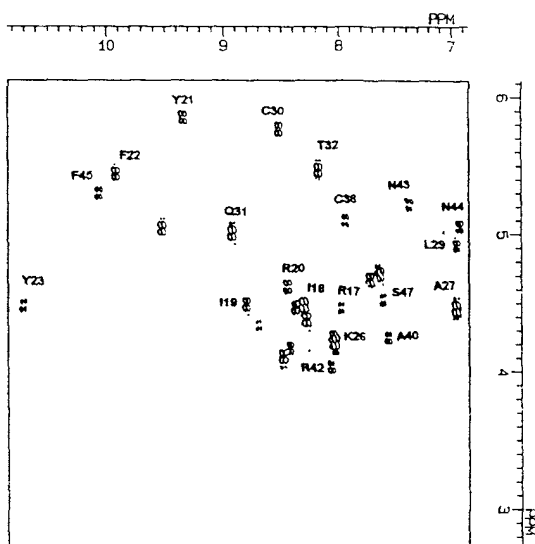


Fig. 1. DQRF COSY spectrum (finger print region only) of BPTI with relaxation delay 2ms. The peaks surviving the relaxation delay are mainly from the residues forming the β -sheet

A number of DQRF-COSY experiments were carried out with relaxation delays ranging from 0.2ms. to 20ms. As relaxation delay is increased, the complexity in the finger print NH-C α H region is dramatically reduced. All the assignments were done by standard procedures aided by previous NMR studies on BPTI.⁶ After a relaxation delay of 2ms. the cross peaks in the fingerprint regions were found to be exclusively from the aminoacids which are

present in the large antiparallel β -sheet and some residues which are strongly hydrogen bonded to both the strands of β -sheets (Fig.1). It is noteworthy that none of the cross peaks from residues of the α -helix survive through the relaxation delay after 5ms. It is fairly complicated to get a quantitative evaluation of DQ relaxation from routine experiments since the magnitudes of $T_2(DQ)$ are only a few milliseconds and spectral overlapping might cause error in the estimation of linewidths.

The observation that the α -helix and the β -sheet in BPTI have very different DQ relaxation rates points to the fact that the dynamics of the two motifs in BPTI are governed by very different effective correlation times. This would mean that the cross correlation coefficients between the various strongly dipolar coupled partners in the two domains ought to be different.

Acknowledgements: Thanks are due to IIT, Madras for a fellowship to C.S.

REFERENCES

1. Zheng, Z., Czaplicki, J., Jardetzky, O., *Biochemistry* **34**, 5212 (1995)
2. Boulat, B., Bodenhausen, G., *J. Biomol. NMR* **3**(3), 335 (1993)
3. Karplus, M., McCammon, J. A., *Nature* **277**, 578 (1979)
4. Ribeiro, A. A., King, R., Restivo, C., Jardetzky, O., *J. Am. Chem.Soc.* **102**, 4040 (1980)
5. Deisenhofer, J., Steigemann, W., *Acta. Cryst.* **B31**, 238 (1975)
6. Wagner, G., Wuthrich, K., *J. Mol. Biol.* **155**, 347 (1982)

An FT-Pulsed ESR/ESTN(Electron Spin Transient Nutation) Study of Hyperbranched π -Aryl Based Stable High-Spins as Models for Organic Superpara- and Ferro-Magnets

Takeji Takui,¹ Kazunobu Sato,¹ Daisuke Shiomi,² Koichi Itoh,²

Jaume Veciana³ and Concepció Rovira³

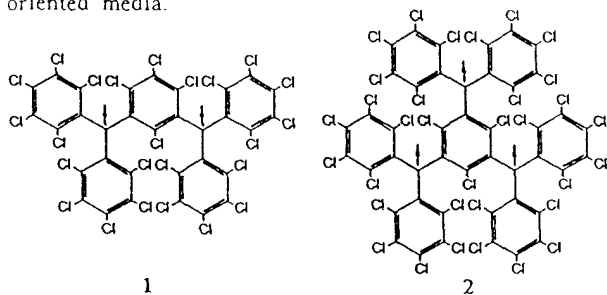
The Department of Chemistry¹ and Department of Material Science,²
Faculty of Science, Osaka City University, Sumiyoshi-ku, Osaka 558, Japan;

Institut de Ciència de Materials,³ Campus de la U.A.B., 08193 Bellaterra, Barcelona, Spain

Introduction

Organic molecular based magnetism (abbreviated to organic magnetism or molecular magnetism) has found ever increasing interest from both the pure and applied sciences for last decade[1]. Recently, organic high-spin polymers and clusters have emerged as models for organic ferro-, ferri-, superpara-magnets, or super high-spin systems with suprafunctionality. With the increasing molecular spin quantum number S and molecular weight of the polymers, however, cw ESR spectroscopy manifests its inherent disadvantages in discriminating high spins from $S=1/2$ and in determining the S 's for the complex mixture of various spin assemblages. The spin identification and discrimination between different spin multiplicities are an increasingly important issue in the research field of organic magnetism and spin chemistry.

An electron spin transient nutation (ESTN) method [2-4] based on FT-pulsed ESR spectroscopy is a useful and powerful tool for the above purposes, being complementary to continuous-wave ESR spectroscopy. This paper illustrates the identification of the ground-state spin multiplicities of stable π -aryl based triplet and quartet molecules (1 and 2)[5,6] by random orientation ESTN spectroscopy, showing the usefulness of the transient nutation method. The present work has been the first report of a successful application of the ESTN method to high-spin systems in organic rigid glasses as non-oriented media.



Experimental and Analysis

Electron spin transient nutation phenomena effectively occur when a microwave irradiation field is suddenly applied to spin systems in a static magnetic field on (near) resonance. Then the spin magnetization, which tends to align in the direction of the static field, starts precessing around a new effective field which is vectorially formed by the static and suddenly applied microwave fields. This precession is treated as the classical vectorial motion of the magnetization or the dynamics of

the fictitious spin of the two level system corresponding to a resonance transition in the rotating frame.

The transient nutation phenomena for both 1 and 2 diluted in frozen toluene were measured at liquid helium temperature by monitoring the peak of a 2-pulse (Hahn) echo while increasing the length of the first excitation pulse. Pulsed ESR experiments were performed on a Bruker ESP380E FT-ESR spectrometer with a dielectric resonator and a 1kW TWT amplifier. The nutation frequencies (ω_n) observed from 1 and 2 were interpreted in terms of an equation of the first-order approximation,

$$\omega_n = \omega_1 \{S(S+1) - M_S(M_S-1)\}^{1/2}, \quad (1)$$

expected for an $|S, M_S-1\rangle \leftrightarrow |S, M_S\rangle$ single quantum transition in the weak extreme limit of the microwave irradiation[2-4]. ω_1 is the frequency which is proportional to the strength of the microwave pulse field.

Results and Discussion

Figure 1 shows an echo-detected field-swept ESR spectrum of 2. The spectrum indicates that the observed ESR signals consist of widely distributed ESR transitions over about 10 mT for 2, which are corresponding to the ESR absorptions due to randomly oriented multiplets.

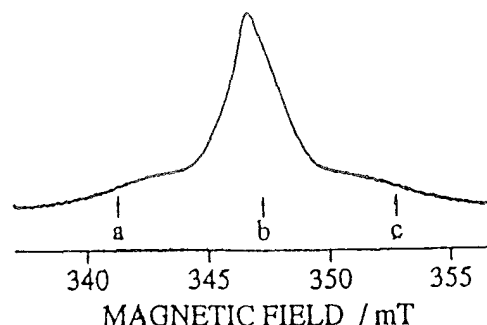


Figure 1. Echo-detected ESR fine-structure spectrum of 2 observed in a toluene glass.

Figure 2 shows the nutation spectra for 2 observed at three magnetic fields (a-c) denoted in Figure 1. The nutation frequency observed at the central magnetic field, 347.29 mT, and those at 341.36 mT and 352.77 mT, were 32.72 MHz and 28.32 MHz, respectively, when the irradiated-microwave power attenuation was in the level of 5dB. This finding coincides with considering a quartet spin state for 2. The nutation frequencies for an $|S=3/2, M_S=-1/2\rangle \leftrightarrow |3/2, 1/2\rangle$ allowed ESR transition in the quartet state and that for a $|3/2, -3/2\rangle \leftrightarrow |3/2, -1/2\rangle$ or $|3/2, 3/2\rangle$ transition are $2\omega_1$

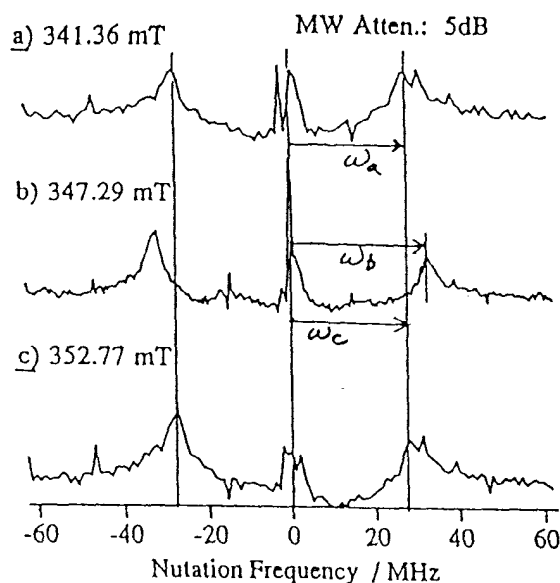


Figure 2. Nutation spectra observed from **2** in a toluene glass. a), b), and c) correspond to the stationary points a, b, and c in Figure 1, respectively, at which the nutation experiment was carried out.

and $3^{1/2}\omega_1$, respectively. The ratio of the observed nutation frequencies (32.72MHz: 28.32MHz) corresponds to that of the expected nutation frequencies for the allowed transitions in the quartet spin state ($2 : 3^{1/2}$), unequivocally identifying the spin state of **2** to be quartet.

The nutation spectra for **1** were observed at five magnetic fields. All the observed nutation frequencies indicated the same values which are $2^{1/2}$ times larger than that (ω_1) for the doublet state of 1,1-diphenyl-2-picrylhydrazyl(DPPH) used as a standard reference. Equation (1) states that the nutation frequency for the $|1, -1\rangle \leftrightarrow |1, 0\rangle$ or $|1, 0\rangle \leftrightarrow |1, 1\rangle$ ESR allowed transition in a triplet state is $2^{1/2}\omega_1$. From the relationship between the observed nutation frequencies for **1** and DPPH, therefore, it is concluded that the spin state of **1** is identified to be triplet.

The microwave power($B_1 = -\omega_1/\gamma$) dependence of the nutation frequencies for **1**, **2**, and DPPH is summarized in Figure 3. The solid line stands for the nutation frequency for DPPH($S=1/2$), the broken line the frequency for **1**($S=1$), and the dot-dashed and the double dot-dashed lines the frequencies for **2**($S=3/2$). The nutation frequencies clearly depend on the S and M_S of the monitored ESR transitions, indicating the usefulness of the ESTN spectroscopy for the identification and discrimination of spin multiplicities in the complex mixtures of high-spin assemblages even in non-oriented systems.

The structures of these hyperbranched molecules, **1** and **2** are strongly steric-hindered because of their perchlorinated phenylrings. In spite that the π -spin system is extremely twisted from a planar form, the predicted ground-state high-spin multiplicities of the molecules are unaffected, showing that the delocalized π -spin system constructs a topologically controlled robust π -spin polarization network and that super high-spin molecules with dendritic structures are possible by extending the

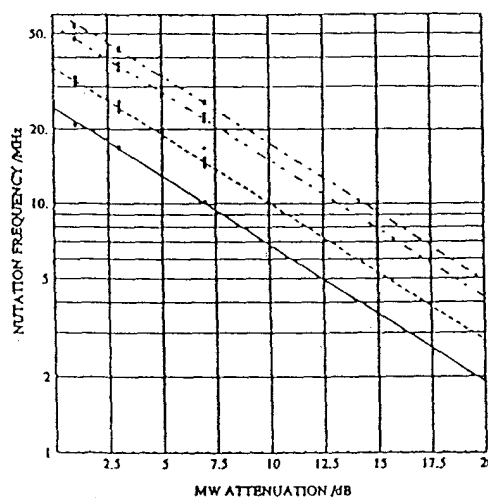


Figure 3. Microwave power dependence of the nutation frequencies for DPPH, **1**, and **2**. The solid line stands for DPPH ($S=1/2$), the broken one for **1** ($S=1$), and both the dot-dashed ones for **2** ($S=3/2$), respectively.

π -spin polarization network.

In conclusion, we have applied the ESTN spectroscopy to the hyperbranched π -aryl based molecules in organic glasses in order to determine their spin multiplicities independently of cw-ESR spectroscopy. The nutation frequencies for the molecules depended on the S and M_S of the monitored ESR transitions, allowing us to determine the spin multiplicity. The ESTN spectroscopy has especially great advantages for the identification and discrimination of spin multiplicities in the complex mixtures of high-spin assemblages. This work shows that these can be done experimentally and without spectral simulations in random orientation ESR spectroscopy.

Acknowledgments

This work has been partially supported by a Grants-in-Aid for Scientific Research on Priority Area "Molecular Magnetism" (Area No. 228/04 242 103 and 04 242 105) and a Grant-in-Aid for Encouragement of Young Scientists (Grant No. 07 740 468) from the Ministry of Education, Science and Culture, Japan and also by the Ministry of International Trade and Industry (NEDO project "Organic Magnets"). The authors are grateful to Professor A. Schweiger(E.T.H., Switzerland) and Professor J. Isoya (University of Library and Information Science, Japan) for their stimulating suggestions.

References

1. For a recent overview, see; (a)J.S. Miller and D.A. Dougherty (eds.), *Mol. Cryst. Liq. Cryst.*, **176**, 1-562 (1989). (b)O.Kahn, D. Gatteschi, J.S. Miller, and F. Palacio(eds.), *Molecular Magnetic Materials*(1991). (c)H. Iwamura and J.S. Miller(eds.), *Mol. Cryst. Liq. Cryst.*, **232/233**, 1-360/1-366(1993). (d)J.S. Miller and A.J. Epstein(eds.), *Mol. Cryst. Liq. Cryst.*(1995).
2. J. Isoya, H. Kanda, J.R. Norris, J. Tang and M.K. Bowman, *Phys. Rev.*, **B41**, 3905(1990).
3. A.V. Astashikin and A. Schweiger, *Chem. Phys. Lett.*, **174**, 595(1990).
4. K. Sato, D. Shiomi, T.Takui, K. Itoh, T. Kaneko, E. Tsuchida, and H. Nishide, *J. Spectrosc. Soc. Japan*, **43**, 280(1994).
5. J. Veciana, C. Rovira, M.I. Crespo, O. Almet, V.M. Domingo, and F. Palacio, *J. Am. Chem. Soc.*, **113**, 2552(1991).
6. J. Veciana, C. Rovira, N. Ventosa, M.I. Crespo, and F. Palacio, *J. Am. Chem. Soc.*, **115**, 57(1993).

Ferric Iron Porphyrin as Studied by Single-Crystal CW and FT Pulsed ESR/ESTN(Electron Spin Transient Nutation) Spectroscopy

Andrew S. Ichimura,¹ Kazunobu Sato,² Daisuke Shiomi,¹ Takeji Takui,² Koichi Itoh,¹
W.C. Lin,³ David H. Dolphin³ and Charles A. McDowell³

The Department of Material Science¹ and Department of Chemistry,² Faculty of Science,
Osaka City University, Sugimoto 3-3-138, Sumiyoshi-ku, Osaka 558, Japan
The Department of Chemistry,³ The University of British Columbia,
2036 Main Mall, Vancouver, B.C., Canada V6T 1Z1

Introduction

Since the pioneering ESR study of paramagnetic metalloporphyrins and active centers of hemoproteins by Ingram *et al.* the related research topics are diverse and interest in metalloporphyrins and their elaborate designs of models for suprafunctionality materials has been ever increasing in many research fields of chemistry, biochemistry and rapidly developing fields in materials science. Meanwhile, magnetic resonance studies of electronic and molecular structures of metalloporphyrins have had their own right. Particularly, from a viewpoint of group-theoretical symmetry, metal ions are located in tetragonal symmetry and much work on the electronic and molecular structures of metalloporphyrins has been made in this context[1]. Nevertheless, until now single-crystal ESR work on metalloporphyrins has been rare[2].

This paper describes cw and FT pulsed ESR/ESTN (Electron Spin Transient Nutation) study of high-spin Fe(III)Cloctaethylporphyrin (Fe(III)ClOEP) magnetically diluted in Ni(II)OEP single crystals, focusing on the Jahn-Teller distortion of Fe(III)ClOEP occurring at low temperature.

Experimental

The symmetry of the host Ni(II)OEP crystal employed for this work is tetragonal with $Z=4$, as shown in Figure 1. Thus, if departure from tetragonal symmetry occurs due to some reasons, the expected high-spin ground state of the ferric ion can reflect the subtle departure. A weakly coordinating axial ligand(Cl^-) can also be sensitive to subtle molecular and environmental changes due to the reduction of tetragonal symmetry.

The single-crystal ESTN spectra of Fe(III)ClOEP were measured with a Bruker ESP380 FT pulsed X-band ESR spectrometer equipped with Oxford cryogenic apparatuses.

Results and Discussion

The angular dependence of the ESR spectra observed at liquid helium temperature showed that Fe(III)ClOEP is in the high-spin ground state as expected for a weakly coordinating fifth axial ligand(Cl^-). The angular dependence was measured in the principal-axis system which nearly coincides with the crystallographic-axis system:

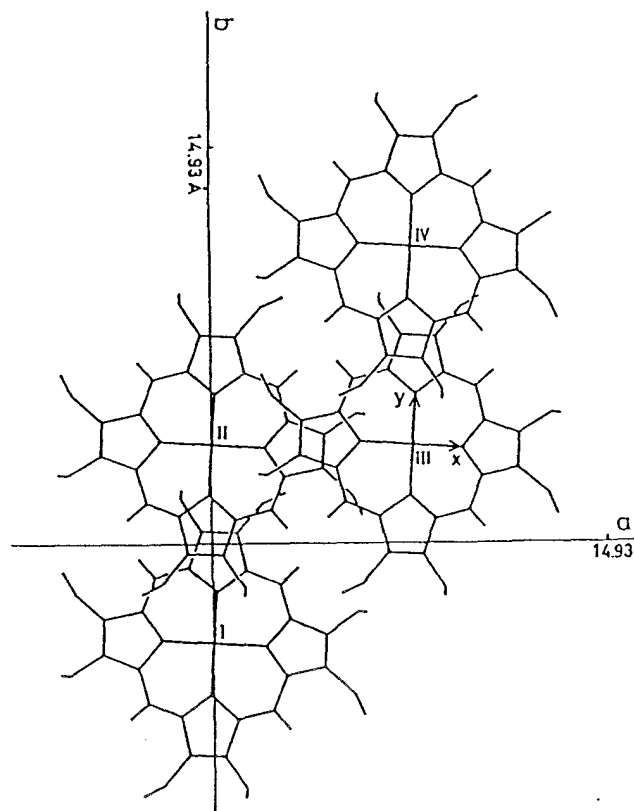


Figure 1. Projection of the crystal structure of the host Ni(II)OEP molecule onto the crystallographic ab plane.

The c axis is perpendicular to the porphyrin molecular plane (see Figure 1).

Energetically non-equivalent Fe(III)ClOEP molecules were discriminated at liquid helium temperature, indicating that Fe(III)ClOEP undergoes the considerable departure from tetragonal symmetry(see Figure 1). With increasing temperature both motional averaging and spectral line-broadening were observed, suggesting that the underlying mechanism is a thermally activated molecular reorientation process (Orbach process) as depicted in Figure 2. The observed reorientation process was much complex because of the possible symmetry reduction lower than C_{4v} for first-coordination atomic sites. This arises from weaker spin-orbit interaction of ferric ion. Spin-orbit interaction intends to retain group-theoretically allowed high molecular symmetry against

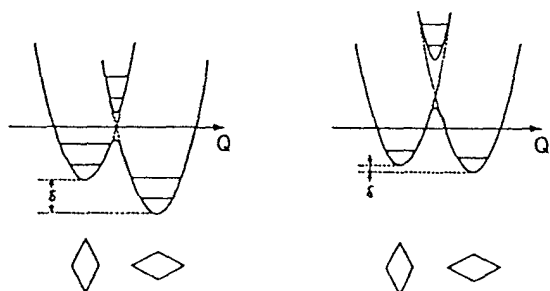


Figure 2. Molecular reorientation process induced by real phonon transitions. δ arises from local electric field which causes the energetical non-equivalence of the degenerate potentials.

vibronic (spin-vibronic coupling included) interaction. Thus, the departure from the high symmetry for ferric ion porphyrin is expected greater than cobalt(II) ion porphyrin [3]. In this context, ferric ion cases are more sensitive to environmental influence and Jahn-Teller instable. Since there is no orbital degeneracy in the electronic ground state of Fe(III)ClOEP, pseudo(second-order) Jahn-Teller effect is a possible underlying mechanism to interpret the observed symmetry reduction. The observation of both the static and dynamic spectra is the most vivid aspect of Jahn-Teller effect and the finding strongly indicates the occurrence of the Jahn-Teller instability of Fe(III)ClOEP.

The observed frozen-in distorted molecular structures of Fe(III)ClOEP and dynamic processes are attributable to static and dynamic regimes of vibronic interaction (Jahn-Teller interaction). The static Jahn-Teller spectra illustrating the reduced (non-axial) symmetry suggested that the fifth axial ligand (Cl^-) is also responsible for the distortion. FT pulsed ESEEM and ^{14}N -ENDOR experiments are under way in order to determine the distorted molecular structures.

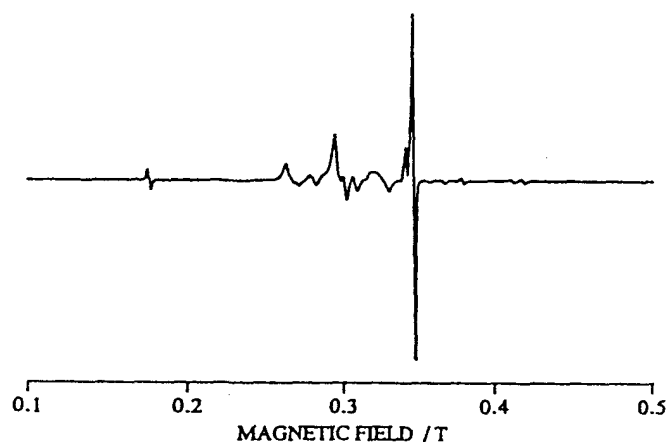


Figure 3. ESR spectrum of Fe(III)ClOEP oriented in the host Ni(II)OEP single crystal observed with magnetic field in the bc plane at liquid helium temperature.

The transition assignments of the cw ESR spectra were made by ESTN spectroscopy based on FT pulsed ESR techniques. The transitions between the lowest Kramers doublet ($|S=5/2, M_s=\pm 1/2\rangle$) of Fe(III)ClOEP were unequivocally identified by ESTN experiments. The FID-detected nutation experiments were carried out in the

extreme limit of weak microwave irradiation ($H_1 \ll H_D$), where H_1 and H_D stand for the Hamiltonian term of a coherent microwave field and fine structure terms, respectively. Single- [4,5] and multiple-quantum [6] transition nutation frequencies appearing in various limits are derived and summarized [4-6].

The extreme limit condition simplified the ESTN spectra for the sextet high-spin state of Fe(III)ClOEP, as expected from theoretical arguments for the weak extreme limit [4,5]. Figure 3 shows the observed ESR spectrum of Fe(III)ClOEP oriented in the host Ni(II)OEP single crystal with static magnetic field in the bc plane at liquid helium temperature. The non-axial symmetry of Fe(III)ClOEP shows up in Figure 3. Such symmetry reduction has never appeared for Cu(II)OEP diluted in Ni(II)OEP. For Cu(II)OEP spin-orbit interaction dominates and the ground spin-doublet state is well isolated from excited states (the nearest excited state is spin-quartet), retaining the tetragonal molecular symmetry.

Nutation experiments in the weak extreme limit were invoked for the same magnetic field orientation as in Figure 3. The observed fine-structure lines gave the same single nutation frequency corresponding to the ESR transition $|S=5/2, M_s=-1/2\rangle \rightarrow |S=5/2, M_s=+1/2\rangle$, which agrees with the equation for the weak extreme limit [6].

Conclusion

Fe(III)ClOEP is Jahn-Teller instable at low temperature and with increasing temperature there occurs transition from the static to dynamic spectrum with enormously broadened linewidths. This is interpretable in terms of the molecular reorientation process associated with a real phonon transition between energetically different potentials.

Acknowledgments

This work has been partially supported by a Grant-in-Aid for Scientific Research on Priority Area "Molecular Magnetism" (Area No.228/04 242 103, 04 242 104 and 04 242 105) from the Ministry of Education, Culture and Science, Japan. One of the authors (T.T.) is grateful to Professor A. Schweiger (E.T.H., Zürich) and Professor J. Isoya (Univ. of Library and Information Science, Tsukuba) for their stimulating suggestions of nutation experiments. One of the authors (A.S.I.) thanks J.S.P.S. for his postdoctoral fellowship.

References

1. D. H. Dolphin (ed), *The Porphyrins*, Academic Press.
2. A. Schweiger, *Structure and Bonding*, 51 (Springer, 1982).
3. T. Takui, W. C. Lin, D. H. Dolphin, and C. A. McDowell, to be published.
4. J. Isoya, H. Kanda, J. R. Norris, J. Tang, and M. K. Bowman, *Phys. Rev.* **B41**, 3905 (1990).
5. A. V. Astashkin and A. Schweiger, *Chem. Phys. Lett.*, **174**, 595 (1990).
6. T. Takui *et al.*, *Bull. Magn. Reson.*, in press.

**An FT Pulsed ESR/Electron Spin Transient Nutation Study
of the Quartet State of Cr(III) in MgO Powder:
Detection of its Apparently Vanishing ZFS**

Kazunobu Sato,¹ Daisuke Shiomi,² Takeji Takui¹ and Koichi Itoh²

¹Department of Chemistry and ²Department of Material Science, Faculty of Science
Osaka City University, Sugimoto, Sumiyoshi-ku, Osaka 558, Japan

The transient nutation, which was first found for nuclear spins by Torrey[1], is a basic phenomenon in magnetic resonance. The transient nutation is the response of spins to an irradiation field. The phenomena depend on the magnetic-field strength of the irradiation and an effective spin quantum number of a spin system. The transient nutation for electron spins was applied to studies of dynamics of excited spin states based on time-resolved ESR spectroscopy[2,3]. On the other hand, the transient nutation in terms of pulsed ESR spectroscopy has been applied only to single-crystal systems, recently[4,5]. Isoya *et al.* have been determined the effective spin quantum number for the nickel impurity in synthetic diamond to be $S=3/2$ with non-vanishing fine-structures due to a distortion of the impurity site from tetrahedral symmetry[4]. Astashkin and Schweiger have demonstrated that the electron spin transient nutation method facilitates the identification of complex EPR spectra from transition metal ions in solid states[5].

In this paper a quartet state of Cr(III) in MgO powder is examined by the electron spin transient nutation (ESTN) method based on pulsed ESR spectroscopy. It has been widely known that the zero-field splitting (ZFS) of the quartet state is vanishing in its octahedral (or cubic) symmetry environment. This paper describes the nutation phenomena observed from the quartet state of Cr(III) in MgO powder with only apparently vanishing ZFS in its cw-ESR spectrum.

Experimental

The electron spin transient nutation phenomena were observed at ambient temperature by monitoring a free induction decay (FID) after an excitation pulse of microwave while increasing the width of the excitation pulse. Then the observed time-domain nutation was transformed to frequency-domain nutation spectrum in terms of the fast Fourier transformation. Pulsed ESR experiments were performed on a Bruker ESP380E FT-ESR spectrometer with a dielectric resonator and a 1kW

TWT amplifier. In order to estimate the nutation frequency, a single crystal of diphenylpicrylhydrazyl (DPPH) was used as a reference standard.

Analysis

The transient nutation phenomena were interpreted based on the time-dependent equation of motion in the rotating frame with an irradiated microwave frequency ω_{MW} . The equation of motion in the rotating frame is given by

$$\frac{d|\Psi(t)\rangle}{dt} = -i(H_0 + H_1)|\Psi(t)\rangle,$$

where

$$H_0 = \beta\mathbf{B}_0 \cdot \mathbf{g} \cdot \mathbf{S} - \hbar\omega_{MW}S_z + \mathbf{S} \cdot \mathbf{D} \cdot \mathbf{S}$$

$$\text{and } H_1 = \beta\mathbf{B}_1 \cdot \mathbf{g} \cdot \mathbf{S}.$$

H_0 and H_1 mean the spin Hamiltonian including an offset term, which consists of the Zeeman (H_{eZ}) and fine-structure (H_D) term, and a microwave irradiation term, respectively. The nutation phenomena are considered as the time evolution of the wavefunction $\Psi(t)$ in the rotating frame. The nutation frequency ω_n estimated from the behavior of the wavefunction depends on not only the irradiated magnetic field strength, $\omega_1 (= \gamma B_1)$, but also effective spin quantum number.

Results and Discussion

Figure 1 shows a typical ESR spectrum of Cr(III) in MgO powder. It has been well-documented that the Cr(III) spectrum is isotropic and that the zero field splitting (ZFS) (or fine-structure) is vanishing at ambient temperature. The observed transition at 0.35T arises from ^{50,52,54}Cr(III) without nuclear spin, and weak quartet satellite lines from a ⁵³Cr(III) isotope with $I=3/2$ which hyperfine coupling is 0.00166cm^{-1} . This hyperfine parameter agrees with the previously documented one for Cr(III) (0.00163cm^{-1}). The signal appearing on the lower field arises from a DPPH single crystal used as the reference standard for the nutation measurements.

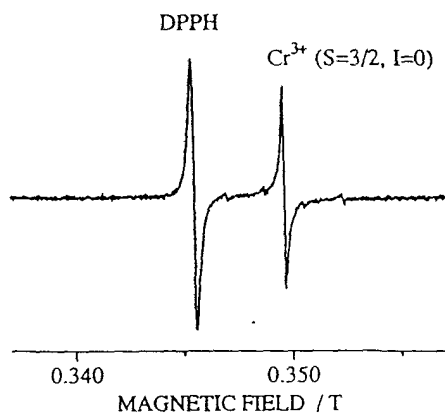


Figure 1. ESR spectrum of Cr(III) in MgO powder.

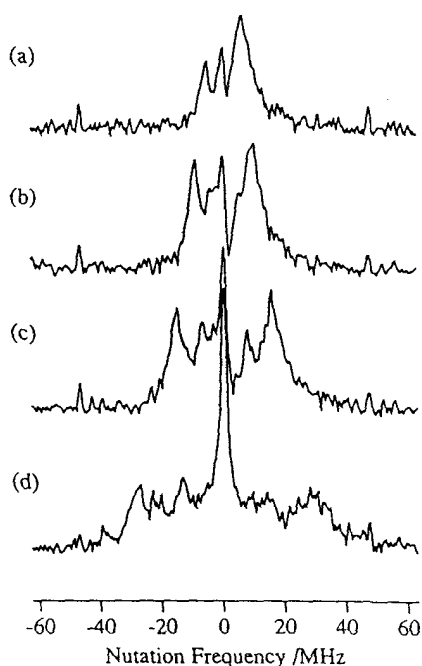


Figure 2. Nutation spectra of Cr(III) in MgO powder observed at ambient temperature. (a)-(d) show the dependence of the nutation on irradiated microwave amplitude: (a) 25dB (b) 20dB (c) 15dB (d) 10dB.

FID-detected nutation spectra of Cr(III) in MgO powder were observed from the central ESR transition at ambient temperature in various microwave amplitude levels, shown in figures 2(a)-(d). In figure 2(d) the nutation spectrum showed the two nutation frequency components about 15 and 30MHz, which correspond to ω_1 and $2\omega_1$, respectively. The nutation frequency component at ω_1 is the same as a nutation frequency expected for a doublet spin state. The nutation frequency for the double spin state was confirmed by measuring the internal reference standard, DPPH. With diminishing the microwave amplitude, the signal intensity at $2\omega_1$ increased in relative to that at ω_1 . In figure 2(a) the signal observed at $2\omega_1$ became dominant. This dependence on

the microwave amplitude indicates that the fine-structure term in Cr(III) in MgO powder is classified in the intermediate regime $H_D \sim H_1$. Moreover it is clear that the ZFS is nonvanishing because a single nutation frequency corresponding to ω_1 is expected to be observed for vanishing ZFS. Thus, Cr(III) in MgO powder is located in lower symmetric environments distorted from octahedral (or cubic) symmetry. This finding contrasts with the well-documented fact that the quartet state of Cr(III) in MgO is characteristic of the vanishing ZFS. We think that information about the fine structure hidden in the unresolved ESR transitions within a line width was obtained in the present nutation experiment, which has never been detected by conventional cw ESR spectroscopy.

As shown in figure 2, another feature is a behavior of the nutation frequency near $\omega_n \sim 0$ MHz. An intensity of the zero frequency component depends on microwave amplitude. Increasing the microwave power, the intensity of the zero frequency component is enhanced. This behavior suggests the occurrence of multiple quantum transitions for the high spin system. The nutation frequency for the multiple quantum transition is reduced due to the scaling effect of the effective field which spin ensembles experience. The nutation frequencies for double and triple quantum transitions are expected to be $7\omega_1^2/4\omega_D$ and $3\omega_1^3/8\omega_D^2$, respectively, in the extreme limit of $H_D \ll H_1$. Although the above expressions can not exactly be applied to this system as Cr(III) in MgO is the intermediate case of $H_D \sim H_1$, it is valid that the multiple quantum transition does occur at nearby zero frequency region.

Conclusions

We have applied the ESTN method based on pulsed ESR spectroscopy to a quartet state of Cr(III) in MgO powder. The nutation phenomena observed from the quartet state with only apparently vanishing ZFS in its cw-ESR spectrum were not interpreted by a single nutation frequency, unequivocally showing the occurrence of non-vanishing ZFS of the quartet state of Cr(III) in MgO powder. This finding indicates that Cr(III) in MgO powder is located in lower symmetric environments distorted from octahedral (or cubic) symmetry.

References

1. H. C. Torrey, *Phys. Rev.* **76**, 1059(1949).
2. S. S. Kim and S. I. Weissman, *Chem. Phys.* **27**, 21(1978).
3. R. Furrer, F. Fujara, C. Lange, D. Stehlik, H. M. Vieth, and W. Vollmann, *Chem. Phys. Lett.* **75**, 332(1980).
4. J. Isoya, H. Kanda, J. R. Norris, J. Tang and M. K. Bowman, *Phys. Rev.* **B41**, 3905(1990).
5. A. V. Astashkin and A. Schweiger, *Chem. Phys. Lett.* **174**, 595(1990).

**A Powder-Pattern ESR Study of the Quartet States
of the Precursors of a Square-Pyramidal Nitridochromium(V) Complex,
Cr(III)(bpb)Cl(H₂O) and Cr(III)(bpb)(N₃)₂ :
Analysis by the Use of Exact Analytical Expressions**

K. Sato,¹ D. Shiomi,² T. Takui,¹ K. Itoh,² T. Shimozone,³
H. Yoshida,⁴ K. Tajima⁴ and N. Azuma³

¹Department of Chemistry and ²Department of Material Science, Faculty of Science
Osaka City University, Sugimoto, Sumiyoshi-ku, Osaka 558, Japan

³Department of Chemistry, Faculty of General Education and

⁴Department of Chemistry, Faculty of Science,
Ehime University, Matsuyama, Ehime 790, Japan

The quartet states of Cr(III)(bpb)Cl(H₂O), **1**, and Cr(III)(bpb)(N₃)₂, **2** (H₂bpb = N,N'-bis(2'-pyridinecarboxamide)-1,2-benzene) were investigated by powder-pattern ESR spectroscopy with the help of exact analytical solutions of the fine-structure spin Hamiltonian. These complexes are precursors of a stable square-pyramidal nitridochromium complex Cr(V)N(bpb). The chemistry of the nitridochromium complexes has attracted little attention so far in spite that Cr(V) forms isolable d¹ paramagnetic complexes.

In the analysis of X-band ESR spectroscopy, the treatments for the quartet species with large fine-structures are usually based on the numerical diagonalization of the fine-structure spin Hamiltonian, requiring long computing time. In fact, several papers dealing with ESR analyses of the quartet states of Cr(III) series, which were based on the numerical calculation of the spin Hamiltonian, have been published[1,2,3]. In this paper, the analysis to determine the fine-structure parameters was performed based on exact analytical expressions for quartet states obtained from a reorganized eigenfield Hamiltonian. Those expressions give both the exact eigenenergies and eigenfields for the canonical orientations of the principal axes of fine-structure tensors. The method saves computation time a great deal. This paper exemplifies the use and application of the analytical expressions.

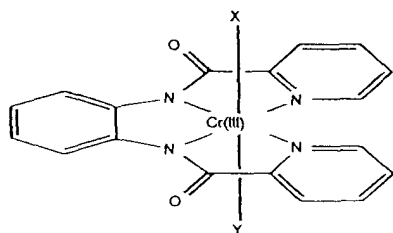


Figure 1 Structure of the complexes, **1** and **2**

1: X=Cl, Y=H₂O 2: X=Y=N₃

Analytical Expressions for a Quartet State

Analytical expressions for a quartet state in principal-axis canonical orientations were derived in terms of the eigenfield method[4]. For the quartet state, there are six resonance fields in general for a given magnetic field, although several fields among them are sometimes meaningless in the case of large fine-structure terms. These six resonance fields are given by the following quadratic and quartic equations in B², which lead to exact solutions for the resonance field:

$$f(B) = 16g_{zz}^4\beta^4 B^4 + 8\left\{3(D_{xx} - D_{yy})^2 - 9D_{zz}^2 - (h\nu)^2\right\}g_{zz}^2\beta^2 B^2 + \left\{-3(D_{xx} - D_{yy})^2 - 9D_{zz}^2 + (h\nu)^2\right\} = 0 \quad (1)$$

and

$$f(B) = a_4 B^8 + (2a_4 a_2 - a_3^2) B^6 + (2a_4 a_0 + a_2^2 - 2a_3 a_1) B^4 + (2a_2 a_0 - a_1^2) B^2 + a_0^2 = 0 \quad (2)$$

where

$$a_4 = -3g_{zz}^4\beta^4$$

$$a_3 = 4g_{zz}^3\beta^3 h\nu$$

$$a_2 = \left[-3\left\{(D_{xx} - D_{yy})^2 - 9D_{zz}^2\right\} + 2(h\nu)^2\right]g_{zz}^2\beta^2$$

$$a_1 = \left[6\left\{(D_{xx} - D_{yy})^2 + 3D_{zz}^2\right\} - 4(h\nu)^2\right]g_{zz}\beta h\nu$$

$$\text{and } a_0 = \left[-3\left\{(D_{xx} - D_{yy})^2 + 3D_{zz}^2\right\} + (h\nu)^2\right](h\nu)^2$$

D_{xx} , D_{yy} , and D_{zz} are defined using fine-structure parameters by

$$D_{xx} = -\frac{1}{3}D + E, D_{yy} = -\frac{1}{3}D - E, \text{ and } D_{zz} = \frac{2}{3}D.$$

The resonance fields calculated by Eqs.(1) and (2) correspond to the Z principal axis in the fine-structure coordinate system. The expressions for the magnetic field parallel to the X and Y axes are straightforwardly obtained by the cyclic permutation with respect to X, Y, and Z.

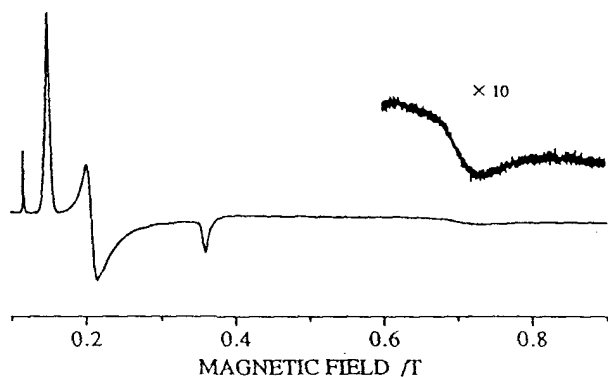


Figure 2. ESR spectrum of 1 in DMF-toluene mixed solvent.

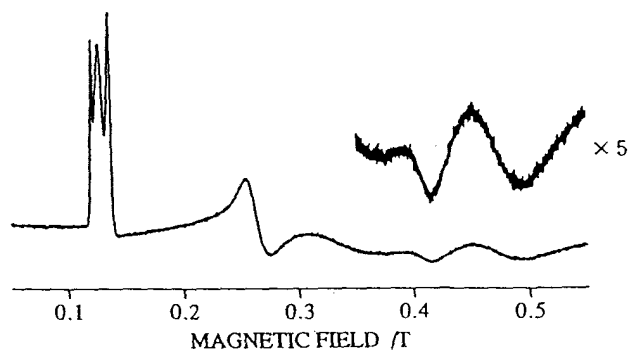


Figure 3. ESR spectrum of 2 in DMF-toluene mixed solvent.

Randomly Oriented ESR Spectra of the Complexes

The powder-pattern ESR spectra of 1 and 2 were measured in glassy dimethylformamide(DMF)-toluene mixed solvent at liquid Helium temperature. Figures 2 and 3 show the ESR spectra of 1 and 2, respectively. The spectra of both complexes indicated a typical quartet spectral pattern with relatively large fine-structure parameter D . For the quartet state with large D value, ESR transitions observed at the lower fields are sensitive to only relative value of D and E . We, therefore, estimated the ratio E/D of the complexes from the low-field ESR transitions, and then determined the fine-structure parameters which reproduced the resonance fields of higher field ESR transitions. The data analyses were based on the analytical expressions given by Eqs.(1) and (2). The determined fine-structure parameters for 1 and 2 in the mixed solvent are summarized in table I.

The fine-structure parameters for 1 reproduced well the observed resonance fields for the canonical axes within an experimental accuracy. The highest ESR signal is responsible for the D value when the fine-structure parameter D is large comparing with microwave transition energy. It, therefore, was difficult to determine the fine-structure parameter D for 1 without detecting the highest resonance-field signal which was observed at about 1.1T.

In the ESR spectrum of 2 in DMF-toluene mixed solvent as shown in Figure 3, three ESR signals were observed near 0.15T. From a relationship of the signal intensities of these transitions, it turned out that the middle transition and the other two transitions were attributed to different species. The behavior of the ESR signal intensities indicated that the former corresponded to a parent complex 2 and the latter to the complex that one of the axial ligands exchanged with a DMF solvent[5]. We determined the fine-structure parameters of the latter complex by the same procedure as for 1, showing the best-fit parameters in Table I. On the other hand, we roughly estimated only the ratio of D and E values because the spectral information on the former complex was very poor. The E/D value was estimated to be nearly 1/3.

Table I Experimentally determined fine-structure parameters of 1 and 2

	1	2
S	3/2	3/2
g value	1.98	1.98
E/D	0.093	0.214
D value	0.68	0.70
E value	0.063	0.15

unit of D or E value: cm^{-1}

Conclusions

The quartet states of 1 and 2, which are precursors of a stable square-pyramidal nitridochromium complex $\text{Cr(V)-N}(\text{bpb})$, have been studied by powder-pattern ESR spectroscopy. The powder pattern ESR spectra of these complexes indicated that the quartet states were characterized by large fine-structure parameters compared with microwave transition energy. We determined the fine-structure parameters for 1 and 2 with the help of exact analytical expressions of the fine-structure spin Hamiltonian which were derived based on the eigenfield method, exemplifying the usefulness of the analytical expressions.

References

1. J. C. Hempel, L. O. Morgan and W. B. Lewis, *Inorg. Chem.* **9**, 2064(1970).
2. S. J. Strach and R. Bramley, *J. Chem. Phys.* **88**, 7380(1988).
3. R. P. Bonomo, A. J. Di Bilio and F. Riggi, *Chem. Phys.* **151**, 323(1991).
4. The derivation of the analytical expressions will be presented in this proceedings by K. Sato, T. Takui, and K. Itoh.
5. T. Shimozone, H. Yoshida, K. Tajima, H. Shikata, N. Azuma, and K. Ishizu, the preprint of the 34th ESR symposium (Japan Chem. Soc. regional meeting), A44, 1995.

Exact Analytical Solutions of Eigenfields and Eigenenergies for High Spins ($S \leq 4$)

K. Sato,¹ T. Takui¹ and K. Itoh²

¹Department of Chemistry and ²Department of Material Science, Faculty of Science
Osaka City University, Sugimoto, Sumiyoshi-ku, Osaka 558, Japan

The recent advances in the field of organic magnetism and spin chemistry have provided a variety of organic high-spin systems ranging from high spin molecules to spin clusters and extremely large high-spin polymers. A perturbation treatment of the spin Hamiltonian has been successfully applied to the analyses of randomly oriented ESR spectra of triplet states and other high-spin states with relatively small fine-structure parameters. Even if the perturbation approach does not hold, the complete analysis of triplet states is not so difficult because the exact analytical solution of the spin Hamiltonian in terms of the eigenenergy method is available. In addition, exact treatments by the numerical diagonalization of the spin Hamiltonian have also been applied to the analyses. For high-spin states, however, those treatments are time-consuming and they often meet non-convergence problem during the analyses of powder-pattern X-band spectra with relatively large fine-structure parameters. A solution for the above problem is the eigenfield method[1,2], although it requires a great deal of computing time if the numerical approach is invoked. The establishment of an easy-to-access and exact approach to the analyses of the high-spin ESR spectra is an important issue in high-spin chemistry. This paper describes an analytical approach based on exact analytical solutions of resonance fields obtained from a reorganized eigenfield equation, presenting useful expressions for eigenfields and eigenenergies for high spins ($S \leq 4$). Those for eigenfields allow us to reproduce straightforwardly observed resonance fields for principal-axis orientations without time-consuming computation.

The Eigenfield Method[1,2]

When a spin Hamiltonian consists of a magnetic field dependent term HG and an independent term F , an eigenfield equation is given by

$$AZ = HBZ \quad (1)$$

where A and B are supermatrices which are defined as

$$A = h\nu E \otimes E - F \otimes E + E \otimes F^*$$

$$\text{and } B = G \otimes E - E \otimes G^*$$

and the eigenvector Z means the direct product of the eigenvectors of the states associated with a particular transition on resonance when H is taken to be the resonance field. E is an identity matrix.

Reconsideration of the Spin Hamiltonian for High-Spin State ESR Spectroscopy

The effective spin Hamiltonian for fine-structure ESR analysis is expressed by

$$H = H_{eZ} + H_D = \beta \mathbf{S} \cdot \mathbf{g} \cdot \mathbf{H} + \mathbf{S} \cdot \mathbf{D} \cdot \mathbf{S} \quad (2)$$

where H_{eZ} and H_D stand for the electron Zeeman and fine structure terms, respectively. In the following argument, we assume that the principal axes of the \mathbf{g} and \mathbf{D} tensors are collinear for simplicity. This limitation is not a requirement for the present approach and can be eliminated. In the Zeeman coordinate system where the direction of the magnetic field is taken parallel to the z axis, *i.e.* $\mathbf{H} = (0, 0, H)$, we can rewrite Eq.(2) as

$$\begin{aligned} H = & \beta H (g_{zz} S_z + 1/2 g_1 S_+ + 1/2 g_1^* S_-) \\ & + D_0 \{-S_z^2 + 1/4(S_+ S_- + S_- S_+)\} \\ & + 1/2 D_1 (S_z S_+ + S_- S_z) \\ & + 1/2 D_1^* (S_z S_- + S_+ S_z) \\ & + 1/4 D_2 S_z^2 + 1/4 D_2^* S_+^2 \end{aligned} \quad (3)$$

$$\begin{aligned} \text{where } g_1 &= g_{zx} + i g_{yz}, \\ D_0 &= -D_{zz}, D_1 = D_{zx} + i D_{yz}, \\ D_2 &= D_{xx} - D_{yy} + 2i D_{xy}. \end{aligned}$$

For an arbitrary direction of the magnetic field, we have to solve the $(2S+1) \times (2S+1)$ spin Hamiltonian matrix in terms of Eq.(3) to obtain the energy eigenvalues. If we consider the case where one of the axes of the Zeeman coordinate system coincides with one of the principal axes of the \mathbf{D} tensor, both g_1 and D_1 vanish because the \mathbf{D} tensor becomes diagonal. Therefore, the spin Hamiltonian matrix is reducible to two sub blocks, H_1 and H_2 , in some cases;

$$H = \begin{pmatrix} H_1 & 0 \\ 0 & H_2 \end{pmatrix} = H_1 \oplus H_2$$

where H_1 and H_2 are $(S+1/2) \times (S+1/2)$ matrices for half-integer spins, and $(S+1) \times (S+1)$ and $S \times S$ matrices, respectively, for integer spins. Then, solving an eigenvalue problem with each block matrix, we can obtain the energy eigenvalues. This reduction of the spin Hamiltonian means that for the direction of the principal axes of the \mathbf{D} tensor it is possible under certain conditions to obtain analytical solutions for energy eigenvalues even for high-spin states whose spin Hamiltonian matrix has a large dimension.

Derivation of Analytical Expressions for Exact Resonance Fields from the Eigenfield Equation

Now we consider the resonance fields in terms of the eigenfield equation. Solving the eigenfield equation of Eq.(1) is equivalent to finding out the solution of the equation

$$|\mathbf{A} - \mathbf{H}\mathbf{B}| = 0. \quad (4)$$

Since the matrix of the left hand side of Eq.(4) is

$$\mathbf{C} \equiv \mathbf{A} - \mathbf{H}\mathbf{B} = h\nu \mathbf{E} \otimes \mathbf{E} - H \otimes \mathbf{E} + \mathbf{E} \otimes H^*,$$

we obtain

$$\mathbf{C} = \mathbf{C}_{11} \oplus \mathbf{C}_{12} \oplus \mathbf{C}_{21} \oplus \mathbf{C}_{22}, \quad (5)$$

where $\mathbf{C}_{ij} = h\nu \mathbf{E}_i \otimes \mathbf{E}_j - H_i \otimes \mathbf{E}_j + \mathbf{E}_i \otimes H_j^*$,

using $\mathbf{E} = \mathbf{E}_1 \oplus \mathbf{E}_2$. Eq.(5) indicates that an eigenvalue problem for the eigenfield equation is also reducible to those of four small block matrices:

$$\mathbf{C} = \begin{pmatrix} \mathbf{C}_{11} & & & \mathbf{0} \\ & \mathbf{C}_{12} & & \\ & & \mathbf{C}_{21} & \\ \mathbf{0} & & & \mathbf{C}_{22} \end{pmatrix}$$

As the eigenfield equation, $|\mathbf{C}|=0$, is reorganized as four small equations, $|\mathbf{C}_{ij}|=0$, in the principal axis orientations, we can obtain whole resonance fields by solving the reorganized eigenfield equation. These reduced forms make the eigenvalue problem easy-to-treat and of small dimension. We obtained the exact analytical expressions for the eigenfields up to octet state ($S=7/2$) by expanding the determinant of each reduced matrix. It was easily derived using the Mathematica ver.2.2 [3]. The determinant of Eq.(5) is given by a polynomial in H^2 because the eigenfield

equation includes the solution for $\omega_i - \omega_j = h\nu$ as well as that for $\omega_j - \omega_i = h\nu$. In the case of an integer spin, the total determinant is factorized into the product of four polynomials in H^2 , corresponding to the determinant of each block matrix, \mathbf{C}_{ij} . Note that in the case of a half-integer spin, the determinant of each block matrix is a polynomial in H , even though the total determinant is a polynomial in H^2 .

We examined the possibility of obtaining analytical solutions of the resonance fields in terms of the eigenfield equation as well as that of obtaining the energy eigenvalues of the spin Hamiltonian by considering the dimension of the reduced block matrices. As we can solve the polynomial in H^2 up to a quartic equation using Cardano's formula for the cubic equation or Ferrari's formula for the quartic equation without mathematical difficulty, it is possible to partially derive exact analytical solutions for principal-axis canonical orientations in high spin systems up to a nonet state for its energy eigenvalues and up to a septet state for its resonance fields.

In conclusions, the exact analytical solutions for energy eigenvalues and resonance fields as well as their parent equations were derived for principal-axis canonical orientations in high-spin state ESR spectroscopy by applying the eigenfield method. If the experimental values for resonance fields are available from a powder-pattern ESR spectrum, it is straightforward to compare them with calculated values using the exact analytical expressions derived here. If the expression for a particular spin multiplicity is obtained for an arbitrary direction of the magnetic field, the eigenvalue problem of a generalized $(2S+1)^2 \times (2S+1)^2$ imaginary matrix results in finding roots of the equation with real coefficients being $S(2S+1)$ order in H^2 . This treatment can remove the disadvantage inherent in the eigenfield method, *i.e.*, the manipulation of supermatrices in view of both required computing time and numerical precision.

References

1. C. N. Banwell and H. Primas, *Mol. Phys.* **6**, 225(1963).
2. G. G. Belford, R. L. Belford and J. F. Burkhalter, *J. Mag. Reson.* **11**, 251(1973).
3. The obtained analytical expressions for the resonance fields in high-spin states are available in disk media. The expressions for the fields in quartet state will be given in the paper of the study of nitridochromium complexes by the authors in this proceedings. The paper exemplifies the use of these expressions.

^{13}C NMR of triglycerides

Marie-Rose Van Calsteren*, Christopher Barr,

*Centre de recherche et de développement sur les aliments, Agriculture et Agroalimentaire Canada
Saint-Hyacinthe (Québec), Canada J2S 8E3*

Paul Angers and Joseph Arul

*Département de sciences et technologie des aliments, Université Laval
Québec (Québec), Canada G1K 7P4*

I. Introduction

Determining the composition of fatty acids at the two glycerol positions of triglycerides usually involves hydrolysis by pancreatic lipase which preferentially removes the acyl groups at positions 1 and 3 (α) of glycerol. Essentially the same information can be obtained from the aliphatic (C-2 and C-3) [1], olefinic [2] and carbonyl (C-1) [1, 3] regions of the ^{13}C NMR spectrum. In palm oil, the carbonyl carbons of the saturated, oleic and linoleic acyl groups at the α glycerol position have slightly different chemical shifts and the same is true for the acyl groups at the β (2) glycerol position [3]. Unsaturated fatty acids attached to the β glycerol position can also be distinguished from those at the α position [2].

In this work we have investigated the possibilities of the method and extended it to determine the distribution of attachment positions of fatty acid chains in butter.

II. Experimental part

Standard triglycerides were obtained from Sigma Chemical (St. Louis, MO). Butter was fractionated by HPLC. Butter oil (100 μl of a 10% solution in chloroform) was injected in a Hewlett-Packard model HP-1050 system equipped with an autosampler, a solvent conditioner, an oven and a UV scanning detector. Spherisorb 5 ODS-2 (5 μm) 250 \times 10 mm semi-preparative and 60 \times 10 mm guard columns were used at 30°C with a gradient from 9:1 to 7:3 acetonitrile/*tert*-butylmethylether at a flow rate of 5 ml/min. Fractions were collected automatically for a period of 100 min after 20 min equilibration.

Samples were dissolved in CDCl_3 containing 1% TMS at a variable concentration depending on the amount of material available. ^{13}C NMR spectra were obtained at 75.5 MHz on a Bruker AM-300 spectrometer in either a 10-mm broadband or a 5-mm dual $^{13}\text{C}/^1\text{H}$ probe, with the temperature controlled at 27°C. Separate power gated, ^1H decoupled spectra of 32 K data points were obtained from the carbonyl, olefinic and aliphatic regions of each sample, with a resolution of 0.069 Hz/point for the carbonyl and olefinic regions and 0.119 Hz/point for the aliphatic region. A single 90° pulse of 9.5 μs with the 10-mm or 5.7 μs with the 5-mm probe was used. The total recycling time was 42.0, 24.5 and 23.4 s respectively, which represents $5 \times T_1$

for the slowest relaxing peak in each region as measured on a triolein sample. The number of scans varied, depending on the sample concentration. Spectra are referenced to TMS as observed in the full spectrum. Chemical shifts were measured as a function of concentration (volume fraction) using triolein as a representative sample. They are reported after adjustment to infinite dilution to compensate for the effects of concentration on chemical shift.

III. Results and discussion

Figures 1-3 show spectra of the aliphatic, olefinic and carbonyl regions respectively of different standard triglycerides and a butter oil fraction. Peaks were assigned to carbons according to published chemical shift values for similar compounds [4, 5] and, when resolved, to a particular attachment position on the glycerol moiety based on intensities. Attachment position can easily be observed on C-1, C-2, C-3 of each type of chain, C-4 of butyric acid and on all olefinic carbons. In butter, butyric acid was found only at the α glycerol position.

A. Concentration dependence of chemical shifts

Chemical shifts depend on magnetic susceptibility and therefore vary with concentration. Data were fitted empirically by linear regression to a polynomial function, starting with first order and increasing the order until the adjusted coefficient of determination showed no significant increase. In general, a quadratic function best fitted the results. Using a mixture of triolein and tripalmitin, it was found that chemical shifts depend on total triglyceride concentration and not concentration of the individual species.

B. Aliphatic region

By integration of the aliphatic region, average chain lengths could be determined. In the calculation, one carbon was added for the carbonyl, carbons α to one double bond were counted twice and the carbon α to two double bonds was counted three times to account for the nonaliphatic carbons of the chains. Also, the proportion of olefinic carbons was determined from the integrals of the allylic carbons. The integral for one carbon was taken as the average of C-2, C-3, C- ω - 2, C- ω - 1 and C- ω . Results (Figure 4) demonstrate the accuracy of the method.

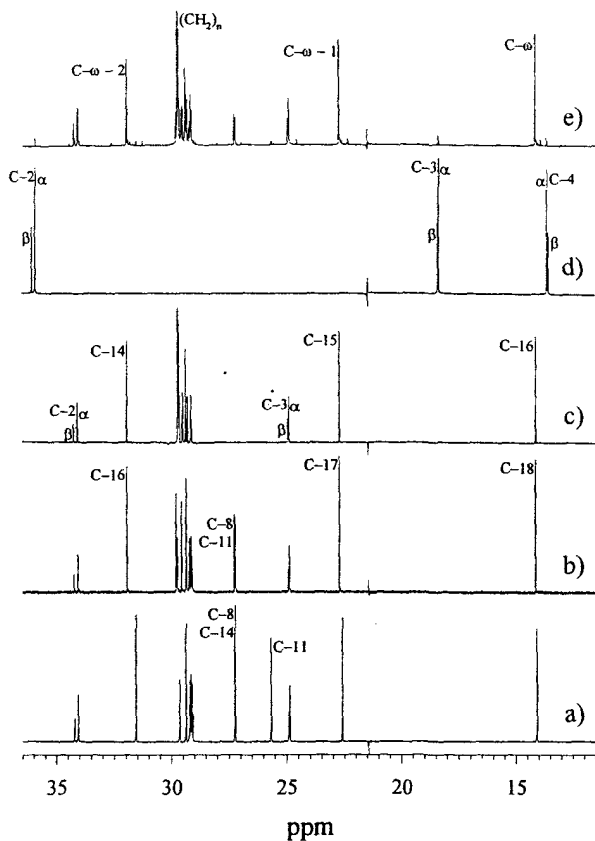


Figure 1. Aliphatic region of the ^{13}C NMR spectrum of: a) trilinolein; b) triolein; c) tripalmitin; d) tributyrin; e) a butter oil fraction.

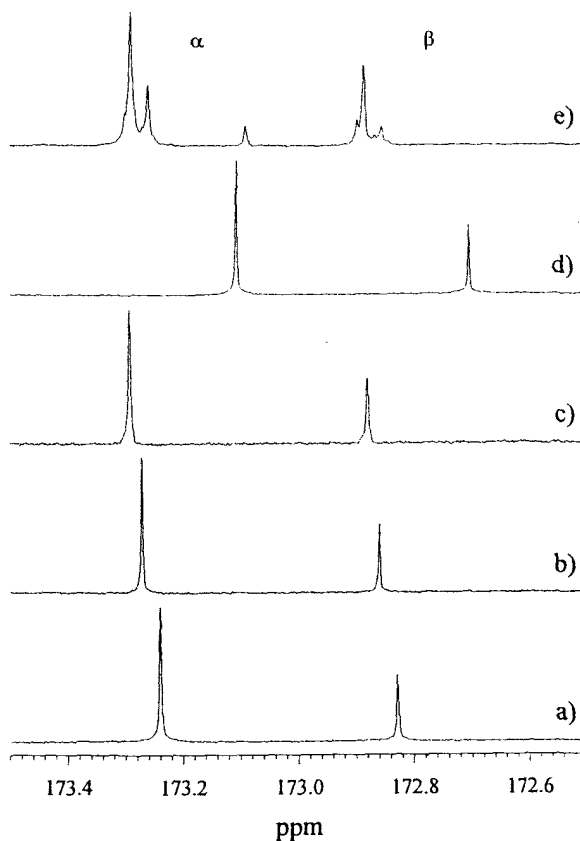


Figure 3. Carbonyl region of the ^{13}C NMR spectrum of: a) trilinolein; b) triolein; c) tripalmitin; d) tributyrin; e) a butter oil fraction.

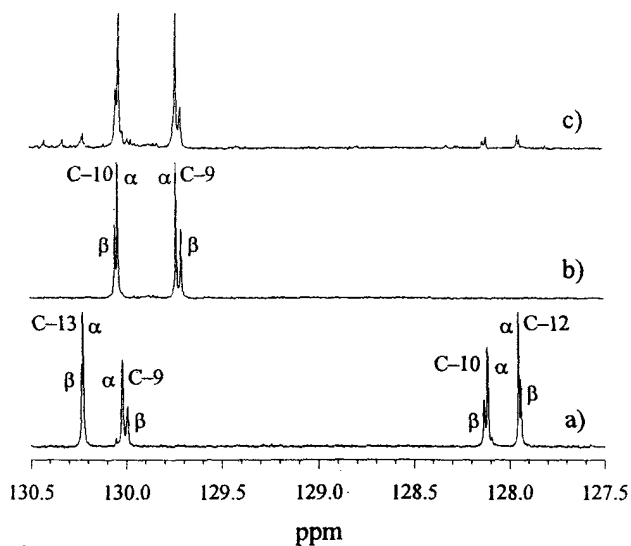


Figure 2. Olefinic region of the ^{13}C NMR spectrum of: a) the randomly mixed-chain triglyceride from tricaproin and trilinolein; b) triolein; c) a butter oil fraction.

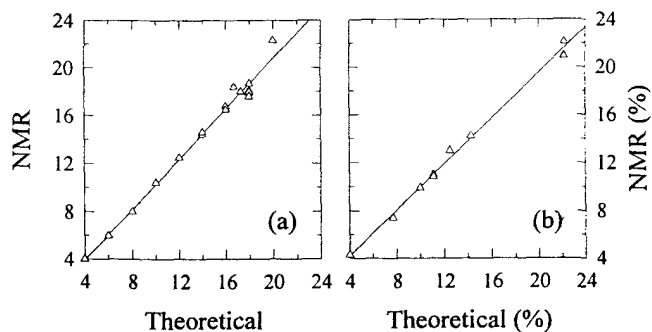


Figure 4. Average chain length (a) and proportion of olefinic carbons (b) determined by integration of the aliphatic region.

C. Olefinic region

Tables 1-2 show that chemical shift differences ($\Delta\delta$), C-10 - C-9 or C-12 - C-11 for the monounsaturated, C-13 - C-9 and C-10 - C-12 for the diunsaturated fatty acids, are characteristic of chain length and attachment position (α or β) as well as position of unsaturations but not isomeric

Table 1. Effect of chain attachment position on chemical shift difference ($\Delta\delta$) C-10 - C-9 or C-12 - C-11 of various monounsaturated triglycerides.

Triglyceride	$\Delta\delta$ (ppm)	
	α	β
trimyrstolein	0.231	0.271
tripalmitolein	0.297	0.337
triolein	0.306	0.346
1,2-dioleoyl-3-palmitoylglycerol	0.305	0.345
3-oleoyl-1,2-dipalmitoylglycerol	0.301	-
trielaidin	0.308	0.344
tri-11-eicosenoin	0.111	0.137

Table 2. Effect of chain attachment position on chemical shift differences ($\Delta\delta$) C-13 - C-9 and C-10 - C-12 of various diunsaturated triglycerides.

Triglyceride	$\Delta\delta$ (ppm)			
	C-13 - C-9		C-10 - C-12	
	α	β	α	β
trilinolein	0.216	0.250	0.171	0.202
trilinolelaidin	0.212	0.243	0.176	0.203

form (*cis* or *trans*) or nature of neighbouring chains. The above chemical shift differences are independent of concentration.

D. Carbonyl region

Except for butyric acid chains, the carbonyl carbons of saturated chains are more deshielded than those of monounsaturated chains and those of diunsaturated chains which are the most shielded. Clusters of peaks for the α and β positions are observed on the butter oil fraction spectrum (Figure 3e) and are due to neighbouring chains.

E. Effect of neighbouring chains

Spectra of mixed triglycerides prepared by transesterification of two different homogenous triglycerides were run to investigate the effect of neighbouring chains. Little effect was observed in all spectral regions when the two starting triglycerides were saturated (tricaproin and tripalmitin). With mixed saturated and diunsaturated triglycerides (tricaproin and trilinolein), no major effect could be seen in the aliphatic and olefinic regions, but the influence of neighbouring saturated or diunsaturated chains is clearly visible in the carbonyl region (Figure 5). In both the α and β regions, the effect of a saturated neighbour is deshielding and that of an unsaturated neighbour is shielding. An effect of the α' neighbour is also observed in the α region.

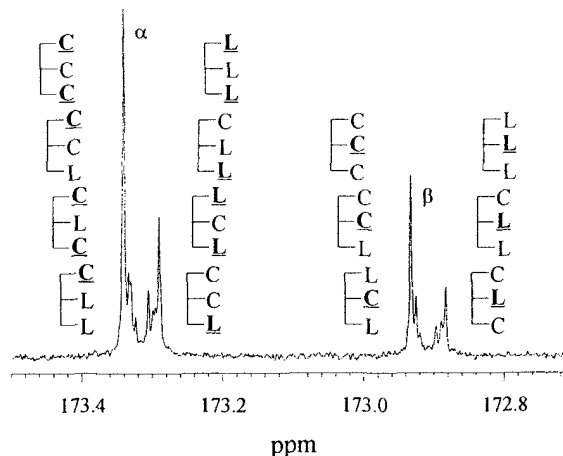


Figure 5. Carbonyl region of the ^{13}C NMR spectrum of the randomly mixed-chain triglyceride from tricaproin and trilinolein.

F. Quantitative analysis

Peaks in the olefinic region were fitted to a sum of lorentzian functions. It was found that when the peaks are highly overlapped, as for C-10, the amplitude of the peaks give better quantitation than the areas, because the width parameter is not as accurately determined.

IV. Conclusion

The aliphatic region is useful for determining average chain length and proportion of olefinic carbons. From the olefinic region, type of unsaturated triglyceride could be obtained from chemical shift differences and attachment position of unsaturated chains could be determined accurately. The carbonyl region gives information on the attachment position of all chains but is complicated by shifts caused by neighbouring chains. More mixed-chain standards, especially those with saturated and monounsaturated starting triglycerides, are required to completely unscramble the carbonyl region.

V. References

- 1 F.D. Gunstone, *Chem. Phys. Lipids* **58**, 159-167 (1991).
- 2 S. Ng, *Lipids* **19**, 56-59 (1984).
- 3 S. Ng, *Lipids* **20**, 778-782 (1985).
- 4 F.D. Gunstone, M.R. Pollard, C.M. Scrimgeour, N.W. Gilman and B.C. Holland, *Chem. Phys. Lipids* **17**, 1-13 (1976).
- 5 F.D. Gunstone, M.R. Pollard, C.M. Scrimgeour and H.S. Vedanayagam, *Chem. Phys. Lipids* **18**, 115-129 (1977).

Aqueous Silica Sols : A Study Of The Spin-lattice Relaxation Time T_1 By The Field-Cycling NMR Technique

J. Van Craen, P. Roose, Y. De Smet, H. Eisendrath
MARE, Department of Physics, Vrije Universiteit Brussel, Brussels, Belgium

Introduction

Spherical macromolecules, mainly consisting of amorphous silica (SiO_2) and some OH groups on the surface, were produced following a reaction scheme introduced by W. Stöber (1).

It was observed that when these particles were dispersed in water, they drastically change the solvent proton T_1 -value. From a series of experiments wherein the magnetic field strength B_0 , temperature, silica concentration, proton content and particle diameter was modified, it could be inferred that magnetization transfer is the dominant relaxation mechanism (2).

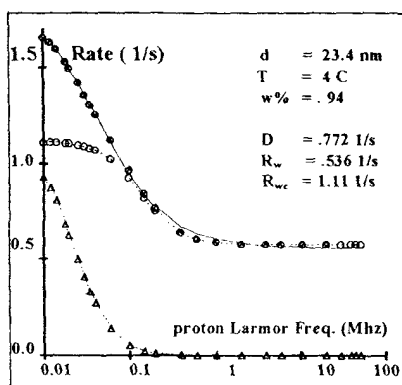


Fig 1: Experimental NMRD spectrum (full line) and its decomposition (●) in a cross-relaxation part (Δ) and a dynamical contribution (○).

A well known cross-relaxation model (3) was used to analyze the NMRD curves and led, through the introduction of some correlation times to a better understanding of the relaxation mechanisms and the molecular motion.

Materials and Methods

The silica particles are obtained through hydrolysis and condensation of tetraethyl orthosilicate (TEOS : $\text{Si}(\text{OC}_2\text{H}_5)_4$) in a mixture of water, ammonia and ethanol. A distillation ultimately produces an aqueous suspension containing particles of nearly equal diameter d . It is imposed by the concentration of the reagents and either measured by photon correlation spectroscopy (PCS) or by N_2 adsorption on the surface

(BET method). In the experiments described here, d was restricted to the range 8-35 nm.

The B_0 dependence of the spin-lattice relaxation time T_1 was determined on a 7.5 Mhz field-cycling NMRD relaxometer. It was decided to characterize the vast number of spectra by the Cole-Cole function as no a-priori theoretical lineshape was available. This expression describes the experimental data very well and reads:

$$1/T_1 = D + A * \frac{[1 + (\nu/\nu_c)^{\beta/2} * \cos(\pi\beta/4)]}{[1 + 2(\nu/\nu_c)^{\beta/2} \cos(\pi\beta/4) + (\nu/\nu_c)^\beta]}$$

ν is the proton Larmor frequency, A evaluates that part of the relaxation rate, at $\nu=0$, that can be attributed to the presence of the sol particles. The D term remains constant over the frequency domain investigated here and is entirely related to the bulk water molecules. ν_c is a characteristic frequency and β determines the slope of the $1/T_1$ curve.

The Cross-relaxation Model

In a previous paper (2), we discuss a simple two phase model that describes the evolution towards equilibrium of M_w , the magnetization of the water phase. It is shown that the interactions involving solvent protons and protons 'bound' to the surface of the macro-molecules enhance the normal water relaxation rate R_w by a new contribution R_{wc} : for $\nu \approx 0$ and for proton fraction p , M_w relaxes with a rate $R \approx R_{wc} + p * R_w$. This result suffices to explain the characteristics of the A term. Unfortunately the behavior of the frequency ν_c could not be explained. Therefore we tried to decompose the spectrum in its individual parts. But then some of approximations, made to obtain R in its simple form, no longer hold and the complete expression for the rate has to be considered:

$$R = [pR_w + R_c + R_{wc}(1+pM) - \Delta]/2$$

with $\Delta = ((R_c - pR_w - R_{wc}(1-pM))^2 + 4pMR_{wc}^2)^{1/2}$

Experimental observations.

When the concentration C is altered, the D term is not influenced, while A follows linearly in most cases. In some samples though a small quadratic term had to be included. PCS measurements of the diffusion

coefficient indicate that inter-SiO₂ particle interactions could be responsible for this effect.

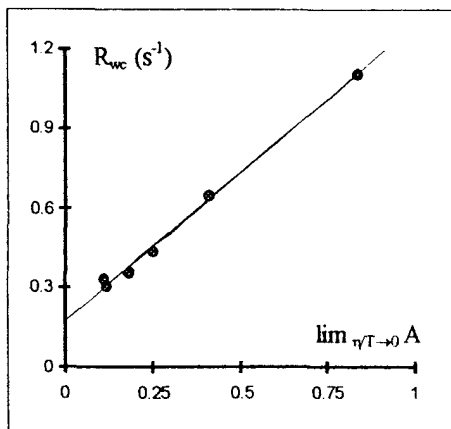


Fig 2: Comparison of R_{wc} obtained from deuterated samples and A in the limit of high temperatures.

When the temperature is increased, A (for $T > 10C$) as well as D decrease linearly with η/T . This result shows that when the drag force on the macromolecules is reduced, they move faster and for $v \approx 0$ the dynamical relaxation mechanisms become less efficient. (the dynamical correlation times are proportional to η/T).

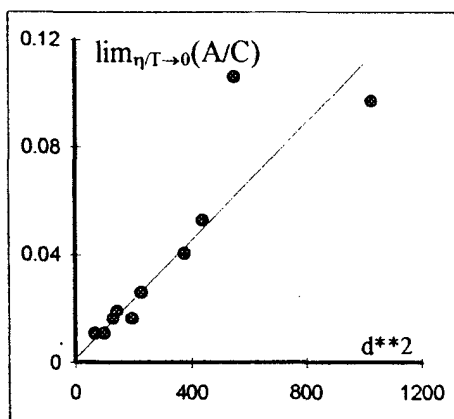


Fig 3: $\lim_{\eta/T \rightarrow 0} (A/C)$ vs diameter squared.

If some of the H₂O solvent molecules are replaced by D₂O it is observed that A decreases but as long as the proton fraction remains larger than 0.5 the linear form $R_{wc} + p \cdot R_w$ still describes the experimental data very well. This proves the point that cross-relaxation effects play an important role in the relaxation of the water protons.

In a sense, raising the temperature ($\eta/T \rightarrow 0$) or diluting the solvent at constant T ($p \rightarrow 0$) must have a similar effect on the relaxation of the solvent protons: the contributions of molecular motion to $1/T_1$ are eliminated and only typical surface effects will affect the relaxation rate. In fig 2 it is shown that the regression parameters are strongly related. It is also clear from fig 3 that $\lim_{\eta/T \rightarrow 0} (A/C)$ is proportional to

the particle surface πd^{**2} . (R_{wc} seems to be rather insensitive to restricted changes in T or p)

Discussion

To evaluate R , $M = M_w(\infty) / M_c(\infty)$ must be estimated and some hypotheses involving $R_c(\omega)$, $R_w(\omega)$ and $R_{wc}(\omega)$ have to be made. Since the dipole-dipole coupling is most likely responsible for the relaxation in this system, $R_c(\omega)$ and $R_w(\omega)$ were represented as $\div (J^{(1)}(\omega, \tau) + J^{(2)}(2\omega, \tau))$ adding a constant to simulate D in R_w . R_{wc} was represented by a single lorentzian function $J(\omega, \tau)$. The correlation time τ of R_c and the amplitudes of R_w and R_{wc} were set equal to actual experimental results. The missing correlation times were ultimately determined by a non-linear least squares fit to an experimental spectrum.

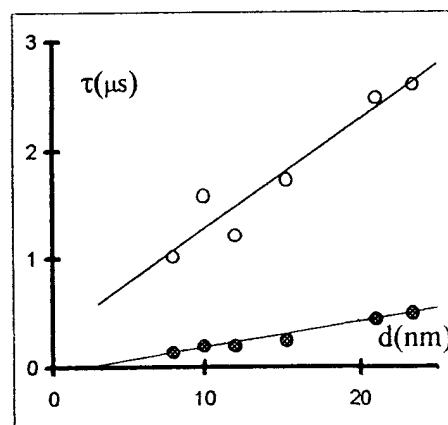


Fig 4: Correlation times τ as obtained from the two phase model: in the water phase (•) and for the cross-relaxation contribution (o).

Some results obtained by this procedure are represented in figs 1 and 4.

An evident conclusion is that if the molecular movement is frozen, the correlation time τ associated to R_w and R_c increase. Unfortunately we still lack a convincing explanation for the way these parameters behave versus the particle diameter d^{**n} . We think however that we are not that far from the solution as our results give a very sound description of the molecular motion.

References

1. W. Stöber, A. Fink and E. Bohn, *J. Colloid Interface Sci.* 26, 62 (1968).
2. P. Roose, J. Van Craen, R. Finsy and H. Eisendrath, *J. Magn. Reson. A* 115,20 (1995).
3. S.H. Koenig, R. G. Bryant, K. Hallenga and G.S. Jacob, *Biochemistry* 17, 4348 (1978).

Solution structure of a biologically-active cyclic LDV peptide containing a β -turn mimetic

John H. Viles, Julia Uppenbrink, Claire M. Moody, Martin Sims, Paul M. Doyle, John Harris, Peter J. Sadler and Janet M. Thornton.

Department of Chemistry, Birkbeck College, University of London, Gordon House, 29 Gordon Square, London WC1H 0PP, UK.
e-mail johnv@chem.bbk.ac.uk

ABSTRACT

The solution structure of cyclo-[Gly-Leu-Asp-Val-BTD] (BTD = β -turn dipeptide) has been determined by two-dimensional $^1\text{H-NMR}$ and systematic conformational searching combined with molecular dynamics studies. The structure contains two hydrogen bonds between the Gly and Val residues, and a type I β -turn with Leu and Asp at the (i+1) and (i+2) positions of the turn. The cyclic compound shows activity in a Scintillation Proximity Assay (SPA) for the inhibition of the interaction between the integrin, $\alpha_4\beta_1$ domain of VAL-4 and vascular cell adhesion molecule-1 (VCAM-1). The structure-activity relationship of the LDV sequence is discussed.

INTRODUCTION

Integrins are cell surface proteins that mediate cell adhesion. They give vital clues for migration, growth, differentiation and can regulate platelet aggregation, immune function, tissue repair and tumor invasion.

Integrins bind to cell adhesion proteins such as fibronectin, fibrinogen, laminin, collagen, ICAM-1 and VCAM-1. These cell adhesion proteins contain minimal sequences, for example RGD or LDV, that are recognised by specific integrin receptor sites.

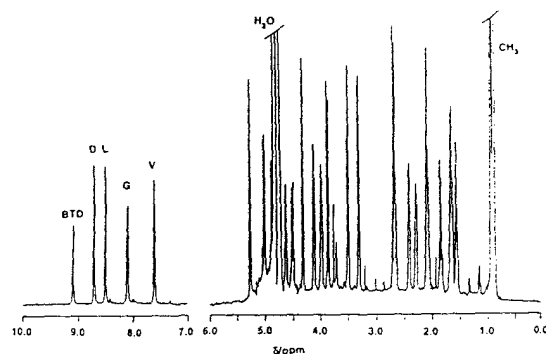
The IDS sequence in VACM-1 which is homologous to LDV is recognised by the $\alpha_4\beta_1$ domain of the integrin VLA-4. We are interested in developing synthetic LDV containing peptides that inhibit cell adhesion between VCAM-1 and $\alpha_4\beta_1$ domain of VLA-4 as potential novel anti-inflammatory agents.

We have synthesized a cyclic pseudo-hexapeptide with the LDV sequence and a bicyclic β -turn mimetic has been incorporated to restrict the conformation of this peptide still further. Both the solution structure and its inhibitory activity with VACM-1 have been determined so as to explore the structure-activity relationship of the minimal LDV sequence.

SYNTHESIS

BTD is a β -turn dipeptide, a type II' β turn mimetic. It was synthesised in 6 steps from L-glutamic acid γ -methyl ester and L-cysteine ethyl ester. Subsequent amino acids were coupled using Fmoc/ piperidine procedures. Cyclisation was achieved at high dilution and after deprotection of the Asp carboxylate, the peptide was purified by reverse-phase HPLC.

RESULTS

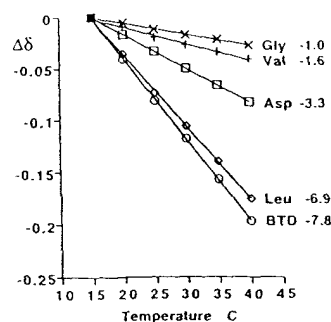


$^1\text{H-NMR}$ of Cyclo-[GLDV-BTD] 500 MHz, 2.4 mM, pH 5.6, 25 $^\circ\text{C}$

Structure calculations were based on the following $^1\text{H-NMR}$ data:

1) NH Temperature Coefficients

The temperature dependence of chemical shift was calculated for NH main chain protons. Above 151 ppb/K NH is solvent accessible, below 131 ppb/K NH is solvent inaccessible or hydrogen bonded.



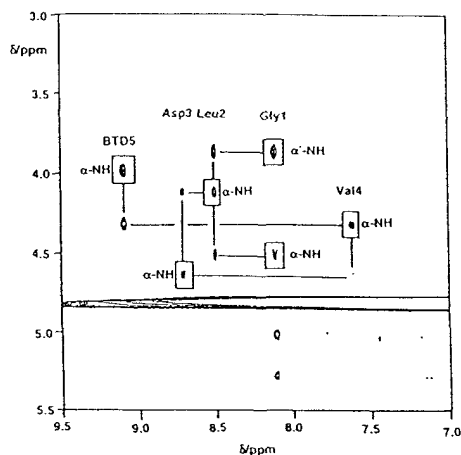
2) $^3J(\alpha\text{CH-NH})$ Coupling

The Karplus relationship was used to determine a range of possible ϕ angles from NH to αCH coupling constant from 1D spectra.

3) nOe Constraints

Cross-peak volumes were measured from 2D ROESY spectra. The methylene cross-peak of BTD was used as an internal standard (1.8 Å). 16 inter-residue ROE's and 25 intra-residue ROE's were observed.

2D ROESY, 500 MHz ^1H NMR, 300 ms mixing time, pH 5.6, 25 °C.



ROE "walk" along main chain
Boxes indicate inter-residue ROE's

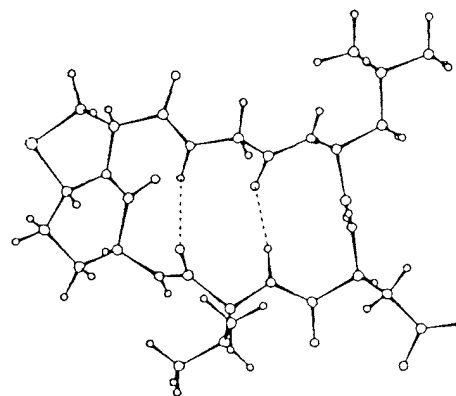
BIOLOGICAL ASSAY

Vascular cell adhesion molecule 1 (VCAM-1) was generated by PCR. Scintillation Proximity Assay was used to study inhibition of VCAM-1 with VLA-4. Inhibition by cyclo-[GLDV-BTD] was an order of magnitude greater than that for the linear 25 residue fibronectin fragment CS1 which contains the LDV sequence.

STRUCTURE

The nOe's observed indicate that the peptide bonds have a *trans* conformation. An initial conformational search was performed by varying ϕ and ψ angles by 10° . Structures that satisfied ring closure, formed two hydrogen bonds, and did not strongly violate the ROE constraints were used as starting structures to perform restrained MD calculations.

200 ps trajectories at 600 and 300K were performed *in vacuo*. The structure that best fulfilled the ROE's and H bonding criteria gave a type I turn at Leu-Asp. The self consistency of the calculated structure compared to the nOe data suggest that a single conformation dominates in solution.



CONCLUSIONS

- BTD and the presence of two strong hydrogen bonds appeared to restrict the cyclic peptide to one conformation.
- It is clear that a conformation with a type I turn at Leu-Asp has a high activity.
- The design of a potential anti-inflammatory drug should contain a flat structure with the $\text{C}\alpha\text{-C}\beta$ hydrophobic and carboxyl functionalities in a plane.
- Other cyclic peptides with the LDV minimal sequence are currently under investigation.

REFERENCES

- RGD and LDV sequence:** Pierschbacher MD, Ruoslahti E (1984) *Nature*, 309, 30-33.
Komoryia, A., Green, L. J., Mervic, M., Yamada, S. S., Yamada, K. M. & Humphries, M. J. (1991) *J. Biol. Chem.* 266, 15075-15079.
- VCAM-1 structure:** Jones, E. J., Harlos, K., Bottomley M.J., Robinson, R.C., Driscoll, P.C., Edwards R. M., Clements J.M., Dudgeon T.J., & Stuart D.I. (1995) *Nature* 373, 539-544.
- Beta Turn Dipeptide BTD:** Bach, A. C., Markwalder, J. A. & Ripka, W. C. (1991) *Int. J. Peptide Protein Res.*, 38, 314-323. Code SEYZUR in CSD
- Karplus Coupling:** Pardi, A., Billeter, M. & Wüthrich, K. (1984) *J. Mol. Biol.*, 180, 741-751.
- NH Temp Coefficients:** Urry, D. W., Ohnishi, T., Long, M. M. & Mitchell, L. W. (1975) *Int. J. Pep. Prot. Res.*, 7, 367-378.

Acknowledgements

Financial support from the BBSRC and Wellcome on a Link grant for the collaboration between academia and industries. MRC NMR facilities at Mill Hill, London, and the CD ULIRS facilities at Birkbeck College, London, and to Jennifer Worden and Neil Burden for their help in the bioassay.

^1H and ^{113}Cd NMR studies of metal binding to isolated albumin and albumin in blood plasma

John H. Viles, A. Tucker, S.U. Patel, and Peter J. Sadler

Department of Chemistry, Birkbeck College, University of London,
Gordon House, 29 Gordon Square, London WC1H 0PP, UK.

ABSTRACT

As the major plasma protein (0.6 mM conc. in blood), albumin (67 kDa) plays a vital role in the transport of many pharmaceuticals and metals (Carter & Ho, 1994). A combination of ^1H NMR and ^{113}Cd is used to probe the binding of Cd^{2+} and Zn^{2+} to a variety of mammalian albumins. An inter-domain binding site is suggested for Zn^{2+} and Cd^{2+} involving 3 His residues. Spectra of ^{113}Cd -albumin in intact plasma indicate that Ca^{2+} competes for Cd^{2+} binding at both sites, and competition with Cu^{2+} and Ni^{2+} is also discussed. ^1H NMR resonances are assigned to the N-terminal residues of albumin and these assignments can be used to characterize the diamagnetic square-planar, N-terminal Ni^{2+} complex in isolated albumin (Sadler et al, 1994) and in intact blood plasma (Patel et al., 1993).

INTRODUCTION:

Structure: □ 585 Residues □ 66.5 kDa □ 17 Disulfide bridges □ One Free Thiol: Cys34 □ 3 Domains □ Largely helical

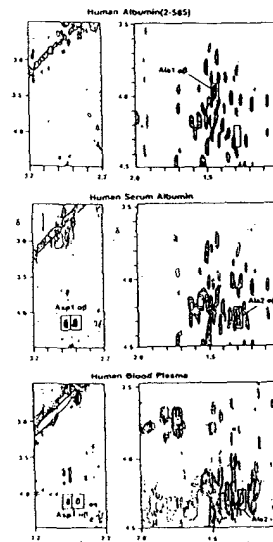
Function: □ Major Plasma Protein, ca. 0.63 mM. □ Maintains osmotic blood pressure. □ Principal carrier of fatty acids □ Binds many hydrophobic molecules: bilirubin, steroids, and hormones. □ Binds many pharmaceuticals e.g. aspirin, auranofin, disulfiram, AZT.

Metal Transport. Albumin has been implicated in the transport of many metal ions, in particular, the binding of Cu^{2+} at the N-terminus. The binding sites for Zn^{2+} , Cd^{2+} and Ca^{2+} on albumin are less well characterized, although three-quarters of Zn^{2+} in plasma is bound to HSA. This accounts for as much as 98% of the exchangeable fraction of Zn^{2+} in serum and is known to be associated with the transport of zinc. About 40% of Cd^{2+} in blood is bound to serum albumin. Of the total Ca^{2+} in plasma (ca. 2.2 mM), one-third to one-half is bound to albumin.

ASSIGNMENTS

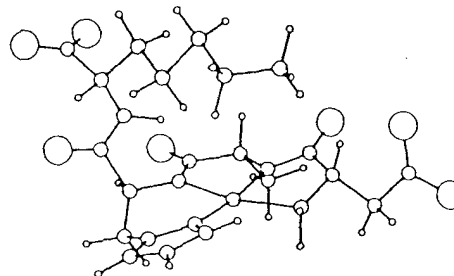
□ 75 spin systems resolvable for isolated HSA.
□ 25 spin systems for HSA resolvable in blood plasma.

□ Use of recombinant albumin with the deletion of the N-terminal residues has enabled the assignment of the N-terminal residues: (Sadler et al, submitted) Asp1-Ala2-His3, in isolated albumin and blood plasma, as shown below.



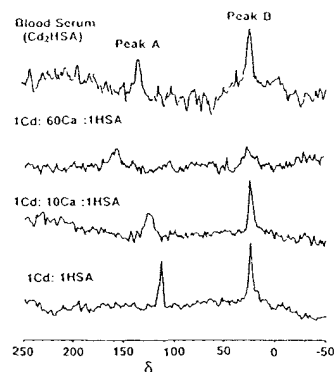
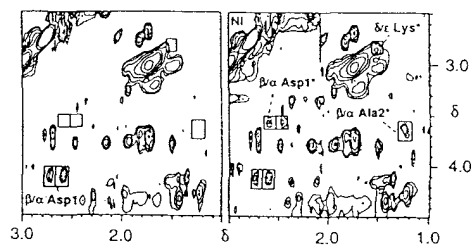
N-TERMINAL METAL BINDING

□ Slow exchange is observed between free albumin and Ni-albumin on the NMR timescale.
□ Nickel complex is diamagnetic, indicating a low-spin square-planar Ni^{2+} complex.
□ Ni^{2+} titration indicates a saturation of the complex at 0.8 mol equiv, consistent with 20% auto-degradation of the first two residues of HSA.
□ ^1H NMR can be used to probe the binding of other metals to the N-terminus. Paramagnetic Cu^{2+} and Co^{2+} also bind to the N-terminus whilst Cd^{2+} and Al^{3+} do not.
□ The shift of Lys4 on coordination of Ni^{2+} is due to ring current shifts from the His3 imidazole ring.



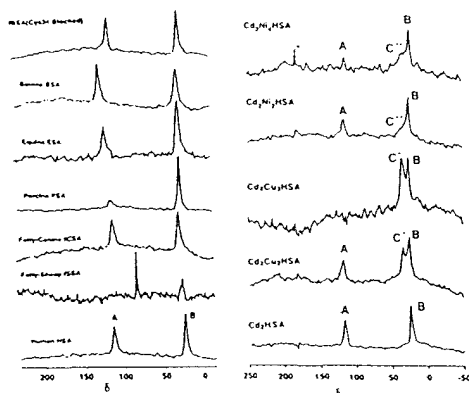
Ni^{2+} and Cu^{2+} N-terminal square planar complex

^1H 2D TOCSY spectrum of blood plasma before and after the addition of 0.5 mol equiv. of Ni^{2+} , adapted from (Patel, Sadler, Tucker and Viles 1993)



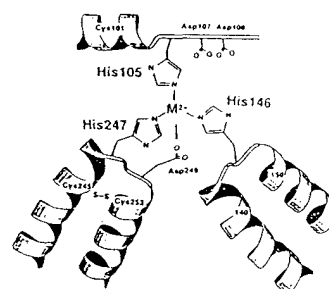
Zn²⁺ AND Cd²⁺ BINDING

^{113}Cd NMR of Mammalian Albumins



- Mammalian albumins give two peaks of equal affinity.
- Peak A, Low Field, 115 ppm. Typical of 2 to 3 nitrogen ligands (His).
- Peak B, High Field, 25 ppm. Typical of 4 oxygens or oxygens + 1 His.
- Cys34 is not a ligand for Cd^{2+} binding as the Cd NMR spectra are unaffected by the use of Cys34 blocked albumin.
- Cd^{2+} does not bind to the N-terminus of albumin as 1 equiv Cu^{2+} or Ni^{2+} does not affect ^{113}Cd NMR spectra of HSA or BSA.
- One equiv of Zn^{2+} displaces Cd^{2+} from site A to site C.
- After saturation of the N-terminus, a second mol equiv of Cu^{2+} or Ni^{2+} also displaces Cd^{2+} from site A to site C.
- ^1H NMR confirms that Zn^{2+} and Cd^{2+} share the same binding site, as the same His C2H resonances are perturbed by Zn^{2+} and Cd^{2+} . In addition, both metals perturb the same high-field-shifted methyl resonances.
- Addition of Ca^{2+} causes the ^{113}Cd peaks to broaden and peak A to shift to low field.
- Physiological level of Ca^{2+} in blood serum has the same effect on Cd binding, as shown below.

Based on sequence comparisons of mammalian albumins, and the position of His residues in the X-ray structure, a binding site for Zn^{2+} and Cd^{2+} can be proposed (Viles and Sadler, submitted)



REFERENCES

- Albumin Reviews**
- Carter, D. C., & Ho, J. X. (1994) Adv. Prot. Chem. 45, 153-203.
- Peters, Jr. T. (1985) Adv. Prot. Chem. 37, 161-245.
- HSA X-ray Structure**
- Carter, D.C., & He, X-M., (1992) Nature 358, 209-215.
- N-terminal metal binding**
- Glennon, J. D., & Sarkar, B. (1982) Biochem. J. 203, 15-23.
- Camerman, N., Camerman, A., & Sarkar, B. (1976) Can. J. Chem. 54, 1309-1316.
- Sadler, P. J., Tucker, A., & Viles, J. H. (1994) Eur. J. Biochem. 220, 193-200.
- Patel, S. U., Sadler, P. J., Tucker, A. and Viles, J. H. (1993) J. Am. Chem. Soc. 115, 9285.
- ^{113}Cd NMR studies of albumin**
- Martins, E. O., & Drakenberg, T. (1982) Inorg. Chim. Acta. 67, 71-74.
- Göumakos, W., Laussac, J., & Sarkar, B., (1991) Biochem. Cell Biol. 69, 809-820.

Acknowledgments

Delta Biotechnology Ltd; NIMR MRC center, Mill Hill and ULIRS for NMR facilities; EPSRC for funding.

DEMONSTRATION OF TISSUE CATION COMPARTMENTATION USING ^{133}Cs NMR

R.M. Wellard, B.P. Shehan*, D.J. Craik*, W.R. Adam

Austin and Repatriation Medical Centre, Banksia St., Heidelberg West, 3081 Australia

*Monash University, Victorian College of Pharmacy, Royal Pde., Parkville, 3052 Australia

Introduction: The regulation of intracellular potassium and its distribution is of interest in both normal and diseased states. This interest arises from a possible role in the mediation of hormone action and in the regulation of cell volume following an osmotic challenge. Of the methods available for the measurement of intracellular potassium most are complex and invasive, requiring disruption of the cell membrane. Nuclear magnetic resonance spectroscopy (NMR) is non-invasive, providing an opportunity for dynamic measurement of intracellular ions. While ^{39}K in tissue can be measured by NMR, the relative insensitivity and small chemical shift range of the ^{39}K nucleus lead us to study a potassium congener, caesium, which is concentrated in cells in a manner paralleling potassium. ^{133}Cs is 100 fold more NMR sensitive than ^{39}K and has a greater chemical shift range, removing the need for shift reagents to differentiate intra- and extracellular compartments. Incorporation of caesium by dietary loading leads to equilibration of a high level of caesium within cells¹, in contrast to other studies which have utilised caesium uptake from the perfusion medium which provides a lower and less stable tissue concentration².

Aims: This study aimed to extend NMR investigations of tissue ^{39}K by using a potassium substitute, caesium, to examine cation compartmentation in isolated perfused rat heart and hepatocytes using ^{133}Cs NMR.

Methods: Rats were fed a caesium enriched diet containing 100 mM/Kg CsCl and given access to 20 mM CsCl in 20 mM KCl drinking fluid for three to five days. ^{133}Cs NMR spectra were measured from isolated Langendorff perfused hearts, isolated hepatocytes and isolated hepatic mitochondria. Use of a phosphate free bicarbonate perfusate allowed concurrent acquisition of ^{31}P spectra. Hepatocytes and mitochondria were studied at 65.60 MHz in packed suspension at 4°C. Spectra from hepatocytes in agarose threads and isolated perfused hearts were acquired at 39.36 MHz and 37°C. Tissue viability was confirmed by the presence of high energy phosphate compounds in ^{31}P NMR spectra.

Results: The ^{133}Cs spectrum of perfused heart (Figure 1) shows a peak corresponding to perfusate and a large asymmetrical down field peak with a shoulder on the downfield side. The isolated

perfused heart is metabolically and functionally stable with time, indicated by constant levels of phosphate metabolites measured in ^{31}P spectra and mechanical work performed. Using χ^2 as an estimate of fit, the irregular caesium peak observed in spectra from perfused hearts is described by two components rather than a single peak ($p < 0.0001$), 1.51 ± 0.18 and 1.12 ± 0.07 ppm ($n = 18$) to higher frequency relative to the buffer peak, respectively. The smaller component represents $30 \pm 6\%$ of the tissue signal. Infusion of rotenone, a mitochondrial electron transport inhibitor ($1 \mu\text{M}$ for 5 min) or valinomycin, a potassium ionophore with some mitochondrial specificity³ (15 nM for 5 min), resulted in a 20% decrease in heart function, measured as work performed. Infusion of valinomycin caused a decrease in pH (7.27 to 7.13, $p < 0.01$) and a partially reversible fall in phosphocreatine concentration ($p < 0.05$), determined from ^{31}P NMR. Hearts infused with rotenone did not show a change in pH. There were no significant changes observed in the two components of ^{133}Cs spectra, due to high degree of variability, particularly in the size and chemical shift of the small component.

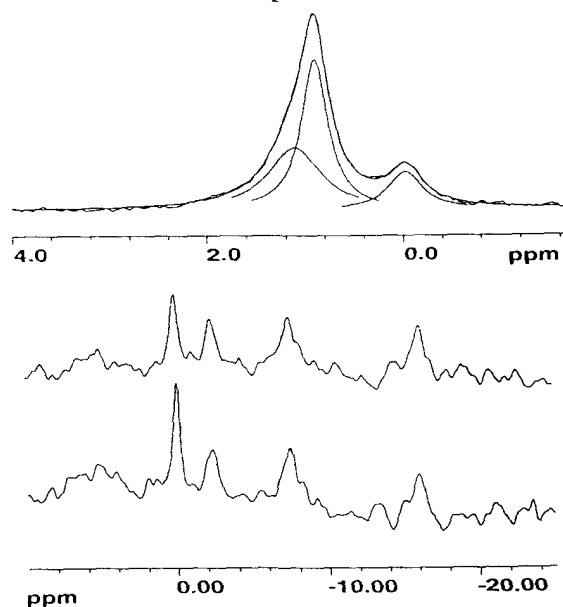


Figure 1 Top: ^{133}Cs spectrum of isolated Langendorff perfused rat heart, acquired at 39.36 MHz. Bottom: ^{31}P NMR spectra (a) at the beginning and (b) after 5 h perfusion.

In an effort to improve peak discrimination we utilised a higher field magnet which required the

use of a different tissue preparation. ^{133}Cs spectra of packed hepatocytes measured at 65.60 MHz more clearly show two peaks, separated by 0.6 ± 0.1 ppm, representing intracellular caesium - similar findings to the isolated perfused hearts. The intensity and chemical shift of these peaks changes with time, but at different rates. Addition of valinomycin results in a faster shift to higher frequency of the major peak and a loss of intensity from the smaller down field peak (**Figure 2**).

As cell viability is an issue, further studies with perfused hepatocytes trapped in agarose threads⁴

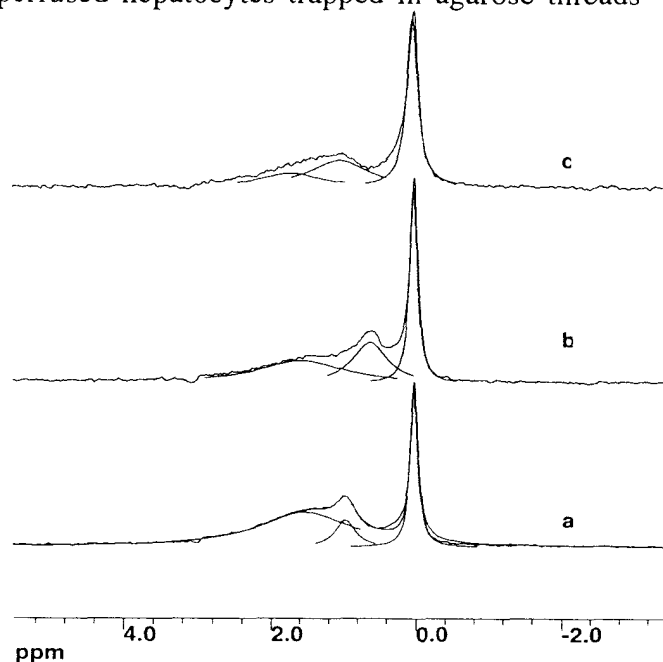


Figure 2 ^{133}Cs spectra of packed hepatocytes: (a) control, 1 h after preparation; (b) following addition of $50 \mu\text{M}$ valinomycin and (c) control, 4 h after preparation.

were performed at 39.37 MHz. ^{133}Cs spectra acquired at 39.37 MHz from perfused hepatocytes cast in agarose gel threads, shown in **Figure 3**, also exhibit broad overlapping peaks, separated by 0.73 ± 0.14 ppm ($n = 4$) and distinct from caesium in perfusate.

At 65.60 MHz, ^{133}Cs NMR spectra of packed isolated hepatic mitochondria show a single labile peak 2.3 ± 0.4 ppm ($n = 4$) relative to ^{133}Cs in buffer. While the chemical shift of caesium in mitochondria is distinct from the chemical shift of peaks observed for hepatocytes, this difference may be an artefact of isolation.

Conclusion: These results show that caesium

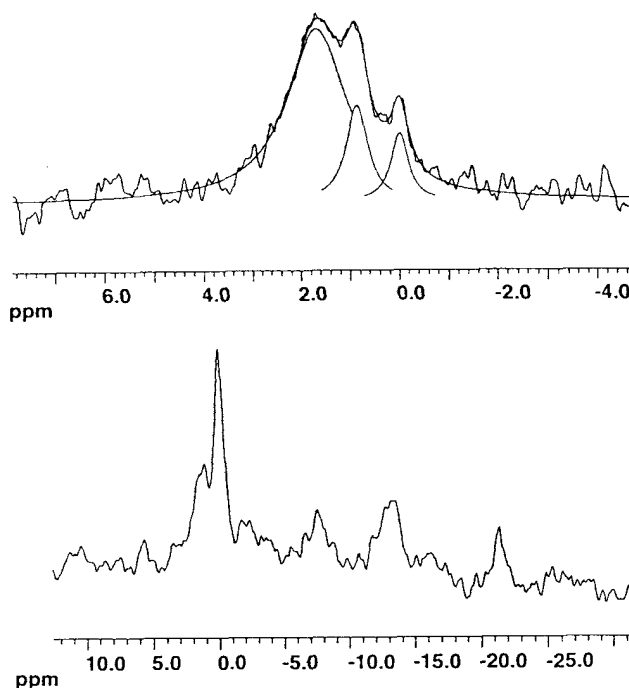


Figure 3 Spectra acquired from hepatocytes in agarose threads. ^{133}Cs spectrum (top) shows three peaks, with the peak at lowest frequency corresponding to caesium in the perfusate. The presence of high energy phosphate compounds in ^{31}P spectra (bottom) was used as an indication of cell viability.

NMR can be used to demonstrate compartmentation of caesium (potassium) in tissues. The chemical shifts of caesium in the intracellular compartments suggest an exchange rate of less than 32 Hz, comparable to that seen between the extra and intracellular compartments. The response of the tissue to metabolic regulation involves a change in the environment within the compartments and redistribution between the compartments. The size and chemical shift of the peaks, together with the changes in intensity with metabolic regulation suggest the two intracellular peaks represent substantial intracellular factors such as mitochondria and cytosol.

References

1. Shehan, B. P.; Wellard, R. M.; Adam, W. R.; Craik, D. J. *J. Magn. reson. Med.* **1993**, *30*, 573-582.
2. Davis, D. G.; Murphy, E.; London, R. E. *Biochem.* **1988**, *27*, 3547-3551.
3. Vogel, S.; Sperelakis, N. *Am. J. Physiol.* **1978**, *235*, H46-H51.
4. Foxall, D. L.; Cohen, J. S. and Mitchell, J. B. *Exp. Cell Res.* **1984**, *154*, 521-9.

A ^{27}Al NMR Study of Aluminium: Humic Substances Interactions

James Hook, Lu Xiaoqiao and R. F. Howe

Department of Physical Chemistry, School of Chemistry, University of New South Wales, PO BOX 1. Kensington, NSW 2052

Introduction

The aqueous chemistry of aluminium is a major interest in acid soils and surface waters with pHs < 5.5 because of the mobility, bio-availability and ecological impact of this metal on the environment¹. The toxicity of aluminium in soils and surface waters is dependent on the concentration of aluminium, pH, and the presence of complexing agents.²⁻⁷ In the environment, the complexation of humic substances with aluminium ion is of importance since speciation of the aluminium ion and its overall concentration have a significant influence on biochemical processes involving aluminium, the transport of aluminium in the environment, and the accumulation of aluminium in sediments.⁹⁻¹¹

In this study, the interactions of humic substances with Al(III) were studied by ^{27}Al NMR spectroscopy. In order to establish the binding nature of functional groups involved in the formation of aluminium complexes observed in humic substances, some hydroxy carboxylic acids were studied as models.

Experimental

Humic substances were extracted by the method described by Thurman¹² from swamp water collected from the vicinity of Smith Lake in New South Wales.

^{27}Al NMR spectra were recorded at 78.14 MHz on ACP-300 spectrometer at 300 K using $[\text{Al}(\text{H}_2\text{O})_6]^{3+}$ (1.0 M $\text{AlCl}_3 \cdot 6\text{H}_2\text{O}$ solution in 20 % D_2O at pH 2.0) as an external reference. Samples were recorded in 10 mm tubes with a concentric 5 mm tube containing D_2O for a lock.

Results

Al(III) ion hydrolyses and a series of hydrolysis products will form as pH of Al(III) ion solution is raised. ^{27}Al NMR spectra of Al(III) ion solutions at various pH were recorded under various conditions. Several hydrolytic species of Al(III) have been identified. The peak with chemical shift at -0 ppm ($W_{1/2} = -12$ Hz) is attributed to the combination of the monomer cations, $[\text{Al}(\text{H}_2\text{O})_6]^{3+}$ and $[\text{Al}(\text{H}_2\text{O})_5\text{OH}]^{2+}$; the peak with chemical shift -3.0 ppm is due to the dimer species, $\text{Al}_2(\text{OH})_4^{2+}$; the peak with chemical shift at -62.5 ppm is due to the soluble $[\text{AlO}_4\text{Al}_{12}(\text{OH})_{24}(\text{H}_2\text{O})_{12}]^{7+}$ cation; and the peak with chemical shift -80 ppm is due to $\text{Al}(\text{OH})_4^-$.

On addition of humic substances to Al(III) ion solution, binding of Al(III) to the ligands in humic substances is evident. The ^{27}Al NMR spectra of Al(III) added to humic substances from peat, soil and brown coal illustrate that these complexes formed have similar chemical shifts and their NMR parameters are summarised in Table 1. The complexes of HS-Al with more ligands are observed as the ratio of humic substance to Al(III) is increased. Typical

spectra of Al(III) with swamp humic substance solution are shown in Figure 1.

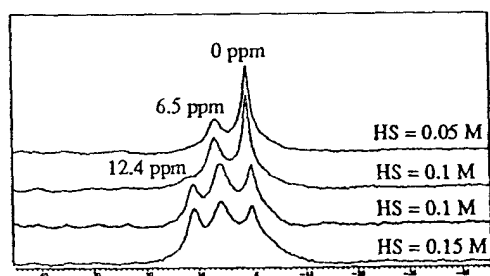


Figure 1. Room temperature ^{27}Al NMR spectra of 6.0 mM Al(III) in the presence of humic substance solution from swamp water at pH 3.0.

Table 1. ^{27}Al NMR Parameters of Al Complexes in Humic Substances from Various Sources.

Sample	C_{Al} (mM)	pH	^{27}Al (ppm)	$W_{1/2}$ (Hz)
Swamp water	6.0	3.0	-0	276
			6.5	356
			12.4	302
			16.5	220
Peat	10.0	3.0	-0	130
			5.8	264
Surface soil	10.0	3.0	-0	45
			6.5	282
Brown coal	10.0	3.0	-0	150
			6.1	324
			11.4	276

The ^{27}Al NMR spectra (Figure 2) of HS-Al recorded as a function of pH show that complexes of Al(III) in the humic substance solutions are affected by pH over a pH range from 2.5 to 5. At pH above 5, no signals were detected, indicating that complexes of Al(III) with humic substances are not stable at high pH.

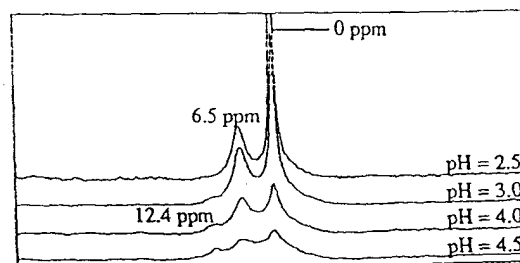


Figure 2. Room temperature ^{27}Al NMR spectra of 6.0 mM Al(III) with 0.10 M humic substances at various pH.

^{27}Al NMR spectra of Al(III) ion with some hydroxy carboxylic acids, such as oxalic acid, tartaric acid,

citric acid, salicylic acid, maleic acid and phthalic acid as possible ligands were also recorded under different conditions. Typical ^{27}Al NMR spectra of oxalic acid at various molar ratios of L/Al(III) and pH are shown in Figure 3 and 4 respectively. The NMR parameters of Al(III) ion with these acids are listed in Table 2.

Table 2. ^{27}Al NMR Parameters of Aluminium Complexes in the Carboxylic Acids.

C_{Al} (mM)	pH	Acids	$\delta^{27}\text{Al}$ (ppm)	$W_{1,2}$ (Hz)	Assignment
10.0	3.0	Oxalic	-0	32	$[\text{Al}(\text{H}_2\text{O})_6]^{3+}$
			6.7	180	$[\text{Al}(\text{H}_2\text{O})_4\text{L}]^+$
			11.5	238	$[\text{Al}(\text{H}_2\text{O})_2\text{L}_2]^-$
			16.4	157	$[\text{AlL}_3]^{3-}$
10.0	3.0	Citric	-0	-	$[\text{Al}(\text{H}_2\text{O})_6]^{3+}$
			-9.9	~760	$[\text{Al}(\text{H}_2\text{O})_4\text{L}]^+$
			-21.0	~900	$[\text{Al}(\text{H}_2\text{O})_2\text{L}_2]^-$
10.0	3.0	Tartaric	-0	71	$[\text{Al}(\text{H}_2\text{O})_6]^{3+}$
			-12.0	~800	$[\text{Al}(\text{H}_2\text{O})_4\text{L}]^+$
			-20.0	~1000	$[\text{Al}(\text{H}_2\text{O})_2\text{L}_2]^-$
10.0	3.0	Salicylic	-0	-	$[\text{Al}(\text{H}_2\text{O})_6]^{3+}$
			-3.4	680	$[\text{Al}(\text{H}_2\text{O})_4\text{L}]^+$
10.0	3.0	Maleic	-0	38	$[\text{Al}(\text{H}_2\text{O})_6]^{3+}$
			-2.1	117	$[\text{Al}(\text{H}_2\text{O})_4\text{L}]^+$
10.0	3.0	Phthalic	-0	37	$[\text{Al}(\text{H}_2\text{O})_6]^{3+}$
			-2.2	212	$[\text{Al}(\text{H}_2\text{O})_4\text{L}]^+$

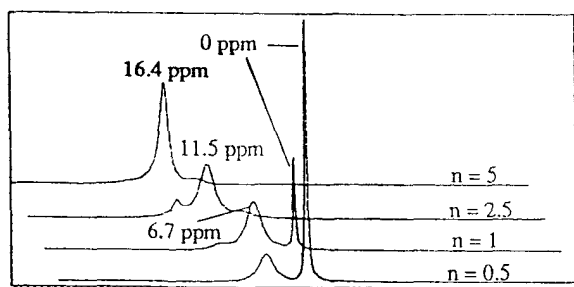


Figure 3. Room temperature ^{27}Al NMR spectra of 12 mM Al-oxalic complexes at various molar L/Al ratios (n) at p 3.0.

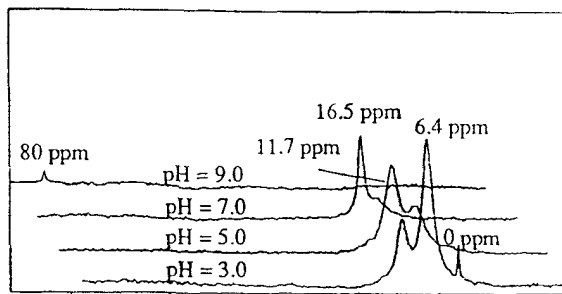


Figure 4. Room temperature ^{27}Al NMR spectra of 12 mM Al with 10 mM oxalic acid at various pH.

Conclusions

In this study, ^{27}Al NMR spectroscopy has been used to examine aluminium speciation and the uptake of aluminium by humic substances from various sources.

In the presence of humic substances up to three different ^{27}Al signals are observed at 6.5, 12.4 and 16.0 ppm. The concentration of complexed aluminium in the presence of swamp humic substances depends on the concentration of humic substances and solution pH.

Similar spectra were obtained with humic substances extracted from surface soil, peat, and brown coal, indicating that the presence of common aluminium binding sites in these humic substances.

Comparison of ^{27}Al NMR spectra of aluminium complexed to different carboxylic acid suggests that sites similar to oxalic acid are responsible for binding aluminium. The three different ^{27}Al signals are assigned to aluminium bound to one, two or three dicarboxylic acid ligands respectively.

Significant complexation of aluminium occurs at low pH, suggesting that humic substances play an important role in the transport of this metal in acidic environments.

References

- (1). G. Sposito (Ed.), 1989. The Environmental Chemistry of Aluminium, CRC, Press, Boca Raton, FL.
- (2). C. T. Driscoll, 1984. Int. J. Environ. Anal. Chem., **16**, 267.
- (3). A. K. Alva, M. E. Summner, Y. C. Li, W. P. Miller, 1989. Soil Sci. Soc. Am. J., **53**, 38.
- (4). R. S. Cameron, G. S. P. Ritchie, A. D. Robson, 1986. Soil Sci. Soc. Am. J., **50**, 1231.
- (5). N. V. Hue, G. R. Craddock and F. Adams 1986. Soil Sci. Soc. Am. J., **50**, 28.
- (6). D. R. Parker, T. B. Kinraide, L. W. Zelany, 1988a. Soil Sci. Soc. Am. J. **52**, 67.
- (7). D. R. Parker, T. B. Kinraide, L. W. Zelany, 1988b. Soil Sci. Soc. Am. J. **52**, 438.
- (8). C. L. Chakrabarti, Y. Lu, J. Cheng, M. H. Back, W. H. Schroeder, 1993. Anal. Chim. Acta., **276**, 47.
- (9). B. J. Plankey and H. H. Patterson, 1988. Environ. Sci. Technol., **22**, 1454.
- (10). G. L. Kerven, D. G. Edwards, C. J. Asher, P. S. Hallman and S. Kokot. 1989. Aust. J. Soil Res., **27**, 79.
- (11). M. S. Shuman, 1992. Environ. Sci. Technol., **26**, 593.
- (12). R. L. Thurman, "Organic Geochemistry of Nature Waters", 1985.

Calendar of Forthcoming Conferences in Magnetic Resonance

September 29-October 4, 1996

*Missouri Magnetic Resonance Symposium
(MMRS) and FACSS Meeting, Kansas City,
Missouri (USA)*

For information contact:

(MMRS) Frank D. Blum
Dept. of Chemistry
Univ. of Missouri-Rolla
Rolla, MO 65409-0010
Phone: 573-341-4451
e-mail: fblum@umr.edu
FACSS
198 Thomas Johnson Dr. S-2
Frederick, MD 21702-4317

October 18-20, 1996

*Beckman Institute Workshop on MR Signal
Processing, University of Illinois, Urbana, Illinois,
(USA)*

For information contact:

Ms. Judy Jones
Beckman Institute
405 N. Mathews Avenue
Urbana, IL 61801
Phone: (217) 244-5582
Fax: (217) 244-8371
e-mail: jjones@director.beckman.uiuc.edu

October 20-27, 1996

*The European Initiative for Training in NMR -
Theory and Applications of Nuclear and Electron
Relaxation, Villa Gualino, Torino (Italy)*

For information contact:

Dr. Mauro Fasano
NMR Laboratory
University of Torino
e-mail: fasano@silver.ch.unito.it

December 8-13, 1996

*The European Initiative for Training in NMR -
NMR of Polymers (Solution and Solide-state),
Villa Gualino, Torino (Italy)*

For information contact:

Prof. Silvio Aime
NMR Laboratory
University of Torino
e-mail: aime@silver.ch.unito.it

May-25-31, 1997

*7th Chianti Workshop on Magnetic Resonance
Nuclear and Electron Relaxation, Pisa (Italy)*

For information contact:

Lucia Banci
University of Florence
Department of Chemistry
Via Gino Capponi 7
50121 Firenze, Italy
Phone: +39-55-275550
fax: +39-55-2757555
e-mail: lucia@risc1.lrm.fi.cnr.it

Elena Gaggelli
University of Siena
Department of Chemistry
Pian dei Mantellini 44
53100 Siena, Italy
Phone: +39-577-298008
fax: +39-577-280405
e-mail: gagelli@unisi.it

March 23-27, 1997

*38th ENC (experimental NMR Conference),
Orlando, Florida, (USA)*

For information contact:

ENC
1201 Don Diego Avenue
Santa Fe, NM 87501
Phone: (505) 989-4573
Fax: (505) 989-1073

The editor would be pleased to receive notices of future meetings in the field of magnetic resonance so that they could be recorded in this column.

Instructions for Authors

Because of the ever increasing difficulty of keeping up with the literature there is a growing need for critical, balanced reviews covering well-defined areas of magnetic resonance. To be useful these must be written at a level that can be comprehended by workers in related fields, although it is not the intention thereby to restrict the depth of the review. In order to reduce the amount of time authors must spend in writing we will encourage short, concise reviews, the main object of which is to inform non-experts about recent developments in interesting aspects of magnetic resonance.

The editor and members of the editorial board invite reviews from authorities on subjects of current interest. Unsolicited reviews may also be accepted, but prospective authors are requested to contact the editor prior to writing in order to avoid duplication of effort. Reviews will be subject to critical scrutiny by experts in the field and must be submitted in English. Manuscripts should be sent to the editor, Dr. David G. Gorenstein, Sealy Center for Structural Biology, The University of Texas Medical Branch, 301 University Blvd, Route 1157, Galveston, Texas 77555-1157 USA. (409) 747 6800. Fax No. (409) 747 6850.

MANUSCRIPTS must be submitted in triplicate (one copy should be the original), on approximately 22×28 cm paper, type-written on one side of the paper, and double spaced throughout. If the manuscript cannot be submitted on computer tapes, floppy disks, or electronically (see below), please type with a carbon ribbon using either courier 10 or 12, gothic 12, or prestige elite type face with 10 or 12 pitch. All pages are to be numbered consecutively, including references, tables, and captions to figures, which are to be placed at the end of the review.

ARRANGEMENT: Considerable thought should be given to a logical ordering of the subject matter and the review should be divided into appropriate major sections, and subsections, using Roman numerals, capital letters, and Arabic numerals respectively. A table of contents should be included.

TABLES: These are to be numbered consecutively in the text with Arabic numerals. Their place of insertion should be mentioned in the text, but

they are to be placed in order at the end of the paper, each typed on a separate sheet. Each table should be supplied with a title. Footnotes to tables should be placed consecutively, using lower case letters as superscripts.

FIGURES are also to be numbered consecutively using Arabic numerals and the place of insertion mentioned in the manuscript. The figures are to be grouped in order at the end of the text and should be clearly marked along the edge or on the back with figure number and authors' names. Each figure should bear a caption, and these should be arranged in order and placed at the end of the text. Figures should be carefully prepared in black ink to draftsman's standards with proper care to lettering (typewritten or freehand lettering is not acceptable). Graphs should include numerical scales and units on both axes, and all figures and lettering should be large enough to be legible after reduction by 50-60%. Figures should be generally placed on sheets of the same size as the typescript and larger originals may be handled by supplying high-contrast photographic reductions. One set of original figures must be supplied; reproduction cannot be made from photocopies. Two additional copies of each figure are required. Complex molecular formula should be supplied as ink drawings.

REFERENCES to the literature should be cited in order of appearance in the text by numbers on the line, in parentheses. The reference list is to be placed on separate sheets in numerical order at the end of the paper. References to journals should follow the order: author's (or authors') initials, name, name of journal, volume number, page, and year of publication. The abbreviation of the journal follows that used in the Chemical Abstracts Service Source Index. References to books should include in order: author's (or authors') initials, name, title of book, volume, edition if other than the first, publisher, address, date of publication, and pages.

FOOTNOTES should be used sparingly and only in those cases in which the insertion of the information in the text would break the train of thought. Their position in the text should be marked with a superscript Arabic numeral and the footnotes should be typed at the bottom of the relevant page in the text, separated from the latter by a line.

SYMBOLS AND ABBREVIATIONS:

Mathematical symbols should be typewritten wherever possible. Greek letters should be identified in pencil in the margin. In reviews containing a number of mathematical equations and symbols, the author is urged to supply a list of these on a separate sheet for the assistance of the printer; this will not appear in print. Standard abbreviations will follow the American Chemical Society's HANDBOOK FOR AUTHORS names and symbols for units.

PERMISSIONS: It is the responsibility of the author to obtain all permissions concerned with the reproduction of figures, tables, etc, from copyrighted publications. Written permission must be obtained from the publisher (not the author or editor) of the journal or book. The publication from which the figure or table is taken must be referred to in the reference list and due acknowledgement made, e.g. reprinted by permission from ref. (00).

REPRINTS: Thirty reprints of a review will be supplied free to its senior author and additional reprints may be purchased in lots of 100.

INSTRUCTIONS FOR SUBMITTING MANUSCRIPTS ON FLOPPY DISKS OR ELECTRONICALLY: If you have used a word processor to type your manuscript, please forward your manuscript after review and revision, in a computer readable form. Floppy disks or tapes readable on IBM, DEC, SUN, Silicon Graphics, or MacIntosh computers are acceptable. Submission via e-mail (address david@nmr.utmb.edu) is also recommended. You may use ftp anonymous to nmr.utmb.edu (129.109.73.3) and deposit your manuscript in /pub/bulletin.

Please supply us with the code for interpreting superscripts, greeks, etc. on your word processor.

**INTERNATIONAL SOCIETY OF MAGNETIC RESONANCE
(ISMAR)**

MEMBERSHIP APPLICATION AND CALL FOR DUES

Name and Address (Telephone & Fax numbers, e-mail) of ISMAR Member

If this is a new membership application, please check box

If you wish to be registered as a member of the Division of Biology and Medicine,
in addition to ISMAR itself at no extra charge, please check box.

MEMBERSHIP DUES (Yearly)

Regular Member \$25.00
Bona Fide Student \$10.00

1994 \$ _____
1995 \$ _____
1996 \$ _____
1997 \$ _____

SUBSCRIPTION TO "BULLETIN OF MAGNETIC RESONANCE" (Yearly)

ISMAR Members \$30.00
Non-Members \$90.00
Libraries \$90.00

Volume 16 (1994) \$ _____
Volume 17 (1995) \$ _____
Volume 18 (1996) \$ _____

TOTAL \$ _____

**Send this completed form with your
check in US\$ made payable to**

(or)

**Provide your
Mastercard or Visa Account**

International Society of Magnetic Resonance

Prof. Regitze R. Vold, Treasurer
Chemistry & Biochemistry
University of California, San Diego
9500 Gilman Drive
La Jolla, CA 92093-0359 USA

(619) 534-0200; FAX (619) 534-6174
e-mail: rrvold@ucsd.edu

_____ Mastercard _____ Visa

Account # _____

Expires on _____
(month/year)

Signature _____

(Do not wire funds. They will no longer be accepted)